AN INVESTIGATION OF MAGNETIC AND SEMICONDUCTOR MATERIALS WITH CONSTRAINED ARTIFICIAL SUPERSTRUCTURES USING ELECTRON IMAGING TECHNIQUES.

by Stewart John Hefferman

Submitted for the degree of Ph.D. at the University of Glasgow.

January 1991

Any fool can tell the truth, but it requires a man of some sense to know how to lie well.

Samuel Butler, "Notebooks" (1912)

Man will occasionally stumble over the truth, but most times he will pick himself up and carry on.

Winston Churchill

CONTENTS

Acknowledgements

There are many people who contributed (in many different ways!) to the 100 or so pages under this one.

Firstly, I would like to thank certain people who helped above and beyond.... my supervisor, Prof. John Chapman, who give me time and advise whenever needed. Thanks are also due to Prof. R. P. Ferrier for his encouragement (not only to submit!!) and the provision of the electron microscopy facilities at the Solid State group at the University of Glasgow. I am deeply indebted also to Profs. C.D.W. Wilkinson and S.P. Beaumont for the provision of specimen preparation facilities in the Department of Electrical Engineering.

Special mention should also be given to Dr. S. McVitie for the many useful hours spent discussing the work, and to Mr. M. Foad who tirelessly prepared quantum wire specimens.

I would also like to thank Prof. Dr. A. Hubert at the University of Erlangen, Germany, for the use of the M-O facilities. In particular, thank you to M. Rührig who showed me how to use the equipment, and to W. Rave whose programmes were used to produce certain results.

I must take this opportunity to thank Dr. Joe Zweck (for being a very good host!!) and to Prof. Dr. H. Hoffmann for the use of the M-O and VSM facilities at the University of Regensburg. Various other people at Regensburg made the visit most enjoyable, so thank you!

During the course of the last three years, there were various people whose help should not go unacknowledged, they are; Mr. D. Mcdonald, Mr. I. McVicar, Mr. J. Simms, Mrs. M. Waterson and last, but by no means least, Mr. A. Young.

I would also like to thank the SERC for the provision of a grant, and to CAMST for financial support during my visit to Erlangen and Regensburg.

It only remains for me to thank the people who give most towards this thesis.....my family. Thank you, thank you for all the support and encouragement you've given me over the years.

DECLARATION

This thesis is a record of the work carried out by me in the Department of Physics and Astronomy at the University of Glasgow. The work described herein is my own, apart from the manufacture of the GaAs quantum well and wire samples, and the manufacture of the Si_3N_4 membranes which were provided by the Department of Electrical Engineering. Some of the work given in this thesis can be found in the following papers:

"Effect of application of fields on the domain structure in small regularly shaped magnetic particles", S. McVitie, J.N. Chapman, S.J. Hefferman and W.A.P. Nicholson, J. de Phys. **49** (1988) C8-1817.

"In-situ magnetising experiments on small regularly shaped particles fabricated by electron beam lithography", S.J. Hefferman, J.N. Chapman and S. McVitie, J. Magn. Magn. Mat. **83** (1990) 223.

"In-situ magnetising experiments on small regularly shaped permalloy particles", S.J.Hefferman, J.N. Chapman and S. McVitie, J. Magn. Magn. Mat. -in press.

"Mapping induction distributions by transmission electron microscopy", J.N. Chapman, S.McVitie and S.J.Hefferman, -accepted for publication in J. Appl. Phys.

"Evaluation of sidewall damage in nanostructures etched in CH_4/H_2 and $SiCl_4$ by direct TEM observation", M. Foad, S.J.Hefferman, J.N.Chapman and C.D.W. Wilkinson, presented in "GaAs and related compounds", Jersey 1990.

This thesis has not been submitted in any previous application for a degree.

SUMMARY

The work described in this thesis presents an analysis of the magnetic and microstructural properties of small devices fabricated by electron beam lithography. By using this type of specimen preparation process, the shapes of the devices to be studied can be controlled precisely. Two different types of devices were examined, viz. small regularly shaped magnetic particles and secondly, GaAs quantum wires. Although the project was initially two pronged, the amount of data available from the experiments on the magnetic particles shifted the balance firmly in their favour. As a result, most of the chapters are devoted to the experiments on the particles and only chapter 7 is given to the GaAs wires. The first chapter of this thesis reviews the basic concepts of ferromagnetism, domain walls and the theoretical, micromagnetic models relevant to the work. Throughout the thesis, techniques available using electron microscopy are used to examine the properties of the small devices. Chapter 2 describes the basic image formation techniques in the conventional transmission electron microscope, (CTEM), and also the techniques used to reveal the magnetic structure of the particles to be studied.

To examine the magnetic structure and behaviour of the small magnetic particles, various experiments were performed using a specially designed magnetising stage which allowed in-situ experiments to be conducted. This stage is also described in chapter 2 as are some theoretical predictions regarding single domain particles.

Chapter 3 describes the specimen fabrication technique, and some basic characterisation of the physical and magnetic properties of the particles and films are given in this chapter. The main body of experimental results on the small magnetic $Ni_{82.5}Fe_{17.5}$ particles are given in chapters 4 and 5. Different sizes of particles are discussed in each chapter, and a different imaging mode is used. In the latter chapter, hysteresis loops from isolated particles are given for a range of different particles.

The previous two chapters described the results on $Ni_{82.5}Fe_{17.5}$ particles. The composition of this alloy results in the domain structure of the particles being influenced greatly by the shape of the particle. To study the influence of a different composition of material on the domain structure and magnetic behaviour of the particles, the particles were also fabricated from cobalt. Experiments were conducted on cobalt particles and the results are given in chapter 6.

Chapter 7 describes the results obtained from an examination of the microstructural properties of Si doped GaAs quantum wires again fabricated using electron beam lithography. The wires were made using two slightly different processes, and the resultant damage to the wires is described in this chapter.

Finally chapter 8 draws some conclusions from the work, and also gives some suggestions for the continuation of the work.

CHAPTER 1

FERROMAGNETISM, DOMAIN WALLS AND MICROMAGNETICS

1.1 FERROMAGNETISM

For many years it has been observed that even in the absence of an applied field, a certain class of materials, ferromagnets, exhibited a non-zero magnetic moment over a specific temperature range. That this value was non-zero implied that there was an alignment of the moments within the material. It had also been observed that the net moment decreased to zero at a well defined temperature, called the Curie temperature, T_C. The first attempt to explain this phenomenon was proposed by Weiss (1907). He suggested that the alignment of the moments was due to an "internal molecular field". In the range of temperatures below T_C, the field is strong enough to overcome the thermal randomising effects. For a typical ferromagnetic material at room temperature, the field must be of the order of 10^9 $kA.m^{-1}$. Weiss proposed that the internal field was indeed this strong, and that it was proportional to $|\underline{\mathbf{M}}|$. ($\underline{\mathbf{M}}$ is the magnetic moment per unit volume, whose units in S.I. are in $A.m^{-1}$.)

A less phenomenological approach to the concept of ferromagnetism was developed by Heisenberg (1928). In this he explained that the origin of the interaction leading to the parallel alignment of the moments was quantum mechanical in nature.

There can be two contributions to the magnetic moment of an atom. The first comes from the orbital motion of the electron as it circles round the nucleus. The second part is due to the intrinsic motion of the electron itself. The spinning electron experiences a magnetic field which arises from the nucleus. This field has the effect of coupling the two angular motions and is referred to as spin-orbit coupling. In the case of e.g. Ni, Fe and Co, the intrinsic spin of the outermost and unpaired 3d electron gives rise

to the atomic moment. In these metals the orbital moment has been quenched and hence the moment is due almost entirely to the spin of the electron. For the rare earth metals, incomplete inner shells can also contribute to the moment through their orbital motion (Nesbitt (1973)).

The presence of a particular distribution of the directions of magnetic moments within a sample is due to the (local) minimisation of the total energy of the system. There are various contributions to this, and these are given in section 1.2. Section 1.3 examines the domain walls commonly found in bulk and thin films. Lastly section 1.4 presents some of the micromagnetic theories relevant to the study undertaken here.

1.2 CONTRIBUTIONS TO THE TOTAL ENERGY OF A FERROMAGNETIC SYSTEM

1.2.1 EXCHANGE ENERGY

According to the Pauli exclusion principle, the product of the spin and spatial wavefunctions must be anti-symmetric. Hence as the electrostatic potential associated with two atoms is dependent on their separation (i.e. on the overlap of their spatial wavefunctions) it is also related to their spins.

The exchange energy, U, between two atoms having spins $\underline{\mathbf{S}}_i$ and $\underline{\mathbf{S}}_j$, separated by a distance r_{ij}, is given by the expression;

$$U = -2\, J_{ex}(r_{ij})\ \ \underline{\mathbf{S}}_i \cdot \underline{\mathbf{S}}_j \qquad (1.1)$$

where $J_{ex}(r_{ij})$ is the exchange integral. In all but rare earth metals the exchange integral falls off as the distance between the atoms increases. Hence when considering a collection of moments, only nearest neighbour interactions need be considered. It is obvious from eqn. (1.1) that for a positive value of the exchange integral, as is the case for a ferromagnetic specimen, U is minimised for a parallel alignment of $\underline{\mathbf{S}}_i$ and $\underline{\mathbf{S}}_j$.

1.2.2 MAGNETOSTATIC ENERGY

The magnetostatic energy in a ferromagnetic system arises from the interaction of the magnetisation, $\underline{\mathbf{M}}$, with a magnetic field. The total field $\underline{\mathbf{H}}$ can arise from an external source $\underline{\mathbf{H}}_o$ or from free magnetic dipoles or charge. There are two possible sources of magnetic charge, surface and volume charge. These sources give rise to a magnetic field $\underline{\mathbf{H}}_d(\underline{\mathbf{R}})$, the form of which is given by;

$$\mathbf{H}_d(\mathbf{R}) = (1/4\pi) \int_\tau \frac{-\nabla . \underline{\mathbf{M}}}{R^2} \, d\tau + (1/4\pi) \int_S \frac{(\underline{\mathbf{M}} . \underline{\mathbf{n}})}{R^2} \, dS \quad (1.2)$$

where the magnetisation within a sample is given by $\underline{\mathbf{M}}$ and the integration is performed over a body of volume τ and surface area S. $\underline{\mathbf{R}}$ is the position vector from the source to the field point, and $\underline{\mathbf{n}}$ is the unit vector normal to the surface. This field $\underline{\mathbf{H}}_d$ extends both inside and outside the body. Inside the body however it opposes the direction of magnetisation and is therefore referred to as a demagnetising field. The magnetostatic energy, E_m, is given by the expression;

$$E_m = - (\mu_o/2) \int_\tau \underline{\mathbf{M}} . \underline{\mathbf{H}}_d \, d\tau \quad (1.3)$$

μ_o is the permeability of free space and is equal to $4\pi.10^{-7}$ $H.m^{-1}$.
In the case of an externally applied field the expression must be modified, and the new expression is;

$$E_m = - \mu_o \int_\tau \underline{\mathbf{M}} . \underline{\mathbf{H}} \, d\tau \quad (1.4a)$$

$$\underline{H} = \frac{\underline{H}_d}{2} + \underline{H}_0 \qquad (1.4b)$$

1.2.3 ANISOTROPY ENERGY

In some materials, the angle along which the magnetisation vector will preferentially lie is dependent in the crystal structure. These preferred directions are called magnetic easy directions or axes. The anisotropy term describes the energetic favourability of specific orientations of the magnetisation with respect to the crystal axes. In the case of a cubic crystal, the expression for the anisotropy energy, E_a, is given by;

$$E_a = \int_\tau \{ K_1(\alpha^2\beta^2 + \beta^2\gamma^2 + \gamma^2\alpha^2) + K_2\,\alpha^2\beta^2\gamma^2 \}\, \partial\tau \qquad (1.5)$$

where α, β, and γ, are the directional cosines of the magnetisation with respect to the crystal axes. In eqn. (1.5), it is assumed that the crystal and coordinate axes are co-incident. K_1 and K_2 are the anisotropy constants of the material.

A fourth energy term, the magnetostrictive energy may also be present. This arises when a change in the magnetisation of a sample is caused by stress or strain which give rise to an elastic tension. As a consequence of the materials used in this study, (see Chapter 3), this term is of negligible importance. The three main terms are those in sections 1.2.1 to 1.2.3.

1.2.4 EFFECT OF THE ENERGY TERMS ON THE DISTRIBUTION OF MOMENTS

Let us now examine the influence of the above energy terms on the potential distribution of moments within a body. If we consider a uniformly magnetised body, e.g. fig. 1.1(a), its exchange energy is minimised. However there is a large amount of magnetostatic energy due to the surface charge on faces **A** and

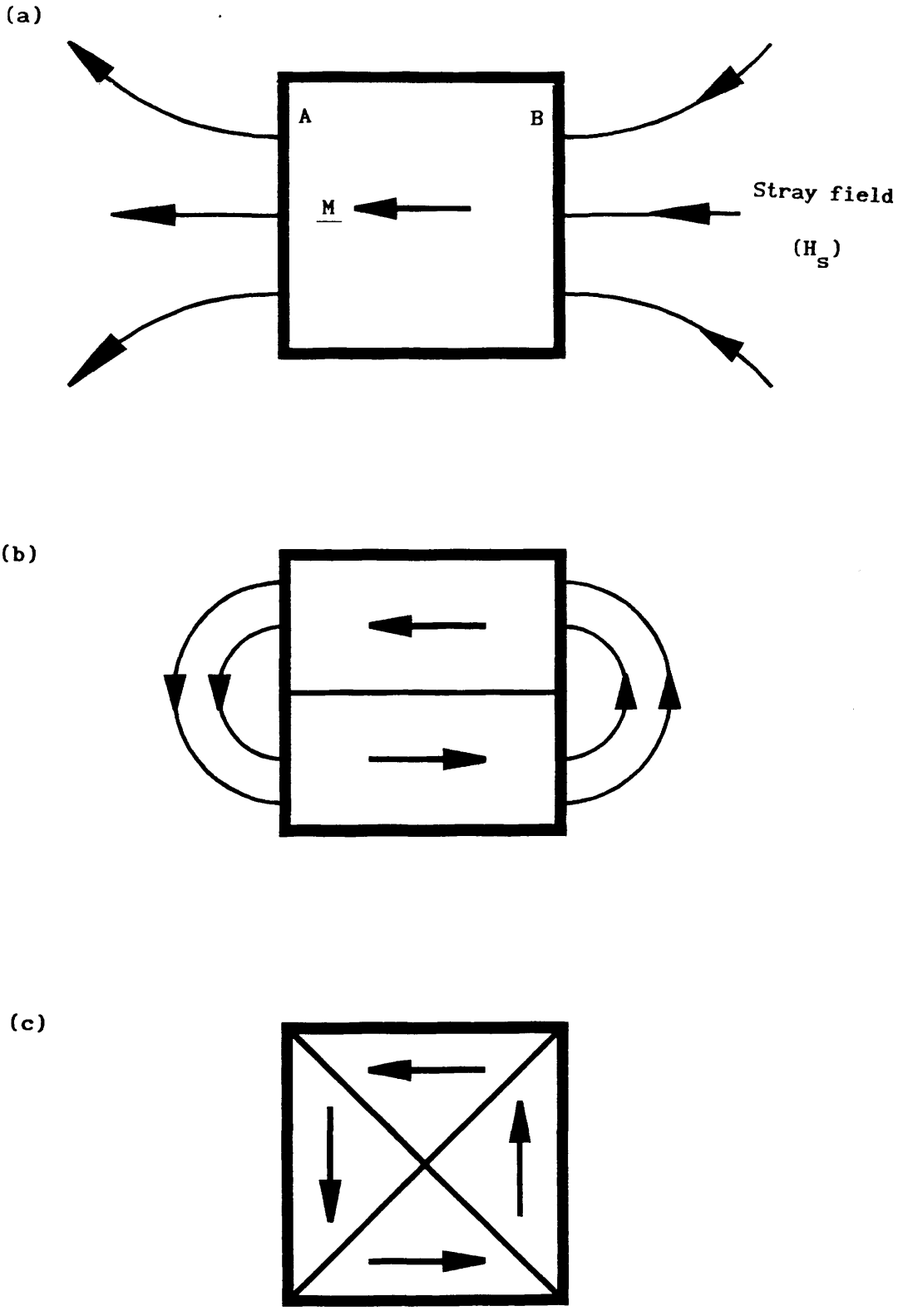

Fig. 1.1 (a) A uniformly magnetised particle.

(b) A particle with two oppositely magnetised domains.

(c) A particle with a solenoidal domain structure.

B. In order to decrease this term, the body may sub-divide into two regions, called domains, as shown in fig. 1.1(b). Domains are regions in which the magnetisation is constant in both magnitude and direction, and they are separated by a transition region called a domain wall in which the magnetisation rotates from one direction to the other. Domain walls are dealt with more fully in section 1.3. The presence of a domain wall will increase the exchange and anisotropy energy, but decrease the magnetostatic energy. A third possible domain structure is that of fig. 1.1(c). In structures of this type, called solenoidal distributions, no surface or volume charge is present, although the total length of domain wall has increased. Whether a particle will adopt fig. 1.1(a), (b), (c), or indeed some other distribution will be determined by a (local) minimisation of the total energy, the contributions to which were given above.

The rotation of moments in a domain wall produces an energy density per unit area. The contributions to this term arise from the exchange and anisotropy energies. It is sometimes convenient to express the energy contributions due to the presence of a domain wall in the form of a "domain wall energy", σ ($J.m^{-2}$), This quantity, σ, is related to the angle through which the magnetisation vector rotates as it crosses the wall, and also to the thickness and material comprising the sample.

1.3 DOMAIN WALLS

A domain wall is a region which separates adjacent domains. In this region the magnetisation vector rotates from one direction to another. The exact form that the domain wall can adopt is a complex problem relating the exchange, anisotropy and magnetostatic energies. There are four types of wall commonly met, and these will be described in sections 1.3.1 to 1.3.4.

1.3.1 BLOCH WALLS

The first model which attempted to explain the structure of domain walls was proposed by Bloch (1932). In this model, the angle of the magnetisation vector within the wall is dependent only on a co-ordinate normal to the plane of the wall itself, fig. 1.2. The magnetisation rotates about the x axis and the structure is such that the wall is divergence free, i.e. $\nabla . \underline{M} = 0$. It can be seen that this type of model is only one dimensional in nature. Contributions to the total energy come only from exchange and anisotropy terms. It is assumed that for bulk specimens, the magnetostatic energy from the surface charge at the top and bottom faces can be neglected. (Although this is true for bulk specimens, it is not in the case of thin films. This point will be discussed further in section 1.3.2).

1.3.2 NEEL WALLS

It was pointed out by Neel (1955) that the magnetostatic energy from the opposite surfaces of a Bloch wall could not be neglected in the case of thin films. He therefore proposed that a different type of wall should be present in sufficiently thin samples. In this type of wall, the magnetisation rotates about an axis perpendicular to the plane of the film, as shown in fig. 1.3. Although this type of wall avoided surface charge, it is clearly not divergence free.

Considerable work was directed towards predicting the true structure and energy of Neel walls, (Collette (1964), Riedel and Seger (1971), Kirchner and Doring (1968)), mainly due to the discovery by Feldkeller (1963) that they were much broader than originally predicted by Neel's model. Initial one dimensional models were superceded by a two dimensional approach although it is generally accepted that this type of wall can be adequately represented approximately by a one-dimensional function. From the models it became apparent that Neel walls were in fact composed of three distinct regions; a

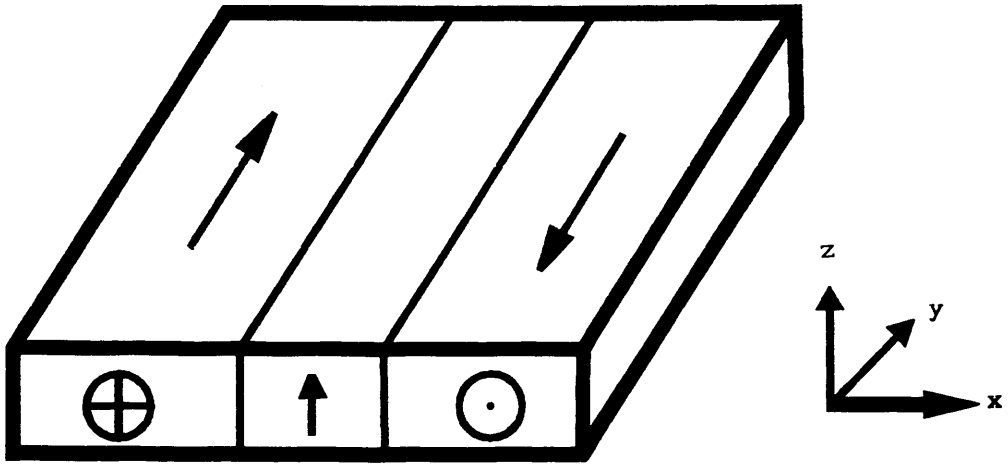

Fig. 1.2 Schematic representation of a Bloch wall.
(The rotation axis is the x-axis.)

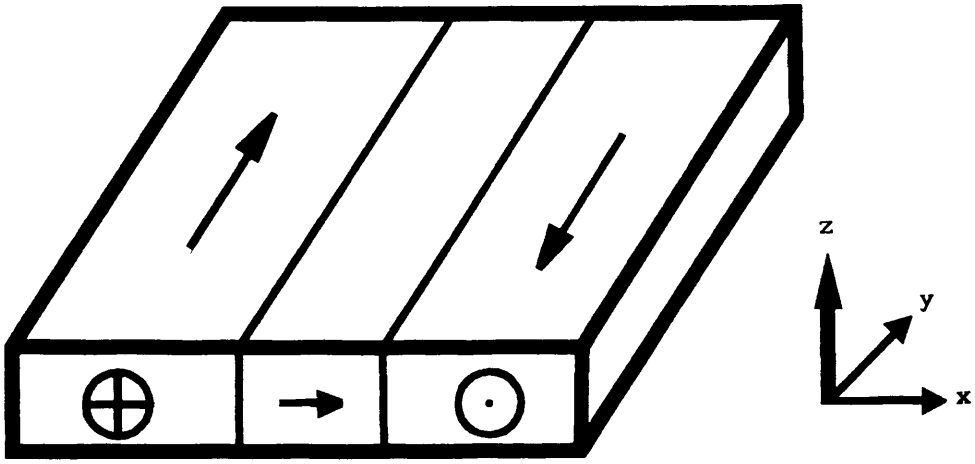

Fig. 1.3 Schematic representation of a Neel wall. (The rotation axis is in the z-axis.)

central core in which the bulk of the rotation takes place, and two long "tails" in which the magnetisation vector gradually rotates over a large distance. The width of the resultant domain wall is dependent, among other factors, on the thickness of the sample.

The essential difference in the two types of wall presented above lies in the axis about which the magnetisation vector rotates.

1.3.3 TWO DIMENSIONAL VORTEX WALLS

Bloch's initial model, as mentioned, had a one dimensional character. The true nature of walls in thin films of finite thicknesses was only revealed when two dimensional models for magnetically soft materials were proposed by LaBonte (1969). In this paper the essential difference over the one-dimensional models was that the magnetisation vector was also allowed to vary throughout the thickness of the film. Using such two dimensional models, these "2 dimensional vortex walls" were found to have the expected rotation of moments at the core, but at the top and bottom surfaces, the magnetisation lay in the plane of the film. This is shown schematically in fig. 1.4. These latter features of the wall are often called the Neel components of the Bloch wall, and it should be noted that they have different polarity at opposite surfaces. The energy of LaBonte's wall was about half that of a one dimensional model. There have been many other attempts to predict the structure and energy of 2-D vortex walls. Although these are too numerous to mention, one, that of Hubert (1969) deserves particular note. In this paper he presented a model of a wall in which various parameters were allowed to vary in order to keep the wall stray-field-free. The energy of the wall, contributions to which arose only from the exchange and anisotropy terms, was then minimised. The magnetostatic term arising from the stray field was zero due to the initial assumption that the wall was stray-field-free. The directions of $\underline{\mathbf{M}}$ which he predicted were almost identical to those of LaBonte (1969), indicating that the stray field free

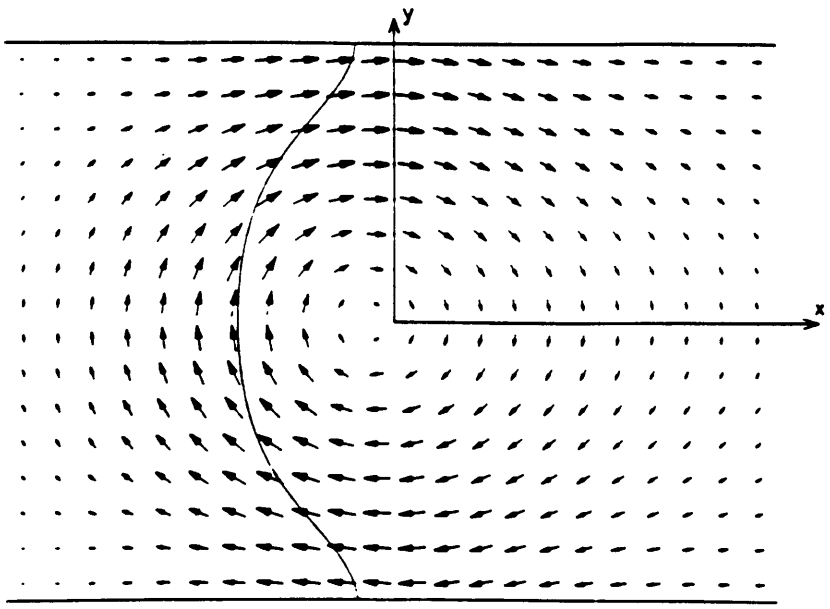

Fig. 1.4 Vortex structure of 180° two dimensional domain wall following Jakubovics (1974). The direction of magnetisation in the domains is along ±z.

The curved line denotes γ=0, where γ is the direction cosine between the z-axis and the x-y plane.

model was an accurate approximation. The surface energy densities that he calculated were considerably lower than previous estimates, especially in the thickness range above 60nm.

1.3.4 CROSS-TIE WALLS

In addition to the two types of wall described above, a third is also possible. This is called a cross-tie wall and is, in essence, a combination of the Neel and Bloch type walls. It was first observed experimentally by Huber (1958). A schematic diagram of a length of this type of wall is shown in fig. 1.5. It can be seen that the main section of the wall is constructed from Bloch lines of alternating polarity. The Bloch lines are separated by Neel walls, again of alternating polarity. The magnetisation around each Bloch line can be convergent or circularly rotating. In the case of the convergent magnetisation, there exists a lower angle domain wall, perpendicular to the main wall section, which is known as a cross-tie. Once again many authors have attempted to model these walls. However due to the complex nature of the magnetisation distribution, this has proved no easy task. The model proposed by Kosinski (1977) is found to agree most closely with experimental observations.

1.3.5 DISCUSSION

Sections 1.3.1 to 1.3.4 outlined the four different types of domain wall which are met. Why a particular sample should adopt one type of domain wall and not another is a complex problem in which the anisotropy, exchange and magnetostatic energies all play important roles. In order to predict which type of wall should be present at a particular thickness, various authors (e.g. Middelhoek (1963)) have calculated the energies of the various types of wall at differing thicknesses. From experimental observations which have been reported for $Ni_{82.5}Fe_{17.5}$, it is found that in the case of 180° walls;

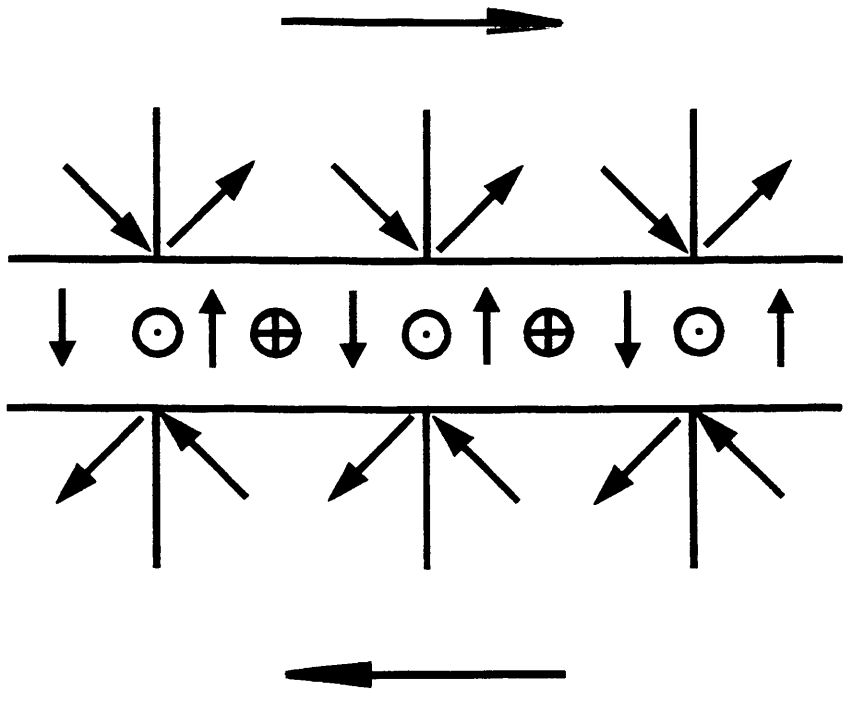

Fig. 1.5 Schematic diagram of a length of cross-tie wall.

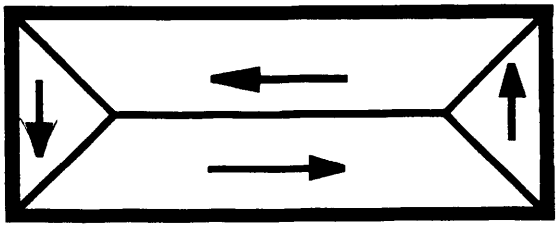

Fig. 1.6 Example of a particle in a Landau-Lifshitz domain structure.

i) 2-D vortex walls occur at thicknesses in excess of 60nm.

ii) Cross-tie walls occur in the range 20nm to 60nm.

iii) Neel walls occur in samples thinner than 20nm.

1.4 MICROMAGNETICS

The existence of domains was proved experimentally by Bitter (1931). The first theoretical attempt to model such distributions was made by Landau and Lifschitz (1935). They considered a body in a demagnetised state, with a solenoidal domain structure. The actual domain structure was determined by minimising the total length of domain wall subject to the conditions imposed by the anisotropy. The resulting domain structure was a flux-closure, or solenoidal type, such as fig. 1.6.

The energy minimisation technique of Landau and Lifschitz was superceded by a self-consistent micromagnetic approach which was formalised by Brown (1962). This new theory was then extended in the case of ideally soft magnetic materials by Van den Berg (1984). Both micromagnetic approaches will be examined briefly, although the latter, being of more relevance, will receive more emphasis.

1.4.1 MICROMAGNETIC THEORY (BROWN 1962)

The theoretical framework which could predict domain structures of particles was detailed by Brown (1962). His theory examined the equilibrium distribution of moments within a body and the stability of such a distribution. The distribution of moments within an equilibrium structure satisfies the condition that the torque on each moment is zero. The model necessarily includes the energy terms detailed in section 1.2. The stability of a particular domain structure is examined by applying a small perturbing force to the distribution of moments. The theory may be stated mathematically in the two equations, given below;

$$\underline{v} \times \left[2A \nabla^2 \underline{v} - \frac{\partial e_k}{\partial \underline{v}} + \mu_o M_s \underline{H} \right] = 0 \text{ in } v \qquad (1.7a)$$

$$\underline{v} \times \left[-2A \frac{\partial \underline{v}}{\partial v} - K_s (\underline{n} . \underline{v}) \underline{n} \right] = 0 \text{ on } S \qquad (1.7b)$$

for a body of volume V, and surface area S. $\underline{\mathbf{H}}$ is the total Maxwell field, e_k is the anisotropy energy density, $\underline{\mathbf{M}}$ has been replaced by $M \underline{v}$, where $\underline{v}$ is a unit vector in the direction of $\underline{\mathbf{M}}_s$ and K_s is the surface anisotropy constant. From eqns. 1.7 it should be possible to calculate the equilibrium domain structure of any body. Unfortunately, due to the non-linearity of the equations, it becomes a very large and complex problem in all but the simplest geometries of very small particles, or when one of the dimensions is made infinite.

1.4.2 MICROMAGNETIC THEORY (Van den Berg 1984)

Brown's theory was extended by Van den Berg for the case of ideally soft magnetic materials. In such materials, it is possible to neglect the anisotropy term, and so the resulting domain structure is determined by the exchange and magnetostatic energies. Because of local saturation he concludes that the exchange energy is a second order effect, and as such can be ignored. From this assumption he then proposes a theoretical framework from which the magnetisation distributions of a body may be determined. The governing equations are given below;

$$\underline{\mathbf{M}} \times \underline{\mathbf{H}} = 0 \qquad \text{in V} \qquad (1.8a)$$

$$\underline{\mathbf{M}} \times \underline{n} = 0 \qquad \text{on S} \qquad (1.8b)$$

$$\underline{\mathbf{M}} . \underline{\mathbf{M}} = M_s^2 \qquad (1.8c)$$

From which it can be shown;

$$\underline{H} = c(x,y,z)\ \underline{M} \qquad \text{in V} \qquad (1.9)$$

Van den Berg also showed that for stable domain structures $c(x,y,z) \geq 0$. This implies that for stable, but not necessarily solenoidal domain structures, $\underline{H}$ is either parallel to $\underline{M}$ or equal to zero. The applicability of this condition in the case of stable non-solenoidal domain structures is discussed in greater detail in Chapter 8. Using eqns. 1.8 and 1.9, he proposed that for solenoidal distributions;

$$\underline{M} \cdot \underline{n} = 0 \qquad (1.10a)$$

$$\nabla \cdot \underline{M} = 0 \qquad (1.10b)$$

The equations 1.9 and 1.10, were then used as the starting point from which, through the use of differential geometry, he derived an algorithm which could predict the (solenoidal) domain structure of a 2 dimensional body. The algorithm is described below, and is illustrated in fig. 1.7;

i) A circle contained entirely within a particle, touching its sides at two or more places, has its centre located at the position of a domain wall.

ii) The locus of all centres, satisfying i) locate the positions of the domain walls.

iii) The direction of magnetisation is easily found by satisfying the two conditions;

a) $\underline{M} \cdot \underline{n} = 0$

b) The normal component of the magnetisation vector across a domain wall must be continuous.

According to this theory, is is also possible to create different solenoidal domain structures by subdividing the body and then applying the algorithm to each part individually. An example of the domain structure when a body is subdivided (along the broken line) is shown in fig. 1.8. As the number of subdivisions increases, the total length of domain wall also increases. It

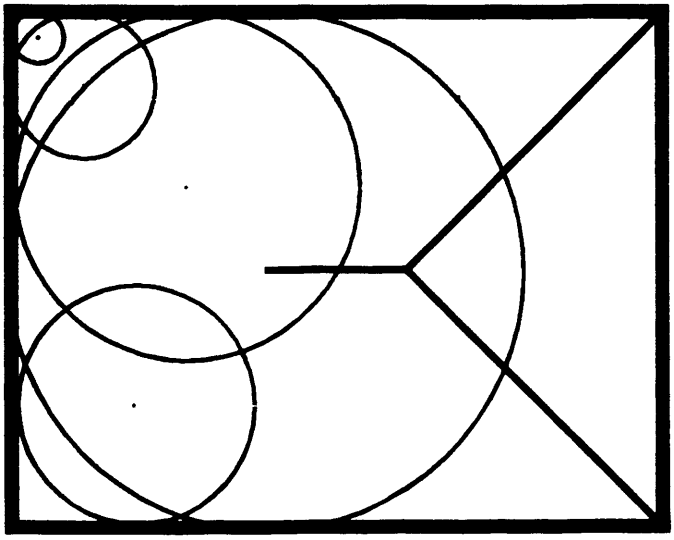

Fig. 1.7 Example of applying the Van den Berg algorithm to a two dimensional particle.

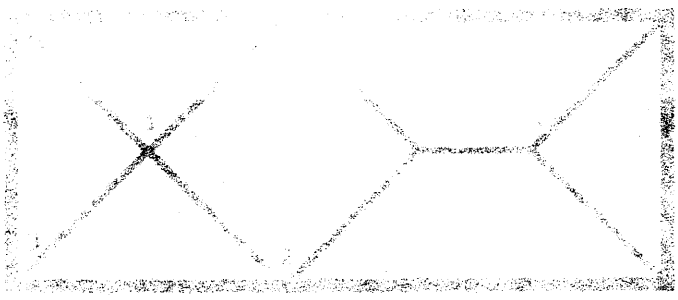

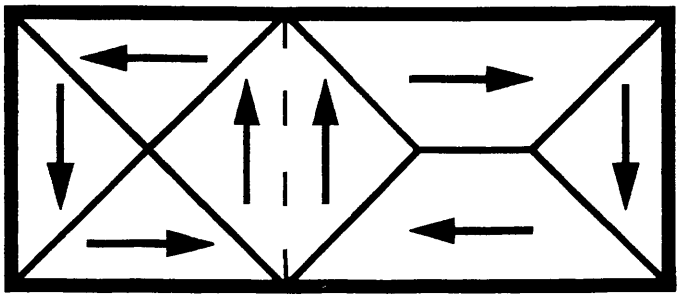

Fig. 1.8 Example of applying the Van den Berg algorithm to two sections of a particle.

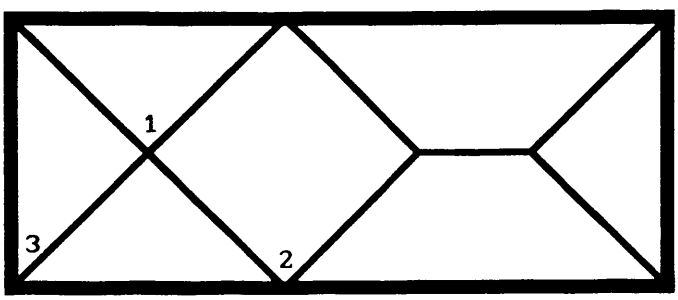

Fig. 1.9 Schematic diagram showing (1), free (2), edge and (3), corner clusters.

should be noted that there is no limit imposed on the number of subdivisions, and so there are an infinite number of domain structures possible. No account of the domain wall energy is included and hence there is no way of predicting any energetic preference for one particular domain structure over another.

1.4.3 CORNER AND EDGE CLUSTERS

Another concept introduced by Van den Berg was that of edge, free and corner clusters. Again the results will be quoted without proof. Examples of free, edge and corner clusters are shown in fig. 1.9. As can be seen, a cluster is a point at which ≥ 1 domain walls intersect with either another wall or with an edge or corner of a particle. Where the intersection occurs determines the type of cluster. Edge and corner clusters will be described in sections 1.4.3. Free cluster are not considered here. A full theoretical treatment of all three types of clusters is given in Van den Berg's Ph.D thesis (1984). However there are specific relationships which govern the behaviour of clusters, and these will be stated below.

1.4.3.1 CORNER CLUSTERS

These can be subdivided into two groups, shown schematically in fig. 1.10. The difference between these two structures is in the directions of $\underline{\mathbf{M}}$ in the domains bounding the edge of the particle. It can be shown formally that;

i) Clusters of type in fig. 1.10(a), (where the magnetisation vectors in the domains bounding the edge of the particle both point towards the cluster) must have an even number of walls originating from the corner cluster.

ii) Clusters of the type in fig. 1.10(b), must have an odd number of domain walls originating from the cluster.

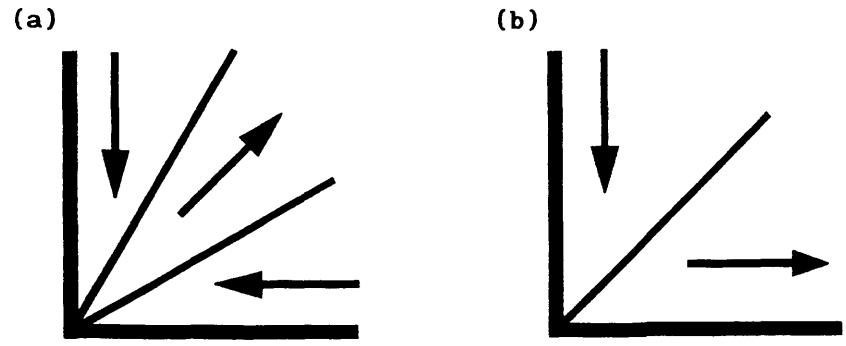

Fig. 1.10 Schematic diagram showing two different types of corner clusters.

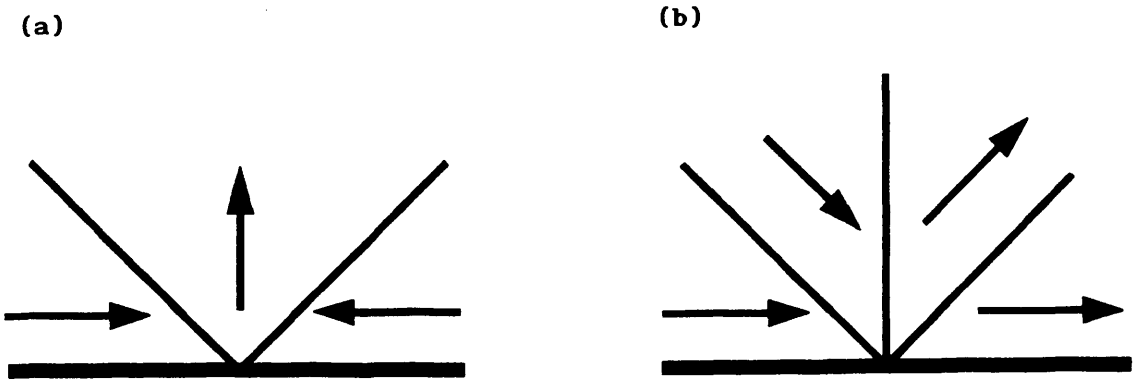

Fig. 1.11 Diagram showing two types of edge clusters.

1.4.3.2 EDGE CLUSTERS

Again these can be divided into two groups, shown in fig. 1.11. In fig. 1.11(a), the two domains bounding the edge of the particle are antiparallel and so the number of domain walls originating from the edge cluster must be an even number. In fig. 1.11(b), the outermost domains are parallel, and in this case an odd number of domain walls must originate from the edge cluster. The position of each domain wall with respect to the particle edge is uniquely determined by the angle of magnetisation in domains adjacent to each other in the cluster. Hence knowledge of the positions of the walls leads to the directions of $\underline{\mathbf{M}}$ in each domain. (There is a 180° ambiguity in the predicted direction of $\underline{\mathbf{M}}$.) The importance of edge clusters is noted, and their relevance to the present study will become more apparent in Chapters 4, 5 and 6 when experimental results will be presented.

CHAPTER 2

IMAGE FORMATION IN A CONVENTIONAL TRANSMISSION ELECTRON MICROSCOPE (CTEM), THE MAGNETISING STAGE AND SINGLE DOMAIN PARTICLES

2.1 INTRODUCTION

In attempting to understand the properties of magnetic materials, it is very important to be able to extract information on the magnetic domain structure of a sample. In this section, techniques which can do this will be discussed along with a brief note on some of the advantages and limitations of each.

The first experimental evidence for the existence of magnetic domains was given by Bitter (1931). The technique involves the colloidal suspension of small acicular magnetic particles which tend to accumulate at regions of the sample where surface magnetic charge is present. The "Bitter" technique reveals the positions of domain walls - although no information is given on the directions of magnetisation within each domain. The resolution of the technique is usually limited by the wavelength of the light illumination source, although it can be performed in a scanning electron microscope, SEM, (Goto et al (1977)). In this case, the colloidal pattern has been dried, and only static domain structures can be examined.

Two techniques which can provide quantitative information on the directions of $\underline{\mathbf{M}}$ in a sample use the Faraday and Kerr effects on plane polarised light. In the former technique, as a plane polarised light source is transmitted through a specimen, the angle of the plane of polarisation rotates, and this change is directly related to the direction of $\underline{\mathbf{M}}$ in the medium. The Faraday technique (Dillon (1958)) can only be used in the case of thin specimens, and again the resolution is limited by the wavelength of the illumination source.

The Kerr magneto-optic (M-O) technique relies on analysing the change to the angle of polarisation of a plane polarized light source which has been

reflected from the surface of the sample. The technique can give quantitative information on the directions of the surface magnetisation of a sample, and has been used extensively for both static and dynamic experiments, (e.g. Rührig et al (1990), Rave et al (1990)). Kerr M-O images obtained from samples used in this study are presented in section 5.4.

In recent years, monochromatic light sources used in Kerr microscopes have been replaced by more stable laser sources (Argyle et al (1987)). This fact becomes especially important when attempting to map quantitatively the surface magnetisation distribution of a sample. Both the Faraday and Kerr M-O imaging modes are relatively simple to implement and dynamic experiments can easily be performed. The resolution of the Kerr M-O technique is limited by the wavelength of the illumination source, although a value of 0.3μm has recently been been demonstrated, (Rave et al (1990)).

A relatively new technique which offers the capability of imaging the magnetic domain structure at the surface of a sample is magnetic force microscopy (MFM), e.g. Martin et al (1989). A small ferromagnetic tip is placed at a relatively small distance (<<1μm) from the magnetic specimen, and is subsequently scanned over the specimen. As this happens, the magnetic field from the specimen causes a displacement of the tip which can then be measured directly in order to produce an image which contains information regarding the distribution of magnetic field beyond the surfaces of the sample. There are many different experimental modifications to the basic method depending on how the displacement of the tip is measured and also what parameter is measured e.g. magnetic field, field gradient. The different techniques are described more fully elsewhere (Martin et al (1989)).

One method of electron microscopy which can provide induction maps is the Differential Phase Contrast (DPC) (Chapman and Morrison (1983)) mode. This can only be performed in a scanning transmission electron microscope (STEM) and therefore will be discussed separately from the CTEM modes of Lorentz electron microscopy which are described in sections 2.2.2 and 2.2.3. The major advantage of this method over the CTEM modes is that the intensity of

each pixel in a pair of D.P.C. images is directly related to the components of induction perpendicular to the direction of the electron, integrated along the incident electron direction. Quantitative induction maps (Chapman (1990)) have been demonstrated with a resolution of 10nm.

2.2 IMAGE FORMATION IN A CONVENTIONAL TRANSMISSION ELECTRON MICROSCOPE (CTEM) AND LORENTZ ELECTRON MICROSCOPY

2.2.1 IMAGE FORMATION IN A CTEM

In a conventional transmission electron microscope, electrons are emitted from a heated tungsten or lanthanum-hexaboride (LaB_6) filament which is held at a high negative potential. After leaving the filament the electrons form a cross-over and are accelerated towards a grounded annular anode. Situated between the anode and the specimen are two condenser lenses which control the effective source size and angular convergence of the electrons which finally reach the specimen plane. Small source sizes give higher coherence illumination, although the current density in the plane of the specimen is reduced. The use of a highly coherent beam is desirable but the practical problems associated with low current densities must also be considered.

The above arrangement consisting of an electron source and two condenser lenses can produce a plane wave, $\psi_o(\underline{r})$, which is incident on the specimen. The interaction of the incident beam with the specimen is described by a "transmittance function", $h(\underline{r})$, which for specimens acting as pure phase objects, (i.e. the amplitude of the incident beam is not affected), is given by;

$$h(\underline{r}) = \exp(-i\,\phi(\underline{r})) \qquad (2.1)$$

where $\phi(\underline{r})$ is the phase change suffered by the electrons due to the specimen and $(\underline{r})$ is the position vector in the plane of the specimen. It

was pointed out by Aharonov and Born (1959), that the phase difference, $\phi(x)$, introduced between two electrons which originate from the same point and travel different paths before rejoining, is proportional to the magnetic flux enclosed by the two paths. In the case of a one-dimensional magnetic object, in which the geometric path lengths of the electrons are the same, the form of $\phi(x)$ is given by

$$\phi\ (x) = \frac{2\ \pi\ e\ N}{h} \qquad (2.2)$$

where N is the total magnetic flux enclosed by the two paths. Hence two electrons satisfying the above condition and incident along the z direction will suffer a phase difference $\phi\ (x)$ between two points x_1 and x_2 given by;

$$\phi\ (x) = \left\{ \frac{2\ \pi\ e\ t}{h} \right\} \int_{x_1}^{x_2} B_y(x)\ dx \qquad (2.3)$$

where $$B_y(x) = \frac{1}{t} \int_{-\infty}^{\infty} B_y(x,z)\ dz$$

The electron disturbance upon exiting from the specimen is described by $\psi_e(\underline{r})$ where,

$$\psi_e(\underline{r}) = h(\underline{r})\ \psi_o(\underline{r}) \qquad (2.4)$$

The emergent wave, $\psi_e(\underline{r})$ is then projected onto the back focal plane (bfp) of the objective lens, and the form of $\Psi_{bfp}(\underline{k})$ is given by;

$$\Psi_{bfp}(\underline{k}) = FT\ [\ \psi_e(\underline{r})\ ] \qquad (2.5)$$

where FT denotes a Fourier Transform and $\underline{k}$ is the position vector in reciprocal space. An objective aperture may then be introduced in the bfp,

and is described by an "aperture function", A ($\underline{k}$), given by;

$$A(\underline{k}) = 1 \qquad \text{inside the aperture} \qquad (2.6a)$$

$$= 0 \qquad \text{otherwise} \qquad (2.6b)$$

Another factor which must be introduced at this stage arises from the defocus and aberration of the image forming lens, and is expressed by the function $\omega(\underline{k})$, where;

$$w(\underline{k}) = \exp(-2\pi i\{\left[\frac{C_s}{4}\lambda^3 (k_x^2+k_y^2)^2\right] + \left[\frac{\lambda}{2}\Delta (k_x^2+k_y^2)\right]\}) \qquad (2.7)$$

where λ is the wavelength of the electrons, k_x and k_y are the components of the position vector in reciprocal space, Δ is the defocus of the image forming lens and C_s is the third order spherical aberration coefficient of this lens. Combining equations 2.6 and 2.7, t ($\underline{k}$) is defined as;

$$t(\underline{k}) = w(\underline{k})\, A(\underline{k}) \qquad (2.8)$$

The form of the complex wave on the image (x',y') plane is given by the Fourier Transform of the modified back focal plane disturbance. Hence the image intensity I (x',y') is given by;

$$I(x',y') = \left|\iint\{\Psi_{bfp}(\underline{k})t(\underline{k})\exp[-2\pi i(k_x x'+k_y y')]dk_x dk_y\right|^2 \qquad (2.9)$$

The above equation contains all the information necessary to describe the CTEM modes of Lorentz electron microscopy. It should also be noted that for an aperture function which is unity everywhere and an aberration free lens, contrast variations in the final image can still be introduced through a non-zero value of Δ in eqn. 2.7; this is relevant to the Fresnel mode.

2.3.2 FRESNEL LORENTZ ELECTRON MICROSCOPY

For the case of the one dimensional magnetic body considered above, in the Fresnel mode it can be shown (Jakubovics (1975)) that the intensity of the final image is given by the expression;

$$I(x',y') = \left| \exp(i\,\phi\,(x')) * \exp(\pi i(x'^2 + y'^2)/\,(\lambda\,\Delta\,)) \right|^2 \qquad (2.11)$$

where * denotes the convolution integral. Contrast arises in the final image where there is a variation of the in-plane component of induction in the sample, e.g. across domain walls.

An alternative, classical description of the Fresnel mode may be understood from fig. 2.1. Electrons passing through regions of the sample which are oppositely magnetised are deflected in opposite directions. If the image forming lens is focused on a plane which is non-coincident with the specimen, ($\Delta \neq 0$ in eqn 2.7) domain walls are shown as regions of high or low intensity, fig. 2.2(a). The intensity and diffuseness of these lines give an indication of the magnitude of the in-plane rotation and also the angle of rotation of the magnetisation across a domain wall.

The Fresnel mode can be used to calculate the domain wall width (Reimer and Kappert (1968)) although this procedure is not straightforward. A Fresnel image from a 95nm thick, 4.00 by 2.00μm, $Ni_{82.5}Fe_{17.5}$ particle is shown in fig. 2.2(a), in which domain walls appear as light and dark lines. No direct information to indicate the directions of $\underline{\mathbf{M}}$ within each domain is given, but the magnetisation distribution of such a simple structure can be deduced from fig. 2.2(a) and is shown schematically in fig. 2.2(b).

2.2.3 FOUCAULT LORENTZ ELECTRON MICROSCOPY

A second mode of Lorentz electron microscopy which can be practised in a CTEM is the Foucault technique. In this mode, an aperture is introduced in the

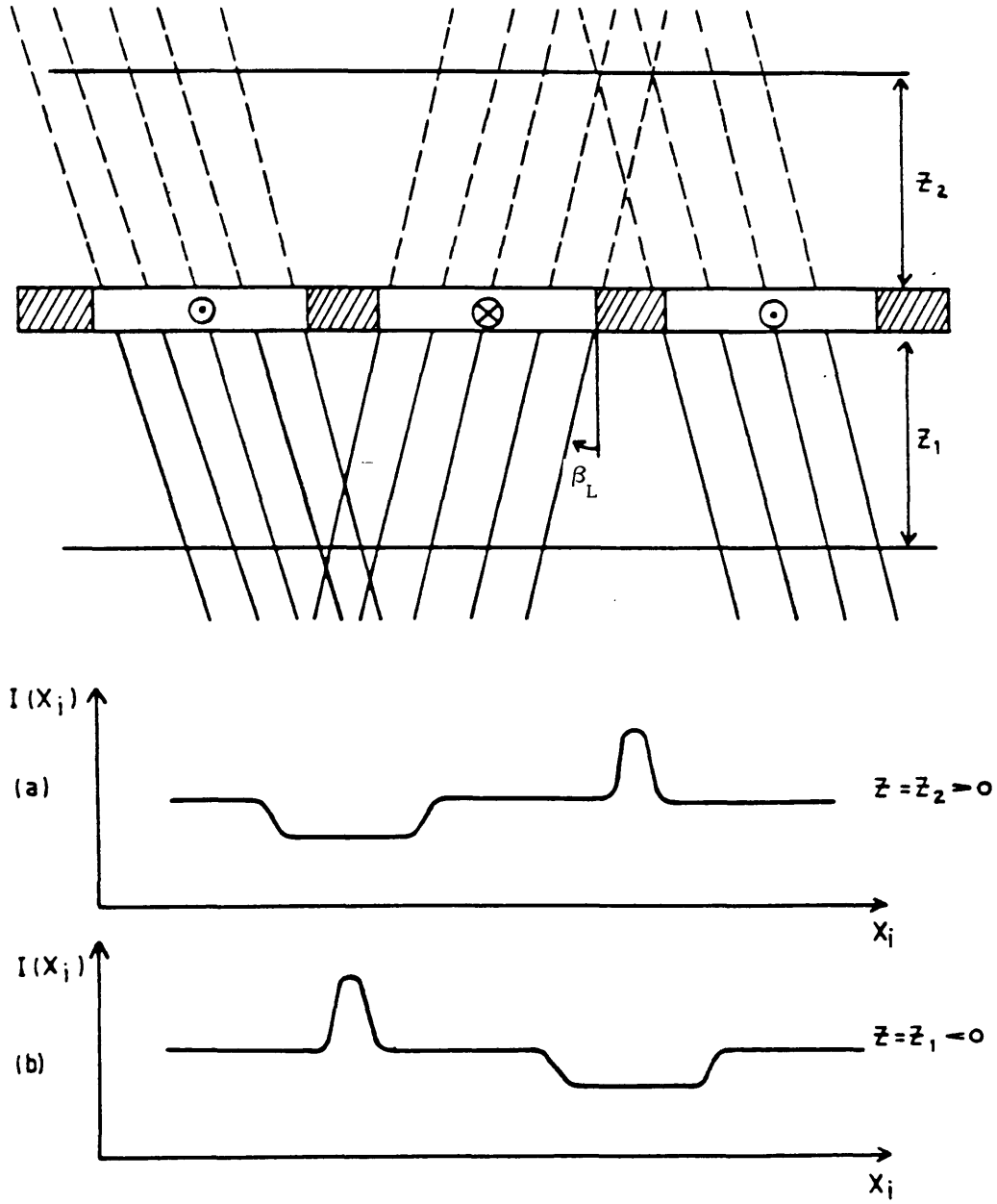

Fig. 2.1 Classical description of the Fresnel mode.

(a)

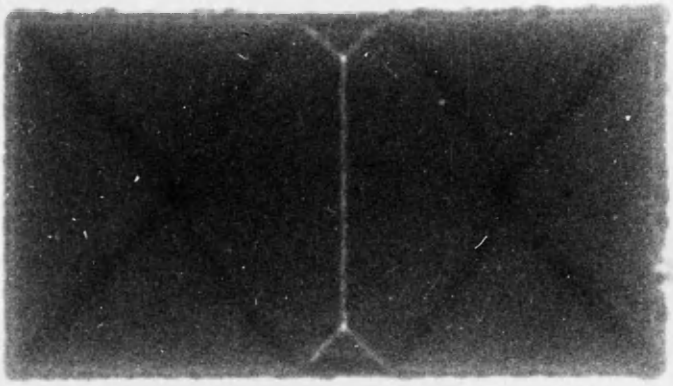

(b)

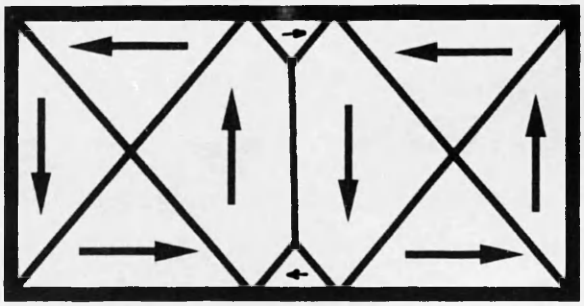

F ig. 2.2 (a) Fresnel image of a 4.00 by 2.00μm, 95nm thick $Ni_{82.5}Fe_{17.5}$ particle. (b) Schematic diagram showing the magnetisation distribution from the Fresnel image, above.

bfp and subsequently used to obstruct parts of the transmitted beam. Once again the contrast can be understood from eqn. 2.9. The aperture, which has been displaced from the symmetry position about the optic axis is defined by $A(\underline{k})$;

$$A(\underline{k}) = 1 \qquad (k_x - k_{x_1})^2 + (k_y - k_{y_1})^2 \leq A_p^2 \tag{2.11a}$$

$$= 0 \qquad \text{Otherwise} \tag{2.11b}$$

$$(k_x - k_{x_1})^2 + (k_y - k_{y_1})^2 = A_p^2 \tag{2.11c}$$

where the centre of the aperture has been displaced to the position (k_{x_1}, k_{y_1}), and A_p is the radius of the aperture in the back focal plane. This particular aperture function can be seen to modify the intensity of the final image. There are however some distinct problems with the Foucault imaging mode which must be realised before interpretation of the images can take place. The first concerns the aperture, which in contrast to that described by eqn 2.11 does not have a completely abrupt edge, nor is its position exactly reproducible. A more fundamental problem arises from the non-linear relationship between the intensities in a Foucault image and the spatial variation of the in-plane components of induction of the sample (Jakubovics (1975)). Therefore it is unwise to extract information from Foucault images from regions of the sample over which the intensity is varying rapidly e.g. across domain walls. The Foucault mode cannot be used to obtain quantitative information at high spatial resolution, but can quickly and easily provide information from large areas of the sample.

A classical description of the Foucault mode can be understood from fig. 2.3. The objective aperture which has been displaced off-centre, obstructs parts of the transmitted beam, and by suitable positioning of the aperture it is possible to selectively allow different parts of the transmitted beam to form

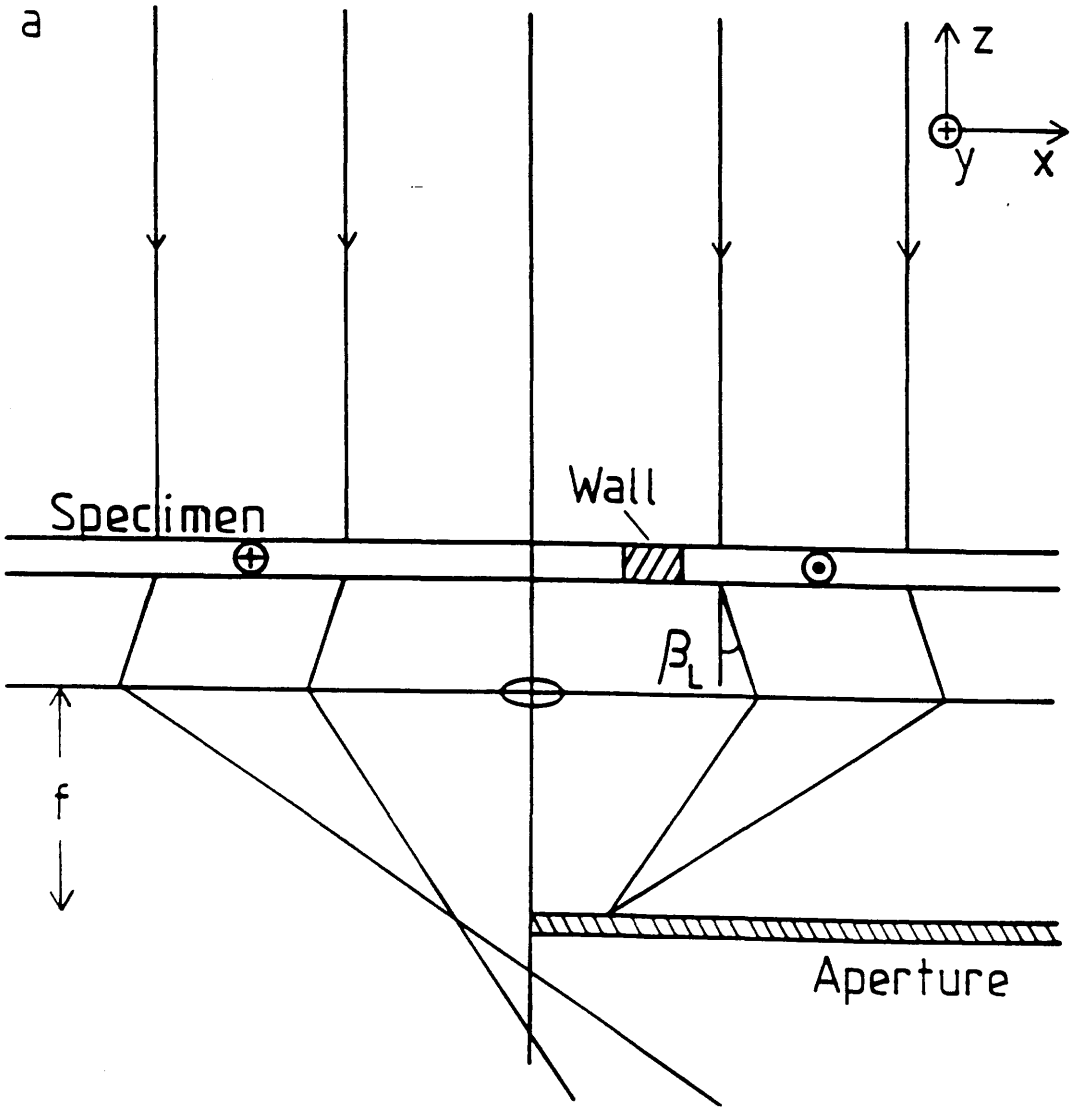

Fig. 2.3 Classical description of the Foucault imaging mode.

the final image. In this way it is possible to map different components of induction.

In normal practice two Foucault images are taken, mapping induction parallel to two orthogonal directions in a sample. A pair of Foucault images from a 4.00 by 1.00 μm, 60nm thick $Ni_{82.5}Fe_{17.5}$ particle is shown in fig. 2.4(a) and (b), with the magnetisation distribution given in fig. 2.4(c). Although this technique results in images with a high level of contrast, quantitative data should be extracted cautiously.

2.2.4 SUMMARY

The two CTEM modes of Lorentz microscopy described in sections 2.2.2 and 2.2.3 provide a means of qualitatively mapping the magnetisation distribution of a sample. The use of more than one of the above techniques gives information of a complementary nature which would otherwise be difficult to obtain. In this study the Fresnel and Foucault modes were used to complement each other in cases where images of one type proved difficult to interpret. These two modes were deliberately chosen because of their suitability to experiments in which the imaging conditions are not very stable - this was especially relevant when performing the set of in-situ magnetising experiments discussed in chapters 4 to 6.

2.3 DISCUSSION OF THE JEOL 1200EX AND 2000FX CTEMs.

During the course of this project almost all of the experimental data were acquired on either the JEOL 1200EX or 2000FX CTEMs. These will be described briefly in sections 2.3.1 and 2.3.2, where the advantages specific to each machine will also be highlighted.

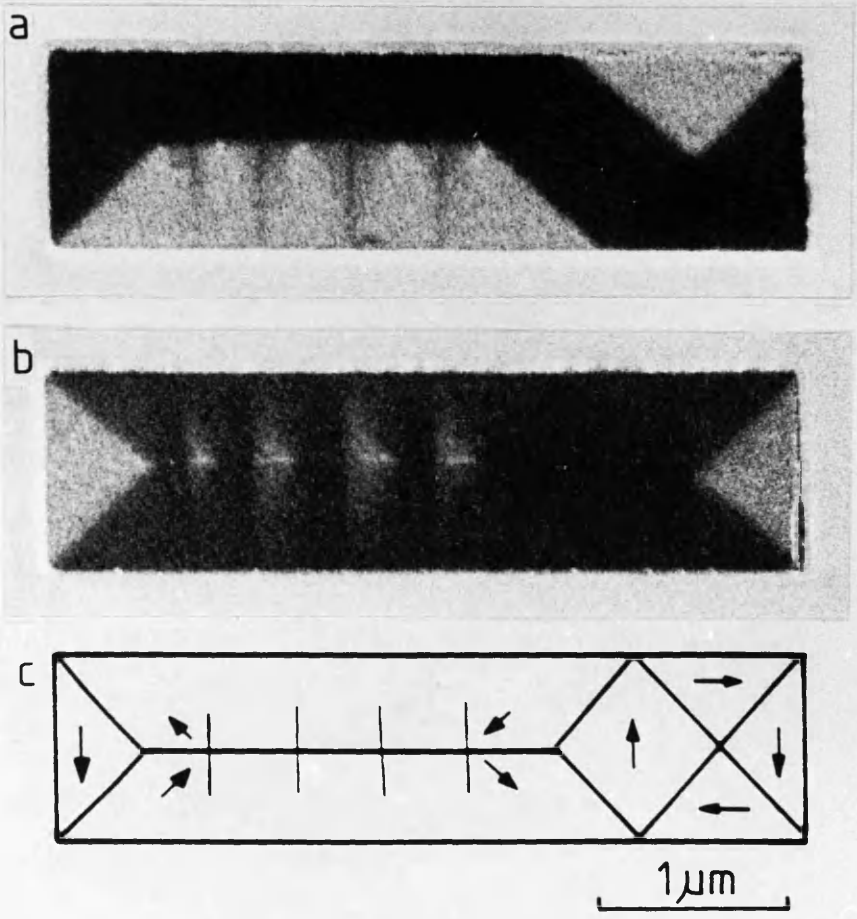

Fig. 2.4 (a) and (b), pair of Foucault images which map induction parallel and perpendicular to the long axis of the particle. (c) the magnetisation distribution inferred from (a) and (b), above.

2.3.1 THE JEOL 1200EX CTEM

The most important difference between the 1200EX and 2000FX microscopes at the University of Glasgow is the type of objective lens which is present. In the 1200EX, as is the case for most CTEMs operating under high magnification conditions, the specimen is situated in a magnetic field of 0.5 to 1.0T. Clearly this is unacceptable when examining magnetic specimens as any domain structure present would normally be erased. However the 1200EX does offer a high resolution, (lattice resolution 0.3nm) and is very well suited to give a full description of the microcrystalline properties of the specimens (section 3.4). The high resolution also enables analysis of semiconductor quantum wells and wires results from which will be presented in chapter 7.

Using the 1200EX, analysis of the magnetic properties of samples is limited to the special case where the sample is in field-free-space, i.e. when the objective lens is switched off. In this mode the mini objective lens is used as the image forming lens, and magnification changes are controlled by three intermediate lenses, (I1, I2 and I3), which are also situated after the specimen. The currents through I1, I2 and I3 are controlled individually by using a "free lens controller". Operating the microscope with the free lens controller allows a maximum magnification of x5500 to be obtained with the specimen situated in field-free-space. This was found to be sufficient to be able to examine some samples, and the results obtained are described in chapter 4.

2.3.2 THE MODIFIED JEOL 2000FX CTEM

The modified JEOL 2000FX at Glasgow University is optimised for the analysis of magnetic specimens and differs from the 1200EX in two main respects. Firstly the accelerating voltage is 200kV compared with 120kV, but the second and by far most significant difference is the type of objective lens which is present. The main advantage of this particular objective lens, which is

similar in design to that described by Tsuno (1983), is that under normal operating conditions, the specimen is situated in a magnetic field of only 640 $A.m^{-1}$, in a direction out of the plane of the specimen. Even under these circumstances, the lattice resolution is approximately 2 nm.

Another significant advantage with this instrument is that the objective aperture is situated exactly in the back focal plane of the objective lens, and hence the microscope is ideally suited for performing high magnification Foucault imaging. During the course of the experiments it was found that contrast variations in Foucault images were extremely sensitive to the position of the aperture, and hence very fine control over it's position was necessary. In order to have Foucault imaging conditions which are as reproducible as possible, the following procedure was adopted;

1) Firstly the microscope was aligned as normal such that the incident and transmitted beams were directed along the optic axis.
2) The imaging conditions were then changed to diffraction mode, for which the incident beam should comprise parallel illumination, and also the post specimen lenses should be focused on the back focal plane of the objective lens. To achieve these conditions, the objective aperture is first inserted symmetrically about the transmitted beam. As the aperture is situated in the back focal plane, fine adjustments to the focus and astigmatism of the post specimen lenses, and subsequently the incident illumination, can also be made at this point.
3) Using the coarse aperture controls, the aperture is then moved off axis to obstruct parts of the transmitted beam, as shown in fig. 2.3.
4) The post specimen lenses are then focused on the specimen plane.
5) Very slight changes to the position of the transmitted beam with respect to the aperture are then achieved by altering the currents through the condenser lens alignment coils. This is done in order to optimise the quality of the final Foucault image, which is visually inspected during this last step. Only very small changes are made to the position of the transmitted beam so that it remains essentially on the optic axis.

Final Foucault images were initially viewed using a low light level TV camera, optically coupled to a YAG scintillator onto which the electrons were incident. A frame store with a frame averaging facility ensured that suitably noise free images could be obtained. By this means, fine domain detail could be observed whilst the experiment was in progress. Permanent images were obtained by recording the images on magnetic tape or, more usually, on photographic film which could be inserted above the YAG scintillator.

2.4 THE MAGNETISING STAGE

In order to gain further insight into the magnetisation processes of the samples under investigation, it would be highly beneficial if observations of dynamic experiments could be made "in-situ", i.e. whilst the sample is actually in the microscope. A specially designed magnetising stage was designed and built to perform this task. The main advantages of this stage are summarised below;

1) The stage is able to apply constant fields of up to 12 $kA.m^{-1}$ (150 Oe) to the specimen, although in normal practice, the field cannot be maintained much in excess of 10 $kA.m^{-1}$ for prolonged periods as the coils heat up, outgas and the general stability of the imaging conditions deteriorate.
2) When acquiring permanent images, the field from the magnetising stage has to be very stable, as any instabilities are transported into discernible movements of the transmitted beam, which subsequently degrade the quality of the final image. A highly stable current source is therefore required, as is good thermal conductivity of the stage itself.
3) The sample is able to be rotated separately with respect to the field without having to take it out of the microscope. Accurate alignment of the sample with respect to the field can then take place with relative ease. The sample can be aligned to an accuracy of $\mp$ 5° to any desired direction.

4) The stage itself can fit into the standard side-entry airlock of the JEOL 100, 1200 and 2000 CTEMs. This allows the flexibility of using various techniques available on different microscopes in order to obtain the most information from the sample.

The stage itself is shown in fig. 2.5. The specimen is situated in a cylindrical barrel which can be rotated separately with respect to a set of solenoidal formers using the control marked A. Feedthroughs, marked B, for the current supply to the solenoids are also situated at this end of the rod. The coils themselves are fixed on either side of the specimen, and comprise two soft iron formers each wrapped with 40 turns of 0.25mm insulated copper wire. A close-up of the specimen environment is shown in fig. 2.6. The field applied to the specimen ($\underline{H}_{ext}$) is directly proportional to the current through the coils, and a graph showing the total field at the specimen (for both increasing and decreasing cycles) is given in fig. 2.7. It can be immediately seen that within the experimental errors, there is no significant hysteresis.

Due to space limitations, no compensation coils are incorporated into the stage. The effect of the applied field ($\underline{H}_{ext}$) is to deflect the electron beam away from the optic axis. To compensate for this the incident beam is tilted prior to the specimen using the ALIGNMENT TILT coils so that the effect of the applied field is then to return the beam back onto the optic axis. Any astigmatism which is introduced may be corrected in the JEOL 2000FX using the OBJECTIVE STIGMATORS, and in the JEOL 1200EX using the INTERMEDIATE STIGMATORS.

Using the magnetising stage it is possible to observe directly the effect of a constant applied field to the domain structure of a specimen.

The magnetising stage can also be used to apply pulsed, as well as steady fields, although in the pulsed mode only remanent states can be examined. Pulsed fields ($\cong 10^{-3}$ s duration) far in excess of 10 $kA.m^{-1}$ can be applied as the coils are only energised for a relatively short time, and so do not heat up appreciably. For pulsed mode operation, a high current amplifier was

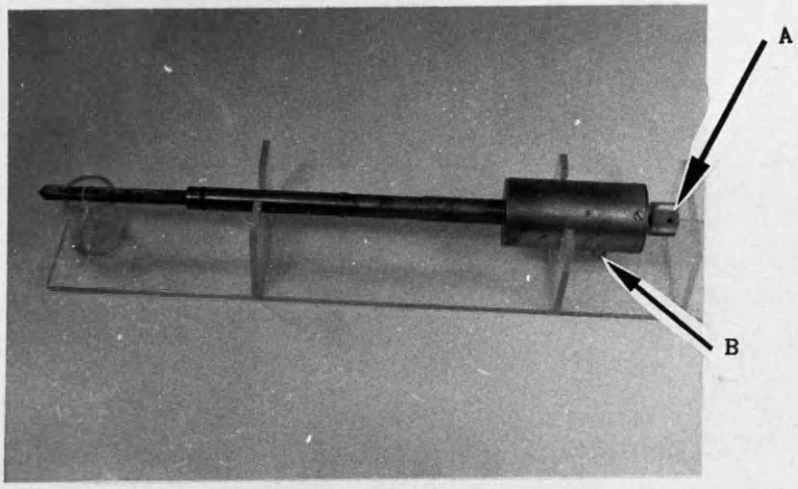

Fig. 2.5 The magnetising stage. The rotation control is marked A and the feedthrough for the current supply is marked B.

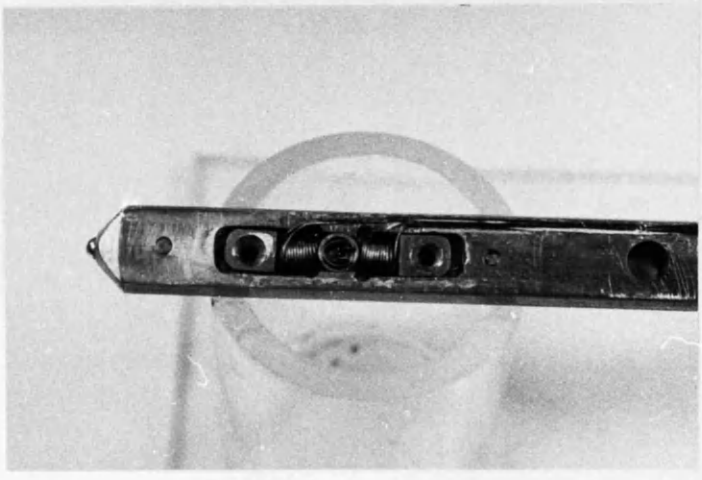

Fig. 2.6 Close-up of the specimen environment in the magnetising stage.

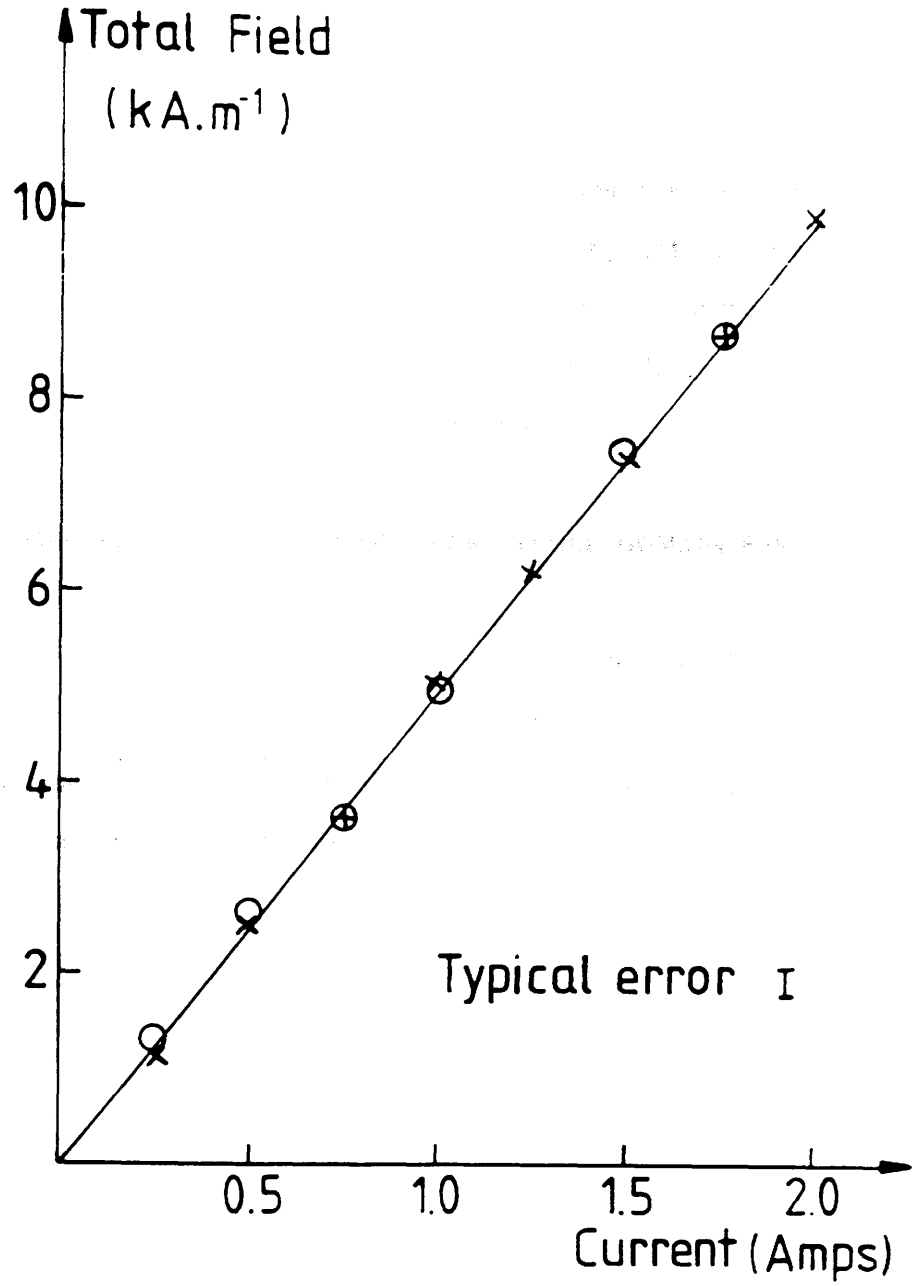

Fig. 2.7 Calibration curve of the field at the specimen versus current supplied to the coils. The crosses denote the increasing cycle, while the circles represent the decreasing cycle.

constructed which could supply square wave pulses of up to 10A to the coils. Assuming that the value of μ_r for the soft iron formers does not vary for currents up to 10A, the maximum field which can be applied to the specimen in the pulsed mode is $64kA.m^{-1}$. The coils themselves have a time constant of approximately 10^{-5} secs, and so do not significantly affect the shape of the pulse. (The calculation of the time constant is shown in appendix 1)

The magnetising stage was used extensively throughout this project, and results obtained from it are given in chapters 4 to 6.

2.5 THEORETICAL PREDICTIONS FOR SINGLE DOMAIN PARTICLES

One of the primary objectives of this project was to investigate the magnetic properties of small regularly shaped particles. As will be described in chapter 3, the particles used in this study were essentially two dimensional rectangular shapes with varying in-plane aspect ratios. Previous studies on two dimensional $Ni_{82.5}Fe_{17.5}$ particles in which shape anisotropy was dominant (McVitie (1988)), indicated that single domain (SD) particles would not be found. If, however, some anisotropy were introduced into these particles which would result in single domain states, it would be highly beneficial if some theoretical predictions were known about such particles in advance.

The magnetic induction $\underline{\mathbf{B}}(\underline{r})$ from a SD particle of dimensions 2a by 2b by 2c, centred about the origin and uniformly magnetised along the y-axis ($\underline{\mathbf{M}}(x,y,z) = (0, M_s, 0)$) is given by the expression;

$$\underline{\mathbf{B}}(\underline{r}) = \mu_o(\underline{\mathbf{H}}(\underline{r}) + \underline{\mathbf{M}}(\underline{r})) \qquad (2.12)$$

where the components of $\underline{\mathbf{H}}(\underline{r})$ are given by (Corb (1988), McVitie (1988));

$$H_x = f\{(x-a), (x+a), (y-b), (y+b), (z-c), (z+c)\} \qquad (2.13a)$$

$$H_y = g\{(x-a), (x+a), (y-b), (y+b), (z-c), (z+c)\} \qquad (2.13b)$$

$$H_z = h\{(x-a), (x+a), (y-b), (y+b), (z-c), (z+c)\} \qquad (2.13c)$$

(For conciseness, the exact form of these equations is given in appendix 2.)

An electron incident along the z direction into the vicinity of a SD particle is deflected through an angle $\beta_L(x,y) = (\beta_{L_x}, \beta_{L_y})$, the components of which can be written separately as;

$$\beta_{L_x}(x,y) = (e\lambda/h) \int_{-\infty}^{\infty} B_y(x,y,z)\, dz \qquad (2.14a)$$

$$\beta_{L_y}(x,y) = -(e\lambda/h) \int_{-\infty}^{\infty} B_x(x,y,z)\, dz \qquad (2.14b)$$

Using eqns. 2.12, 2.13 and 2.14 the values of $\beta_L(x,y)$ were calculated for various shapes of SD particles. Each component of $\beta_L(x,y)$ was then compared to β_s, which is defined as

$$\beta_s = (e \lambda t B_s / h) \qquad (2.15)$$

where t = 2c (the thickness of the SD particle), and the saturation induction is equal to B_s. The value of

$$\frac{\beta_{L_i}}{\beta_s} \times 100 \qquad i = x \text{ or } y$$

will be referred to as the relative deflection angle.

For a particle of dimensions 2a = 1.00 μm, 2b = 4.00 μm, 2c = 60nm, and $\mu_o M_s$ = 1 T, the components of $\beta_L(x,y)$ were evaluated for electrons with various different initial co-ordinates (x,y). The limits of the integral (eqn. 2.14) in the z direction are taken to be sufficiently far away from the particle

that the magnitude of the induction is negligibly small. The various initial co-ordinates (x,y) from which the relative deflection angles were calculated are shown relative to the particle in fig. 2.8. Four different graphs are presented in figs. 2.9 to 2.12 corresponding to different initial coordinates.

In particular, for electrons with x co-ordinate x =0, the value of β_{L_x} (0, y) was calculated for a range of y co-ordinates and the relative deflection angles are shown in fig. 2.9. For the same particle, electrons with initial x co-ordinate x= a, relative deflection angles are given in fig. 2.12 for a range of initial y coordinates. Similar graphs are given in figs. 2.10 and 2.11, for electrons having initial co-ordinates y = 0 and y = b respectively.

The calculation was then extended to calculate the components of β_L (x,y) at an array of points inside and outside the particle. The position of each point in the array with respect to the particle is shown as the shaded region in fig. 2.13. After calculating each component of β_L (x,y), the relative deflection angle was then plotted in a simulated three dimensional graph in which the z co-ordinate represented the relative deflection angle. These graphs are given in figs. 2.14 and 2.15, for which;

for fig. 2.14, $$z = \left\{ \frac{\beta_{L_x}}{\beta_s} \times 100 \right\} \text{ vs } (x,y)$$

and for fig. 2.15, $$z = \left\{ \frac{\beta_{L_y}}{\beta_s} \times 100 \right\} \text{ vs } (x,y)$$

As shown in fig. 2.13, only one quarter of the possible array was used due to the symmetry of the calculation. This type of procedure can also be used to generate images by converting each of the deflection angles into an integer between 0 and 255. Each point of the array then denotes a pixel which has an intensity value defined as the integer between 0 and 255. By plotting each component of β_L (x,y) separately, it is possible to generate images sensitive to induction along specific directions. Two such images are given in figs.

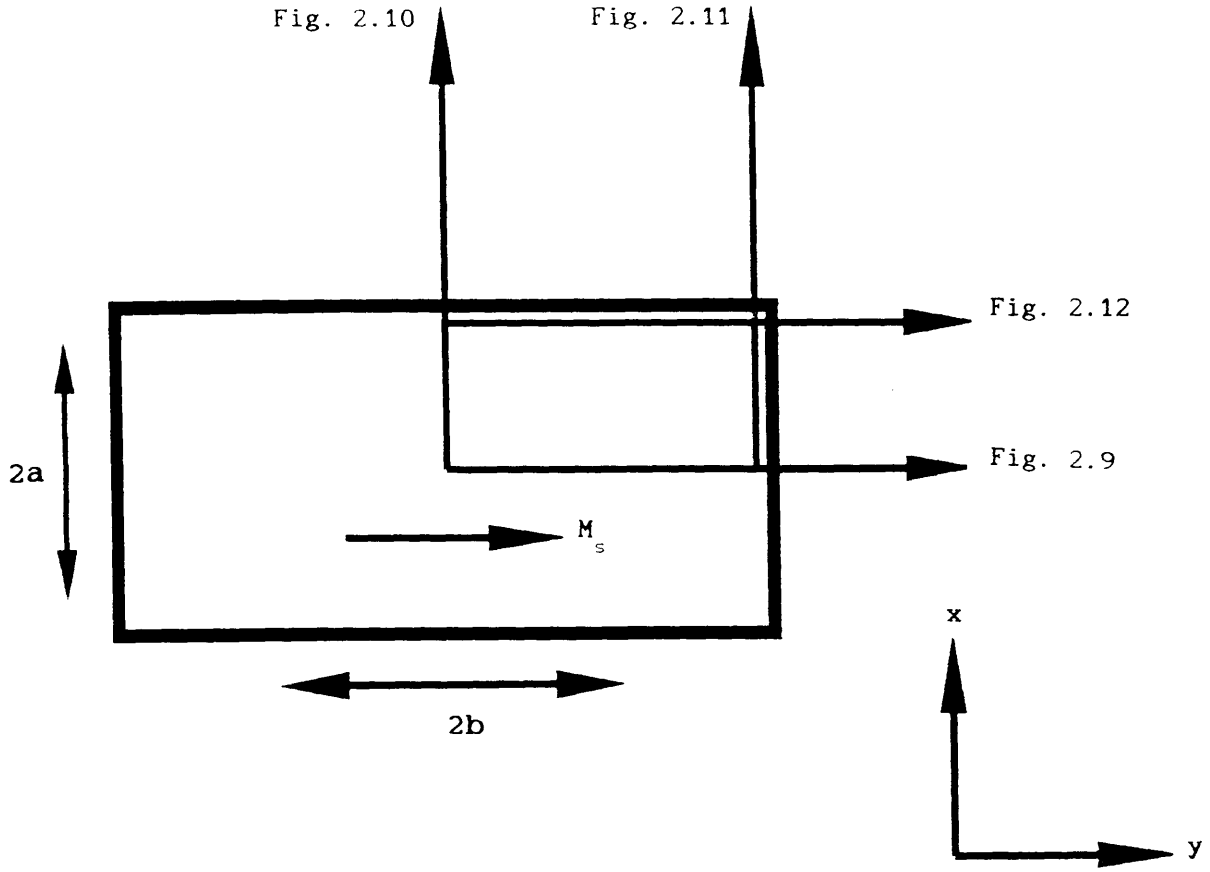

Fig. 2.8 Diagram showing the positions of figs. 2.9 to 2.12 relative to the particle.

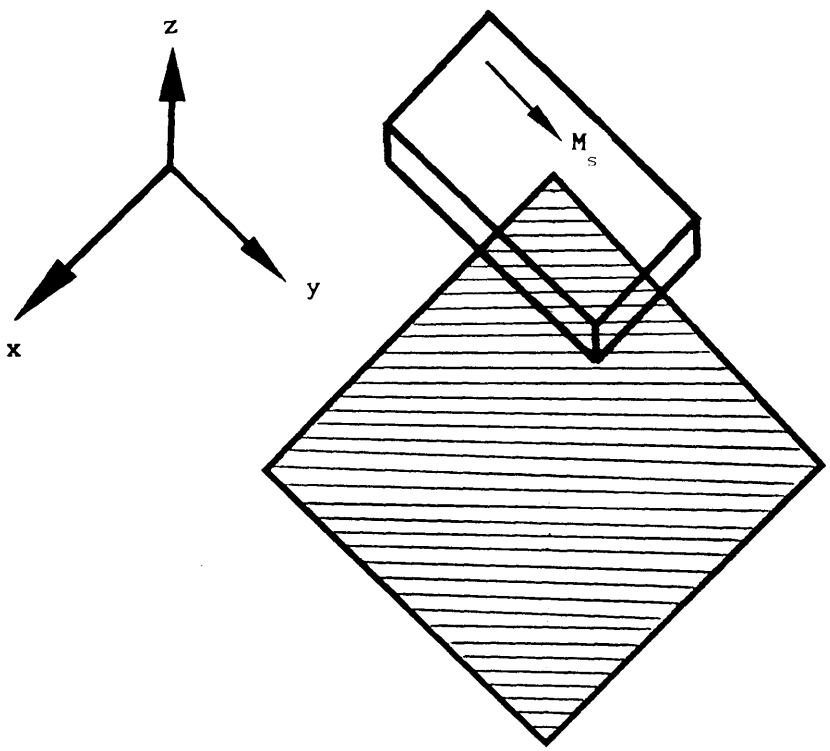

Fig. 2.13 The initial co-ordinates of the electrons are shown as the shaded region, which lies above the particle.

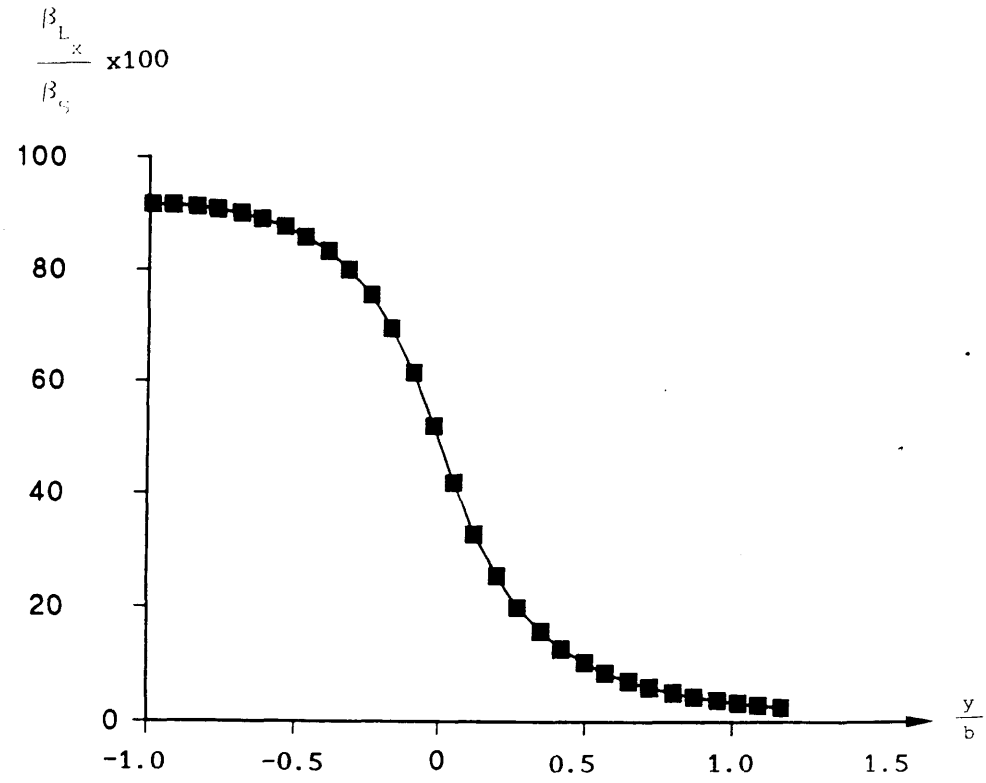

Fig. 2.9 Graph showing the relative deflection angle versus $\frac{y}{b}$, along (0, y).

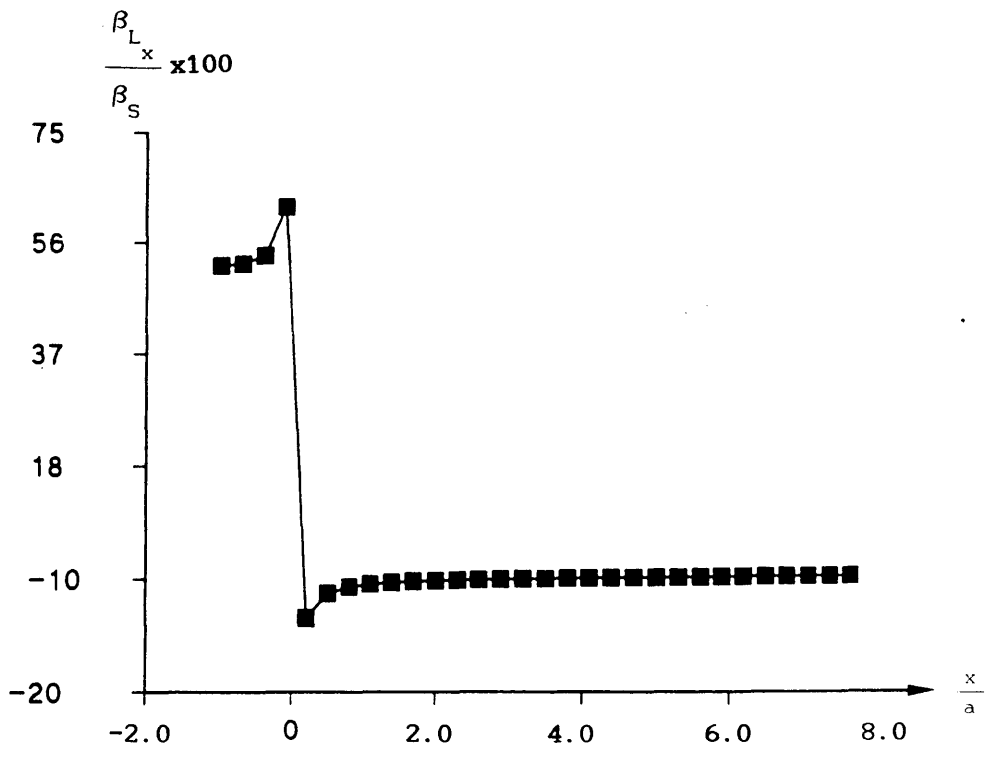

Fig. 2.10 Graph showing the relative deflection angle versus $\frac{x}{a}$, along (x, 0).

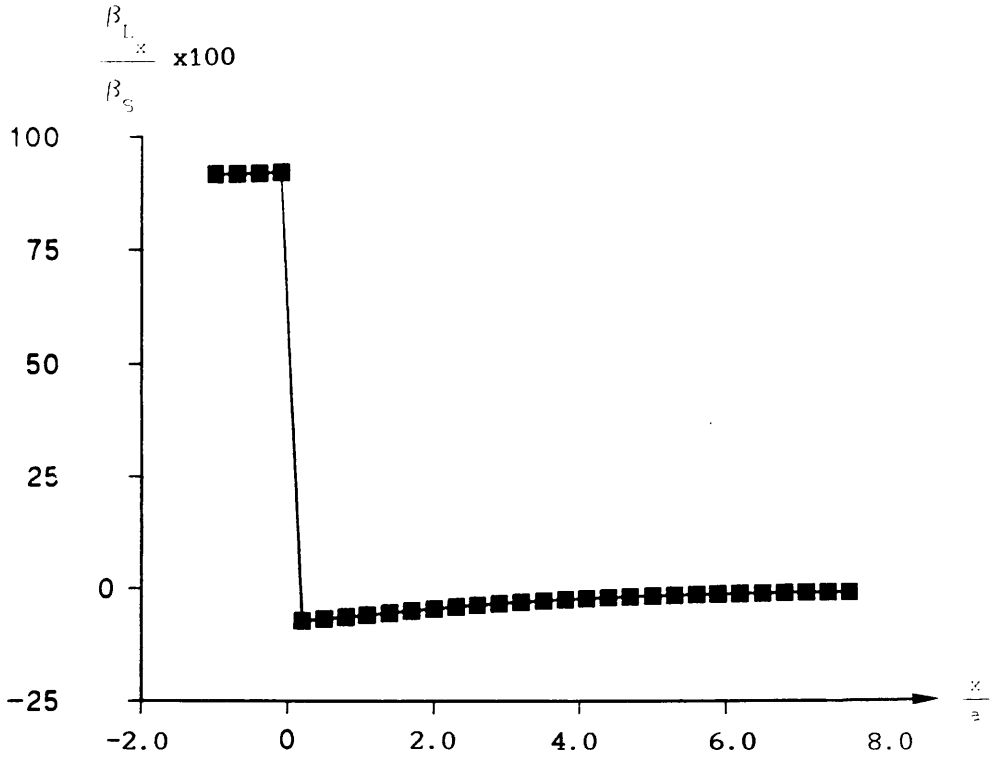

Fig. 2.11 Graph showing the relative deflection angle versus $\frac{x}{a}$, along (x, b).

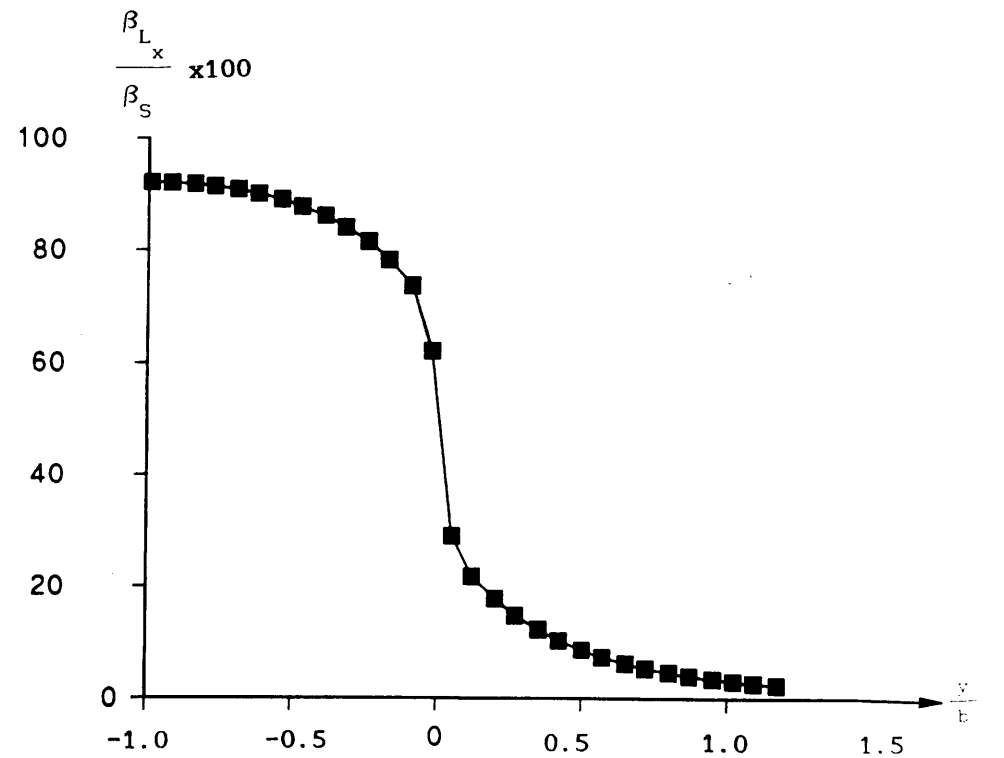

Fig. 2.12 Graph showing the relative deflection angle versus $\frac{y}{b}$, along (a, y).

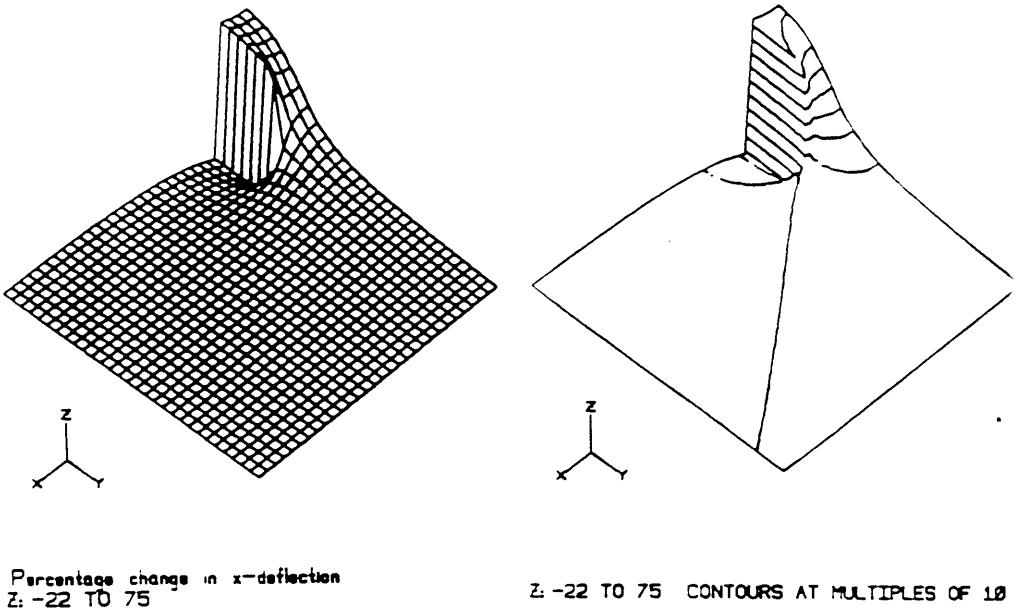

Fig. 2.14 The x component of the relative deflection angle, plotted as the z co-ordinate versus (x,y) for the range of initial x and y co-ordinates shown in fig. 2.13.

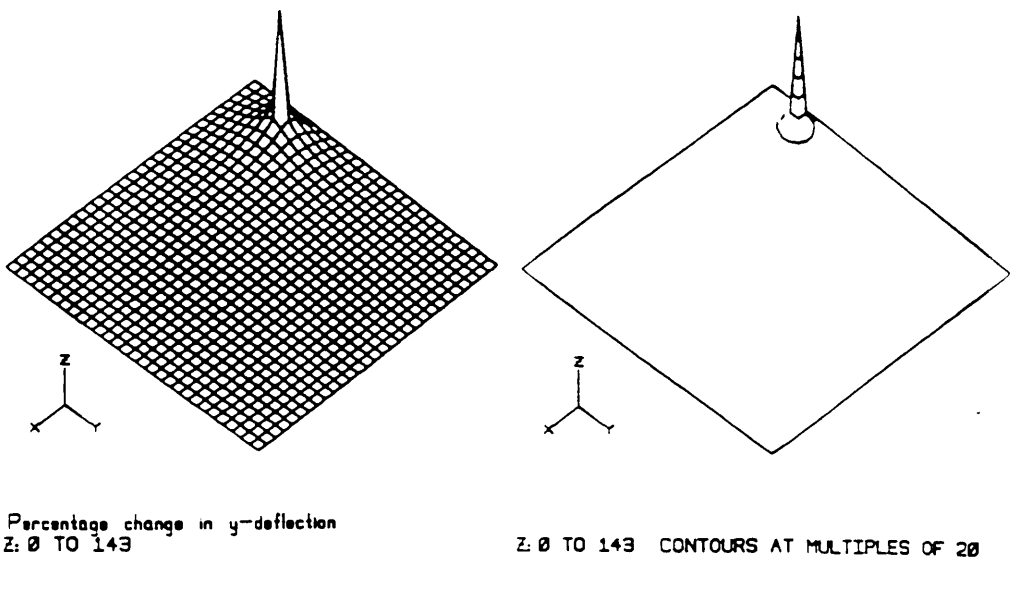

Fig. 2.15 The y component of the relative deflection angle plotted as the z co-ordinate versus (x,y). Initial x and y co-ordinates as fig. 2.13.

2.16 and 2.17. The edges of the particle have been shown by a dashed line for clarity. As the value of the demagnetising field is greatest at the ends of the particle, the value of the relative deflection angle are smaller near the ends of the particle. This can be seen from fig. 2.9, in which, as the value of the demagnetising field decreases towards the centre of the particle, the value of the intensity (i.e. the relative deflection angle) increases.

Just outside each of the corners of the particle, there is a relatively large value of B_x, and this gives rise to the large "spike" in fig. 2.15.

The discontinuous nature of B_y across the long edges of the particle is apparent in e.g. fig. 2.14. Images such as those presented in figs. 2.16 and 2.17 would be particularly helpful to compare with data found from real SD particles.

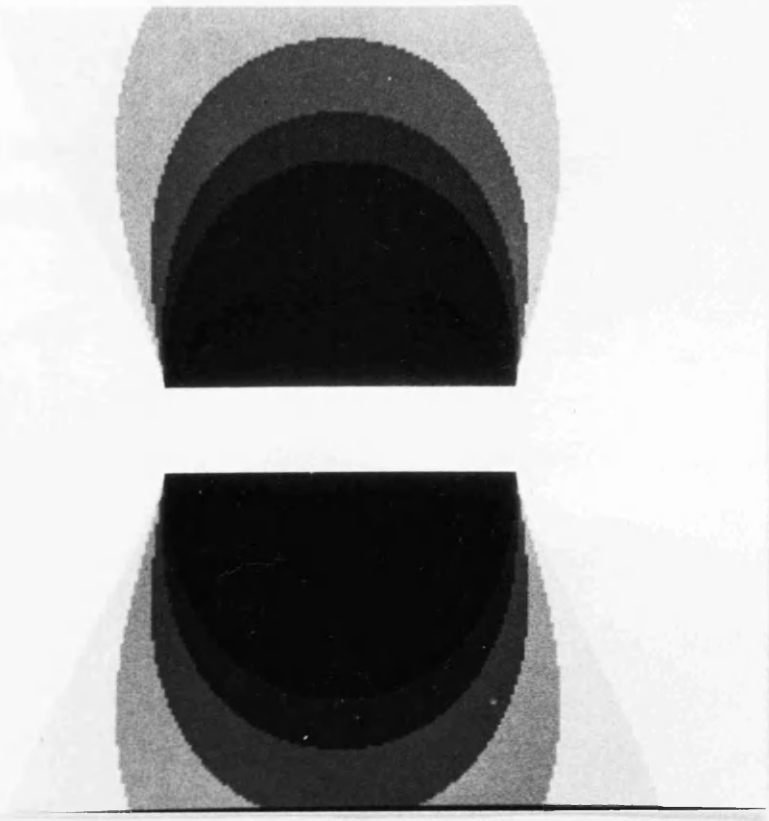

Fig. 2.16 Simulated image obtained from fig. 2.14 mapping induction parallel to the long axis of the particle.

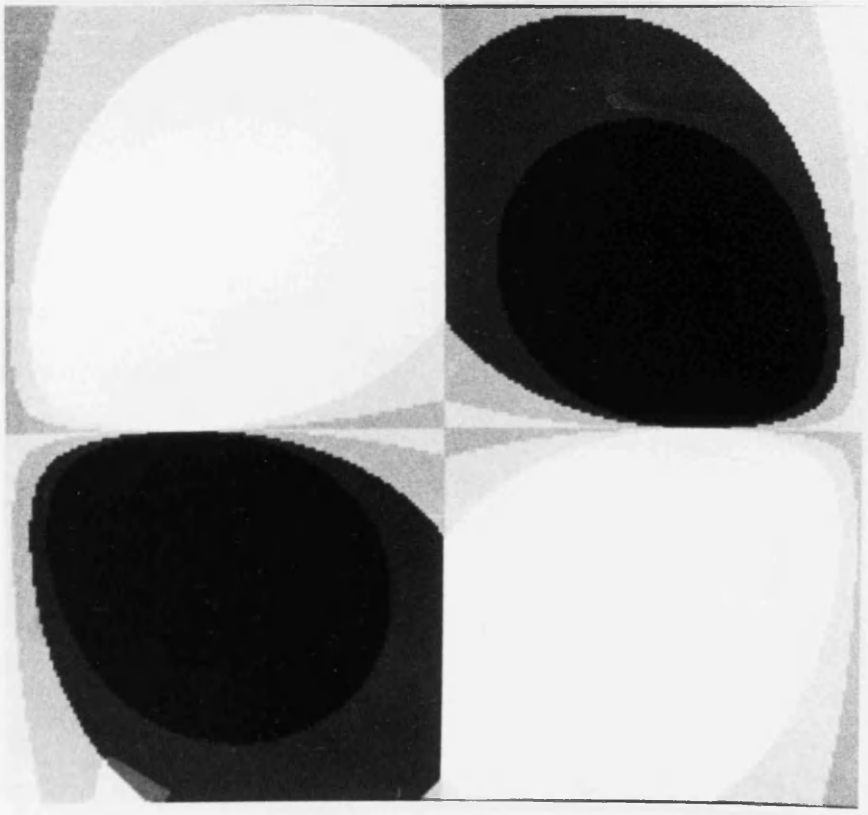

Fig. 2.17 Simulated image obtained from fig. 2.15 mapping induction parallel to the short axis of the particle.

CHAPTER 3

REGULARLY SHAPED PARTICLES- SPECIMEN PREPARATION, BASIC PHYSICAL AND MAGNETIC CHARACTERISATION.

3.1 INTRODUCTION

It was first pointed out by Franklin and Dorfman (1930) that the contribution to the total energy of a ferromagnetic system arising from the presence of domain walls is a surface term, and in contrast, the magnetostatic energy is a volume term. When the dimensions of a body become very small, there should be a point at which the existence of domain walls is energetically unfavourable compared to a single domain state of the same particle. This fact prompted calculations by Kittel (1946) in which he compared the energies of simple domain configurations to that of the same body in a uniformly magnetised state. He was thus able to predict the "critical dimensions" at which single domain particles should become energetically favourable. The predicted values relied heavily on the magnetic parameters used, and could vary dramatically depending on the choice of parameters. For example, the energy associated with the two domain structures shown in fig. 3.1 were compared for a particle of dimensions "LxWxW" and $(\frac{L}{W}) = 5$. The wall energy per unit area, σ, was 3×10^{-3} $J.m^{-2}$, and M_s = 1700 gauss. In this case, single domain particles are energetically favoured when $L \leq 1.4 \times 10^{-5}$ cm. Such calculations in which the non-uniform state was guessed rather than obtained by a minimisation of the free energy, were also performed by Neel (1947). In general the energy of the non-uniform state was over-estimated.

A more rigorous approach would involve solving eqn. 1.7 subject to appropriate boundary conditions, and would result in a three dimensional magnetisation distribution. This has proved an almost intractable problem in most cases, although the situation is improving as faster and more powerful computers become more readily available. This has led many authors e.g.

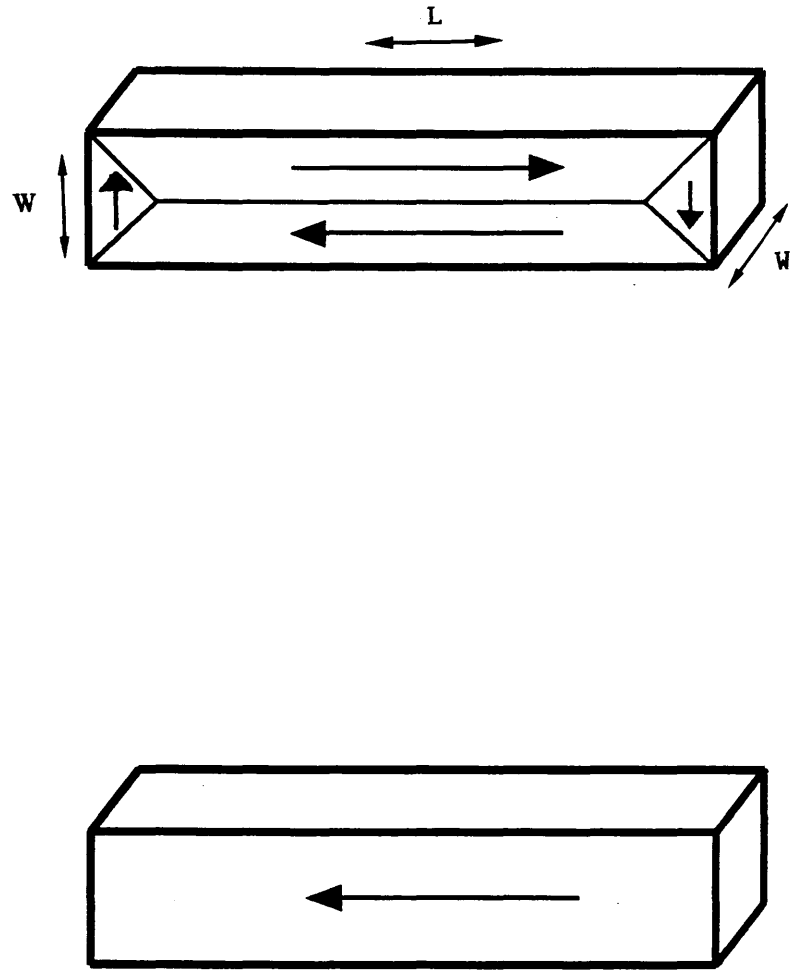

Fig. 3.1 Two possible domain structures for a particle.

Schabes and Bertram (1988a and 1988b), Fredkin and Koehler (1990), Zhu and Bertram (1988), Williams and Dunlop (1989) to calculate the equilibrium domain structure of small platelets, thin films or cubes. In this type of analysis the particle or film is discretised into many small elements in which each element may then either be uniformly magnetised or have a dipole located at its centre. In both cases, the magnitude of the magnetisation is held constant, although its orientation may vary. In order to predict the equilibrium domain structure, one of two procedures is normally adopted; firstly a particle can be subjected to a saturating field, which is then reduced to zero, (Fredkin and Koehler (1990)) or alternatively, a random distribution of moments is assumed as a first guess, and this state is allowed to relax until an energy minimum is reached (Williams and Dunlop (1989)). Of paramount importance to both methods is the size and number of elements which comprise the whole particle. As the number of elements increases, the amount of computing time necessary for the calculation rises very quickly. The other important factor which must be taken into account is the magnetostatic energy term which, unlike the exchange term, can be non-negligible even when the separation between the dipoles or uniformly magnetised elements is relatively large. As a consequence most theoretical work has concentrated on a relatively small number of elements,

Theoretical modeling of particles of a size comparable with those used in the present study are currently being undertaken by Fredkin and Koehler. This model will be discussed more fully in chapter 8, by which time all the experimental results will have been presented.

Recent experimental studies of small magnetic elements have been motivated by their potential use as magnetoresistive sensors or data storage elements. In this latter category, the use of particles which can sustain two different but well defined domain structures has led to work by e.g. Lo et al (1988), and Cosimini et al (1988). In both examples a sense current is used to determine the change in resistance, (R), of each storage element as the

applied magnetic field, (H), is varied. The quantity $(^{dR}/_{dH})$ can be used to indicate the magnetic state an element. Examples of elements suitable for use as storage elements were also given by McVitie and Chapman (1988), and the set of dynamic experiments subsequently performed on these are extensively described in chapters 4 to 6.

Most of the experimental studies have been performed on particles which were fabricated by photolithography followed by vacuum evaporation or sputter etching. The limited resolution of the photolithography technique restricts the size of the particles which can be investigated. As a result most have their smallest in-plane dimension ≥10μm, e.g. Huijer (1979), Vershinin (1982), Argyle et al (1987), Corb (1988) and Rührig (1990). The particles used in this study can be made considerably smaller (section 3.3) due to the use of electron beam lithography, which has a much superior resolution. Sections 3.2 and 3.3 of this chapter present details on the choice of particles used in this study and the fabrication process respectively. Section 3.4 is devoted to the basic physical and magnetic characterisation of particles and thin films.

3.2 CHOICE OF PARTICLE DIMENSIONS

One of the main objectives of this project was to investigate further the influence of a particle's shape on its domain structure and magnetic behaviour in the presence of an applied field. This requires that all three of the particle dimensions be varied independently and systematically. If we consider a particle with in-plane dimensions $L_1=L_2=4\mu m$ an array of particles in which L_1 and L_2 are varied in a suitable manner is shown in fig. 3.2. (L_3 may be varied in the metal deposition step of the fabrication process, as detailed in section 3.3.5.) The array is symmetric about y=x and using this feature, any anisotropy introduced in the fabrication process could be detected in the magnetic behaviour of particles of identical dimensions made orthogonal to each other. In the array of particles (fig. 3.2) collectively

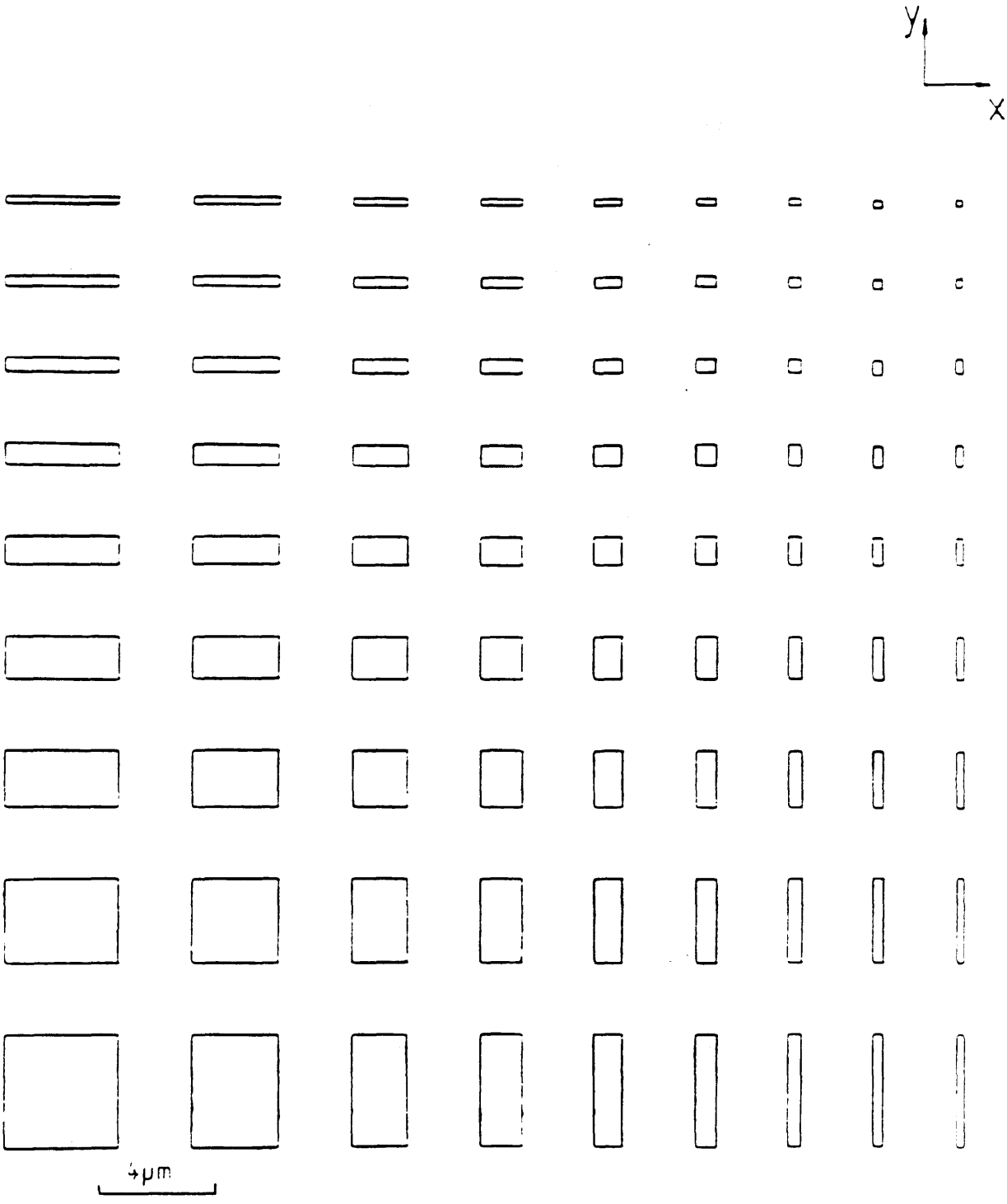

Fig. 3.2 Schematic diagram of the pattern used to define PAT1.

called PAT1, the in-plane dimensions are in the range 4.00μm to 0.25μm with the in-plane aspect ratio (R) varying from 1 to 16. In order to eliminate inter-particle interactions, the particles had to be spaced sufficiently far apart. Using eqns. 2.13, the magnetic field components H_x and H_y from a uniformly magnetised block of dimensions L_1= 0.5μm, L_2 = 2μm, L_3 = 30nm and $\mu_o M_s$ = 1 T, were calculated by McVitie (1988) From these calculations it was decided that the particles should be separated by a distance of 2μm. Fig. 3.2 shows the array of particles and their relative spacing to scale.

3.3 SPECIMEN PREPARATION

As mentioned in section 3.1, much of the experimental work of other authors was concerned with particles whose smallest dimension is of the order of 10μm. Particles made by photolithography followed by vacuum evaporation or sputter etching were compared by Van der Voort and Van den Berg (1984). The major difference in the magnetic behavior of the particles was attributed to edge effects, introduced as a consequence of the resolution of the photolithography technique. Edge effects will be discussed for electron beam lithographically defined particles in section 4.3.3. To produce smaller particles it is necessary to use a technique with a much higher resolution. Electron beam lithography is one method which can produce structures with spatial resolutions ≥10nm, (Mackie (1984)), as was demonstrated previously (Mackie (1984) and McVitie (1988)). In the following sections 3.3.1 to 3.3.6 a detailed description will be given of the fabrication process.

3.3.1 Si_3N_4 MEMBRANES

A schematic diagram of the fabrication process is shown in fig. 3.3. A 2mm square block of Si, (thickness 335μm) has a thin layer of Si_3N_4 on it's top surface, and it is this material which acts as the support material for the particles. The Si block is then back etched to reveal a "window" of Si_3N_4.

ELECTRON BEAM LITHOGRAPHY PROCESS

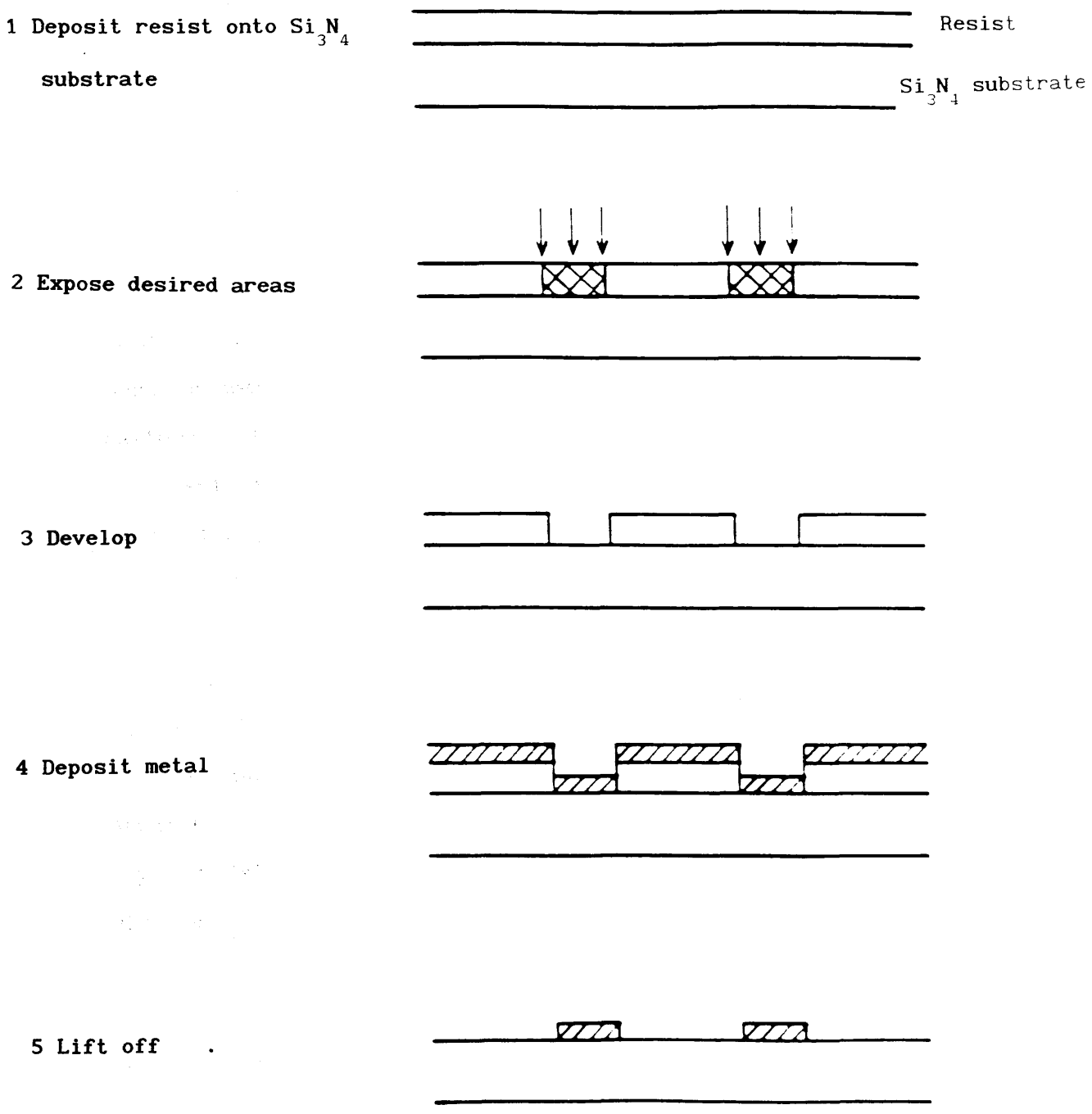

Fig. 3.3 Particle specimen preparation using Electron Beam Lithography.

The window is approximately 100μm square. The choice of support material for the particles is primarily influenced by the fact that the specimens are to be investigated by 100 to 200kV Transmission Electron Microscopy (TEM). In this case the total thickness of particle and support material, through which the electrons must be transmitted, must not exceed approximately 200nm. As the thickest samples were to be 95nm, this required the support material to be ≤100nm. Si_3N_4 is one possibility which satisfies this requirement and is also strong enough to withstand normal handling during the fabrication process. The Si_3N_4 membrane windows are fabricated using a procedure described by Mackie (1984).

3.3.2 DEPOSITION OF RESIST

A resist is a material which changes its molecular structure when it is "exposed" by a suitable source of radiation. In this case, an electron source is used to define the pattern, and so the resist must be sensitive to electrons. One possibility is Polymethyl Methylacrylate (PMMA), which has been used for resolution tests in electron beam lithography (Mackie (1984)). In fact the system used was a combination of two resists, having high and low molecular weights (Mackie and Beaumont (1985)). Use of the two layer system produces the undercut profile, (shown in fig. 3.4), once the pattern has been developed and this eases the lift-off step described in section 3.3.6. As the focused electron beam impinges onto the resist, there are many elastic and inelastic scattering events which cause the beam to become broader. A Monte Carlo simulation of a 50keV electron source incident onto a 2μm thick layer of PMMA on top of a thick Si substrate is shown in fig. 3.5. Although the beam spreads out in the PMMA layer, most of its energy is deposited in the substrate. It should be noted that the broadening of the beam in the PMMA further exaggerates the undercut profile, fig. 3.4.

The membranes initially were protected from dust and air by a layer of resist. Prior to depositing the electron sensitive resist, this was removed

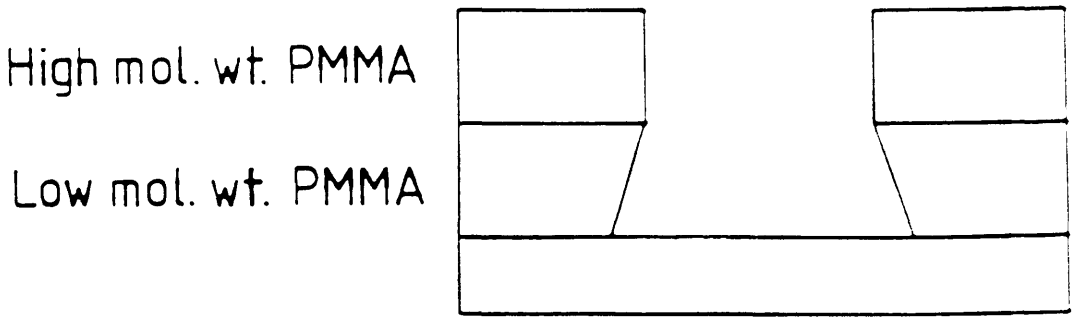

Fig. 3.4 **Diagram showing the undercut profile which results from using two layers of resist.**

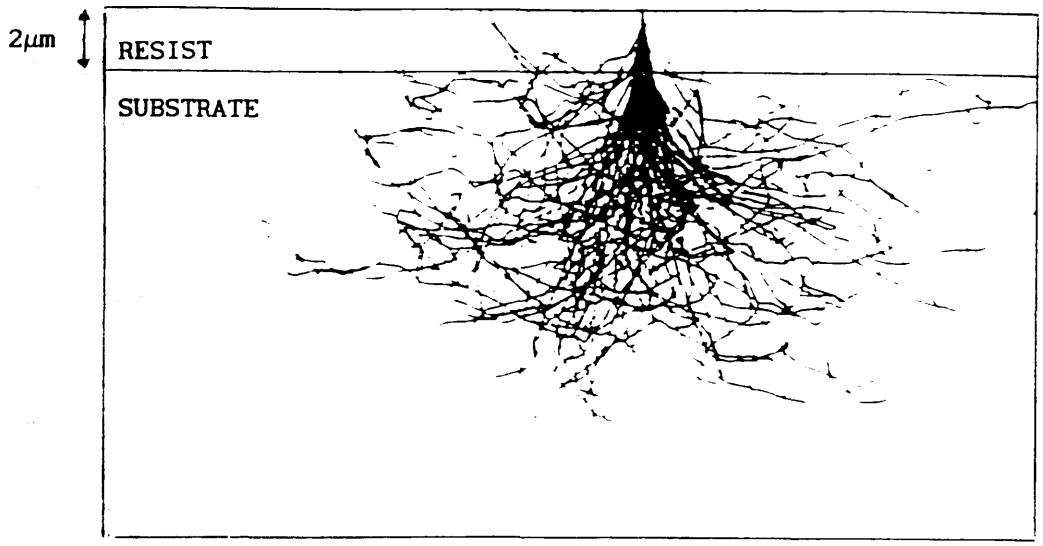

Fig. 3.5 Monte Carlo simulation of 50keV electrons incident onto a 2μm thick PMMA layer on top of a thick Si substrate.

by placing the specimen in a solution of sulphuric peroxide. After approximately five minutes the sample was removed and rinsed in deionised water before being blown dry using N_2. The nitrogen gas source was held at an oblique angle so that the membranes did not break.

The layers of PMMA were deposited onto the membrane using the "spinning" technique. During this procedure the sample is normally held under vacuum on a rapidly rotating chuck. Unfortunately the membranes would break if they were to be held in this way, and so the sample had to be held to the vacuum chuck by first affixing the sample to a glass slide using double sided tape. The first layer of PMMA (a solution of 4% BDH in xylene, having the lower of the two molecular weights) was dropped onto the sample and spun at 4000 r.p.m. for thirty seconds. This resulted in an 80nm thick layer of resist. BDH is the commercial name for PMMA. The sample was then placed in an oven at 180C for approximately one hour. The second layer of resist, having the higher molecular weight (2.5% elvacite in xylene), was deposited in a similar manner, after which the entire sample was again placed in the oven, this time for a minimum of eight hours.

At this point the specimen measured 3cm by 2cm, and as such is too large for use in either the TEM or SEM. In order to produce suitably sized specimens the sample had to be broken up. This was achieved by scribing a square grid in such a way that when the sample was cleaved along the scribe lines the new smaller specimens were 2mm square, with a Si_3N_4 membrane window in the centre of each. The smaller samples are suitable for use in the TEM or SEM and are ready for exposure of the pattern.

3.3.3 EXPOSURE OF THE PATTERN

A pattern such as that shown in fig. 3.2, is exposed by scanning a focused beam of electrons over the specimen in a user determined manner. The beam of electrons is produced using a modified Scanning Electron Microscope, SEM, which, in this project, was a Philips PSEM 500. Pattern generation and

exposure will be dealt with separately in sections 3.3.5.1 and 3.3.5.2.

3.3.3.1 GENERATION OF REQUIRED PATTERN

Once the desired pattern, e.g. fig. 3.2, has been decided, it is necessary to store these data in a form which can subsequently be recognised by the KIM microprocessor which controls the scan coils of the SEM. Patterns were written using a software package developed by Mackie (1984) called DESIGN or more recently on the commercially available MYCAD. Both programmes generate a file in which the co-ordinates of each rectangle is stored using its top-left, bottom-right co-ordinates. Each rectangle has its size stored as a number of pixels, and not as a physical length, with the position of each recorded relative to a frame which is 4096 by 4096 pixels square with its origin located at the bottom left corner. Data on the exposure for each pixel is also stored in this file, and is simply a number in $\mu C.m^{-2}$ stating how much charge must be given to each pixel to ensure complete exposure. This number will directly affect the "dwell time" - i.e. the amount of time that the beam will remain at each pixel point.

3.3.3.2 EXPOSURE OF THE PATTERN

There are two possible ways in which a pattern can be exposed. In normal SEM operation the beam is unblanked at every exposure position and hence requires information on every pixel point, i.e. whether it should be exposed or not. Consequently this involves a high throughput of information. An alternative method is that of "vector scanning", in which the beam is used only to scan the areas requiring to be exposed. This greatly reduces the amount of data needing to be processed, and is the method employed here.

When exposing a pattern it is very important that any hysteresis in the scan coils is adequately corrected. Incorrect scanning would lead to badly defined particles. Two possible methods for scanning a pair of rectangles

are shown in fig. 3.6. In fig. 3.6(a), the beam moves from position A, to position B, but due to the finite time constant of the scan coils, the correct y co-ordinate is approached only asymptotically, resulting in a particle with a badly defined, or rounded corner. (Sharp corners are very important, and will be discussed in Chapter 4.) In order to overcome this problem, the pattern should be scanned as shown in fig. 3.6(b). In this way any skewing is contained within the particle, and so is effectively masked.

The particles dimensions, as mentioned before, are stored as a number of pixels. The physical size of each pixel can be changed by varying the magnification of the microscope. A table showing commonly used values of magnification, frame and pixel size is given in table. 3.1. For PAT1, in which, for the largest particle, $L_1=L_2=4\mu m$, a magnification of x2500 was used, and as can be seen from the corresponding frame size this occupies one quarter of the available area on the membrane. To double the in-plane dimensions of the particles only requires that the magnification of the SEM be halved. Although the above description was concerned with rectangles, diamonds and triangles can also be scanned by using rectangles of increasing (and/or decreasing) size, as shown (not to scale) in fig. 3.7.

3.3.3.3 OPERATING CONDITIONS FOR THE SEM

When scanning a pattern the SEM was operated at 50kV, with a spot (probe) size of 8nm. A Faraday cup was situated in the vicinity of the specimen in order that the beam current can be measured. This is necessary for calculating the correct dwell time per pixel, in order to get complete exposure of the resist.

To maximise the use of the available space on the membrane, patterns should be scanned parallel to the edges of the membrane. This requires that the x and y axes of the scan coils be coincident with the edges of the membrane, and this is achieved simply by rotating the specimen once it is inside the microscope. However the ξ and ζ axes of the goniometer must also be

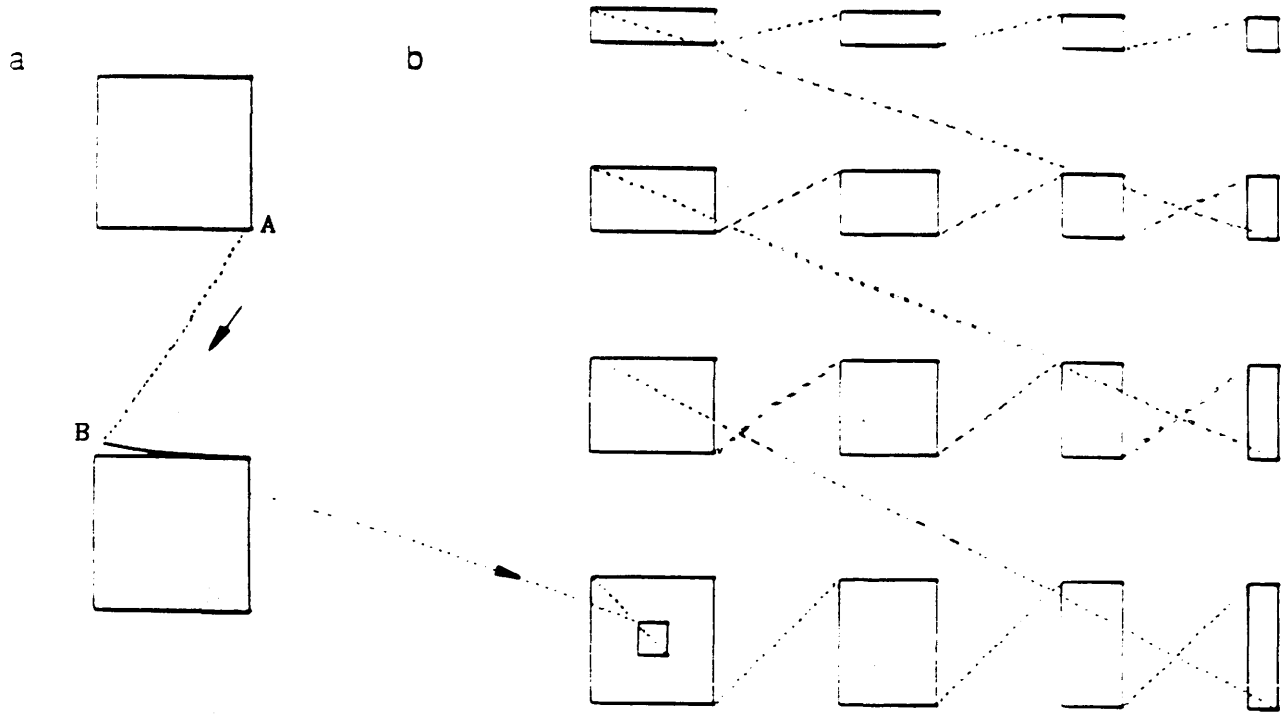

Fig. 3.6 **Possible procedure for scanning rectangles (a) incorrectly and (b) correctly.**

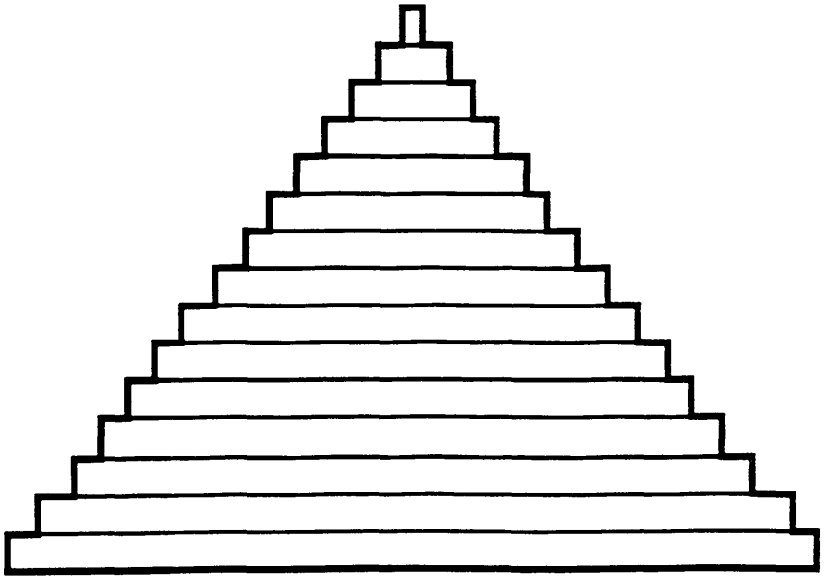

Fig. 3.7 Diagram which is not to scale showing how diamonds and triangles are scanned using rectangles.

Magnification	pixel size X	pixel size Y	frame size X	frame size Y
80k	0.38	0.29	1.56	1.19
40k	0.76	0.58	3.11	2.38
20k	1.52	1.15	6.23	4.71
10k	3.05	2.32	12.5	9.5
5k	6.1	4.64	25	19
2.5k	12.2	9.27	50	38
1250	24.4	18.5	100	76

pixel sizes in nm : frame sizes in µm

Table 3.1 Values of pixel and frame size for commonly used magnification settings.

considered as they control the stage movement, and their relationship with the frame and scan axes must be calculated when scanning more than one pattern. This problem is overcome by noting the angle between the frame and goniometer axes. Movement parallel to the edges of the membrane window is then performed as a combination of ξ and ζ stage movements. Information on the position of each pattern is contained in a "position file" and this is used to guide the stage to the correct position prior to scanning each pattern. Once the relationship between the three sets of axes has been determined, the entire process is controlled by the computer. Only the magnification need be changed by the user.

3.3.4 DEVELOPING THE EXPOSED PATTERN

Those parts of the resist exposed to the electron beam are removed by immersing the sample in a 3:1 mixture of iso-propyl alcohol (IPA) and methyl iso-propyl ketone. The solution had previously been heated to 23C and the sample was placed in it for 30 seconds. After this time it was removed and washed and rinsed with fresh IPA, again for 30 seconds. The sample was then blown dry with N_2 at an oblique angle.

3.3.5 DEPOSITION OF METAL

Permalloy or cobalt was evaporated over the entire sample under a vacuum of $<10^{-6}$ Torr. The samples were fixed to a microscope slide and positioned approximately 20cm directly above the source of the metal, which itself is held in a tungsten-molybdenum boat. The sample was placed as close as possible to a quartz crystal on a copper support column, which was water cooled, to ensure that neither the substrate nor the crystal heated up. The latter has a specific resonant frequency which is related to the thickness of metal deposited on its surface. By calibrating the change in resonant frequency with thickness of metal deposited, as determined by interferometric

methods, it is possible to prepare specimens whose thickness is accurately known. During the evaporation process it was found that evaporation rates of 1.0Å.sec^{-1} gave good results. Faster evaporation rates induced stress in the material, and adhesion to the substrate was not good, McVitie (1988).

3.3.6 LIFT-OFF

The metal deposited in the previous step obviously covers the entire specimen and is in direct contact with both the Si_3N_4 and the unexposed resist. To remove this latter material, the specimen was placed in acetone. This has the effect of "lifting-off" the unexposed resist, along with the metal which is attached to its surface. Once lift-off has finished, the sample is rinsed in fresh acetone and then blown dry.

Before the specimen is placed in the microscope, it is coated with a thin layer (20nm) of carbon. This is because Si_3N_4 is not a good conductor and if placed directly in the electron microscope it tends to charge up or in the worst case could even break.

Some samples were also fabricated on solid GaAs substrates using the above procedure. These samples, although not suitable for analysis using TEM, are much more robust and were analysed using oil immersion Kerr microscopy, and results are presented in section 5.4.

3.4 BASIC CHARACTERISATION OF THE PARTICLES AND THIN FILMS

3.4.1 BASIC PHYSICAL CHARACTERISATION OF THE PARTICLES

Particles were fabricated as described in section 3.3. In order to examine their shape and microcrystalline form, they were examined using a JEOL 1200EX CTEM under normal high magnification imaging conditions, (section 2.2). Shown in fig. 3.8 is a high magnification (in focus) image of a 4.00 by 4.00μm $Ni_{82.5}Fe_{17.5}$ particle of thickness 60nm. It can clearly be seen that

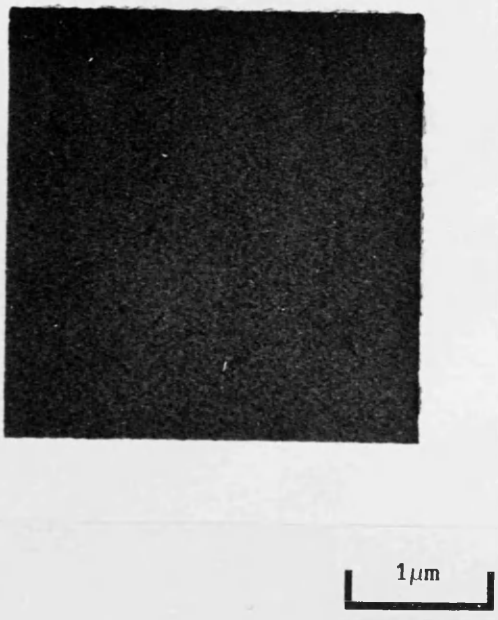

Fig. 3.8 High magnification image of a $Ni_{82.5}Fe_{17.5}$ particle.

the lithography process has resulted in very well defined particles. The edge definition, calculated from the variation in the spatial extent at the edge of the sample was found to be at best 10nm. From a high magnification image fig. 3.9(a), the polycrystalline form can be seen. In the case of permalloy, the crystallites were found to have an average diameter in the range 5 to 10nm. The cobalt crystallites had a much more diverse range of sizes and shapes, and crystallites having circular as well as more acicular profiles were found, fig. 3.9(b). The in-plane dimensions were found to be in the range 5 to 50nm. In both cases the values of crystallite sizes are in agreement with previous results for films evaporated at normal incidence, (Chopra (1969) and Tanaka (1985)). Using selected area diffraction (SAD) patterns, the crystal structure of both materials were determined. A SAD pattern from a Co particle is shown in fig. 3.10, from which it was found that cobalt had a hexagonal close packed structure. Permalloy was face centered cubic with a lattice parameter of 0.34nm.

Local variations in the crystal structure were also investigated by taking diffraction patterns from relatively small areas of the particles. This is done by selecting the smallest "spot", or source size, (section 2.2.1), and then focusing the incident beam on the specimen plane. A doubly exposed micrograph, fig. 3.11 gives an approximate indication of the size of this source which was found to be approximately 100 $\mp$ 20nm. Due to the size of the beam when it is focused on the specimen plane, diffraction patterns from the convergent beam can be used to study the structure of relatively small parts of the specimen. Using a convergent incident beam, the resulting diffraction pattern, is shown in fig. 3.12. Diffraction patterns of this type were obtained from various cobalt samples in order to determine any local variation of the crystal structure or if any texturing was present. In all the samples, (including those with more irregular domain structures (section 6.6)), no preferred orientation of the c-axis was found, and all samples had a reproducibly similar microstructure.

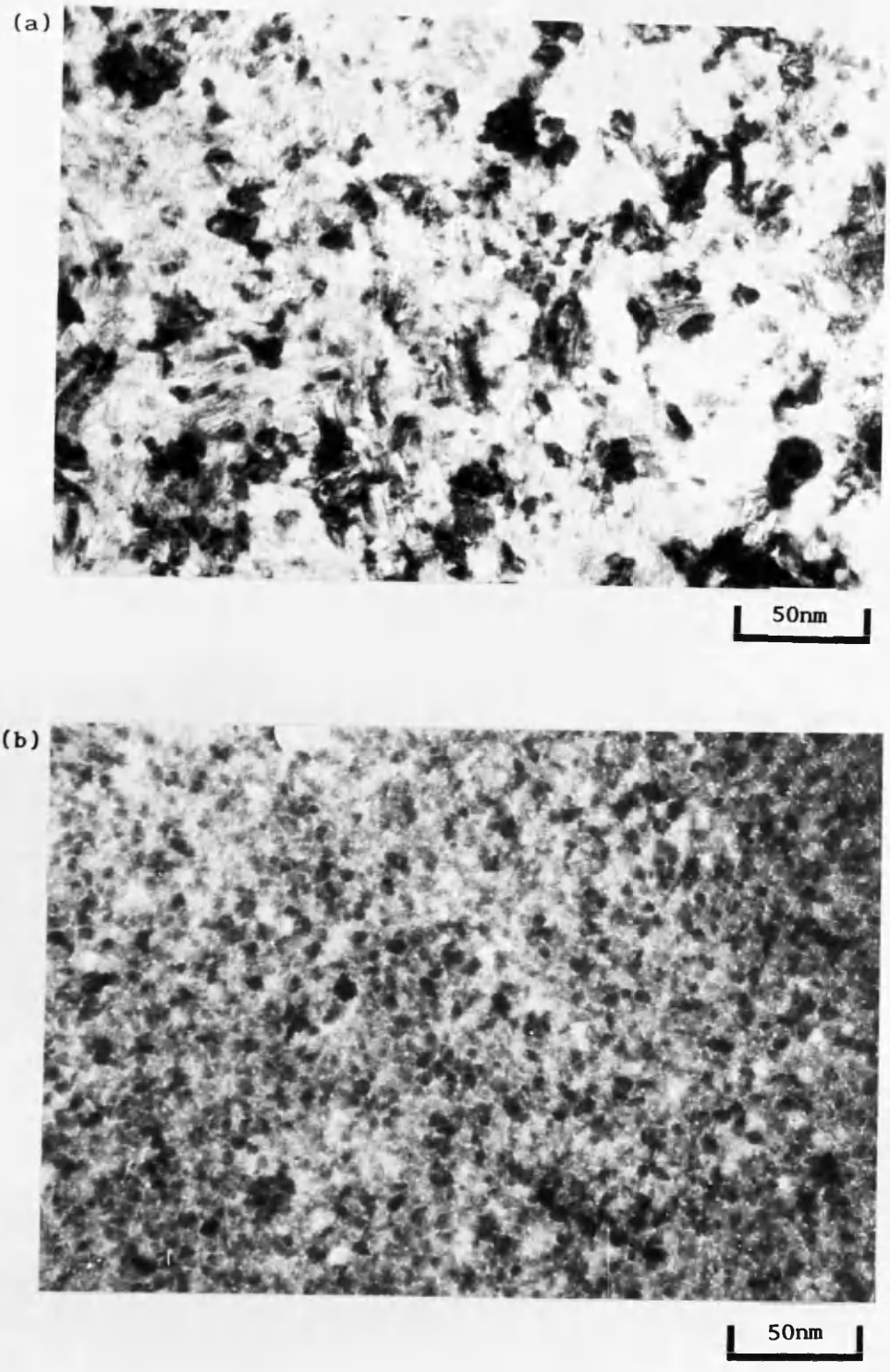

Fig. 3.9 High magnification image showing the size and form of the crystallites from an b) $Ni_{82.5}Fe_{17.5}$ particle and a) Cobalt particle.

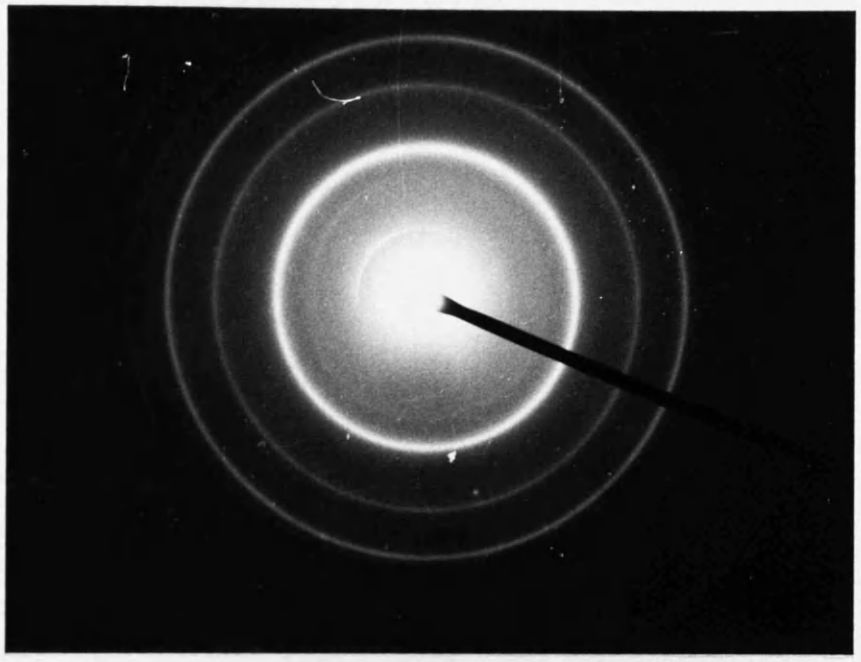

Fig. 3.10 Selected area diffraction pattern from a cobalt particle.

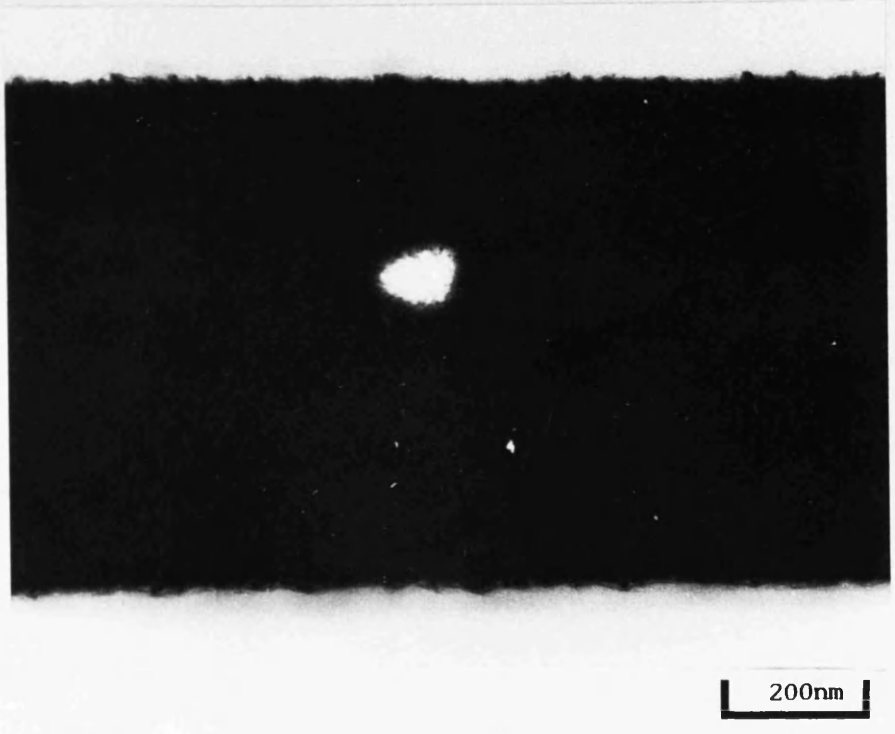

Fig. 3.11 Doubly exposed micrograph showing size of source used to obtain convergent beam diffraction patterns.

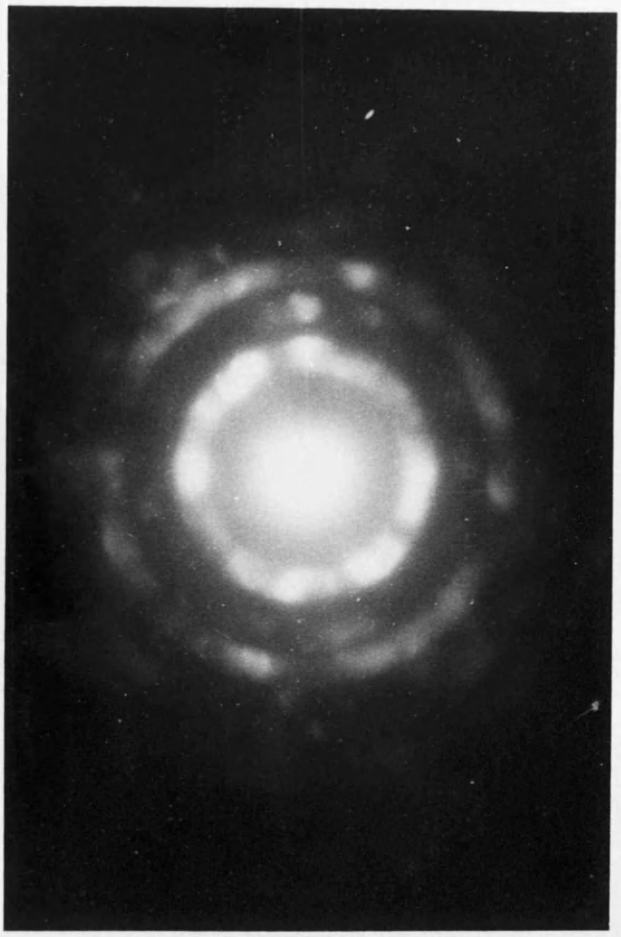

Fig. 3.12 Diffraction pattern obtained from a Cobalt particle using the convergent incident beam method.

The samples were all evaporated at normal incidence in the presence of only a small residual field present in the laboratory. To check if any anisotropy was induced during the evaporation process, extensive thin films of cobalt and permalloy were prepared. The films were prepared under exactly the same evaporation conditions as were used for the particles. In this case however, a circular glass disk of thickness 0.15mm and diameter 13mm was used as the substrate. The glass substrate was again fixed to the copper support column to ensure that it did not heat up.

The macroscopic magnetic properties of the films were then examined, at the University of Regensburg (Germany), using two techniques, i) a vibrating sample magnetometer (VSM) and ii) magneto-optical (M/O) techniques. The former is well documented (Flanders and Doyle (1962)) and can be used to obtain volume hysteresis loops from thin films. In-plane hysteresis loops were obtained by applying a field along orthogonal directions that were approximately aligned along axes which would have been parallel to those the membrane usually lay along. The VSM allows $\underline{\mathbf{M}}_s$, $\underline{\mathbf{M}}_r$ and $\underline{\mathbf{H}}_c$ to be found. The last of these quantities is given for the two types of films in table 3.2. Hysteresis loops from VSM measurements obtained from cobalt and permalloy samples are shown in figs. 3.13 and 3.14 respectively.

In the M/O technique the net surface magnetisation from a circular area approximately 2mm in diameter was obtained using a plane polarised laser beam. The surface magnetisation causes a change in the angle of polarisation due to the Kerr effect (section 2.1), which can then be detected using a polarisation spectrometer. Surface hysteresis loops obtained from applying a field in any direction through 180° could easily and rapidly be obtained in order to investigate if a magnetic easy axis existed. In both the cobalt and permalloy films, no easy axis was found. Hysteresis loops obtained from both the permalloy and cobalt samples using this technique are shown in figs. 3.15 and 3.16 respectively. Coercivities for the evaporated thin films, obtained

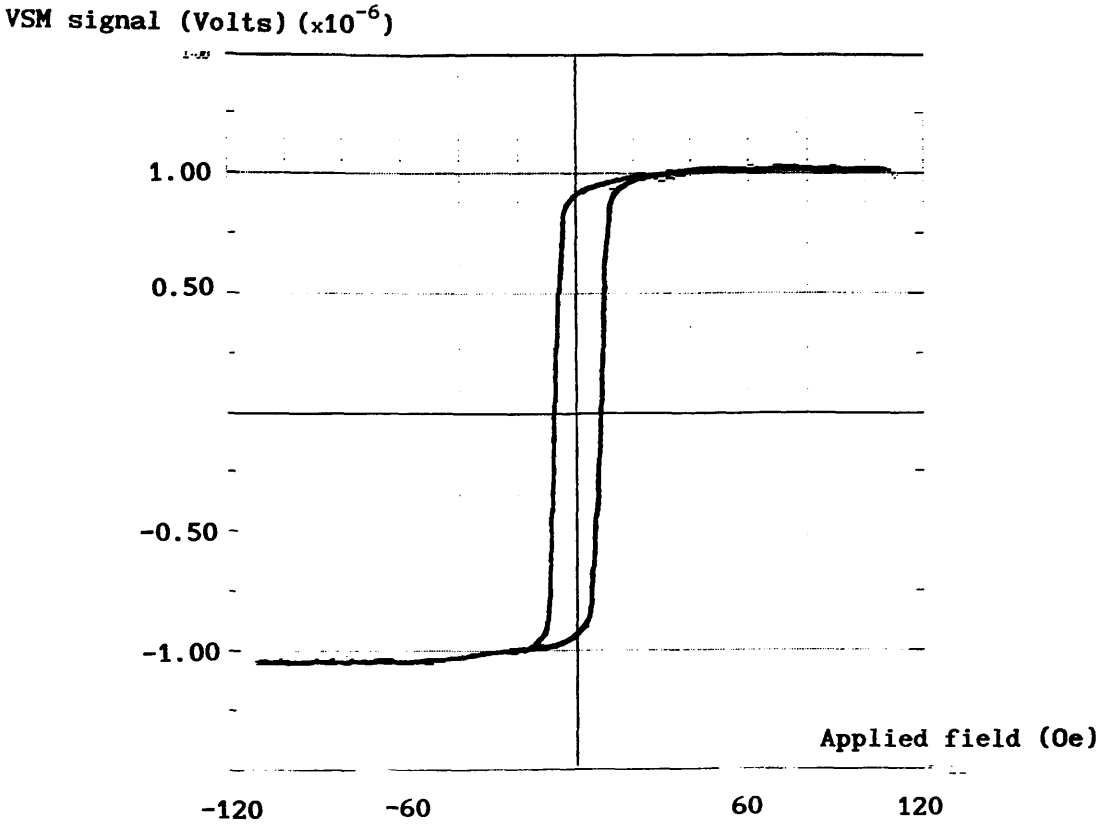

Fig. 3.13 A hysteresis loop obtained from a 60nm thick NiFe sample using the VSM technique.

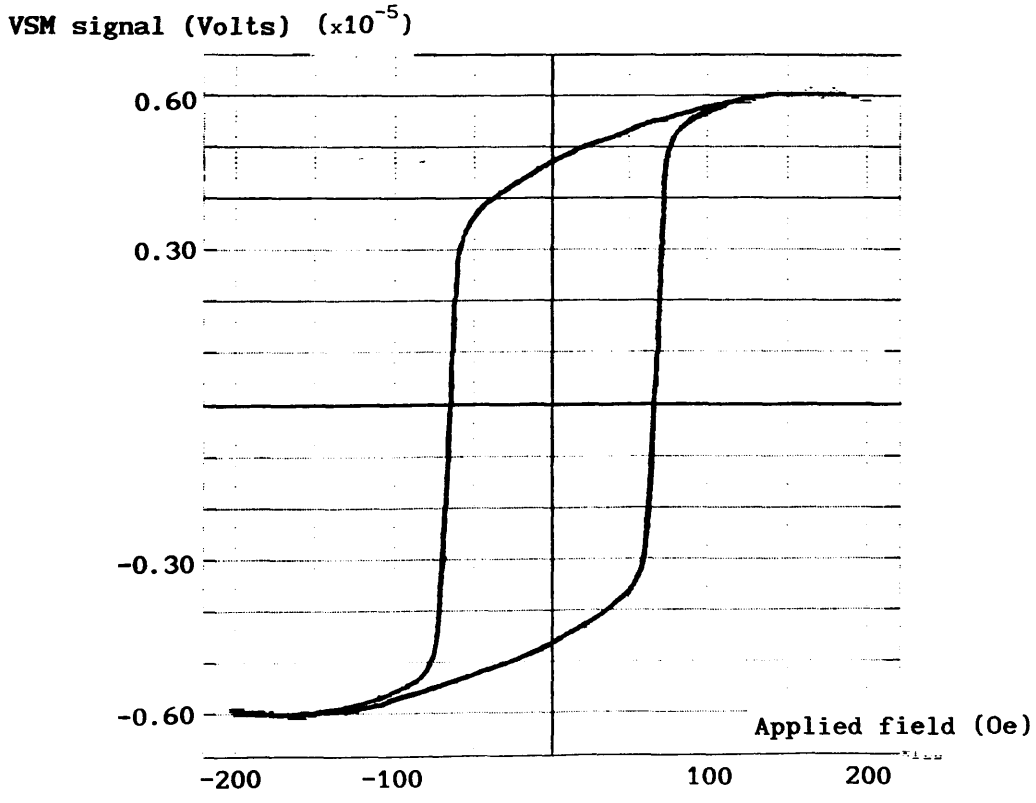

Fig. 3.14 A hysteresis loop obtained from a 60nm thick Co sample using the VSM technique.

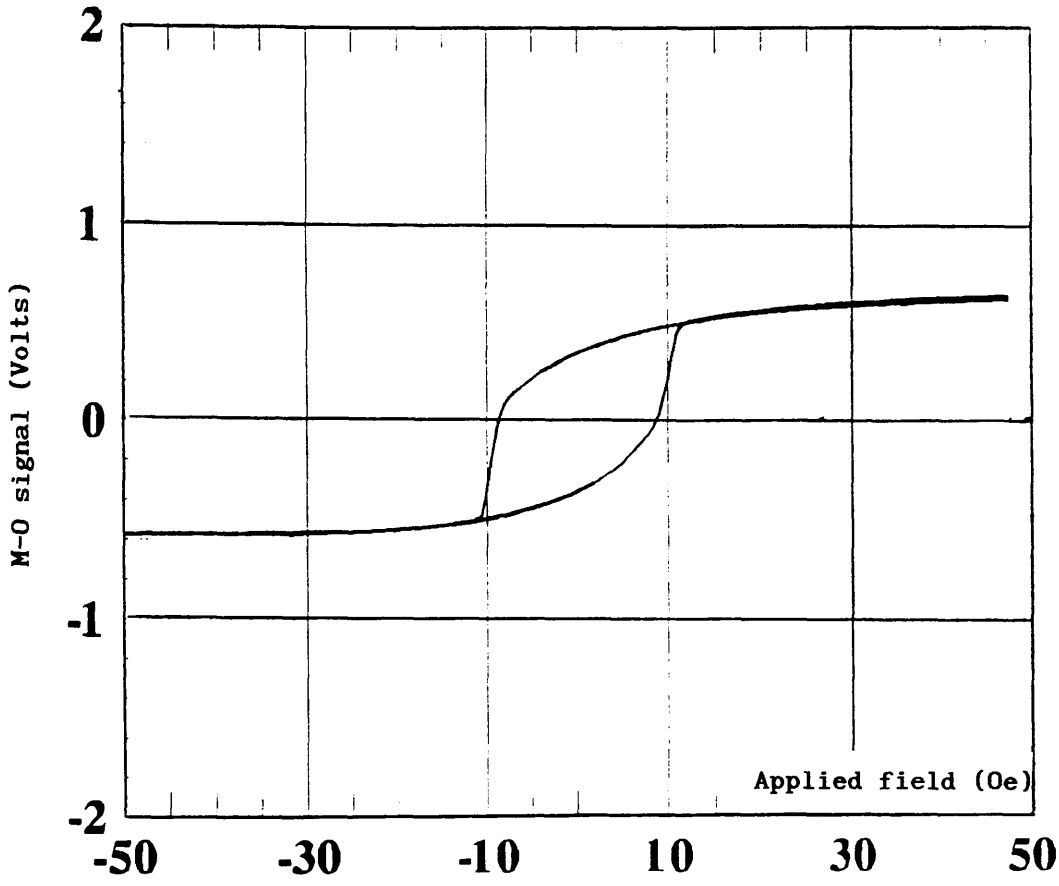

Fig. 3.15 A hysteresis loop obtained from a 60nm thick NiFe sample using the M-O technique.

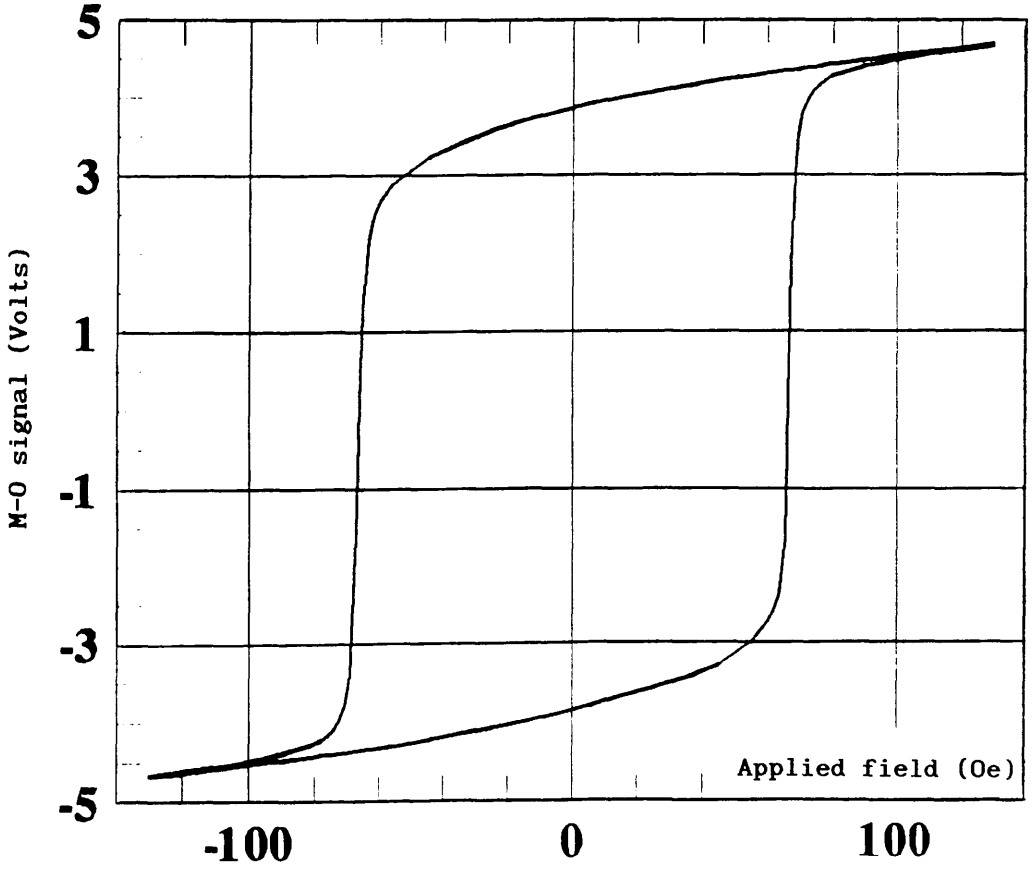

Fig. 3.16 A hysteresis loop obtained from a 60nm thick Co sample using the M-O technique.

by the M/O technique are given in table 3.2. From this table, it can be seen that both the VSM and M-O techniques gave consistent results, and from the M-O data no measurable anisotropy was induced during the evaporation process. Comparing figs. 3.13 and 3.15, or 3.14 and 3.16, it can be seen that in addition to giving similar values of coercivity, the general shape of the hysteresis loops, as determined by either technique, are very similar.

Each of the values quoted in table 3.2 is an average and was formed by obtaining many hysteresis loops such as those shown in figs. 3.13 to 3.16.

60nm thick $Ni_{82.5}Fe_{17.5}$

	V.S.M.	M/O
(a)	5.3	4.0
(b)	3.0	3.6

60nm thick Cobalt

	V.S.M.	M/O
(a)	70.0	69.7
(b)	65.2	66.2

Table 3.2 Values of coercivity H_c (Oe) as measured by the Vibrating Sample Magnetometer, (VSM), and the Magneto-Optic, (M/O), technique. The measurements (a) and (b) were taken orthogonally to each other.

CHAPTER 4

FRESNEL IMAGING OF $Ni_{82.5}Fe_{17.5}$ PARTICLES

4.1 INTRODUCTION

The domain structure of particles of various sizes and thicknesses, fabricated using the method of chapter 3, are described in this chapter. Three different thicknesses of $Ni_{82.5}Fe_{17.5}$ samples were initially examined in their as-grown states and the results are given in section 4.2. In-situ magnetising experiments were then performed on the particles and a selection of the results are described in section 4.3. Section 4.4 describes the remanent domain structures after the particles had been subjected to both an a.c. demagnetisation and a large saturating field. Finally section 4.5 summarises the most important conclusions which can be drawn from the in-situ magnetising experiments and also highlights some of the difficulties which are encountered when using the Fresnel mode.

4.2 AS-GROWN DOMAIN STRUCTURES

The domain structures of the permalloy samples were initially examined in their as-grown state. The investigations on 20 and 60nm thick particles of similar in-plane dimensions, performed by McVitie (1988) served as a very useful reference with which the as-grown states could be compared. The reproducibility of the as-grown domain structures with those reported previously was very good and the structures found in 17, 60 and 95 nm thick particles are described in sections 4.2.1 to 4.2.3 respectively.

4.2.1 17nm THICK PARTICLES

Fresnel images and schematic diagrams of the as-grown domain structure of

various 17nm thick particles are given in fig. 4.1(a) and (b) respectively. It can immediately be seen that some particles have solenoidal, or flux-closure domain structures while some of the more acicular particles have non-solenoidal domain structures. Those particles which are found to have solenoidal domain structures have an in-plane aspect ratio (R) less than approximately four. Such particles tend to have regular domain structures although the domain walls are sometimes curved when the particle has a non-integral value of R, e.g. the 4.00 by 3.00μm particle which is denoted by * in fig. 4.1(b). Particles having an integral value of R have domain structures which consist mainly of 90° and 180° walls, although, in general, long sections of 180° wall extending along the bulk of any of the particles are not commonly found. A negligible amount of "rippling" was detected in this thickness of sample.

Four different types of non-solenoidal structures were found in particles with R > 4, and are shown in fig. 4.2. It should be noted that the essential difference between the four structures is the relative directions of the domains marked A and A' at the end of the particle and also that the central domain of all the particles is magnetised parallel in the same direction. Domain structures of the type shown in fig. 4.2(a) are referred to as type II(a), while those of fig. 4.2(b) are type II(b). Types II(c) and (d) are shown in figs. 4.2(c) and (d) respectively. In all cases the particle consists of large central domain which is magnetised parallel to the long axis and at each end is a complex end structure which serves to reduce the contribution of the magnetostatic energy to the total energy of the particle. (Non-solenoidal structures are discussed in greater detail in section 5.4.3.)

The least acicular particles having non-solenoidal as-grown domain structures are found to be 4 by 0.75 (R=5.3), 3 by 0.50 (R=6), 2 by 0.38 (R=5.3) and 1 by 0.25μm (R=4). Particles fabricated orthogonal to each other but with the same in-plane dimensions had similar as-grown structures.

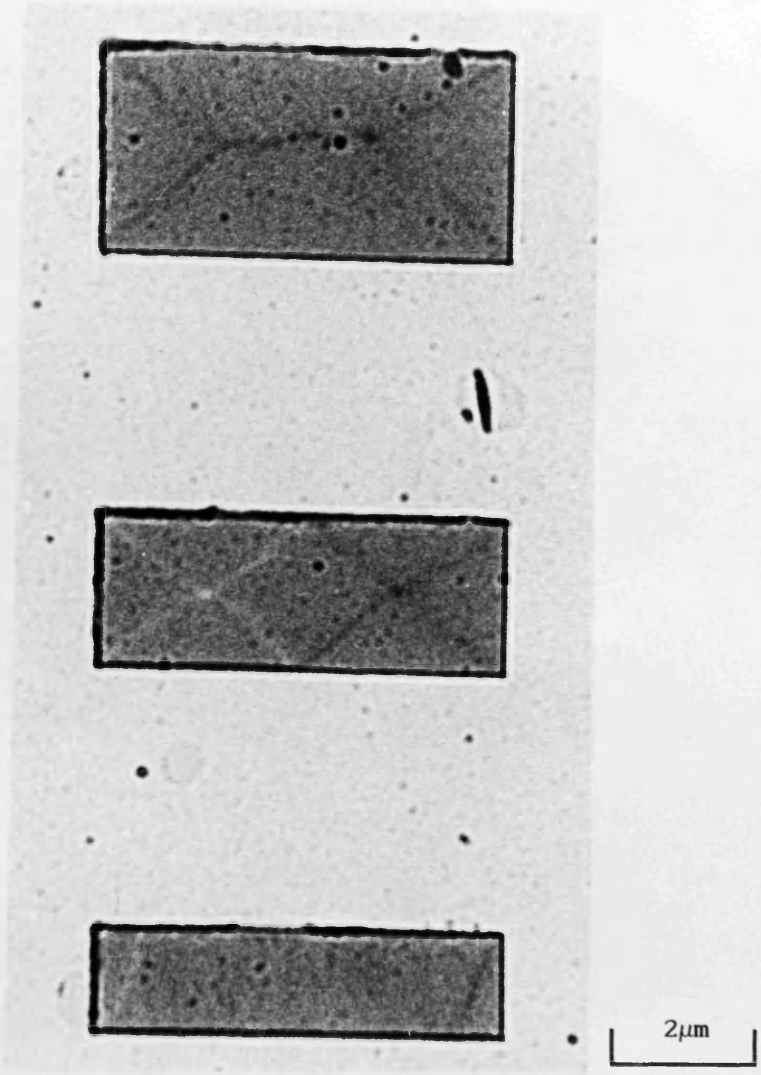

Fig. 4.1(a) Fresnel images showing the as-grown domain structure of various 17nm thick particles.

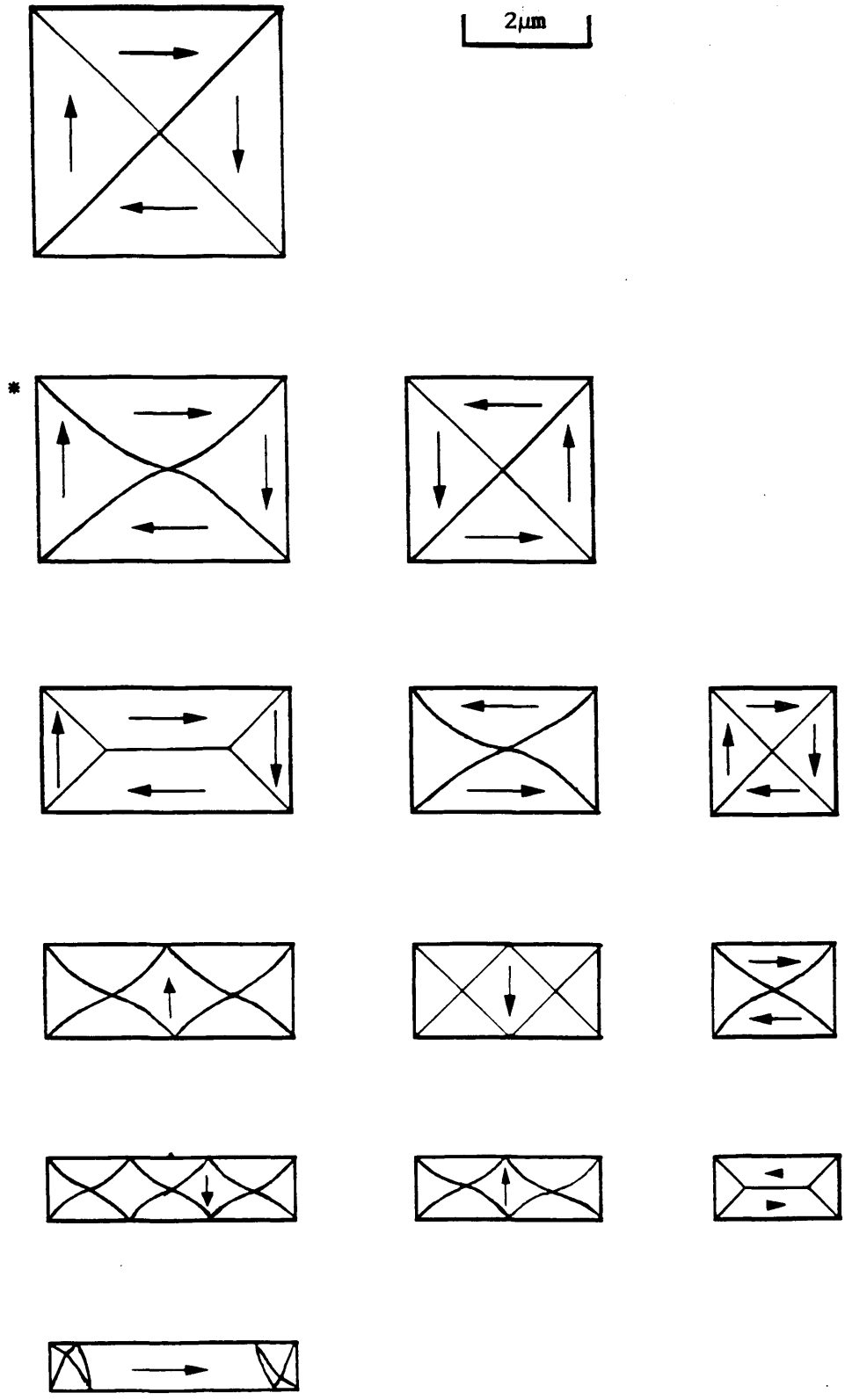

Fig. 4.1(b) Schematic showing the as-grown domain structure of various 17nm thick particles.

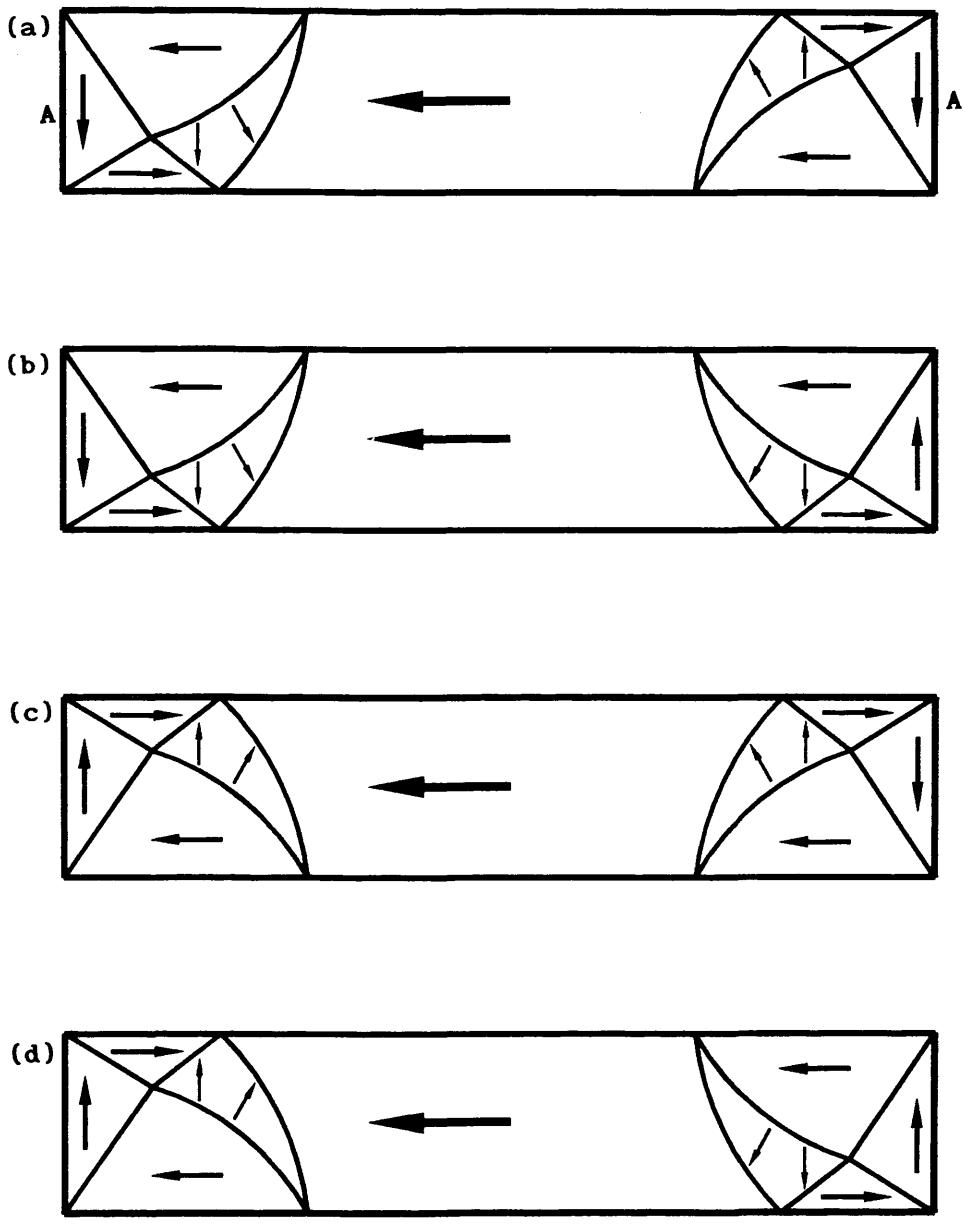

Fig. 4.2 The four different types of non-solenoidal domain structures which are found.

4.2.2. 60nm THICK PARTICLES

The as-grown domain structures of 60nm thick particles are shown in fig. 4.3. In a similar manner to the thinner samples, some particles were found to have solenoidal domain structures while others had non-solenoidal forms. The change in the form of the as-grown domain structure was again found to occur when $R \cong 4$.

All particles with $R \leq 4$ had solenoidal domain structures although in contrast to the 17nm thick sample, no curved walls were found in those particles having $R \neq \mathbb{Z}$, where $\mathbb{Z}$ denotes any integer. Instead, these particles had a short length of 180° cross-tie wall, and the domain structure consisted entirely of 90° and 180° walls. Almost all of the particles which had integral values of R (≤ 4) had domain structures consisting entirely of 90° walls. Long sections of 180° cross-tie walls were not generally found in the as-grown state of any of the particles. From analysis of the solenoidal as-grown domain structures of $R \leq 4$ particles, McVitie (1988) concluded that;

$$2\sqrt{2}\,\sigma_{90}(60) \leq \sigma_{180}(60) \qquad (4.1)$$

where $\sigma_i(j)$ is the domain wall energy per unit area in a sample of thickness "j" nm, in which the magnetisation vector rotates by "i" degrees across the domain wall. Experimental evidence provided by the samples grown in this project support this statement.

Particles having $R > 4$ had type II as-grown domain structures. All of the type II structures occurred and there was no preference for the central domain of these particles to be magnetised along one particular direction. Again particles having similar in-plane dimensions, but fabricated orthogonally to each other displayed similar as-grown domain structures.

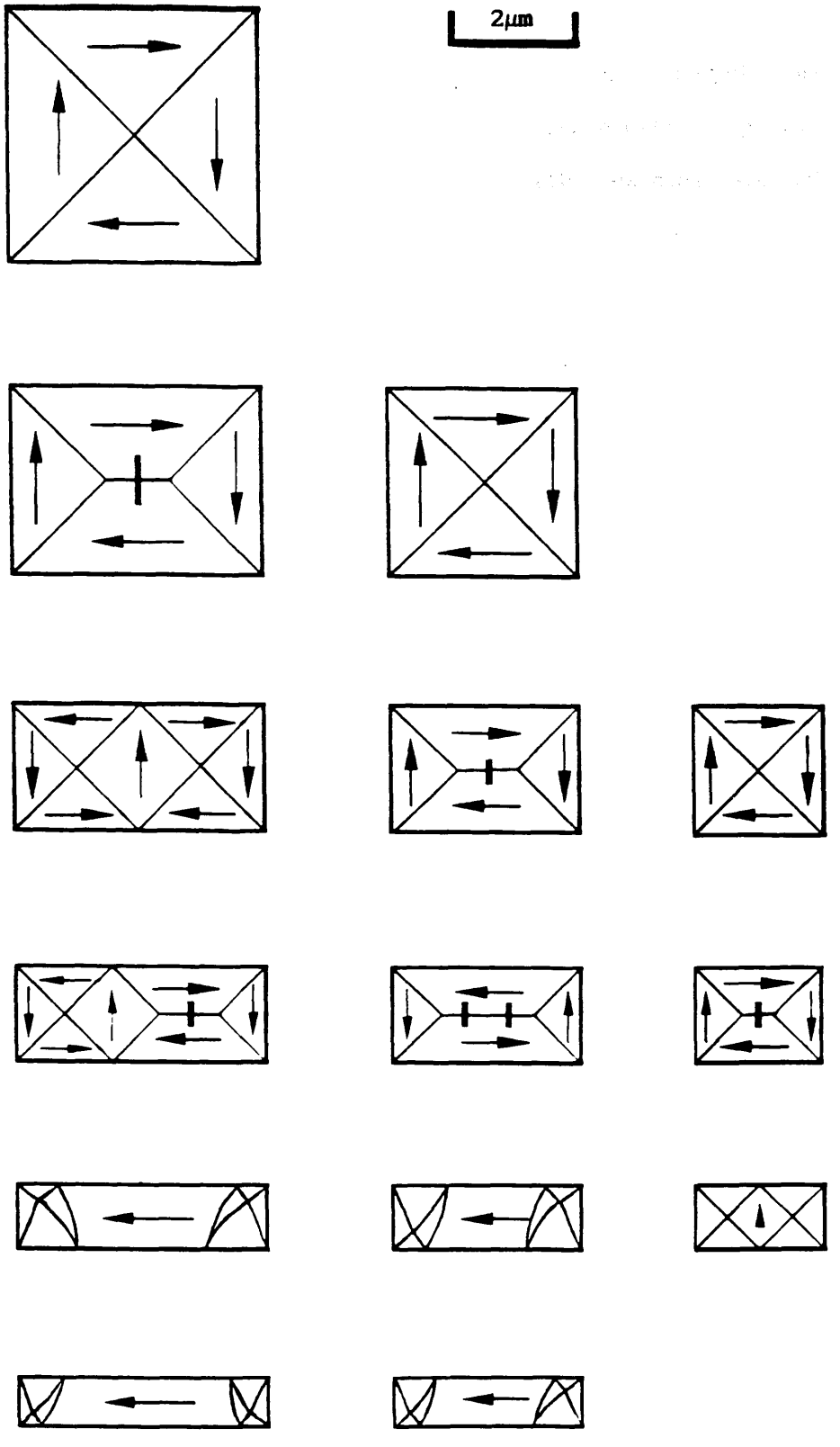

Fig. 4.3 Schematic showing the as-grown domain structure of various 60nm thick particles.

4.2.3. 95nm THICK PARTICLES

The as-grown domain structures of various 95nm thick particles are shown in fig. 4.4. The change from solenoidal to non-solenoidal as-grown structures takes place when the in-plane aspect ratio exceeds approximately 8. Particles with $R < 8$, $R = \mathbb{Z}$, exhibited extremely regular domain structures which consisted entirely of 90° walls. An interesting point to note is that the domain structure of the 4.00 by 2.00μm particle, indicated by A on fig. 4.4, has both 90° and 180° walls. This type of structure has been observed in particles fabricated from alternate layers of iron and permalloy, in which the individual layers were 6.4 and 3.2nm thick respectively, with the total thickness equal to 0.27μm, (Ruhrig (1989)). In those particles with $R < 8$, $R \neq \mathbb{Z}$, no curved domain walls were observed, and the domain structures consisted of only 90° and 180° walls. Cross-ties were observed in some of the 180° walls, although in a similar manner to the previous examples, long sections of 180° walls were not found. Guided by the experimental evidence, (fig. 4.4), it appears that the length of 180° wall which is present in the as-grown state is generally the shortest possible.

Particles with $R > 8$ were found to have non-solenoidal as-grown domain structures, and all type II structures were found.

4.2.4. SUMMARY

In all three thicknesses of particles described in sections 4.2.1 to 4.2.3, two different types of as-grown domain structures were possible; solenoidal and non-solenoidal. Within the range of in-plane dimensions presented, the transition from solenoidal to non-solenoidal as-grown structures takes place at a specific value of R which, although varying with thickness, does not appear to depend significantly on the physical value of the in-plane dimensions. $R^*(t)$ is defined as the value of R at which the transition from solenoidal to non-solenoidal as-grown states occurs for a sample of thickness

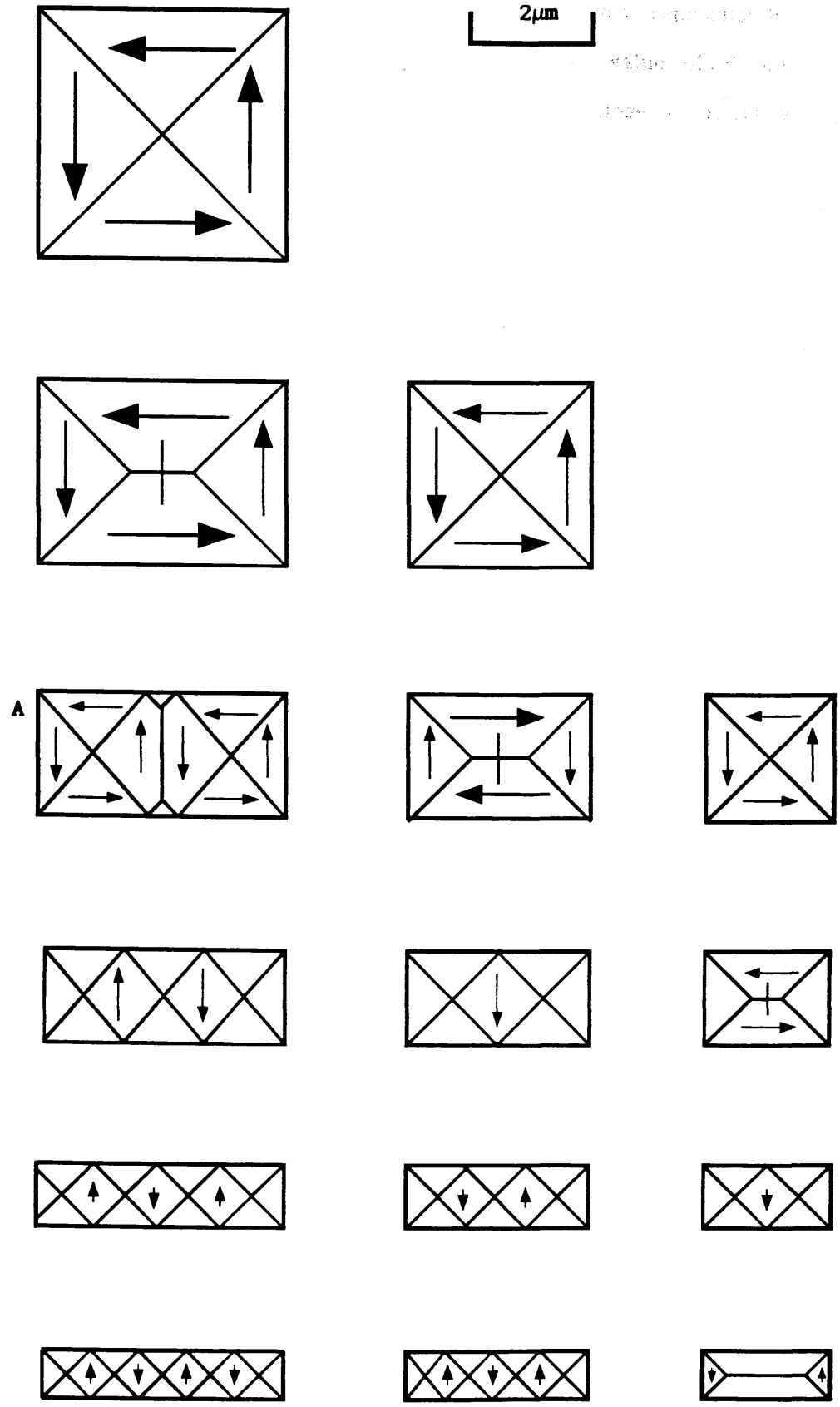

Fig. 4.4 Schematic showing the as-grown domain structure of various 95nm thick particles.

t. After analysing various samples, it was found that the as-grown structures of all the particles were in general highly reproducible, with the only exceptions occurring at those particles whose value of R was close to $R^*(t)$. Particles having an in-plane aspect ratio close to $R^*(t)$ were found in either solenoidal or non-solenoidal as-grown forms.

4.3 IN-SITU MAGNETISING EXPERIMENTS ON 60nm THICK $Ni_{82.5}Fe_{17.5}$ PARTICLES

The aim of this section is to describe how various different solenoidal domain structures react under the influence of an applied field. The potential choice of size, thickness and form of the particles and domain structures is overwhelmingly large. To ease the comparison between particles having different in-plane aspect ratios and domain structures, only 60nm thick particles having solenoidal domain structures are described in this section. The in-situ experiments performed on 17 and 95nm thick particles are described in detail in sections 5.3.1 and 5.3.3. It should be noted that the maximum value of field which can be applied in-situ to the particles is much below that required to saturate the particle. Section 4.3.1 presents results from particles having solenoidal as-grown domain structures, in which the applied field was parallel to the long (easy) axis of the particle. Section 4.3.2 describes the effect of fields which have been directed along the hard axis, i.e. parallel to the short axis of the particle. In both cases, the field was aligned to an accuracy of $\mp 5^\circ$. The long and short axes of the particle are termed easy and hard from magnetostatic considerations. They should not be confused with easy or hard anisotropy axes.

4.3.1 IN-SITU APPLICATION OF AN EASY AXIS FIELD

The results presented in this section apply only to 60nm thick $Ni_{82.5}Fe_{17.5}$ particles existing in solenoidal as-grown domain structures. As stated in

section 4.2.2, the domain structures of particles having an integral value of R consisted almost entirely of 90° walls, while those with non-integral values had both 90° and 180° walls. The effect of applying an easy axis field in-situ to particles having integral and non-integral values of R are discussed separately in sections 4.3.1.1 and 4.3.1.2 respectively.

4.3.1.1 INTEGRAL ASPECT RATIO PARTICLES

The simplest structure which was analysed was that displayed by a square particle. A series of Fresnel images of a 4μm square particle taken at different values of applied field are shown in fig. 4.5. As explained in section 2.2.2, in this mode domain walls are revealed as light and dark lines with the intensity and diffuseness of the lines giving an indication of the magnitude of the in-plane rotation and also the angle of rotation of the magnetisation across the domain wall.

By analysing the series of Fresnel images in fig. 4.5, it is possible to deduce the approximate directions of magnetisation within each of the domains, and the resulting schematic is given in fig. 4.6. From fig. 4.6, it can be seen that the as-grown domain structure of the 4μm square particle consists only of 90° walls which extend into the corners of the particle. (Such a structure is predicted by the algorithm described in section 1.4.2.) As the applied field ($\underline{H}_{ext}$) is increased, the domain which is magnetised parallel to the applied field grows at the expense of the others. As the Bloch line at A is forced closer to the edge of the particle, the domain walls can be seen to bend. It should be noted in fig. 4.6(d), that the walls marked B and B' are initially straight and the curving is most pronounced close to the Bloch line, (A). At a specific value of applied field a short length of approximately 180° cross-tie wall is introduced, as shown in fig. 4.6(e). (That this 180° wall is a cross-tie wall is to be expected from the thickness of the particle.) The angles marked CDE and C'D'E' in fig. 4.6(e) are now approximately 90°. Further increase in the magnitude of the applied

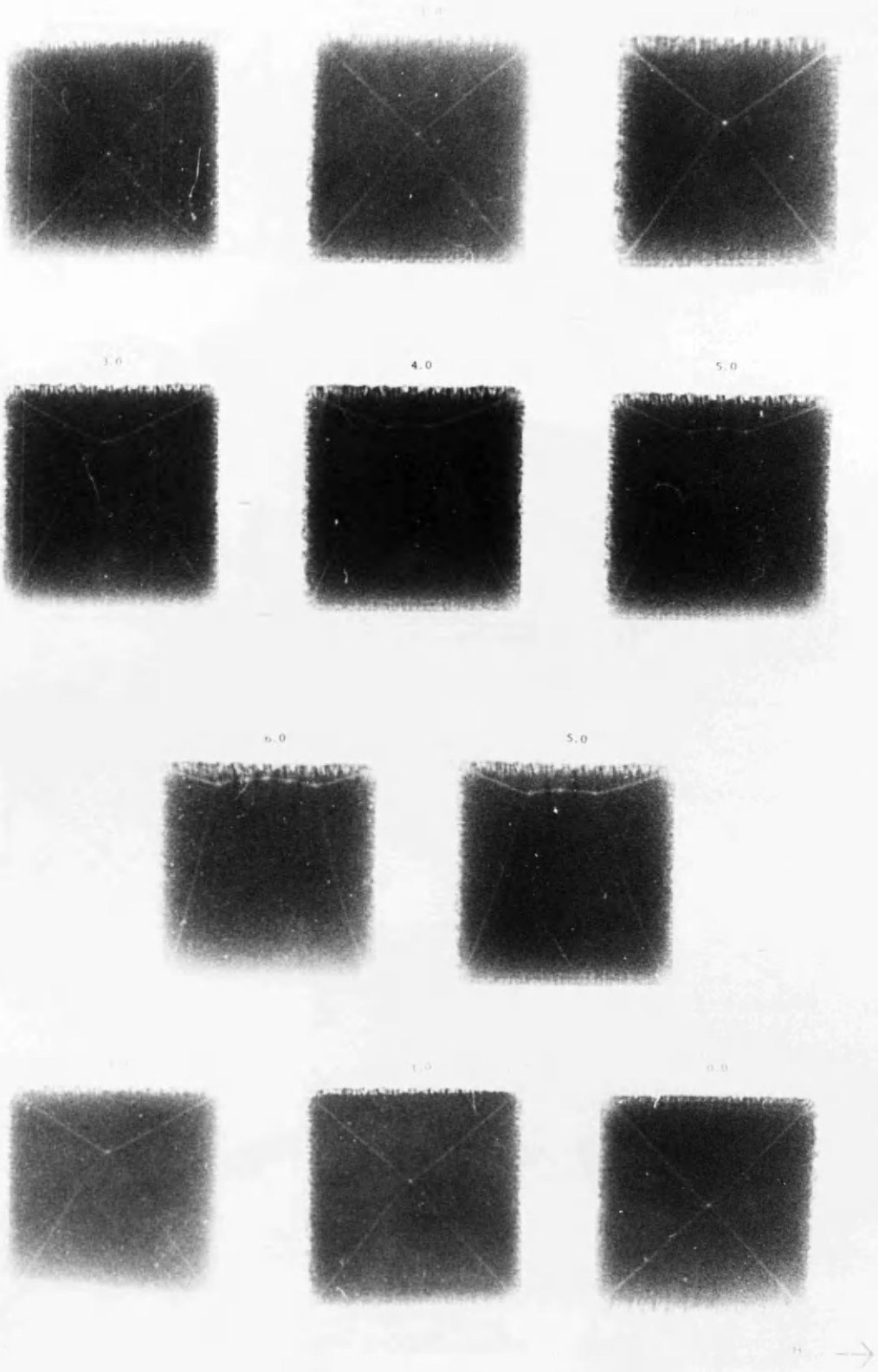

Fig. 4.5 Series of Fresnel images of a 4.00μm particle obtained at different values of applied field.

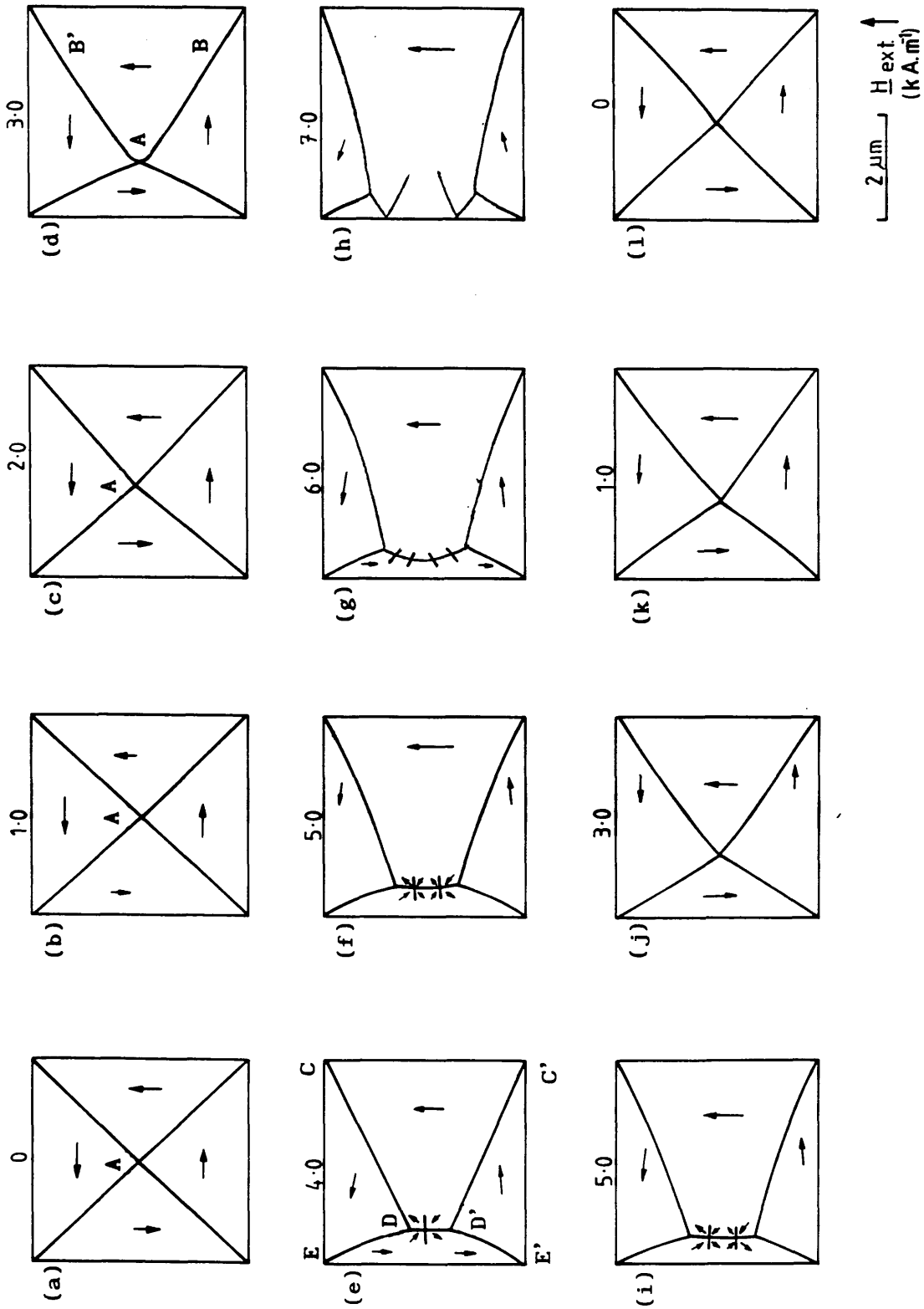

Fig. 4.6 Schematic diagrams showing the approximate directions of the magnetisation in each domain, as deduced from fig. 4.5.

field causes the length of the cross-tie wall to increase as it is driven closer to the edge of the particle. This retains the angles CDE and C'D'E' at approximately 90°. As the cross-tie wall is forced closer to the edge of the particle the density of cross-ties increases, and the cross-tie wall itself starts to bend, resulting in its mid-point being closer to the edge of the particle, fig. 4.6(g). From this point it would be expected that further increase in the magnitude of the applied field would drive the cross-tie wall into the edge of the particle. However, at the next observation point the wall has collapsed and the resulting structure is as shown in fig. 4.6(h). Reduction of the applied field to zero results in a remanent domain structure, fig. 4.6(l), which is identical to the starting configuration. No differences were observed when the field was reversed.

The schematic diagrams obtained from a 3μm square particle are shown in fig. 4.7. The domain walls move in a similar manner to the 4μm square particle, and in general both particles show similar behaviour; in particular the introduction of the short length of cross-tie wall is evident, as is the reformation of the starting domain structure upon reduction of the applied field to zero.

Comparing the domain structure of the 3.00μm square particle at 4.0kA.m^{-1} during the increasing and decreasing cycles, figs. 4.7(c) and (g), it can be seen that there is a certain amount of hysteresis in the process, which (from fig. 2.7), is not due to the magnetising stage. It should be noted that the high densities of cross-ties found in the increasing cycle are not found in the decreasing cycle.

One particle which has an integral aspect ratio, but which behaves very differently from the previous two is the 4.00 by 2.00 μm particle. The results obtained from the in-situ experiments performed on this particle are described below and are shown in figs. 4.8 and 4.9.

An important distinction between this particle and the square particles described above is that this particle has two edge clusters which are denoted by A and A' in fig. 4.9(a). The R=1 particles only have free and corner

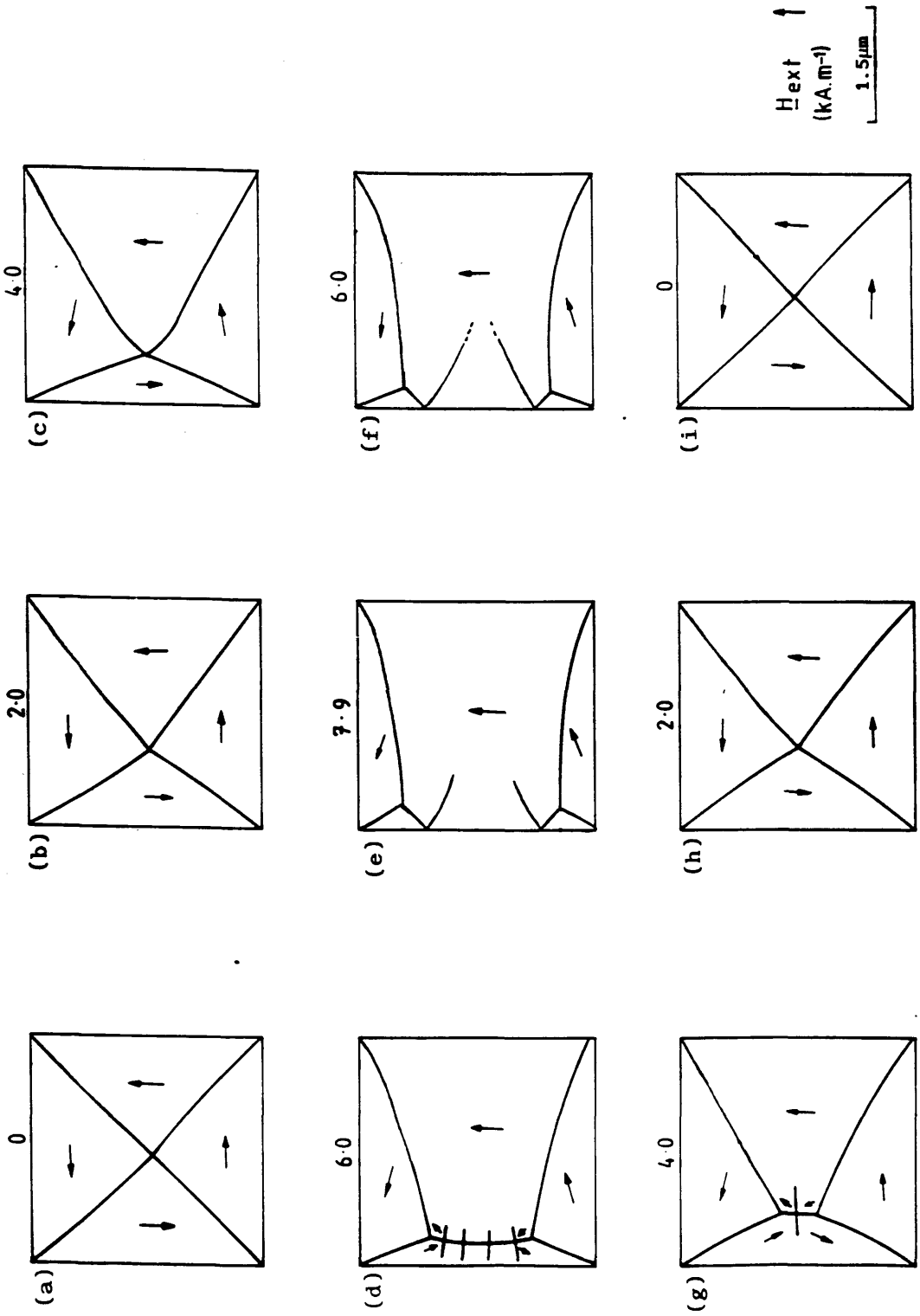

Fig. 4.7 Schematic diagrams showing the approximate directions of the magnetisation in each domain as deduced from the Fresnel images of a 3.00μm square, 60nm thick permalloy particle.

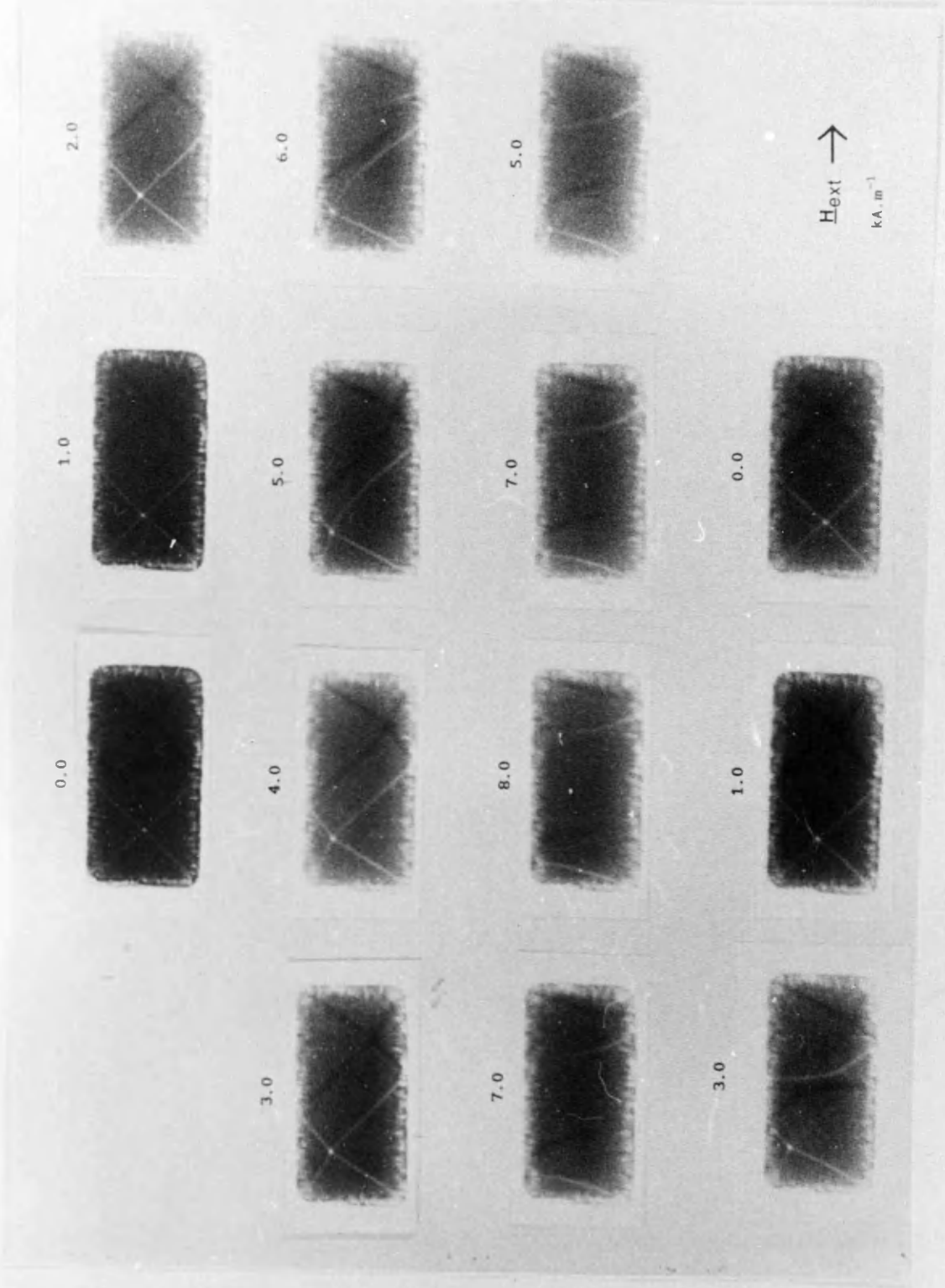

Fig. 4.8 Fresnel images from a 4.00 by 2.0μm, 60nm thick particle.

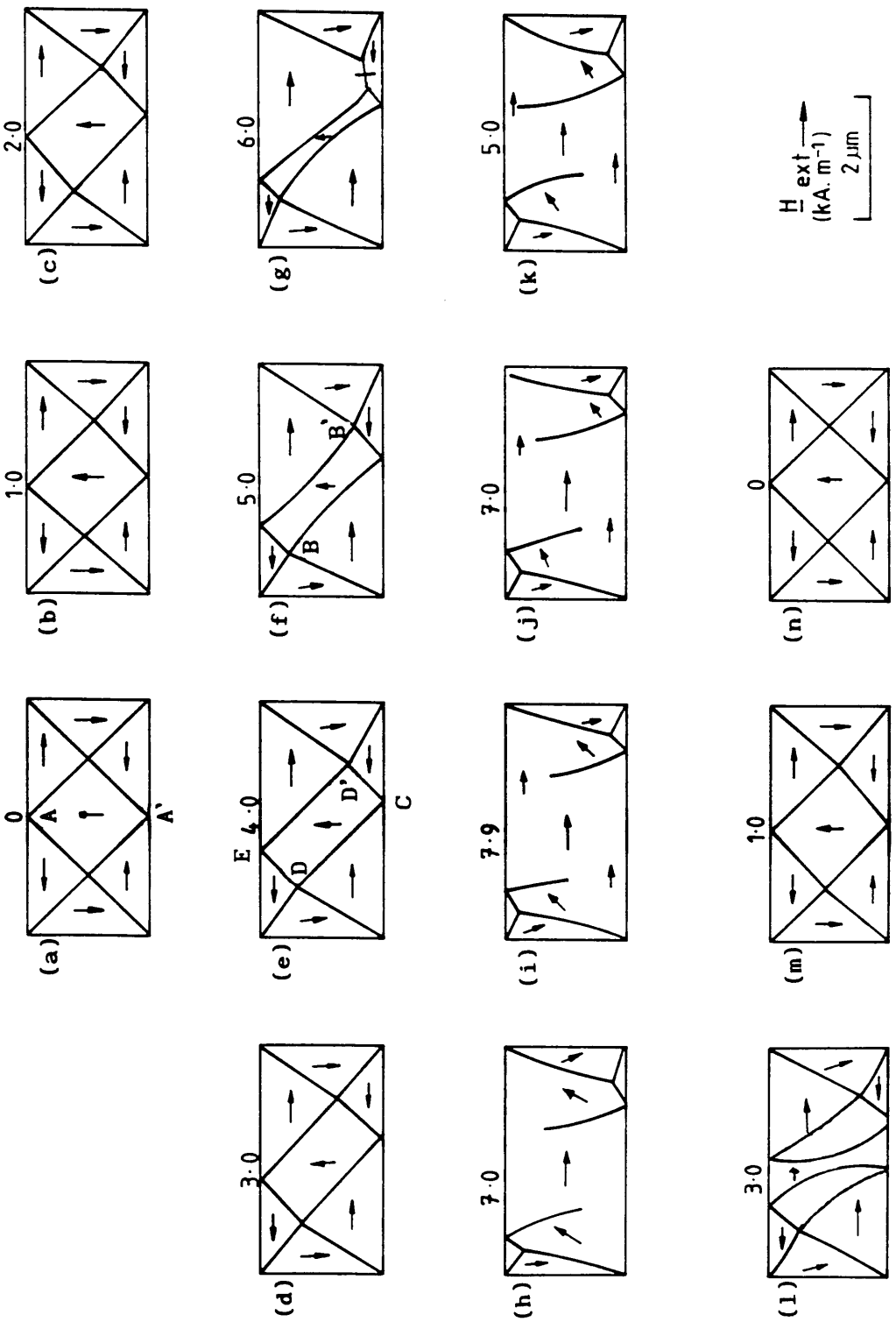

Fig. 4.9 **Schematic diagrams showing the approximate directions of the magnetisation in each domain as deduced from the Fresnel images of a 4.00 by 2.00μm, 60nm thick permalloy** particle.

clusters. This feature proves important because the edge clusters are found to be able to move along the edge of the particle whereas corner clusters are by nature pinned in the corner. As $\underline{\mathbf{H}}_{ext}$ is increased the movement of the edge clusters can be most clearly seen in figs. 4.9(b) to (f) and this movement has the effect of maintaining the angles CDE and CD'E in e.g. fig. 4.9(e) at approximately 90°. As this angle is kept at approximately 90°, the introduction of lengths of 180° wall at B and/or B' (fig. 4.9(f)) is delayed, and in some particles may even be totally avoided. In square particles, which have no edge clusters, the angles CDE and C'D'E' (fig. 4.6(e)) are kept at approximately 90° by the introduction and subsequent motion of the 180° wall. Once the length of cross-tie wall has been forced into the edge of the particle, end closure structures similar to those observed in non-solenoidal structures and e.g. fig. 4.7(e) are seen. Upon reduction of the applied field to zero the remanent domain structure is identical to the starting configuration, although as can be seen from figs. 4.9(d) and (l), there is a slight amount of hysteresis in the process.

4.3.1.2 PARTICLES HAVING NON-INTEGRAL VALUES OF R

In the 60nm thick particles which have non-integral values of R, a short length of 180° cross-tie wall is present in the as-grown state. Fig. 4.10 shows the effect of an applied field to a 4.00 by 3.00μm particle. This particle shows some characteristics which are similar to those displayed by the square particles discussed in section 4.3.1.1. In a similar manner to figs. 4.6 and 4.7, as the cross-tie wall is forced closer to the edge of the particle, the density of the cross-ties increases, and again the wall bends towards the side of the particle. After the cross-tie wall collapses, fig. 4.10(e), the domain structure is in fact very similar to fig. 4.6(h) and 4.7(e). Reduction of the applied field to zero results in a remanent domain structure which is identical to the starting domain configuration, although as can be seen from figs. 4.10(d) and (f), again there is a certain amount of

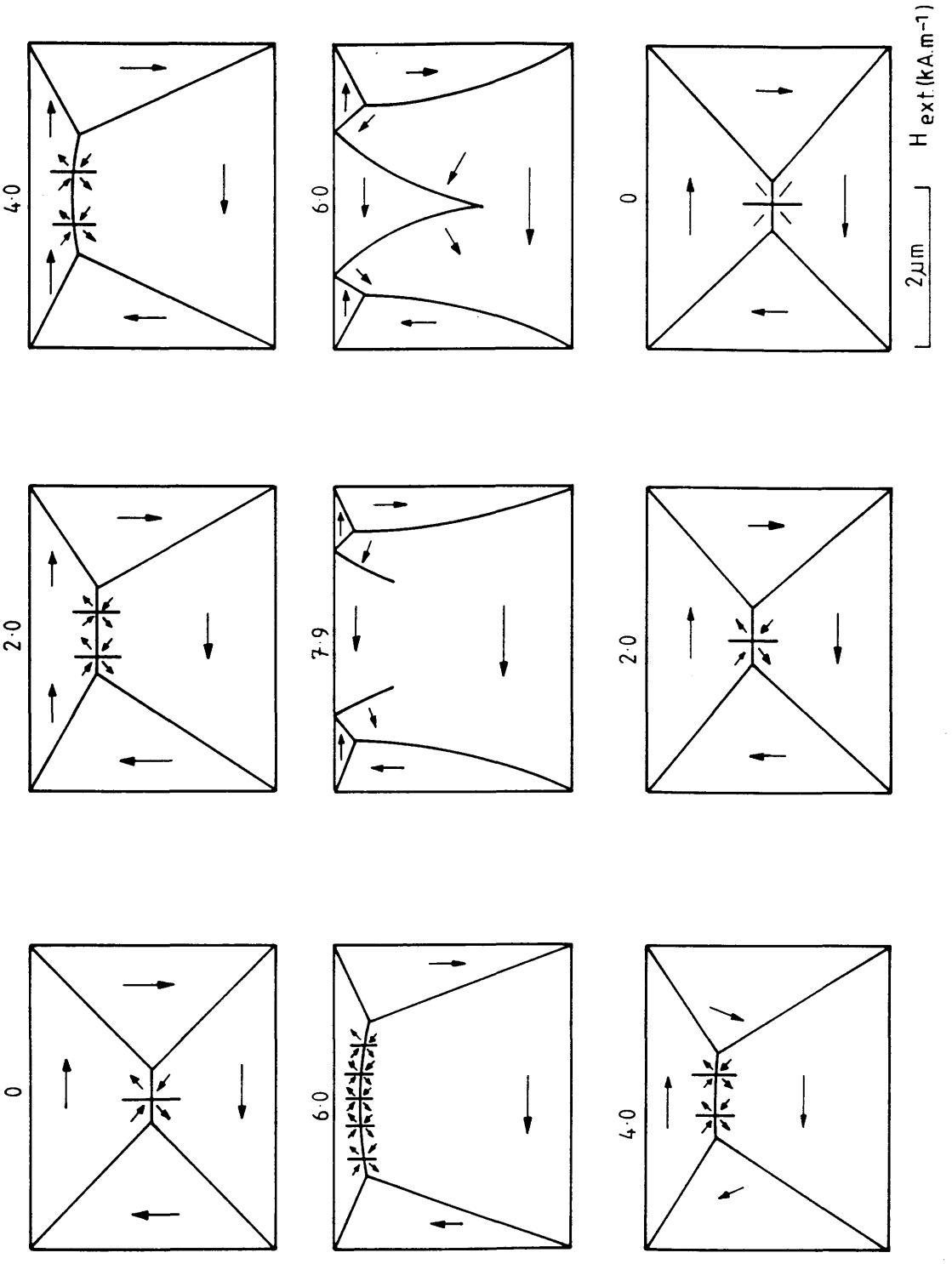

Fig. 4.10 The schematic diagrams of the approximate directions of magnetisation deduced from the Fresnel images of a 4.0 by 3.0μm particle.

hysteresis in the process. It should be noted that neither this particle nor the square particles described in section 4.3.1.1. have edge clusters in their as-grown states.

4.3.2 HARD AXIS IN-SITU MAGNETISING EXPERIMENTS

The particles described in section 4.3.1 were also subjected to an applied field directed along the hard axis. As in the previous section the results from particles having integral aspect ratios are discussed separately from those having non-integral values. All the results were again obtained using the Fresnel mode, and schematic diagrams showing the approximate directions of $\underline{M}$ are given for various particles.

4.3.2.1 INTEGRAL ASPECT RATIO PARTICLES

The schematic diagrams indicating the approximate directions of magnetisation which were deduced from the Fresnel images of a 4.0 by 2.0μm particle are shown in fig. 4.11. In this particular case the field is applied parallel to the central domain and also to the short axis of the particle.

From fig. 4.11(a), the as-grown domain structure consists entirely of 90° walls. As the magnitude of the applied field is increased, the Bloch lines, A and A' (fig. 4.11(b)) are forced further apart, and move towards the short edges of the particle. The edge clusters (B and B') do not move significantly, and this has the effect of making angles CDE and CD'E' in fig. 4.11(c) significantly less than 90°. As would be expected from the behaviour of the particles described in section 4.3.1 a length of 180° is introduced to overcome this effect, as shown in fig. 4.11(d). The maximum field available using the magnetising stage is insufficient to drive the cross-tie wall any further than indicated in fig. 4.11(e). As the field is decreased to zero, again there is a certain amount of hysteresis, (e.g. figs. 4.11(d) and (f)), although the particle again reforms the starting domain structure upon

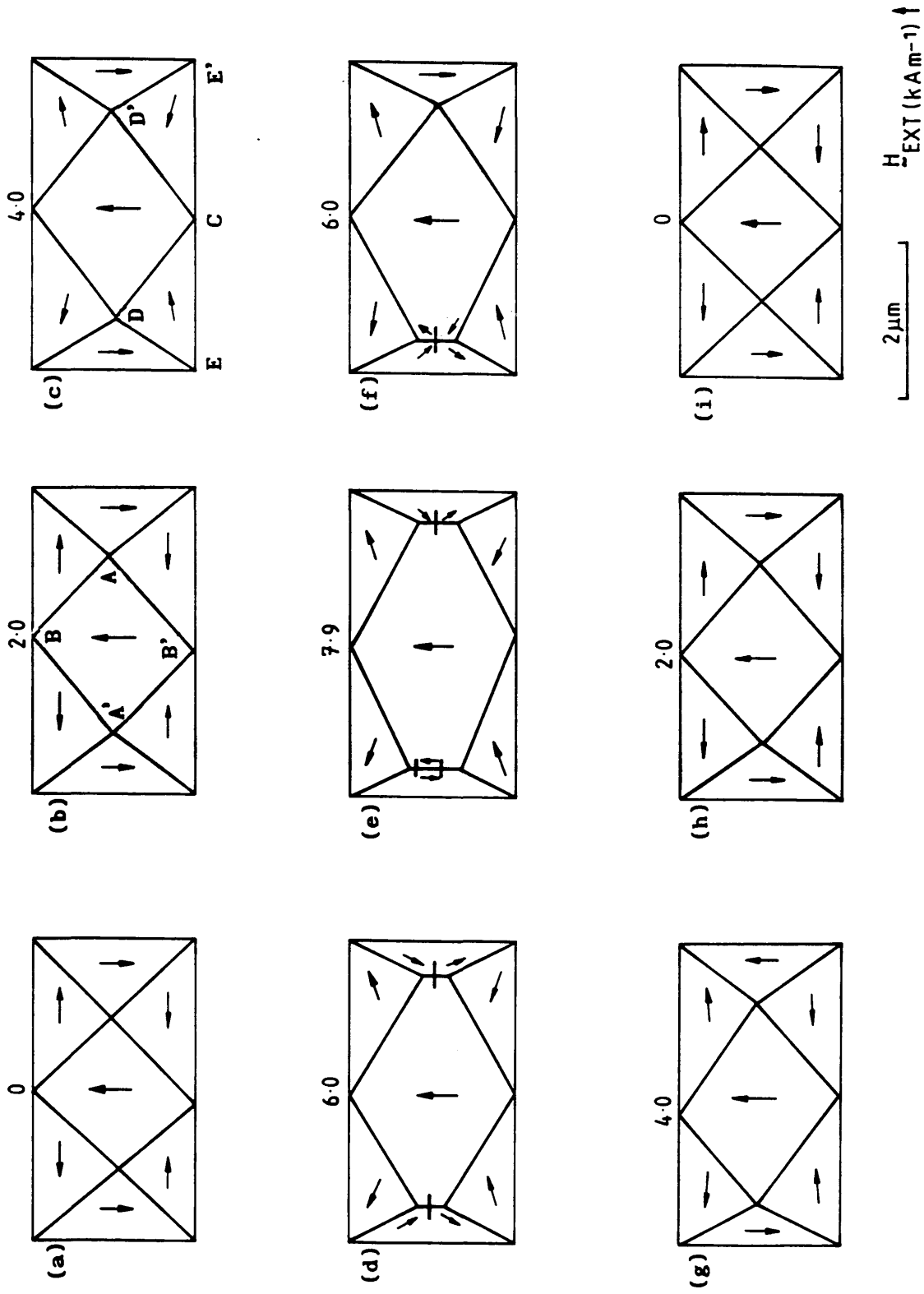

Fig. 4.11 Schematic diagrams showing the approximate directions of the magnetisation in each domain,

reduction of the field to zero.

Shown in fig. 4.12 are the results obtained from this particle when the field is applied anti-parallel to the central domain. In this case the Bloch lines (A and A' in fig. 4.12(a)) are forced closer together. Although the field has been aligned to $\mp$ 5°, it is found that at large values of applied field, each Bloch line moves towards an edge cluster on opposite edges of the particle, as shown in fig. 4.12(e). Reduction of the field to zero reforms the starting domain structure, as has been found for all the particles described so far.

4.3.2.2 NON-INTEGRAL ASPECT RATIO PARTICLES

Common to all of the particles to be described in this section is a short length of cross-tie wall. Fig. 4.13 shows the effect of an applied (hard axis) field to a 3.00 by 1.6μm particle which has a short length of 180° cross-tie wall containing 2 cross-ties. As the value of the applied field is increased, one of the end domains grows as expected. As this happens the Bloch lines and cross-ties making up the 180° wall are forced closer together, fig. 4.13(b). The cross-tie itself can also be seen to bend, with its focus on that side of the particle having the larger domain. At a specific value of applied field, one of the cross-ties merges with a Bloch line, and the resulting structure is as shown in fig. 4.13(c). Once all the cross-ties have ceased to exist, fig. 4.13(e), the domain walls are found to meet at point A, but no Bloch line can be detected until point B. Hence it would appear that there is a short length of approximately a 180° wall present in the particle in fig. 4.13(e).

It should be noted that the as-grown domain structure of the 3.00 by 1.6μm particle described in fig. 4.13, has an odd number of Bloch lines. During this part of the in-situ experiments performed on this particle, only domain structures comprising an odd number of Bloch lines were found. This would be expected by considering the polarity of each Neel component along the length

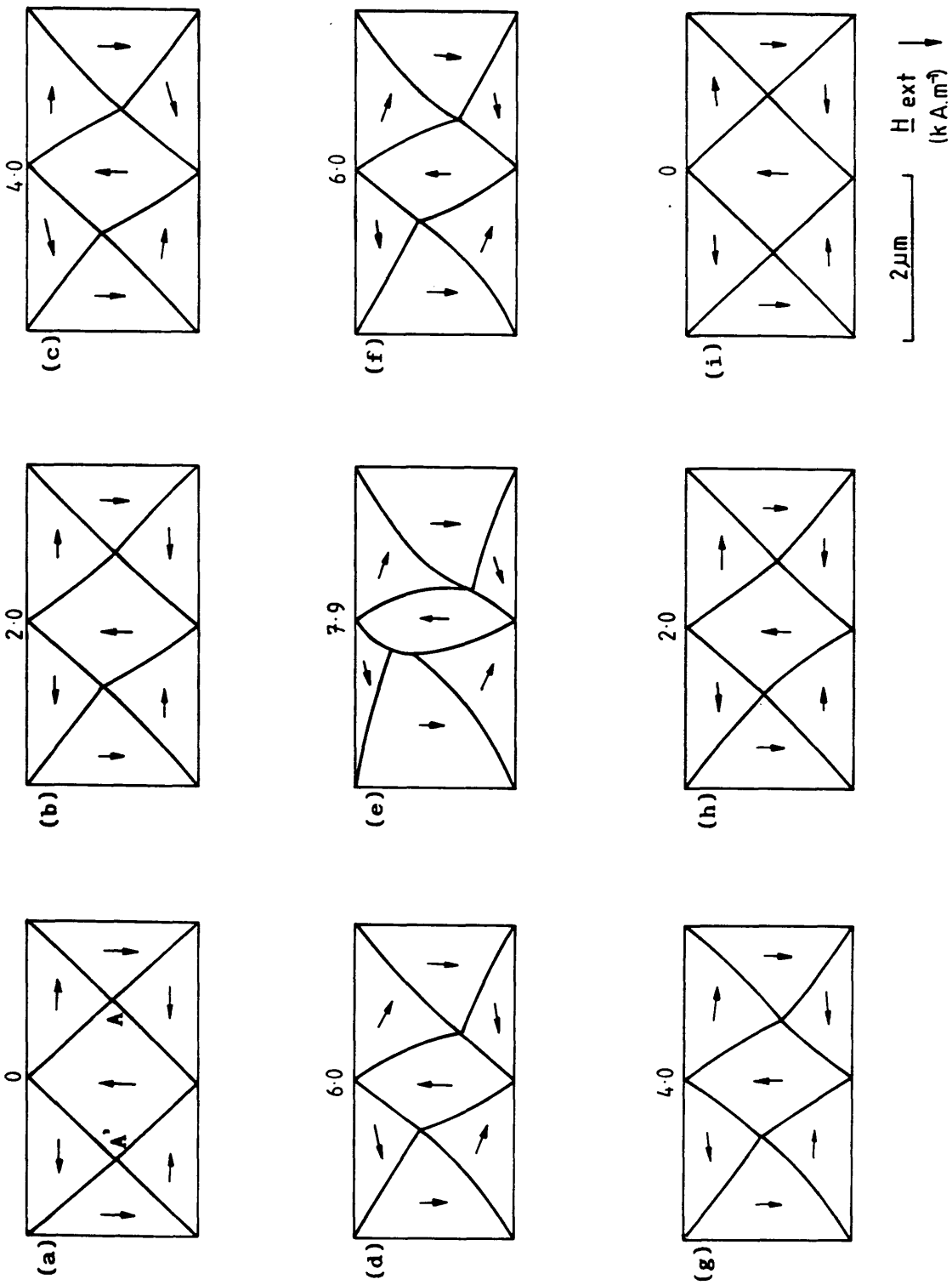

Fig. 4.12 Schematic diagrams showing the approximate directions of the magnetisation in each domain,

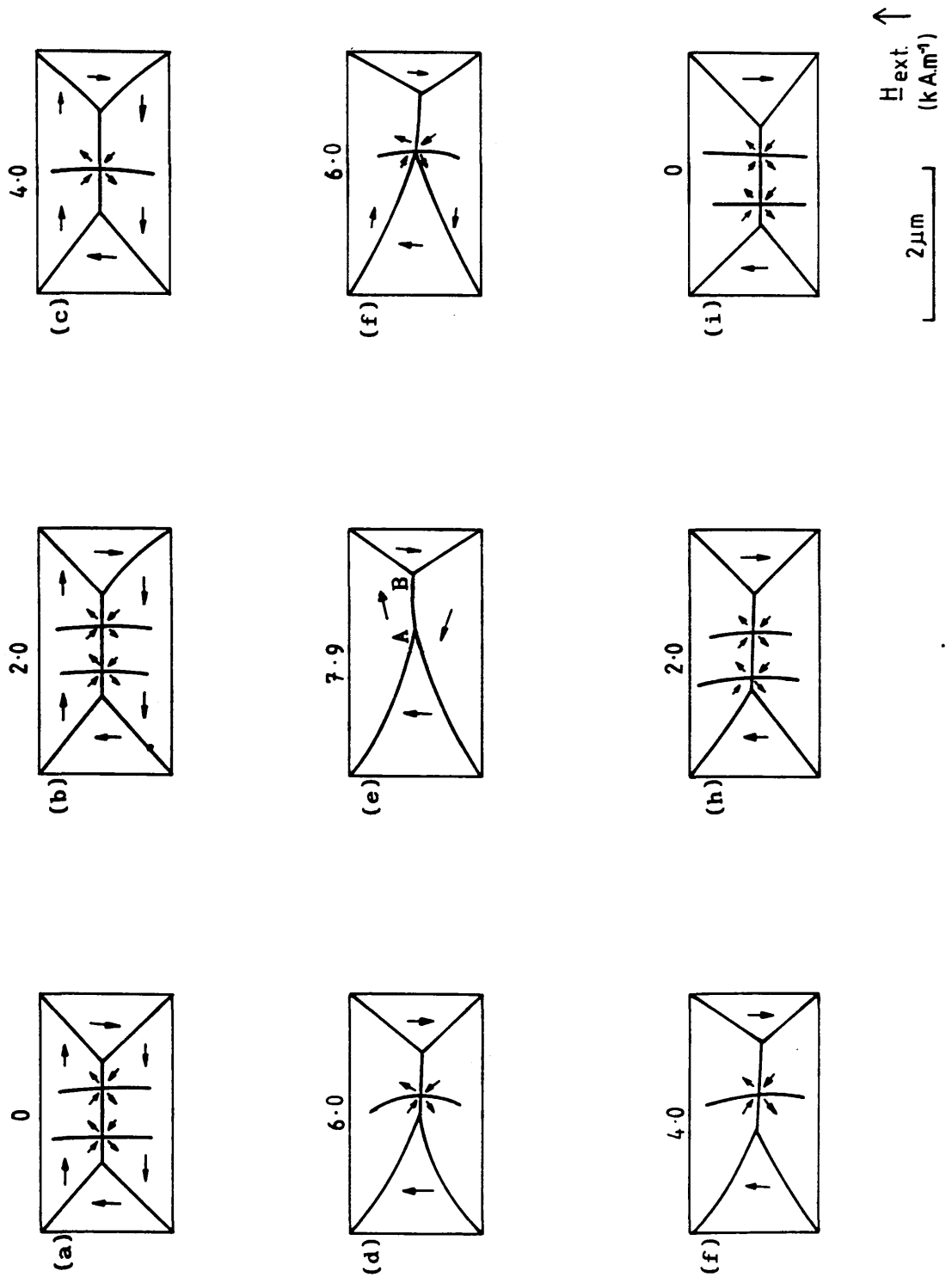

Fig. 4.13 Schematic diagrams showing the approximate directions of the magnetisation in each domain as deduced from the Fresnel images of a 3.0 by 1.6μm, 60nm thick permalloy particle.

of the cross-tie wall. As the magnitude of the applied field is increased, the change in the relative spacing of the cross-ties can also be explained by examining the directions of $\underline{\mathbf{M}}$ close to the wall itself, as shown schematically in fig. 4.14(a) and (b). An applied field is present in (b). From fig. 4.13(d) it can be seen that the mobility of the domain walls further away from the main body of the wall increases as the distance from the wall increases, and hence the wall bends. All particles which have cross-ties in their as-grown domain structure exhibit this type of behaviour. Two examples are shown in fig. 4.15 and 4.16. in which both particles have a short length of 180° cross-tie wall.

4.3.3 IN-SITU EXPERIMENTS ON IRREGULAR DOMAIN STRUCTURES

In certain circumstances, it was found that some of the particles had slightly more irregular domain structures than would normally be expected. One of the more common examples of this is shown in fig. 4.17, which illustrates the effect of a rounded corner on the domain structure of a 3.00μm square particle. From fig. 4.17 it can be seen that the 90° wall, which would be expected to extend into the corner of the particle, is found to "split" and form two 45° walls, as shown in the schematic of fig. 4.18(a). By examining the directions of the components of $\underline{\mathbf{M}}$ normal to the walls marked A,B and C in fig. 4.17, it is both expected and observed that no Bloch line should exist at the point where the wall splits.

The schematic diagrams obtained from Fresnel images taken during the in-situ magnetisation of this particle are shown in fig. 4.18. The general behaviour of this particle is very similar to that of a regular square particle, e.g. fig. 4.6, which has only 90° walls. Once again it is found that a length of 180° cross-tie wall is introduced, and that high densities of cross-ties are present just prior to the wall being driven into the side of the particle. Upon reduction of the field to zero, the remanent domain structure is exactly the same as the starting configuration, and the two 45° walls are again found

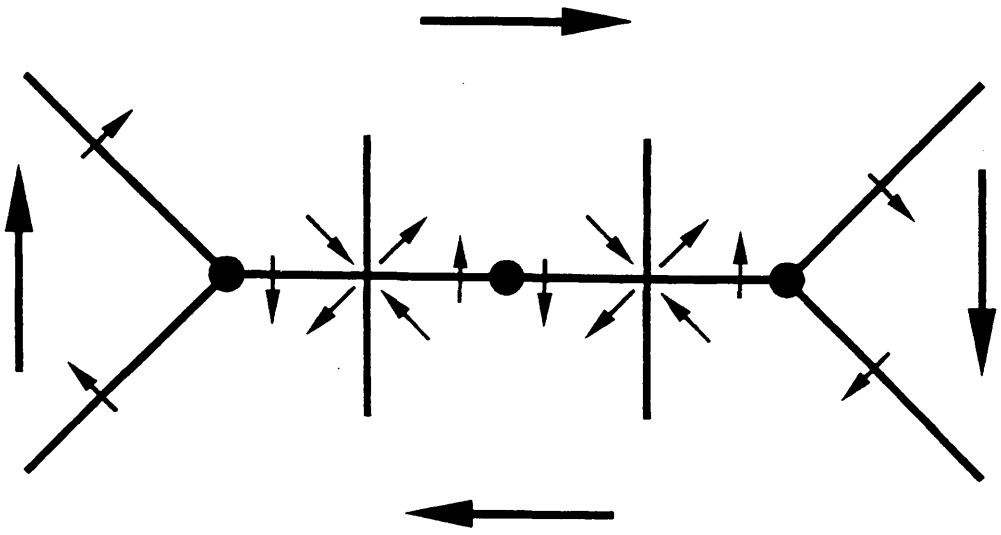

Fig. 4.14 (a) Schematic diagram showing the central portion of the 180° cross-tie wall of the 3.0 by 1.6μm particle. The applied field is equal to zero.

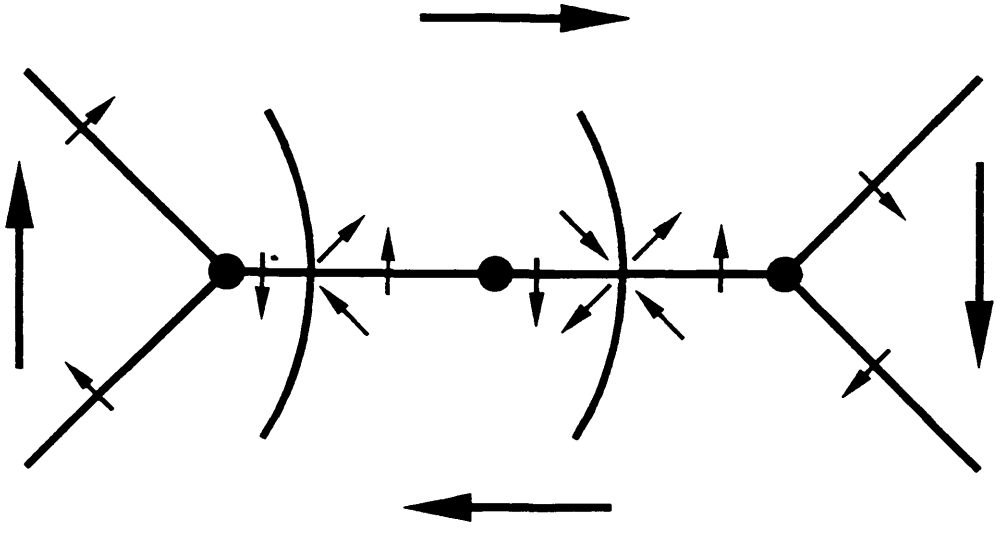

Fig. 4.14 (b) The section of the 180° wall when the applied field has a non-zero value.

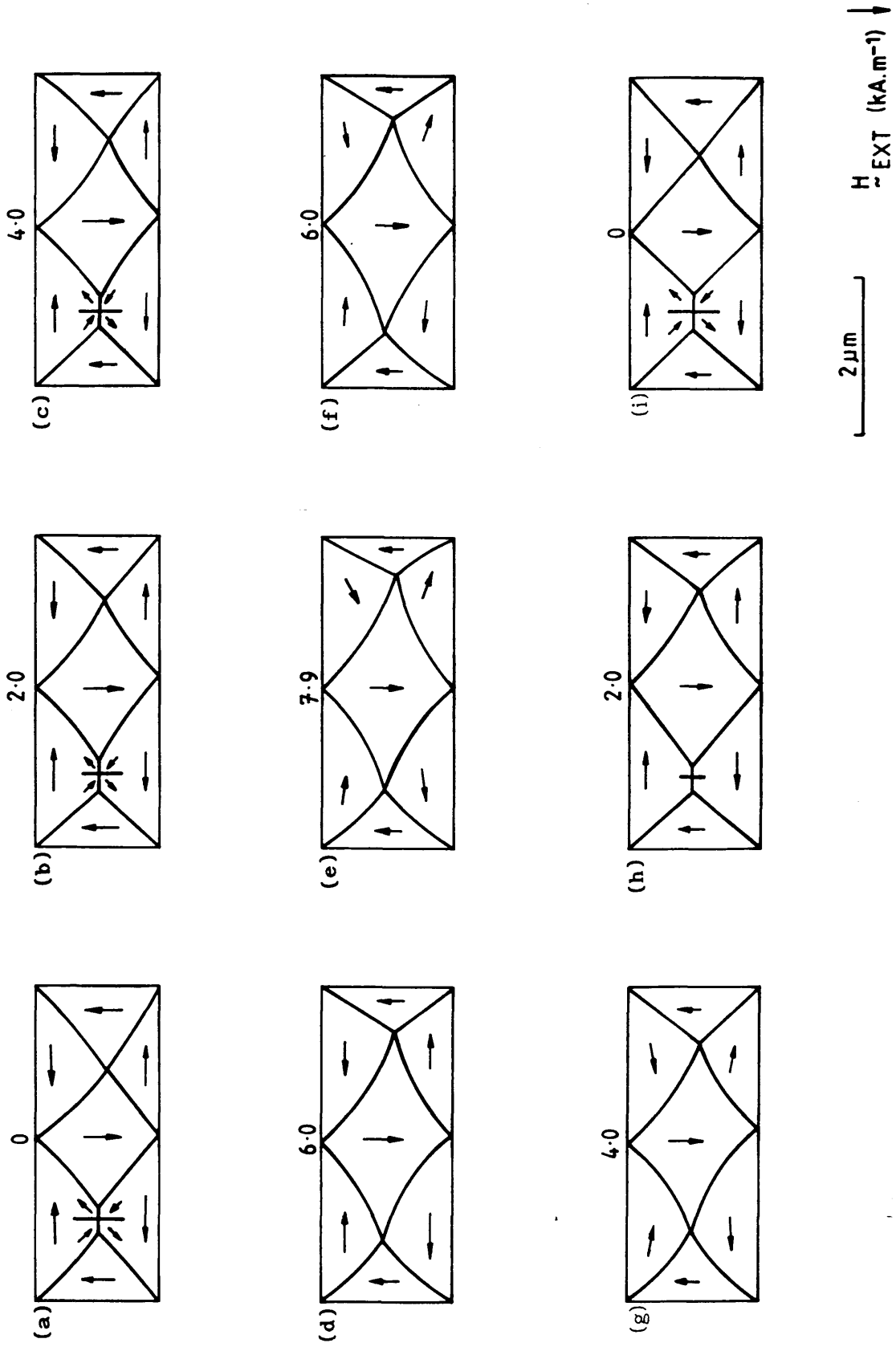

Fig. 4.15 Schematic diagrams showing the approximate directions of the magnetisation in each domain as deduced from the Fresnel images of a 4.0 by 1.5μm, 60nm thick permalloy particle.

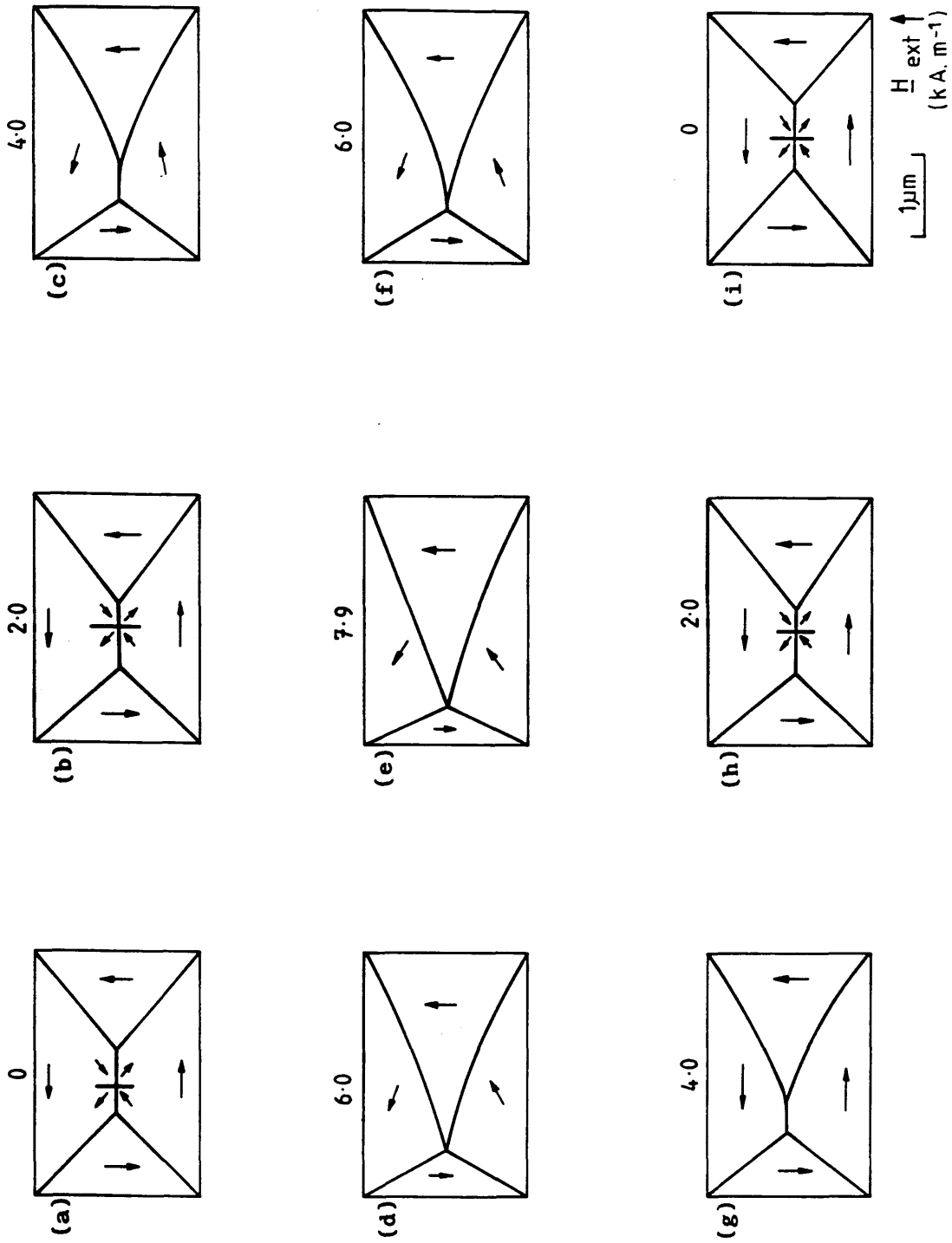

Fig. 4.16 Schematic diagrams showing the approximate directions of the magnetisation in each domain as deduced from the Fresnel images of a 3.0 by 2.0μm, 60nm thick permalloy particle.

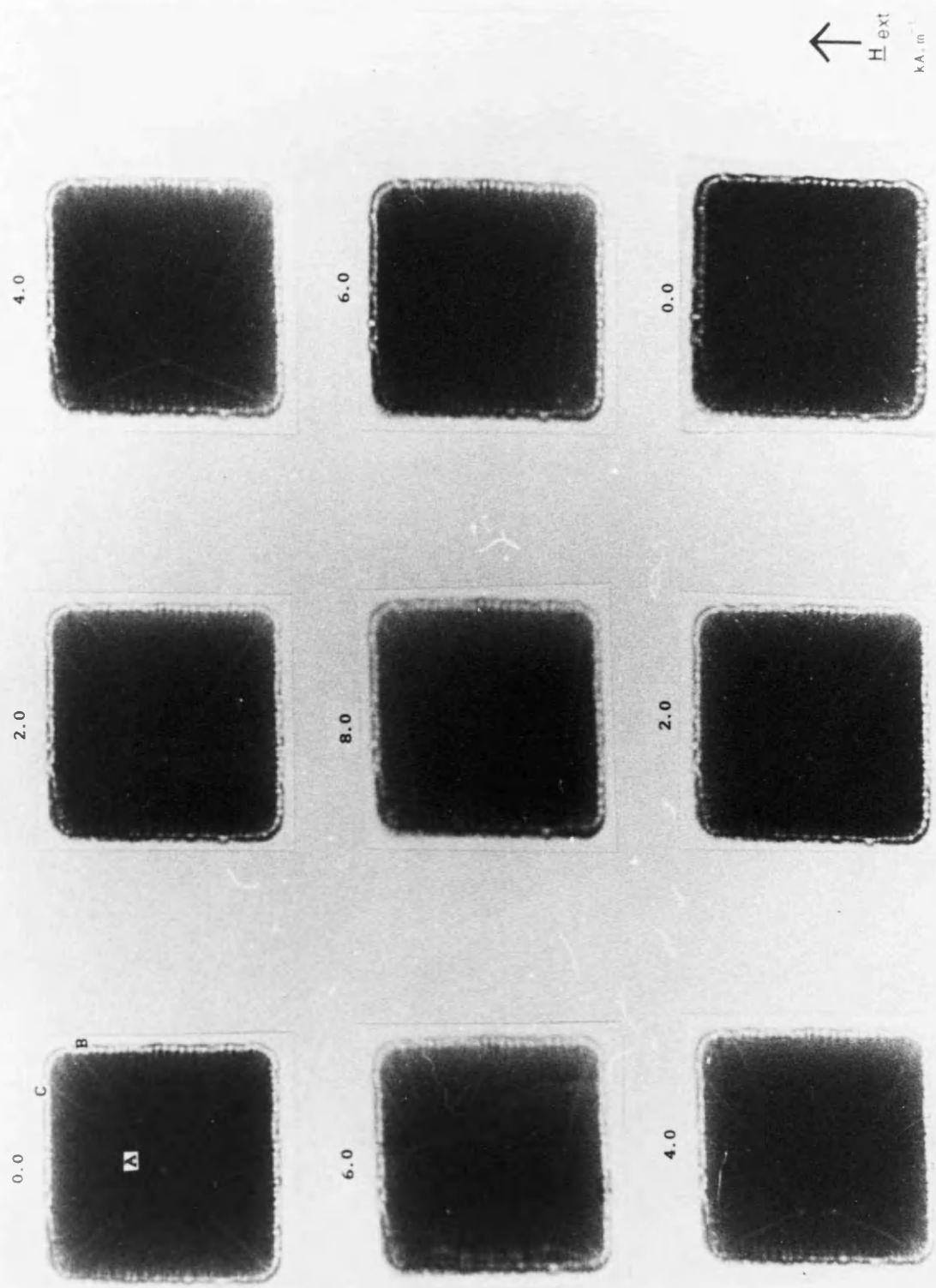

Fig. 4.17 Fresnel images of a 3.00μm particle which has a slightly rounded corner.

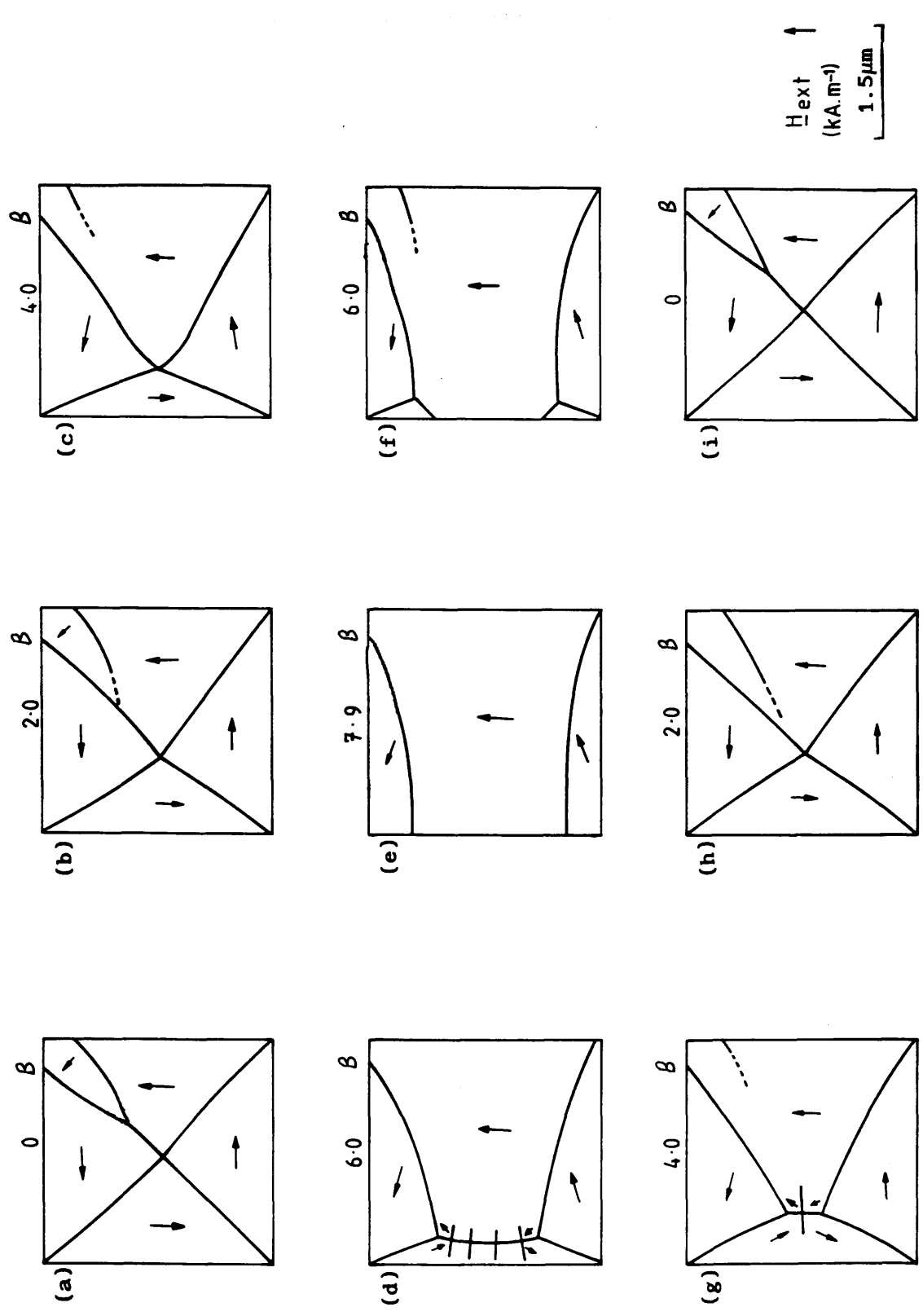

Fig. 4.18 Schematic diagrams showing the approximate directions of the magnetisation in each domain as deduced from the Fresnel images of a 3.0μm square particle.

to be present.

But on fig. 4.18, one important fact which should be noted is the lack of movement of the domain wall at B. Throughout the cycle, it appears that this domain wall is "pinned" at the point which is at the limit of the rounded section of the corner and acts more like a corner, rather than an edge, cluster.

Shown in fig. 4.19 are the schematic diagrams obtained from in-situ experiments performed on a 3.00 by 2.00μm particle which had relatively badly defined corners. In this case, two corners can be seen to have the 45° walls found in the previous example. Neglecting the presence of the the lower angle walls, the particle essentially displays the same features as a "normal" R = 1.5 particle during the course of the in-situ experiments and even although four 45° domain walls are present it is noted that the remanent domain structure is identical to the starting configuration. One very significant difference in the behaviour of this particle is the apparent loss of the end closure structures between fig. 4.19(d) and fig. 4.19(e). Rather than these domains being eradicated, it is more likely that as the value of the applied field is increased, the magnetisation in the end domains rotates towards the direction of the applied field, and hence the angle through which the magnetisation rotates across the wall decreases. In the Fresnel imaging technique, this results in the domain walls becoming more diffuse, and they may even become too diffuse to be visible. The combination of this effect, and the fact that the domain walls are very close to the edge of the particle makes the walls particularly difficult to observe. The situation is further complicated by the Fresnel edge wave, which, in an out-of-focus technique such as Fresnel, will mask any subtle features near the edges of the particles.

A most interesting example of a particularly strange domain structure is shown in the Fresnel image of fig. 4.20. On first impression the structure appears quite irregular, however an important fact which should be noted is that both end domains are magnetised parallel to each other and to the short

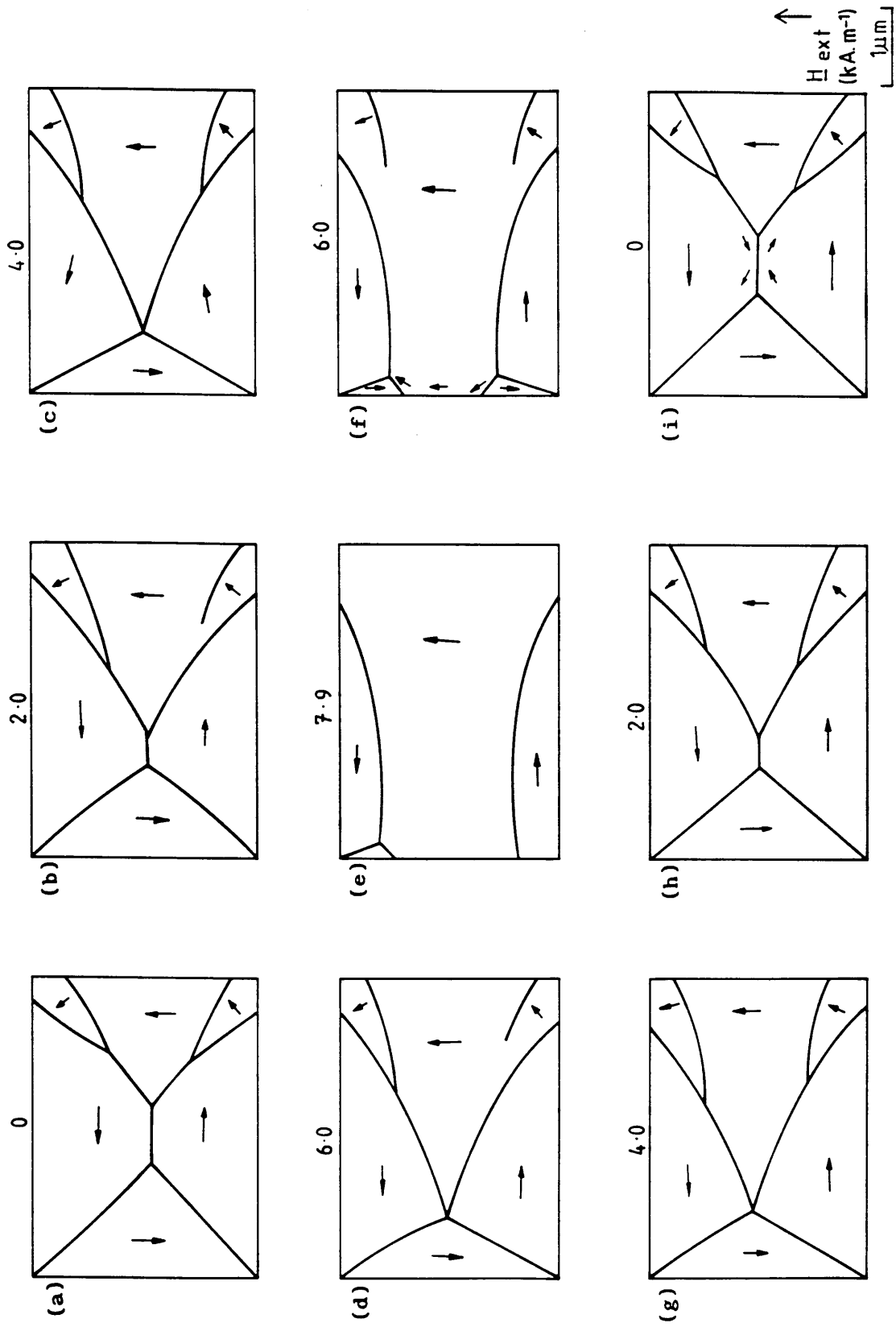

Fig. 4.19 Schematic diagrams showing the approximate directions of the magnetisation in each domain as deduced from the Fresnel images of a 3.0 by 2.0μm, 60nm thick permalloy particle.

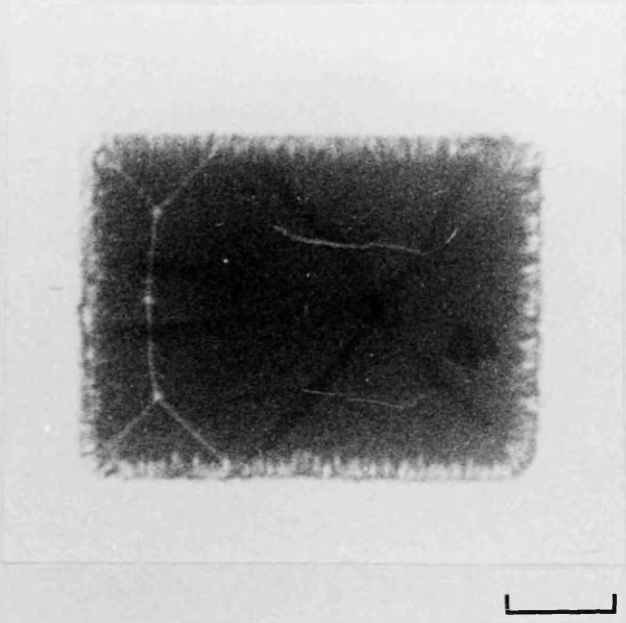

Fig. 4.20 Fresnel image of a 4.0 by 3.0μm particle, with a sightly "abnormal" domain structure.

axis of the particle.

This type of structure serves to illustrate the fact that not all domain structures found in the particles can be predicted by the algorithm of section 1.4.2. Shown in fig. 4.21 is one possible domain structure which could be predicted by applying the algorithm to a particle with a rounded corner. Note that the domain wall at A stops abruptly and does not extend into the corner of the particle, nor does it split into two 45° walls. In order to predict a domain structure in which two 45° wall are present, the algorithm would need to be applied to a particle of a shape such as shown in fig. 4.22.

A set of schematics obtained in the usual manner from the in-situ experiments conducted on the particle of fig. 4.20 is shown in fig. 4.23. As the applied field is increased to 3.0 $kA.m^{-1}$, fig. 4.23(e), the edge clusters have moved, so decreasing the length of the 180° cross-tie wall. The cross-ties themselves can be seen to bend prior to merging with the nearest Bloch line, fig. 4.23(f). At the point at which the cross-ties cease to exist, fig. 4.23(f), the domain structure is in fact quite similar to the 4.00. by 2.00μm shown in fig. 4.8(e). Increasing the magnitude of the applied field forces the Bloch lines closer to the sides of the particle. It should be noted that again the edge clusters move in such a way as to maintain angles CDE and CD'E in fig. 4.23(h) close to 90°. At 6.0 $kA.m^{-1}$, fig. 4.23(h), the domain structure is quite similar to the 4.00 by 2.00μm at 6.0$kA.m^{-1}$, (fig. 4.8(g)). After the collapse of the central domain, fig. 4.23(i) only the end closure structures are present.

During the decreasing cycle an important stage in the development of the remanent structure takes place between figs. 4.23(l) and (m). Between these two values of applied field the domain wall at A has moved into the corner of the particle, and in fig. 4.23(m) there are now two short lengths of 180° wall at the points marked B and B'. It should be noted that if a 180° cross-tie wall forms at B then the remanent domain structure would be similar to that of fig. 4.23(a). Alternatively, as shown in figs. 4.23 (n) to (o),

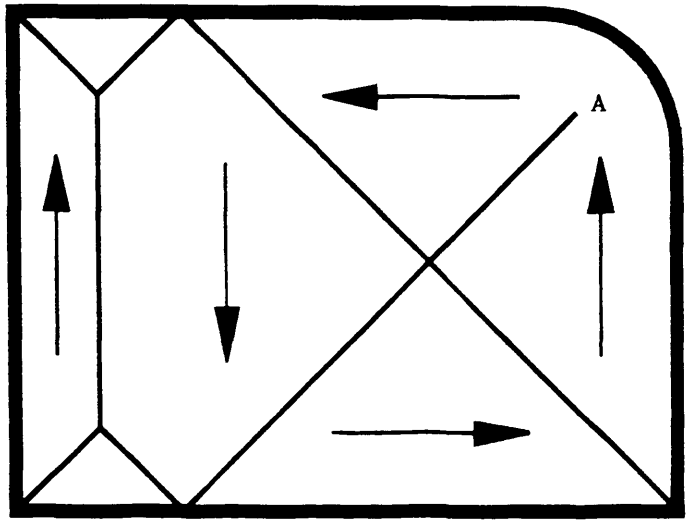

Fig. 4.21 Possible resultant domain structure after applying the Van den Berg algorithm to a particle which has a rounded corner.

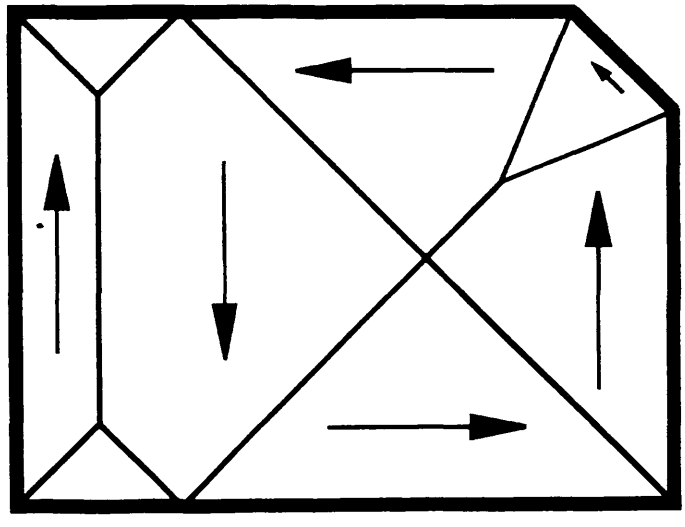

Fig. 4.22 One example of a shape of particle which could result in predicting a domain structure with two 45° walls.

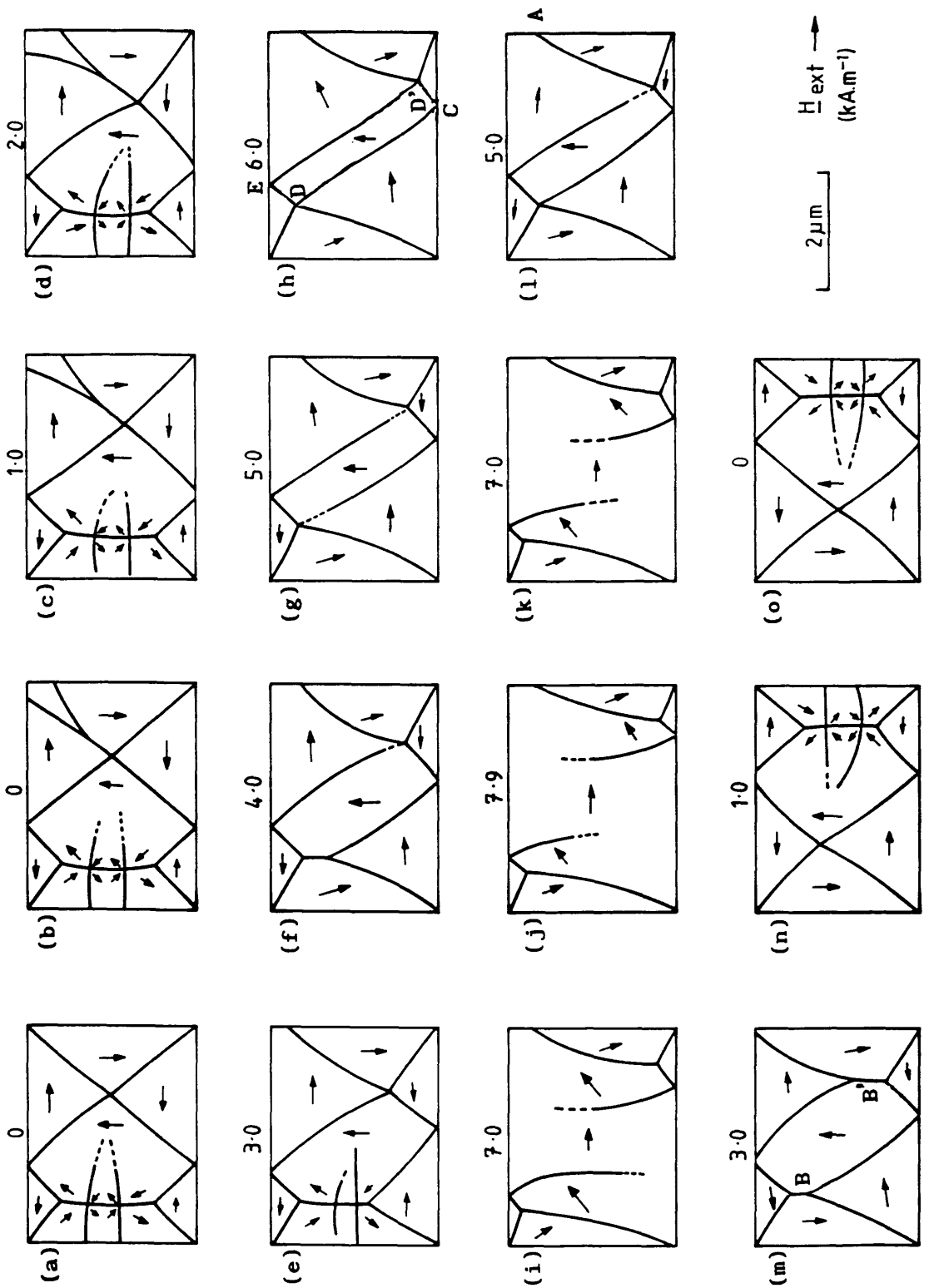

Fig. 4.23 Schematic diagrams showing the approximate directions of the magnetisation in each domain as deduced from the Fresnel images of a 4.0 by 3.0μm, 60nm thick permalloy particle.

once the cross-tie wall has formed at B', the remanent domain structure is as shown in fig. 4.23(o).

As stated above the most important stage in the development of the final form of the remanent domain structure took place as the field was reduced from 5.0kA.m^{-1} to 3.0kA.m^{-1}, as it is between these two values of applied field that the domain wall at A moves into the corner of the particle. Repeated experiments in which the domain structure at 3.0kA.m^{-1} was exactly as shown in fig. 4.23(m) gave remanent domain structures exactly the same as shown in fig. 23(a) or (o), and in this case both types of structure occurred with equal regularity. In contrast, in situations where the domain wall is "pinned" (Becker (1932)) at A, and does not move into the corner of the particle, the remanent domain structure is always as shown in fig. 4.23(b). From fig. 4.23(a) and (O), it was possible to reform the structure of the type shown in fig. 4.23(b). by applying a saturating field along or close to the hard axis direction.

4.4 A.C. DEMAGNETISATION AND APPLICATION OF SATURATING FIELDS

4.4.1 INTRODUCTION

Particles of all three thicknesses (17, 60, and 95nm) were subjected to an a.c. demagnetisation in order to check for the possibility of lower energy domain states. To demagnetise a sample, the power supply to the magnetising stage was changed so that large fields of alternating polarity could be applied to the specimen. The maximum field which could be obtained in this mode was 64kA.m^{-1} and the amplitude of each pulse was under the control of the experimenter. (It is unlikely that this magnitude of field will saturate the particles, especially when directed along the hard direction.) Alternating polarity pulses were delivered to the specimen at a frequency of approximately 5 Hz, although this could be decreased to 0.2 Hz. In order to demagnetise a sample, the amplitude of the 5 Hz alternating pulses was slowly

decreased from 64kA.m^{-1} to zero over approximately 30 seconds. Using this procedure, the particles could be reproducibly demagnetised along specific axes with respect to the specimen. Under normal circumstances, samples were demagnetised along either the hard or easy directions, and the resulting remanent domain structures are described in sections 4.4.2 and 4.4.3.

4.4.2 HARD AXIS DEMAGNETISATION

The remanent domain structures for the three thicknesses of samples following a hard axis demagnetisation are shown in fig. 4.24 to 4.26. Very regular domain structures were found in all samples although the most significant point to note is that long lengths of 180° walls were frequently found in the 17 and 60nm samples. Long sections of 180° walls were not found in the 95nm sample, and at this particular thickness, the total length of 180° wall which was present was the same as that which was present in the as-grown state.
As was found when examining as-grown domain structures, after a hard axis a.c. demagnetisation some of the particles existed in solenoidal states, while others existed in non-solenoidal states. The aspect ratio of the least acicular particle having a non-solenoidal domain structure are shown in table 4.1. In almost all cases, particles deposited orthogonally to each other, which had the same in-plane dimensions showed a similar magnetic behaviour.

4.4.3 EASY AXIS DEMAGNETISATION

The most significant difference between the hard and easy axis demagnetisations occurred in the 17 and 60nm thick specimens. In these two cases, after the samples had been demagnetised along the easy axis, the long sections of 180° walls found after a hard axis demagnetisation were no longer present. Also more of the particles are found in non-solenoidal states and the least acicular particles which display a non-solenoidal structure are given in table 4.1.

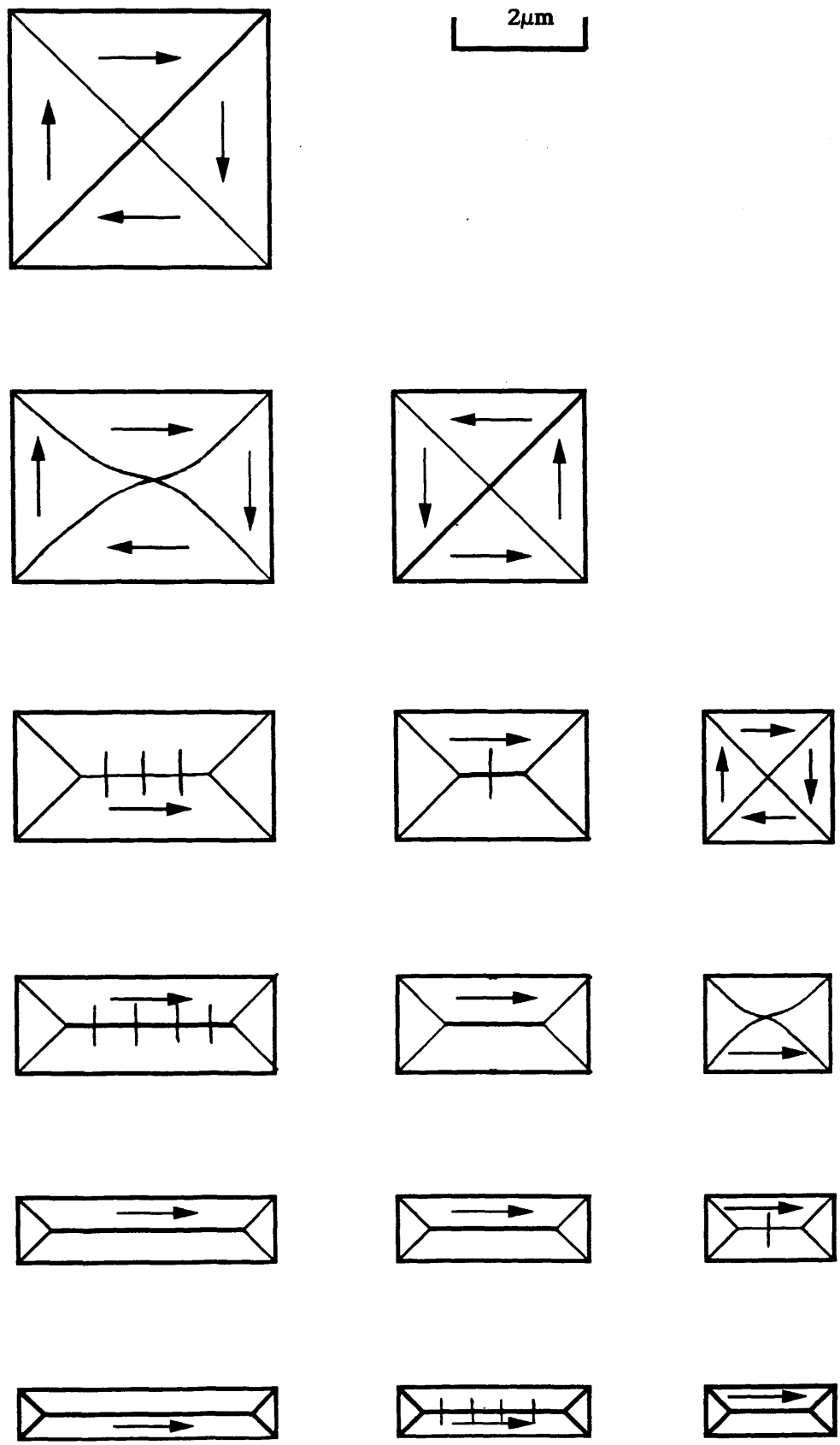

Fig. 4.24 Remanent domain structures of a 17nm thick sample after a hard axis demagnetisation.

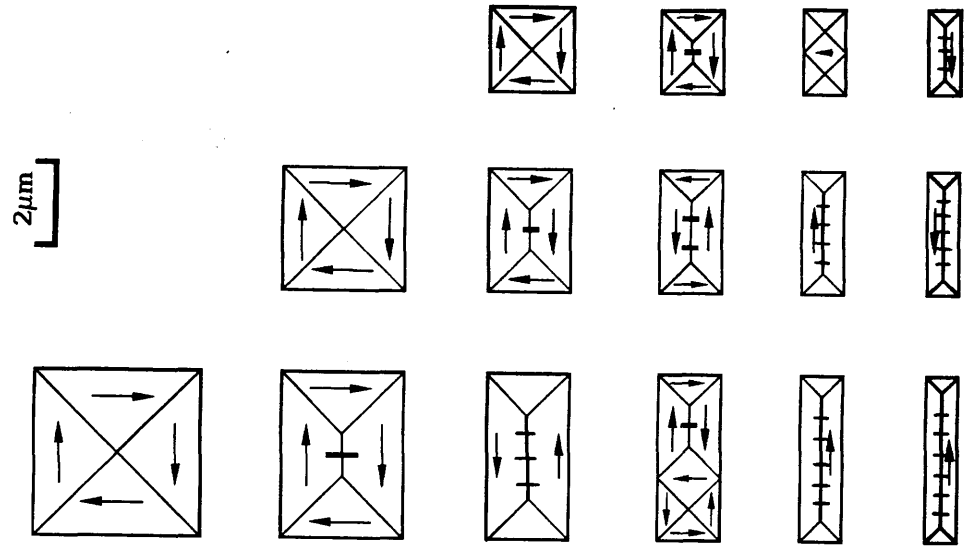

Fig. 4.25 Remanent domain structures of a 60nm thick sample after a hard axis demagnetisation.

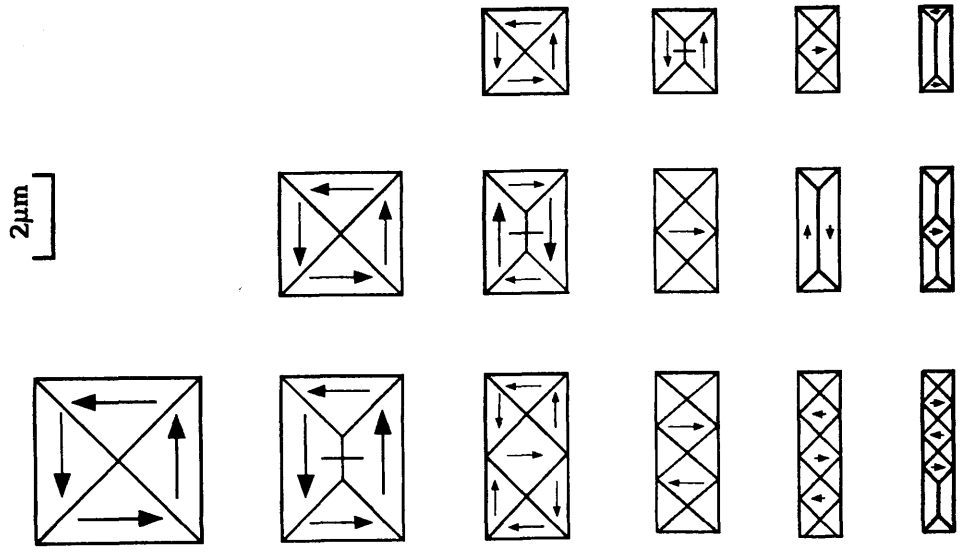

Fig. 4.26 Remanent domain structures of a 95nm thick sample after a hard axis demagnetisation.

TABLE 4.1

First particles to display a Non-solenoidal structure.

17nm thick $Ni_{82.5}Fe_{17.5}$ sample

Length	4 μm	3μm	2μm	1μm
		Breadth (μm)		
(a) As-grown	0.75	0.50	0.38	0.25
(b) As-grown	0.75	0.50	0.38	0.25
Easy (Demag)	1.50	1.00	0.50	0.50
Hard (Demag)	0.50	0.38	None	None

60nm thick $Ni_{82.5}Fe_{17.5}$ specimen

Length	4 μm	3μm	2μm	1μm
		Breadth (μm)		
(a) As-grown	0.75	0.50	0.38	0.25
(b) As-grown	0.75	0.50	0.38	0.25
Easy (Demag)	1.50	1.00	0.50	0.50
Hard (Demag)	0.50	0.38	None	None

95nm thick $Ni_{82.5}Fe_{17.5}$ specimen

Length	4 μm	3μm	2μm	1μm
		Breadth (μm)		
(a) As-grown	0.38	0.38	0.20	None
(b) As-grown	0.38	0.38	----	----
Easy (Demag)	0.25	0.25	None	None
Hard (Demag)	0.25	0.25	None	None

Easy (Demag)	Easy axis demagnetisation.
Hard (Demag)	Hard axis demagnetisation.
None	None of the particles had non-solenoidal domain structures.
----	This group of particles was not suitable for examination.

(a) and (b) These are two sets of particles, in the one array, which were fabricated orthogonally to each other.

In the case of the 95nm thick sample, the structures of most of the particles were identical to those found after a hard axis a.c demagnetisation. Again, the least acicular particle having a non-solenoidal structure is given in table 4.1.

As stated in section 2.4, the maximum field which could be delivered to the specimen in the pulsed mode was 64 $kA.m^{-1}$. This is insufficient to saturate the particle along either the easy or, in particular the hard direction. In order to saturate the sample, specimens of all three thicknesses of specimens were subjected to a 1.2T field applied external to the microscope, and the remanent domain structures obtained are described below in section 4.4.4.

4.4.4 SATURATING FIELDS

The remanent domain structures obtained from saturating the particles along the hard or easy directions for the 17 and 60nm samples give almost identical domain structures to those obtained when the particles were subjected to a similarly directed a.c. demagnetisation. Again the main point to note was that Landau-Lifshitz structures occurred in the two thinner samples when the field was directed along the hard axis.

In the thickest sample, 95nm, although many of the particles displayed solenoidal remanent domain structures, long sections of 180° walls were not found. The remanent domain structures present in this sample always tended to have a 180° wall which was the same length as was found in the as-grown state. For this particular thickness of sample, when the saturating field was directed along either the hard or easy axes, the only particles to show non-solenoidal structures were the 4 by 0.38μm (R = 10.5), 4 by 0.25μm (R = 8) and the 3 by 0.25μm (R =6).

4.5 DISCUSSION AND SOME DIFFICULTIES WITH FRESNEL IMAGING

From the range of particles investigated using the techniques described in sections 4.3 and 4.4, it can be seen that both solenoidal and non-solenoidal domain structures are present in all three thicknesses of samples. Depending on the size and magnetic history of the particle it is possible to predict the domain structure of a particular particle. In general, non-solenoidal as-grown domain structures were obtained in the more acicular ($R > 8$) particles. Less acicular particles, and in particular the group of particles with $R \leq 3$, were always found to have solenoidal as-grown domain structures. Similar conclusions can also be drawn when the particles were saturated or a.c. demagnetised along the hard or easy directions. In the 17 and 60nm thick particles which had been subjected to either a saturating field, or a.c. demagnetisation along the hard axis, remanent domain structures with long lengths of 180° walls were found to occur more frequently than after the same procedure had been carried out along the easy axis. This was not the case for the 95nm thick specimens, when long lengths of 180° walls were not found.

One of the most important facts which emerged from the set of in-situ experiments on the 60nm thick particles is the role of the edge clusters as the domain walls move under the influence of the applied field. This fact was demonstrated most clearly in the 4.00 by 2.00μm particle, fig. 4.8. The edge clusters tended to move in such a way as to delay the introduction of a 180° wall. This resulted in the behaviour of particles with edge clusters being significantly different from those particles having only corner and free clusters.

As shown in section 4.3, the Fresnel mode, when used in conjunction with the magnetising stage provides valuable information about the magnetisation processes of some of the particles. However as can be seen from some of the Fresnel images, they are sometimes rather difficult to interpret. This is especially the case when low angle domain walls are present as these walls

are, by the nature of the imaging mode, rather low in contrast. A more serious drawback is the fact that the domain walls of the narrower (< approximately 0.5μm) particles are virtually impossible to detect due to the presence of a Fresnel edge wave which makes the boundaries of the particles appear quite blurred. Analysis using the Fresnel mode is therefore restricted to the larger particles. Unfortunately, however, the narrower and more acicular particles tend to support non-solenoidal structures, and these would be of particular interest if they could be examined during in-situ experiments.

In order to overcome this problem, these more acicular particles were examined using the Foucault (section 2.2.3) technique. A direct consequence of the form of the non-solenoidal domain structure means that these particles are particularly well suited to examination using this technique. Results obtained from an examination using the Foucault mode of the smaller and more acicular particles, as well as some larger particles are presented in chapters 5 and 6.

CHAPTER 5

FOUCAULT AND KERR MAGNETO-OPTIC IMAGING OF $Ni_{82.5}Fe_{17.5}$ PARTICLES

5.1 INTRODUCTION

In section 4.3, various in-situ experiments performed on 60nm thick $Ni_{82.5}Fe_{17.5}$ particles were described. All the results from section 4.3 were obtained using the Fresnel mode and although a great deal of information can be obtained from these images, problems are encountered when either of the in-plane dimensions becomes less than approximately 0.5μm. These smaller particles can, however, be examined using the Foucault mode and section 5.3 describes some of the in-situ experiments performed on the smaller 17, 60 and 95nm thick particles.

The high contrast levels in a Foucault image, in addition to the fact that it is an in focus technique enables the positions of the domain walls to be determined accurately. Careful interpretation of the Foucault images can lead to the formation of hysteresis loops from individual particles, and the procedure for doing this is described in section 5.2.

Finally section 5.4 presents some results from experiments performed on large 60nm thick $Ni_{82.5}Fe_{17.5}$ particles carried out using the Kerr magneto-optic imaging facilities at the University of Erlangen, Germany. Quantitative surface magnetisation maps from some of the more interesting domain structures are also presented in this section.

5.2 DETERMINATION OF A HYSTERESIS LOOP FROM A SET OF FOUCAULT IMAGES.

The procedure which enabled Foucault images to be obtained in the modified JEOL 2000FX CTEM was described in section 2.2.3. In order to derive as much

information as possible regarding the domain structure of a particle, a pair of Foucault images mapping orthogonal components of induction are normally obtained. One such pair from a 4.00 by 1.05μm particle, was shown in fig. 2.4. During the course of the in-situ experiments, as the value of the applied field increases, and domains grow and shrink in size, a series of Foucault images are obtained at different values of applied field. (In the specific case of particles described in section 5.3, the applied field is always directed along the easy axis of the particles.) The high level of contrast in these images allows the domain structure to be determined and thus the net moment of the particle can be calculated. A value of the net moment (**M**) of a particle was obtained by summing the areas of those domains magnetised parallel to the applied field and then subtracting the area of those domains magnetised anti-parallel to the applied field. (The directions of magnetisation in the domains magnetised (or close to being magnetised) orthogonally with respect to the applied field are disregarded in the calculation.) Hence **M** can be expressed in eqn. 5.1 as;

$$\mathbf{M} = \sum_i A_i - \sum_j B_j \qquad (5.1)$$

Domains magnetised parallel to the applied field have area A_i, and domains magnetised anti-parallel to the applied field have area B_j. A value for the reduced moment (RM) is obtained by dividing **M** by the total area of the particle. The RM is therefore dimensionless. One specific example of this calculation is shown in fig. 5.1. In fig. 5.1(a), those domains which are magnetised parallel to the applied field are shaded, while in fig. 5.1(b), those domains magnetised anti-parallel to the applied field are shaded. Summing and then subtracting the shaded areas in fig. 5.1(a) and (b) gives a value for **M** which, when divided by the total area of the particle, results in a value for the RM.

In order to calculate a hysteresis loop from a particle, the RM value was evaluated at various different values of applied field. A typical hysteresis

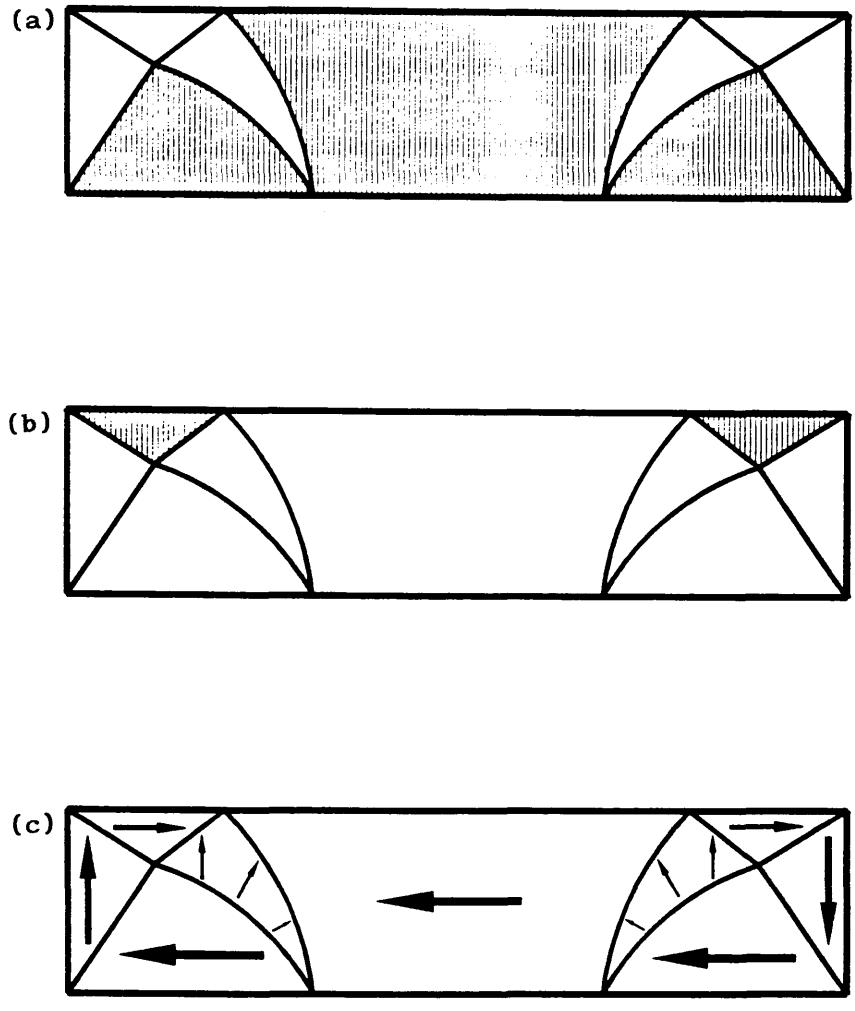

Fig. 5.1 Diagram showing the calculation of the RM. In (a), those domains which are magnetised parallel to the applied field are shaded, while in (b), domains anti-parallel to the applied field are shaded.

loop from a particle is shown in fig. 5.2, and in general approximately 10 values of RM were used to construct each loop. Each of the dots in fig. 5.2 represents a value of applied field at which the RM value was calculated. The actual shape of this loop will be discussed in greater detail in section 5.3.

5.3 FOUCAULT IMAGING OF IN-SITU EXPERIMENTS ON $Ni_{82.5}Fe_{17.5}$ PARTICLES

The higher magnification available using the Foucault mode enabled not only the larger particles to be examined, but also those particles which existed in non-solenoidal states. The latter type of domain structures were extremely well suited to study using this technique as there is a high variation in the image intensity of two non-solenoidal structures which are oppositely magnetised, as shown in fig. 5.3. In sections 5.3.1 to 5.3.3, the in-situ experiments on 17, 60 and 95nm thick particles with $R \geq 4$ are described. Hysteresis loops constructed from pairs of Foucault images using the method described in section 5.2 are given for some of the particles.

5.3.1 IN-SITU EXPERIMENTS ON 17nm THICK PARTICLES

The easy axis a.c. demagnetised states of particles at this thickness were given in section 4.4. In general the resulting domain structures of the particles were highly reproducible, and will therefore serve as a useful starting structure from which in-situ experiments can be conducted. For the particles relevant to this section, starting domain structures were similar to the as-grown structures shown in fig. 4.1(b), and in this particular sample, all of the particles with $R \geq 4$ had type II, (non-solenoidal), distributions.

The five 4μm long particles with $R \geq 4$ were examined extensively, and a hysteresis loop was constructed from each particle. In the case of the 3.98

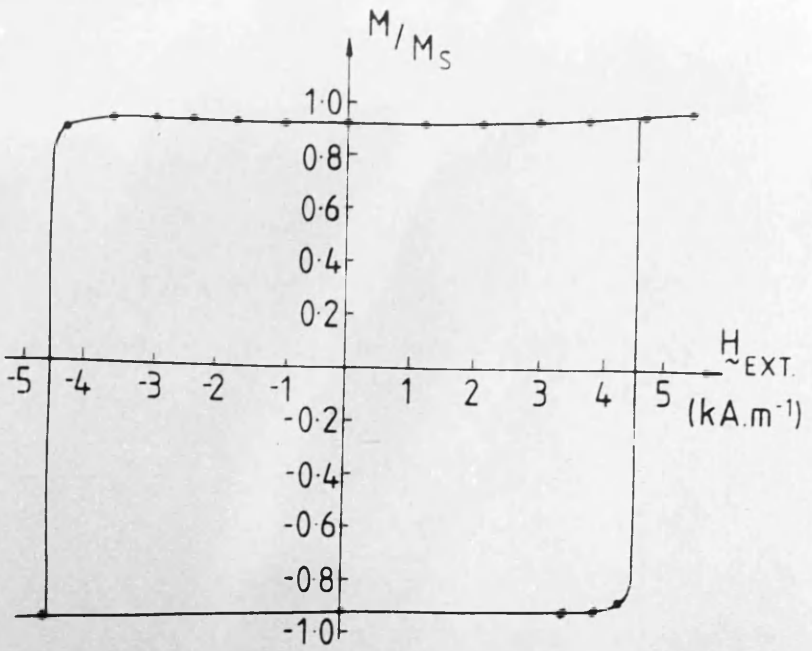

Fig. 5.2 Hysteresis loop deduced from evaluating the RM at various values of applied field. Each point at which a value of RM was calculated is marked with a dot.

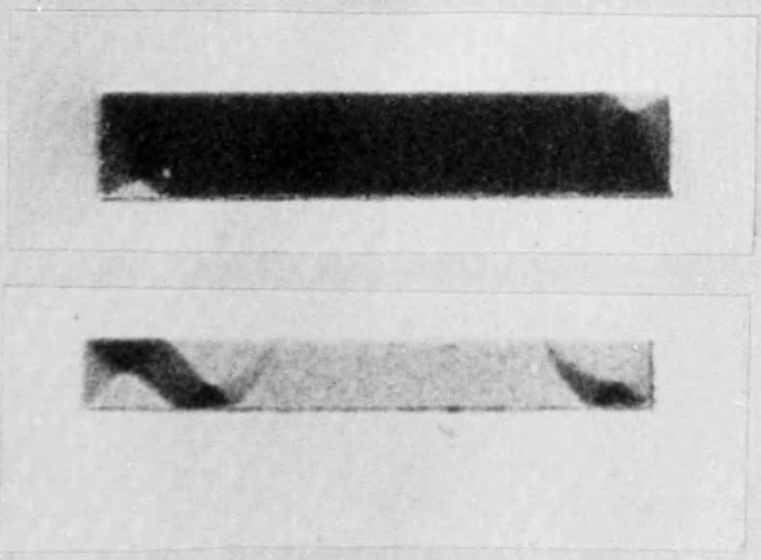

Fig. 5.3 Foucault image of two non-solenoidal domain structures which are oppositely magnetised.

by 1.00μm particle, its a.c. demagnetised state can be seen to be type II(d), as shown in fig. 5.4. On application of a field anti-parallel to the direction of magnetisation in the central section of the particle, the domain structure changed very little until at a well defined field H_s the magnetisation in the central section reversed. Although, as noted, there was little change in the domain structure up to H_s, fig. 5.5 shows that just before switching, some growth of the end domain structure was observed. Further increase in the field up to H_{max} ($=10kA.m^{-1}$) resulted in little further change and, on removal of the field, the remanent state of the particle closely resembled that of the particle in its a.c. demagnetised state but with the magnetisation of the central section reversed. Application of a negative field led to similar results with the direction of magnetisation in the central section once again changing when a field of $-H_s$ was attained. For a particle of a particular size and shape the switching field is reproducible with an accuracy of $\pm 300A.m^{-1}$. The accuracy with which H_s can be determined is influenced primarily by the difficulty associated with increasing the magnitude of the field in increments smaller than this value. A second. but more practical reason is that if the field were increased in smaller divisions, the time taken for each experimental run would be impracticably long, as the microscope has to be reconfigured each time the field is increased.

The hysteresis loops from various 4μm long particles are shown in fig. 5.6. Hysteresis loops of this shape are type A, and the behaviour of all these particles is quite similar to the 3.98 by 1.00μm particle described above.

The squareness of a particle is defined as the value of the remanent reduced moment. Values of squareness and H_s for various particles in two different samples are given in tables 5.1(a) and (b). It should be noted that both the remanent RM value and the value of H_s increases monotonically with R. Both of these points will be discussed in section 5.3.4.

Values of H_s and the RM from 3 and 2μm long particles with $R \geq 4$ are also shown in table 5.1(a) and (b). It was noted that at this thickness, all

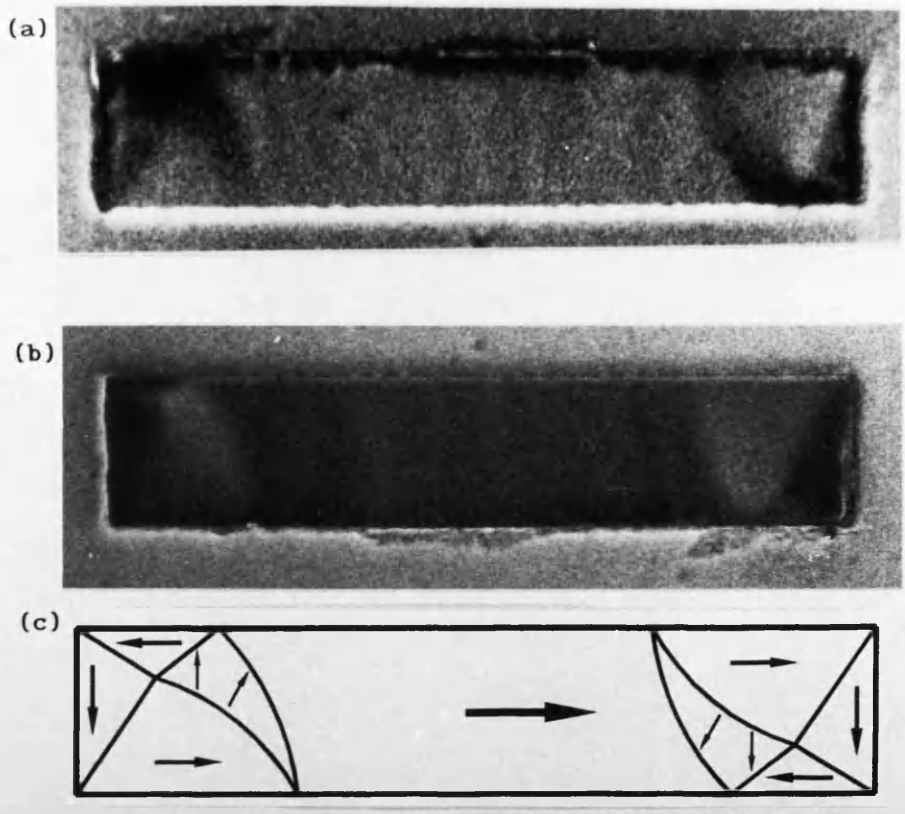

Fig. 5.4 Foucault images showing components of induction (a) parallel and (b) perpendicular to the long axis of a 17nm thick permalloy particle, (c) schematic of the magnetisation distribution deduced from (a) and (b).

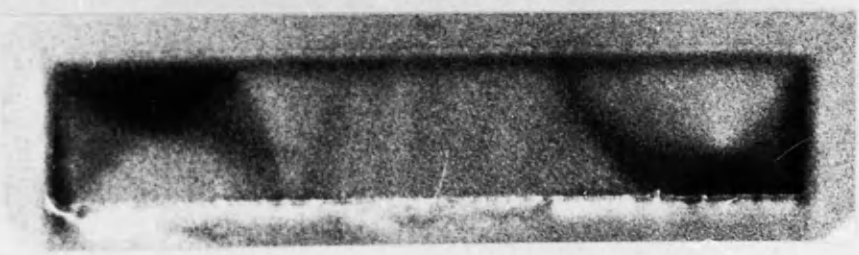

Fig. 5.5 Foucault image of a non-solenoidal magnetisation distribution in a 17nm thick particle with the applied field just less than H_s.

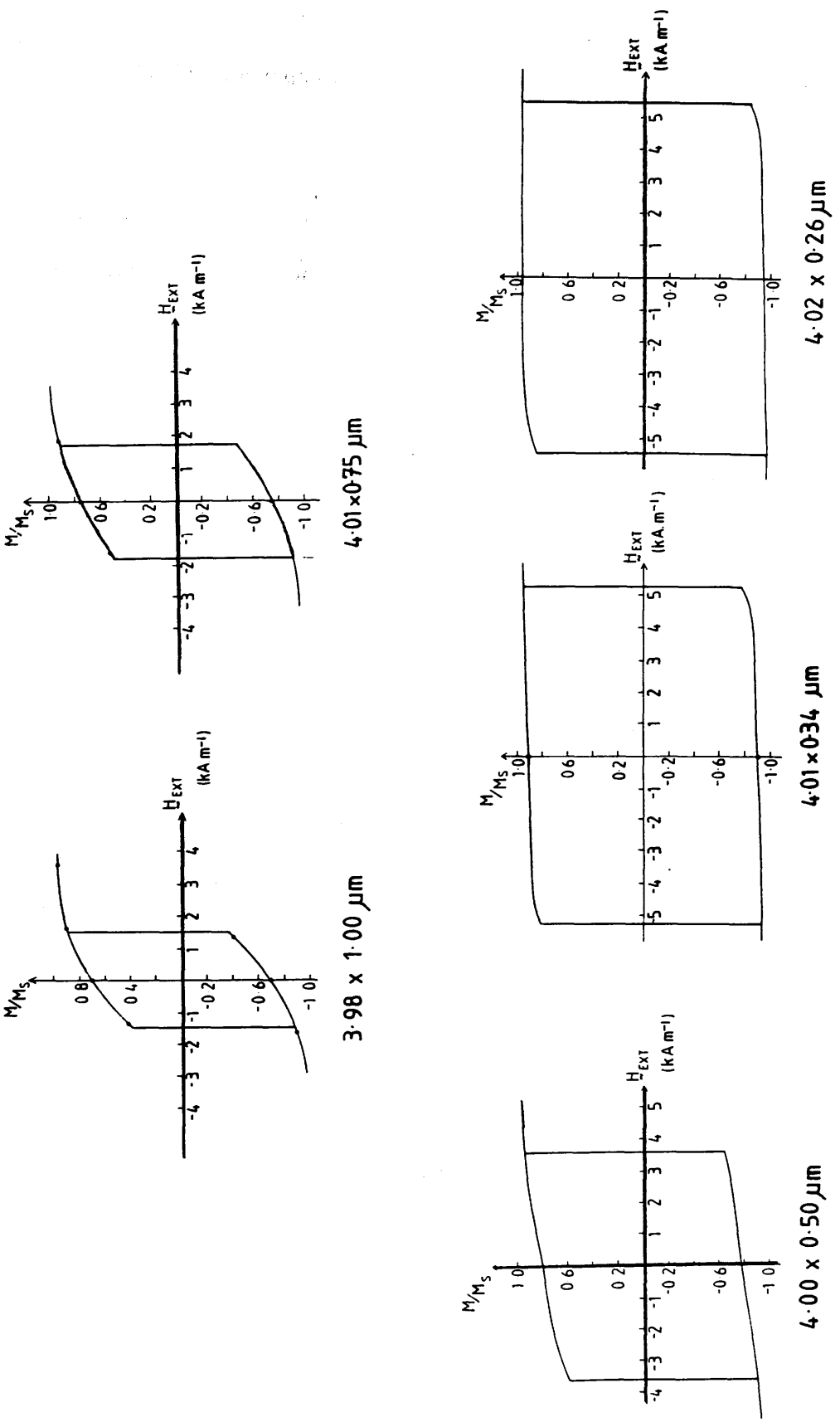

Fig. 5.6 Hysteresis loop from various 4.0µm long, 17nm thick particles. Loops of this shape are denoted type A.

Table 5.1(a): The magnetisation process in 17nm thick permalloy particles.

In-plane dimensions (μm)	R	Hysteresis loop type	Squareness	H_s ($kA.m^{-1}$)
4.00x1.00	4.0	A	0.70	1.5
4.00x0.75	5.3	A	0.76	1.8
4.00x0.50	8.0	A	0.80	3.6
4.00x0.34	11.7	A	0.92	5.2
4.00x0.26	15.6	A	0.96	5.4
3.00x0.75	4.0	A	0.70	1.7
3.00x0.50	6.01	A	0.74	3.6
3.00x0.34	8.92	A	0.83	5.0
3.00x0.26	11.38	A	0.92	6.2
2.00x0.34	5.85	A	0.77	3.2
2.00x0.26	7.7	A	0.80	6.0

Table 5.1(b):The magnetisation process in 17nm thick permalloy particles.

In-plane dimensions (μm)	R	Hysteresis loop type	Squareness	H_s ($kA.m^{-1}$)
3.87x1.00	3.87	A	0.65	1.5
3.87x0.76	5.11	A	0.72	1.8
3.87x0.51	7.67	A	0.77	2.9
3.87x0.40	9.86	A	0.90	4.7
3.87x0.26	15.0	A	0.95	5.5
2.89x0.75	3.84	A	0.63	1.6
2.89x0.50	5.76	A	0.76	2.4
2.89x0.38	7.53	A	0.78	4.4
2.89x0.27	10.66	A	0.89	4.7
1.96x0.40	4.98	A	0.73	2.6
1.96x0.27	7.23	A	0.78	5.0

particles with R ≥ 4 had type A hysteresis loops.

5.3.2 IN-SITU EXPERIMENTS ON 60nm THICK PARTICLES

A set of experiments was performed on 4, 3 and 2μm long, 60nm thick particles which had 4 < R < 16. For those particles which were 4μm long the three particles with the highest R values displayed similar characteristics to those of the 17nm thick particles discussed in section 5.3.1. The remaining two 4μm long particles with lower values of R showed markedly different properties, and are discussed below.

Firstly in their a.c. demagnetised state, they both supported a solenoidal domain structure of the kind shown in fig. 5.7. On application of a field, favourably oriented domains grew at the expense of those less suitably oriented and the net moment of the particle increased with field. This continued until a critical field, denoted H_{s1}, was attained whereupon an irreversible change took place. Fig. 5.8 shows Foucault images of the domain structure just below and above H_{s1}. In the former case the magnetisation distribution is clearly a distorted form of that existing in zero field; indeed, if H_{ext} was removed before H_{s1} was attained the structure reverted to its original form. However, as H_{ext} was increased to H_{s1} the 180° wall was driven into the side of the particle and the structure changed to a form immediately recognizable as the non-solenoidal structure already discussed in connection with the 17nm thick particles in section 5.3.1. H_{s1} thus denotes the field at which a transition from a solenoidal to a non-solenoidal structure takes place. Further increase of the field to H_{max} and its subsequent reduction to zero led to little further change and at remanence the particle displayed a non-zero moment as have all the particles discussed in section 5.3.

Application of a reverse field also had little effect until a field denoted by H_{s2} was reached. Just before this field the magnetisation distribution closely resembled that shown in fig. 5.5. However, at H_{s2}, instead of the

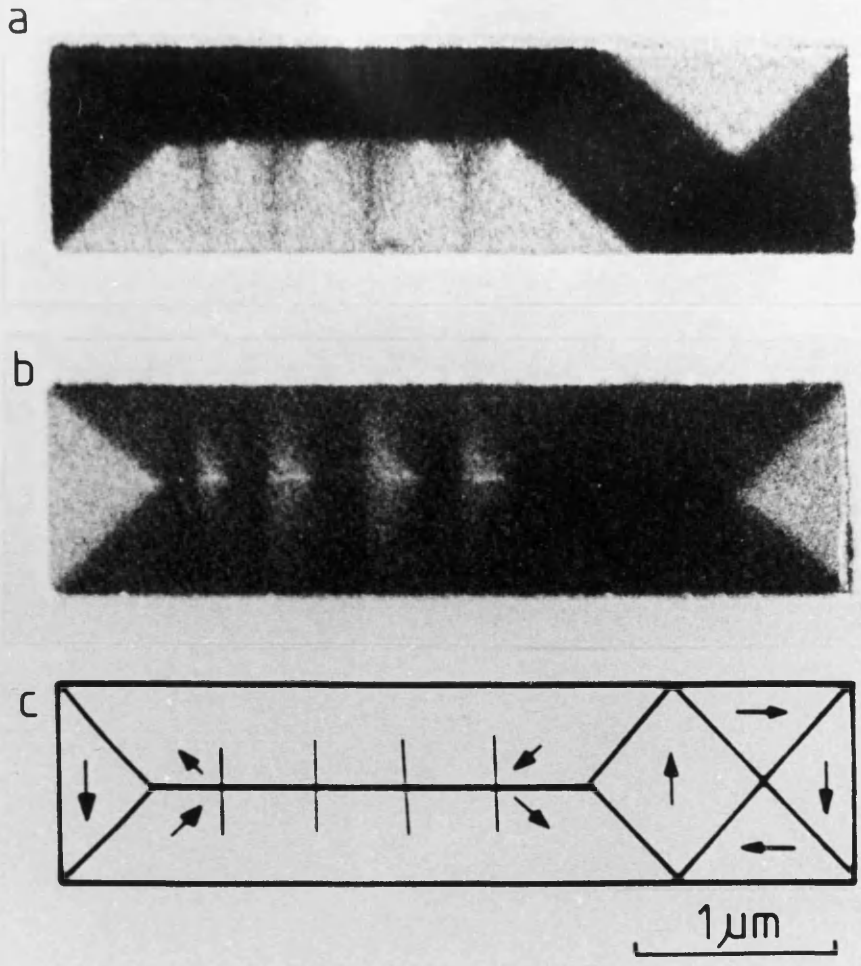

Fig. 5.7 A 60nm thick particle with R = 4, which has a solenoidal distribution.

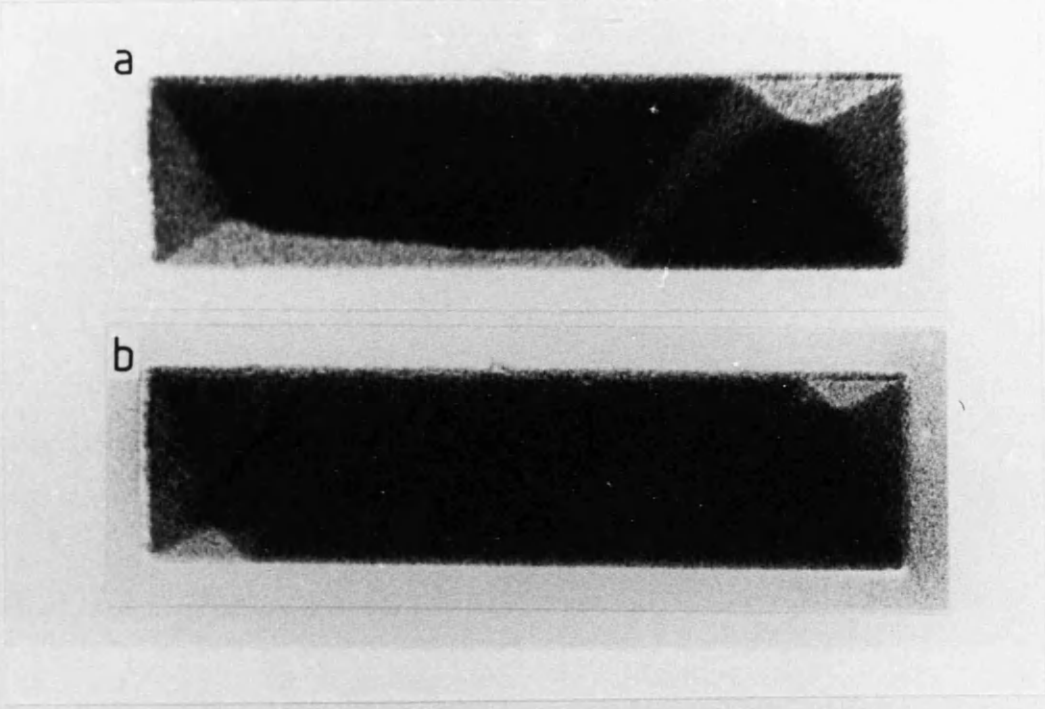

Fig. 5.8 Foucault image of the particle shown in fig. 5.7 with an applied field (a) just less than H_{s1} and (b) just greater than H_{s1}.

magnetisation direction of the central portion of the particle simply reversing, a distorted form of the original solenoidal distribution (with similar features to those apparent in fig. 5.8(a) resulted. Removal of the reverse field at this point then restored the domain structure in the particle to its original a.c. demagnetised form. H_{s2} then denotes the field at which a transition from a non-solenoidal to a solenoidal distribution takes place.

Increase of the reverse field beyond H_{s2} led to further distortion of the solenoidal distribution until at $-H_{s1}$ the structure once more reverted to a non-solenoidal form. The hysteresis loop for the complete cycle is shown in fig. 5.9(a) for the 60nm particle with R = 3.8 and this type of loop is denoted as type B. It is apparent that particles with hysteresis loops of type B can exist in three remanent states corresponding to the two non-solenoidal distributions with oppositely magnetised central portions and the solenoidal state with zero net moment.

Details of switching fields and squarenesses for the two 60nm particles just considered are given in table 5.2. It should be noted that the difference between $|H_{s1}|$ and $|H_{s2}|$ is smaller for the particle with R = 5.3 than for the particle with R = 3.8. The hysteresis loops from 4μm long particles of varying in-plane aspect ratios are given in fig. 5.9.

Data on the 3 and 2μm long particles are also given in table 5.2. In a similar manner to the 4μm long particles, for those particles having type A hysteresis loops the values of both the squareness and H_s are found to increase monotonically with R. Particles having the same value of R but different lengths have very similar values of squareness. Points such as these are discussed in section 5.3.4.

5.3.3 IN-SITU EXPERIMENTS ON 95NM THICK PARTICLES

Details of the 95nm thick particles investigated are given in table 5.3(a) and (b). In the case of the 4μm long particles, only the most acicular of

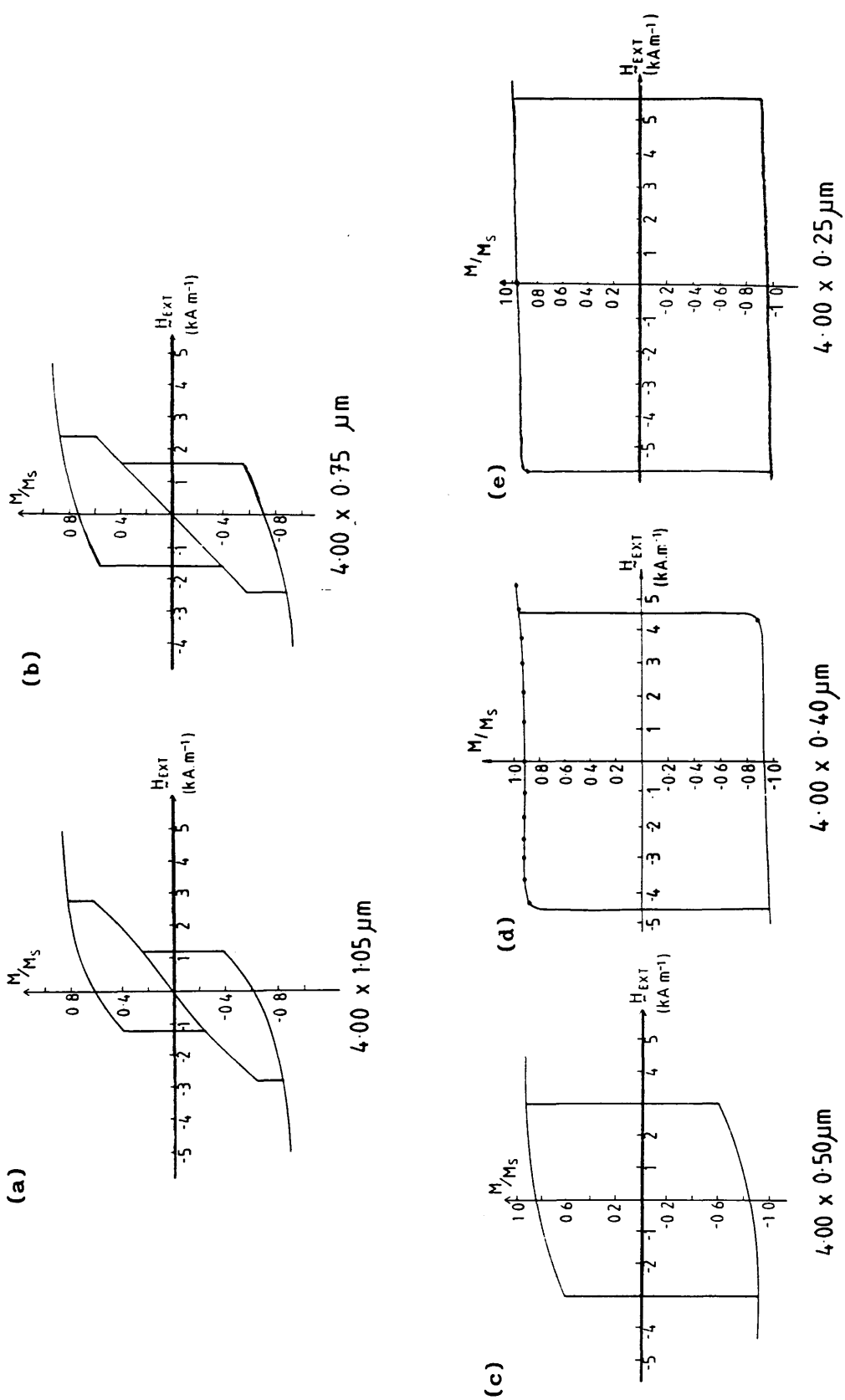

Fig. 5.9 Hysteresis loops from 60nm thick particles with length 4.00µm.

Table 5.2(a): The magnetisation process in 60nm thick permalloy particles.

In-plane dimensions (μm)	R	Hysteresis loop type	Squareness	H_s ($kA.m^{-1}$)	H_{s1} ($kA.m^{-1}$)	H_{s2} ($kA.m^{-1}$)
4.00x1.05	3.8	B	0.62		2.8	-1.2
4.00x0.75	5.3	B	0.72		2.4	-1.5
4.00x0.50	8.0	A	0.84	3.0		
4.00x0.40	10.0	A	0.92	4.5		
4.00x0.25	16.0	A	0.97	5.7		
3.00x0.75	3.8	B	0.63		1.4	-3.0
3.00x0.50	6.0	A	0.72	2.3		
3.00x0.34	8.8	A	0.80	4.1		
3.00x0.26	11.5	A	0.90	4.8		
2.00x0.34	5.9	A	0.70	3.6		
2.00x0.26	7.7	A	0.83	4.3		

Table 5.3(a): The magnetisation process in 95nm thick permalloy particles.

In-plane dimensions (μm)	R	Hysteresis loop type	Squareness	H_s ($kA.m^{-1}$)	H_{s1} ($kA.m^{-1}$)	H_{s2} ($kA.m^{-1}$)
4.21x1.03	4.0	C	----		3.9	1.9
4.19x0.76	5.5	C	----		3.0	0.6
4.24x0.53	8.0	B	0.60		2.1	-0.9
4.24x0.39	10.8	B	0.77		1.9	-1.5
4.24x0.29	14.4	A	0.85	2.4		
3.10x0.76	4.1	C	----		3.9	2.0
3.10x0.53	5.8	C	----		2.7	0.4
3.10x0.37	8.4	B	0.77		2.3	-1.3
3.10x0.25	12.4	A	0.85	2.2		

Table 5.3(b): The magnetisation process in 95nm thick permalloy particles.

In-plane dimensions (μm)	R	Hysteresis loop type	Squareness	H_s ($kA.m^{-1}$)	H_{s1} ($kA.m^{-1}$)	H_{s2} ($kA.m^{-1}$)
4.00x1.00	4.0	C	----		3.9	2.0
4.00x0.75	5.3	C	----		3.0	0.7
4.00x0.50	8.0	B	0.60		2.0	-0.9
4.00x0.40	10.0	B	0.77		1.9	-1.3
4.00x0.25	16.0	A	0.85	2.4		

the particles shows a type A hysteresis loop, whilst particles of this length with R = 8 and 10 show type B loops. As with the 60nm thick (R = 4 and 5.3) particles discussed above, the difference between $|H_{s1}|$ and $|H_{s2}|$ decreases monotonically with increasing R value. The two particles with the lowest R-values, however, show somewhat different properties. In their a.c. demagnetised state they support a regular solenoidal domain structure which changes to a non-solenoidal distribution on application of a field H_{s1}. This state persists as the field is increased to H_{max} but, on reduction of the field, the transition back to a distorted solenoidal distribution occurs at a field H_{s2} which satisfies $0 < H_{s2} < H_{s1}$. Thus in their remanent state these particles have zero net moment and exist in only a single solenoidal state. The hysteresis loops of these particles, one of which is shown in fig. 5.10(a) and whose shape we denote as type C, look quite different from the hysteresis loops of the other 4μm long particles which are shown in fig. 5.10(c), (d) and (e).

Data on the values of H_s and RM for various 4 and 3μm long particles are given in tables 5.3(a) and (b).

5.3.4 SUMMARY AND DISCUSSION

Figs. 5.6, 5.9 and 5.10 show quite different hysteresis loops have been obtained for particles of different shapes and sizes. However, the ability to observe the domain structure throughout the magnetisation process has shown that rather similar domain structures exist in all particles. What changes is the field range over which each is stable. Thus for particles supporting hysteresis loops of either type B or C, transitions from a solenoidal to a non-solenoidal structure occur at a field value of H_{s1} whilst those from a non-solenoidal to a solenoidal structure occur at a field value of H_{s2}. H_{s2} can be negative (type B) or positive (type C), but its magnitude must be less than that of H_{s1}. The characteristic ways in which these two irreversible changes come about are now discussed more fully.

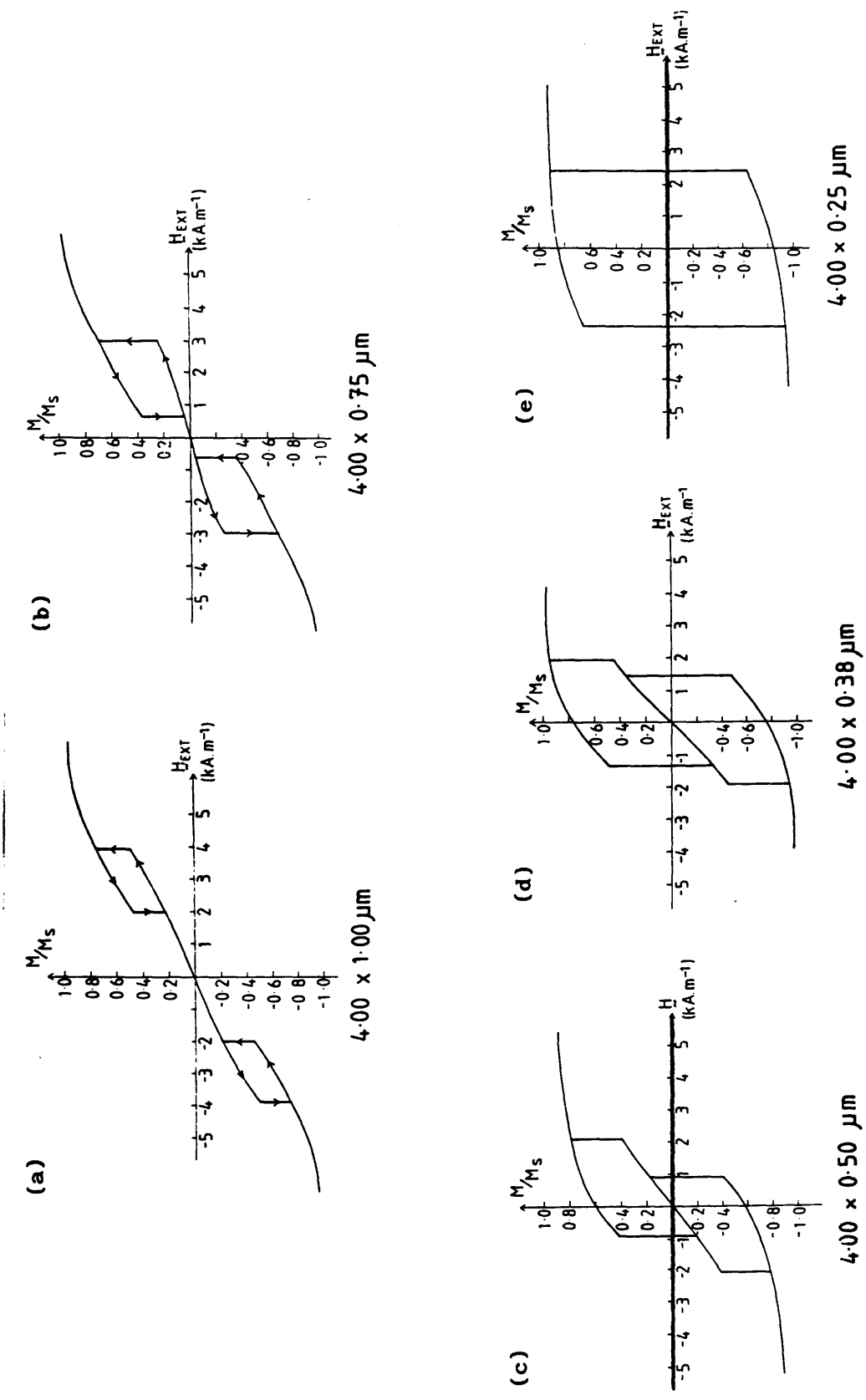

Fig. 5.10 Hysteresis loops from 95nm thick particles with length 4.00µm.

Fig. 5.11 shows schematically the domain structure just below and above H_{s1}. The key to the irreversibility of the process is the loss of the 180° wall from the central section of the particle, and its replacement by a region of uniform magnetisation across the width of the particle. The transition back to a distorted solenoidal structure then involves the regeneration of a 180° wall. Based on observations such as those shown in figs. 5.4 and 5.5, the process begins close to the curved sections of wall in the complex end domain structure. Two such points are denoted by N and N' in fig. 5.12(a). Although the actual transition is too rapid to observe, just before it happens there is domain growth involving motion of the point N towards the centre of the particle. It seems reasonable that growth should occur in this region as the torque exerted by the total internal field on the spins between the two sections of curved wall is likely to be considerable. The domain structure after the reintroduction of the 180° wall is shown in fig. 5.12.(b) and (c). In both cases the larger domain is parallel to the applied field. However, as the transition occurs when H_{s2} is positive for particles supporting a type C loop and when it is negative for particles with a type B loop, the equilibrium position of the newly generated wall differs in the two cases.

From observations such as these it is possible to suggest what happens in the case of particles with a type A loop. Extrapolating from what is observed for type B particles it appears that once a 180° wall is generated, no equilibrium position exists for it between the sides of the particle. Instead it sweeps straight across, touches the other side and is immediately eradicated leaving the structure shown schematically in fig. 5.12(d). Another way of expressing this is that $|H_{s2}| > |H_{s1}|$ for these particles and as such the solenoidal state is never stable.

The fields at which transitions between the various structures take place depend on the shape of the particle. The total field at a point in a particle is the vector sum of the applied field and the local demagnetising field, and the latter is present in any particle supporting a non-solenoidal

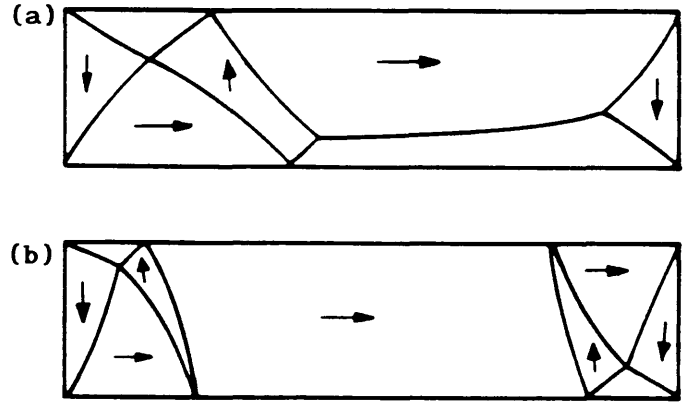

Fig. 5.11 Schematic magnetisation distribution (a) just below H_{s1} and (b) just above H_{s1}.

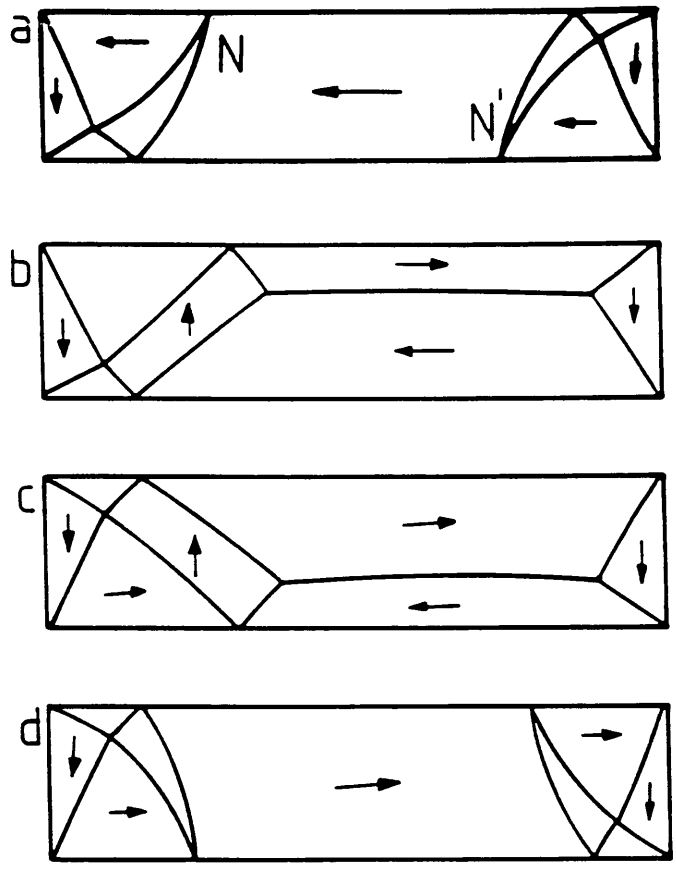

Fig. 5.12 Schematic magnetisation distribution (a) before the transition from a non-solenoidal magnetisation distribution, (b) just above H_{s2} for a particle with a type C hysteresis loop, (c) just above H_{s2} for a particle with a type B hysteresis loop, and (d) just above H_s for a particle with a type A hysteresis loop.

structure, even in zero applied field. For the particles under consideration here the demagnetising field arises mainly from volume magnetic charge in the region where the domain walls curve towards the ends of the particle. (Note that the end domain structure ensures that there is little or no surface magnetic charge as would be the case in a uniformly magnetised particle. The actual form of the magnetisation distribution in the vicinity of the end closure structure will be discussed in greater detail in section 5.4.3.) Although the demagnetising field is non-uniform and cannot be related simply to the dimensions of the particle (Van den Berg (1984)), guided by the calculations of Rhodes and Rowlands (1954), it can be shown that its magnitude increases both with particle thickness and width. Thus, if the transition from a non-solenoidal state occurs when the total field in the particle at points such as N in fig. 5.12(a) reaches a critical value, the field that must be applied to cause the transition will depend on the particle dimensions.

Examining the results in tables 5.1(a) and (b), for particles of 17nm thickness where non-solenoidal states were observed throughout, the argument above suggests that as the demagnetising field decreases with increasing R, the switching field H_s should increase with R. This is in accordance with observation. For table 5.2 a slightly more complex situation exists in that both type A and B hysteresis loops are observed. However, the table shows that the transition from a particular non-solenoidal structure occurs at an applied field whose magnitude increases monotonically from 1.2 to 5.7kA.m^{-1} as R increases from 3.8 to 16. This is again consistent with the explanation of the transition occurring when the internal field reaches a particular value. A similar variation with R is seen in table 5.3 for 95nm thick particles, although here the transition from the non-solenoidal structure occurs for the two particles with the lowest values of R whilst the applied field is parallel, not opposing, the magnetisation in the central portion of the particle. In these two particles the demagnetising field is sufficiently strong that it must be offset by a positive applied field to stabilise the

non-solenoidal structure at all in these two particles.

It should also be noted that as the dimensions of particles with a particular aspect ratio is decreased, the value of H_s in particles with type A hysteresis loops, and H_{S2} in type B, increases. This arises due to the fact that as the dimensions of the particle decrease, the total amount of volume charge in the end closure structures decreases. This has the effect of decreasing the magnitude of the demagnetising field in the particle, hence the magnitude of the switching field increases. That these areas become closer together does not significantly affect the value of H_S, as the reversal appeared to originate at points N and N' in fig. 5.12.

The difference in behaviour of the three thicknesses of particles can be attributed partly to the rapid increase in demagnetising field which occurs with increasing thickness. Thus, for thicker particles, transitions from the non-solenoidal state tend to occur at lower values of reverse applied field, or for the least acicular particles, they occur before the field is reversed at all. However, the other factor which must be taken into account when comparing the behaviour of particles of different thickness is the fact that the domain wall type and energy/unit area both change with thickness (Hubert (1970)). This has a profound influence on the range over which the solenoidal and non-solenoidal structures are each stable and in particular with which state is found at remanence.

It is useful to consider what contributions there are to the total magnetic energy of a particle in each state. In the solenoidal state there is neither a net volume nor a surface magnetic charge so that the magnetostatic energy of the particle can be taken as zero; indeed, for permalloy particles of negligible anisotropy, the total magnetic energy of a particle with a solenoidal domain structure consists of domain wall energy alone (Van den Berg (1987)). It should be noted that the possibility of surface charge arising from out of plane components of magnetisation, e.g. in cross-tie walls, and also the possibility of magnetostatic charge associated with charged walls are accounted for in the wall energy density term. Whilst

domain wall energy is also present in particles with a non-solenoidal structure, there is now a contribution which is magnetostatic in origin and is associated with the demagnetising field already discussed. As the thickness of the particles increases, the ratio of the wall energy/unit area to the demagnetising energy tends to decrease. Thus, for a given value of R, the field range over which the solenoidal structure is favoured would be expected to increase for particles of greater thickness. Examination of tables 5.1, 5.2 and 5.3 confirms that this is observed in practice.

Finally, tables 5.1, 5.2 and 5.3 show that for particles of all thicknesses there is a general increase in squareness with R. This simply reflects the fact that the form of the end domains in all the non-solenoidal structures is very similar. Although a more detailed description will be given in section 5.4.3, it can readily be seen that the end closure structures extend into the centre of the particle a distance approximately equal to the width of the particle. It then follows that for particles of fixed length, the length of the uniformly magnetised central region of the particle increases with R. Hence as the particle becomes more acicular, the value of the remanent RM of the particle approaches its maximum value.

5.4 MAGNETO-OPTIC IMAGING OF 60nm THICK $Ni_{82.5}Fe_{17.5}$ PARTICLES

One of the most interesting domain structures found in the particles were the type II domain structures. Unfortunately, a direct result of the contrast mechanism in both the Fresnel and Foucault imaging modes means that it is particularly difficult to produce quantitative induction maps using either technique. A further difficulty with any of the modes of Lorentz microscopy is that the electron interacts with induction rather than magnetisation, and hence producing a magnetisation map is a most complex problem. To investigate further the region of the sample near and around the curved domain wall, it would be particularly beneficial if a magnetisation map around this region could be obtained.

Although the magneto-optic Kerr microscopy technique is one method of achieving this, two initial problems had first to be overcome. Firstly in the groups of particles described in chapter 4 and section 5.3, the only particles which had non-solenoidal domain structures generally had their smaller in-plane dimension < 1μm. As the resolution of the Kerr M-O technique is ~0.3μm, particles of this size obviously are not suitable. Hence the particles which were subsequently used in the Kerr microscope had to be made considerably larger. With the fabrication technique described in section 3.3, the size of the particles can be increased simply by decreasing the magnification of the SEM and readjusting the dwell time per pixel. The magnification of the SEM was decreased by a factor of 8, and this resulted in the largest particle in PAT1 being 32μm square; the most acicular particle was 32μm by 2μm.

In the normal fabrication process the particles are on a Si_3N_4 substrate. Using oil-immersion Kerr microscopy this thin fragile support is neither necessary nor desirable, and hence was replaced by a thick GaAs substrate. This made the samples much more robust, and suitable for analysis. Prior to examination in the Kerr microscope, the samples were coated with a thin layer of ZnS which acts as an anti-reflection layer.

Images were obtained using a Hg discharge lamp as the illumination source. With the sample immersed in oil, (yielding a numerical aperture of 1.25) using the green and yellow mercury lines, the resolution, according to the Rayleigh criterion, (Gartenhaus (1977)), is about 0.3μm. Polarised illumination is incident on the specimen and contrast is generated by analysing the variations of the angle of polarisation in the reflected beam. (The contrast mechanism is discussed in greater depth in section 5.4.3.) Superficially whilst both Kerr M-O and Foucault images appear quite similar, it should be noted that the Kerr M-O images map components of surface magnetisation, whilst the Foucault images map specific components of induction integrated along the electron's direction. Section 5.4.1 describes the as-grown domain structure of the larger 60nm thick particles used for

analysis using Kerr microscopy. The dynamic behaviour of these larger particles were also analysed and some results are described in section 5.4.1. The remanent domain structures following an a.c. demagnetisation along either the easy or hard axes are described in section 5.4.2. Finally in section 5.4.3 the Kerr microscope was used to provide surface magnetisation maps from some of the more interesting domain structures.

5.4.1 AS-GROWN STRUCTURES AND DYNAMIC EXPERIMENTS

The array of particles which constitute PAT1 were fabricated at various different magnification settings of the SEM. The largest particle was 32μm square; all particles described in section 5.4 are 60nm thick. In their as-grown states, all of the particles having $R \leq 5$ had solenoidal structures of the type which would be expected for particles with their particular R value. In short, for the range of dimensions investigated, the domain structure of a 32μm long, R = (*) particle, is quite similar to a 4μm long, or any other length of particle, with R = (*).

In a similar fashion to the 60nm thick particles described in section 4.2.2, the change from solenoidal to non-solenoidal as-grown domain structures occurred when the in-plane aspect ratio exceeded approximately 5.

A number of dynamic experiments were conducted on the larger particles to verify that their dynamic behavior was in fact similar to the smaller (4μm to 1μm long) particles investigated using TEM, and which were described in section 4.3.2. Shown in fig. 5.13 is the as-grown domain structure of a 32μm square particle. Although this structure essentially consists of 90° walls, there is a small section of "tulip" (Hubert (1990)) wall in the corner marked A. A schematic diagram of this type of wall is shown in fig. 5.14. The "tulip" wall was never found in the small particles described in section 5.3 and chapter 4, but regularly occurred in 32μm and 24μm long particles. It occurred less frequently as the dimensions of the particle decreased and the difference between "tulip" walls and the 45° walls of fig. 4.22 should be

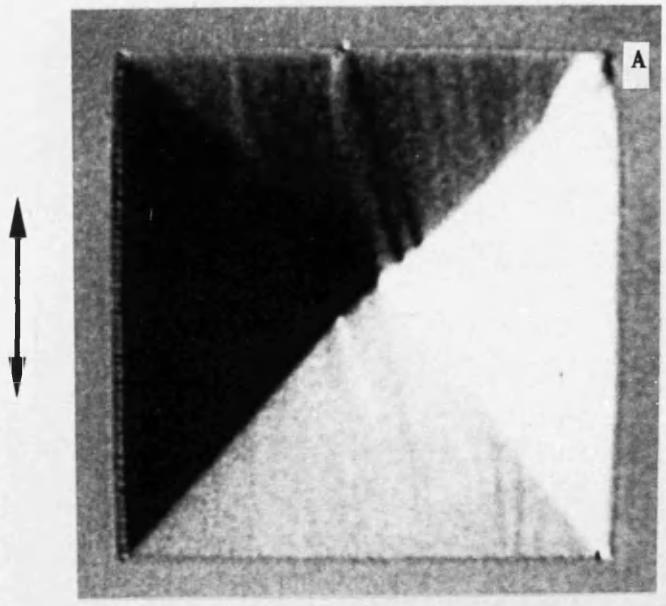

Fig. 5.13 Kerr M-O image showing the as-grown domain structure of a 32μm square, 60nm thick particle.

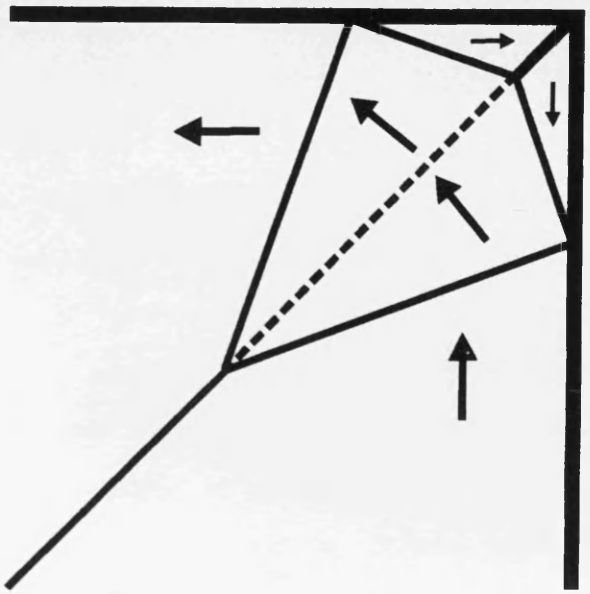

Fig. 5.14 Schematic diagram showing the directions of magnetisation near a "tulip" wall.

noted.

Upon subjecting the 32μm square particle to an applied field, the particle behaves quite similarly to the square particles described in section 4.3.2, and again a short length of cross-tie wall is introduced as the Bloch line is forced close to the edge of the particle, fig. 5.15. A slight difference between the magnetic behaviour of this particle and the smaller particles occurs once the cross-tie wall touches the edge of the particle. In this case the domain structure is as shown in fig. 5.16. Although a part of the cross-tie wall no longer exists, parts still remain, and the domain structure is quite different from fig. 4.6(h), which shows a 4μm square particle just after the collapse of the cross-tie wall. Apart from this difference, the behaviour of the larger particle in the presence of an applied field is quite similar to the smaller particles and again the remanent domain structure is found to be identical to the starting configuration.

Under the influence of an applied field, most of the particles displayed behaviour which was in general quite characteristic of their thickness and in-plane aspect ratio. However another slight difference emerged as these larger particles approached the transition from non-solenoidal to solenoidal states. Previous experiments on relatively large particles (Van den Berg (1984)) had demonstrated the existence of a "concertina" structure, (an example of which is shown in fig. 5.17), just prior to this transition occurring. In the smaller sets of particles described in section 5.3, the beginnings of a concertina structure could be observed, particularly in particles with type B hysteresis loops, but the structure was not as extensive as that shown both by Van den Berg (1984) or the particle in fig. 5.17. In the case of the larger particles examined in the Kerr microscope, transitions from non-solenoidal to solenoidal states frequently occurred via a concertina structure. Shown in fig. 5.18(a) and (b) is the domain structure of a 32 by 8μm particle just before and just after the transition from non-solenoidal to solenoidal type domain structures. These two images should be compared to fig. 5.12(a) and(b), which show a 4 by 1μm particle

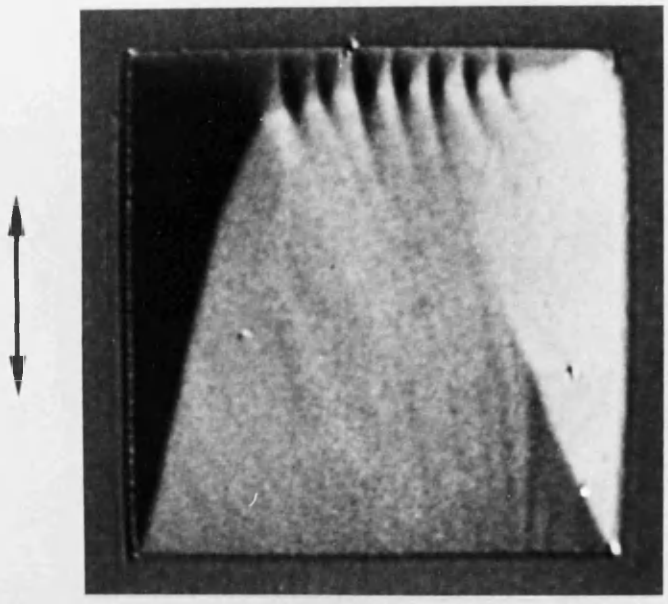

Fig. 5.15 Kerr image showing the domain structure of a 32μm square particle just prior to the collapse of the length of cross-tie wall.

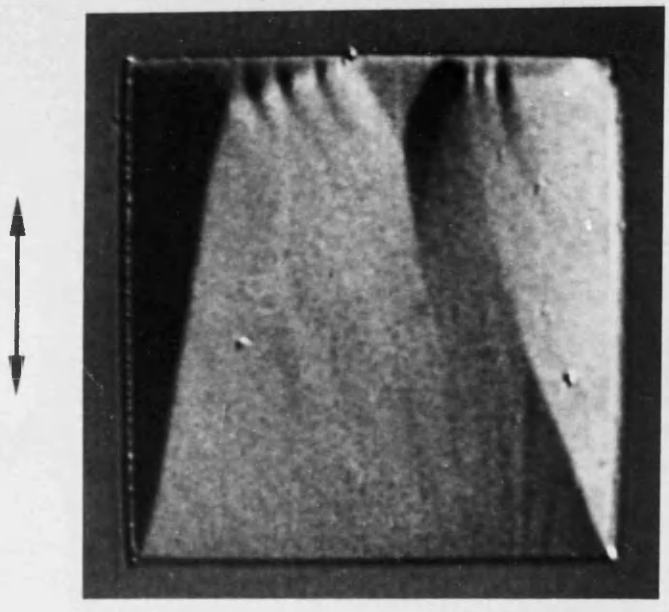

Fig. 5.16 Kerr M-O image of the 32μm particle just after the collapse of the cross-tie wall.

(a)

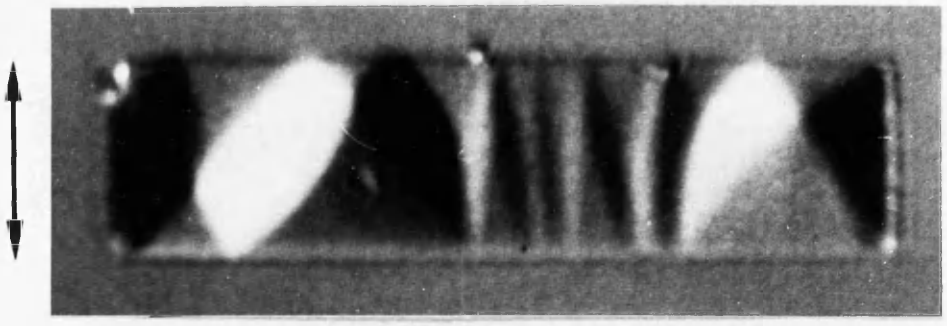

(b)

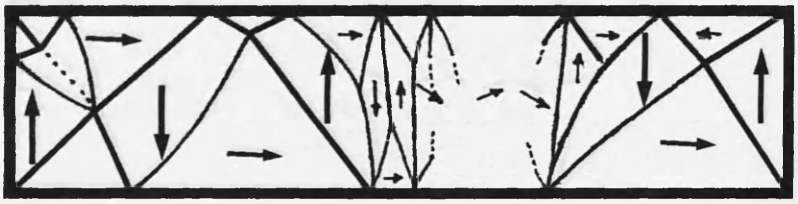

Fig. 5.17 (a) Kerr M-O image showing a "concertina" structure.

(b) Schematic representation of the directions of magnetisation in a concertina structure.

(a)

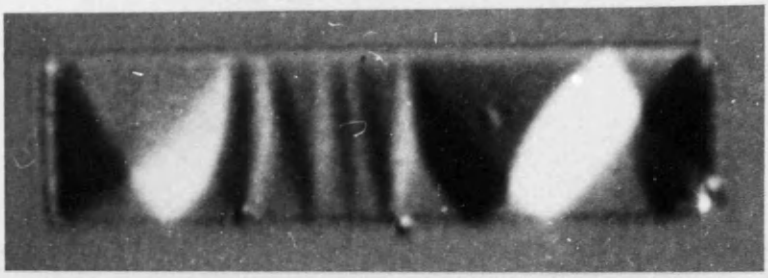

(b)

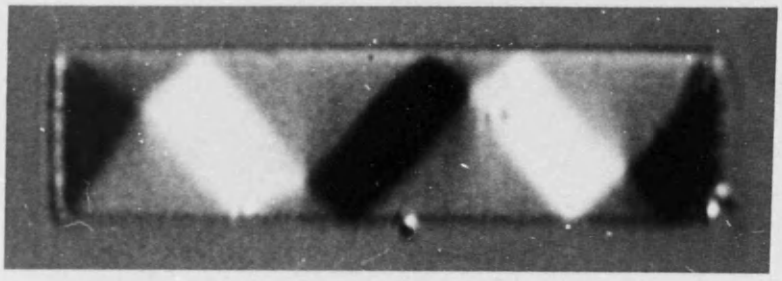

Fig. 5.18 Kerr M-O images from a 32 by 8μm particle just before and just after the transition from non-solenoidal to solenoidal domain structures.

before and after having undergone the same transition. Although the larger of the two particles has R ≅ 4 and a type B hysteresis loop, concertina structures are not confined only to particles with type B hysteresis loops. Fig. 5.19 shows a 32 by 16μm particle (which has a type C hysteresis loop), just prior to the transition from a non-solenoidal to a solenoidal domain structure which contains a short length of cross-tie wall. This particular particle has a Landau-Lifshitz remanent domain structure. The particle can also exist in a remanent domain structure which consists of 90° walls and its dynamic behaviour when existing in this type of starting domain structure is very similar to the 4 by 2μm particle described in fig. 4.8. The Kerr image corresponding to fig. 4.8(g) - after the introduction of a length of cross-tie wall is given in fig. 5.20. Upon reduction of the applied field to zero, the particle has a remanent domain structure which consists entirely of 90° walls, as would be expected for a particle with R = 2, in which the end domains are magnetised in the same direction.

As the particles become more acicular, the development of the concertina structure along the length of the particle becomes less extensive. The 32 by 2μm particle has a type A hysteresis loop, and the concertina structure is not observed.

5.4.2 HARD AND EASY AXIS A.C. DEMAGNETISATIONS

The large particles used for study using dynamic experiments in the Kerr microscope were also studied in their a.c. demagnetised states. Again particles were demagnetised along the easy and hard axes, and each case will be described separately in sections 5.4.3.1 and 5.4.3.2.

5.4.3.1 EASY AXIS DEMAGNETISATION

The a.c. demagnetised states of an array of 60nm thick $Ni_{82.5}Fe_{17.5}$ particles with R = 1 to 16 and long in-plane dimension equal to 32, 24, 16, 12 and 8μm

(a)

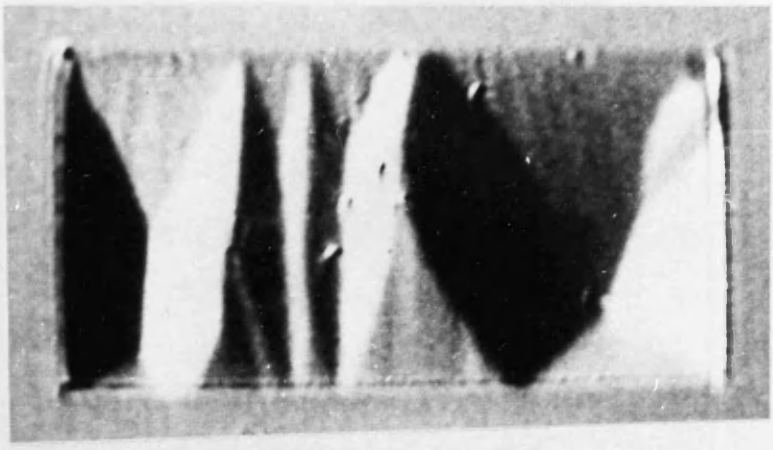

Fig. 5.19 Kerr M-O image from a 32 by 16μm particle just before the transition from non-solenoidal to solenoidal domain structures.

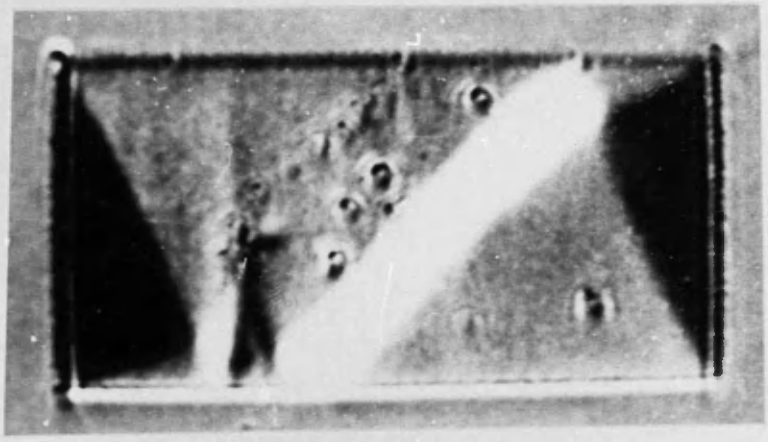

Fig. 5.20 Kerr M-O image of a 32 by 16μm particle with a short length of cross-tie wall.

were analysed. From previous results (section 4.4.3), it was expected that the transition from solenoidal to non-solenoidal remanent states would occur when the value of in-plane aspect ratio exceeded approximately 5. In fact the a.c. demagnetised states of the larger particles were very similar to those of the smaller (< 4μm long) particles, and the only difference of note is that the "tulip" walls occurred more frequently in the larger particles. The transition from solenoidal to non-solenoidal remanent states occurred at approximately R = 4 for the 4μm long particles and the same transition occurred at approximately R = 8 for the 32μm long particles. A table showing the least acicular particle having a non-solenoidal structure is given in table 5.4.

5.4.3.2 HARD AXIS DEMAGNETISATION

The remanent domain structures of the particles described above were also examined after a hard axis a.c. demagnetisation. In section 4.4.3, the particles were demagnetised using a field which had been aligned to ± 5°. The experimental arrangement at the University of Erlangen (Germany) enabled very small changes to the field direction to be made, and it was possible to align the applied field to an accuracy of about ±0.5°. This fact proved very important as the remanent domain structures of the larger, more acicular particles (R ≥ 6) were very dependent on the exact direction of the applied field.

When the field was aligned to ±5° to the hard axis, the remanent a.c. demagnetised states of the larger particles were very similar to those described in section 4.4.2. A more interesting case occurred however when the field was aligned almost exactly along the hard axis. When the field is aligned to an accuracy of about ±0.5° to the hard axis, it is found that almost all of the particles can exist in solenoidal states. For those particles which are 32μm long, only the R = 16 particle could not exist in a solenoidal state. In all other cases the type of remanent solenoidal

TABLE 5.4

First particles to display a Non-solenoidal structure.

60nm thick $Ni_{82.5}Fe_{17.5}$ specimen

Length	32 μm	24μm	16μm	12μm
		Breadth		
Easy (Dmag) (a)	4.0 μm	3.0 μm	None	None
Hard (Dmag) (a)	2.0 μm	2.0 μm	None	None
Easy (Dmag) (b)	3.0 μm	2.0 μm	None	None
Hard (Dmag) (b)	None	None	None	None

Length	32 μm	24μm	16μm	12μm
		Breadth		
Easy (Dmag) (c)	4.0 μm	2.0 μm	None	None
Hard (Dmag) (c)	2.0 μm	None	None	None
Easy (Dmag) (d)	2.0 μm	2.0 μm	None	None
Hard (Dmag) (d)	None	None	None	None

Length	16 μm	12μm	8μm	6μm
		Breadth		
Easy (Dmag) (a)	2.0 μm	1.5 μm	1.0 μm	None
Hard (Dmag) (a)	2.0 μm	None	None	None
Easy (Dmag) (b)	1.5 μm	1.5 μm	1.0 μm	None
Hard (Dmag) (b)	1.0 μm	1.0 μm	None	None

Length	8 μm	6μm	4μm	3μm
		Breadth		
Easy (Dmag) (a)	1.0 μm	0.75μm	0.5 μm	None
Hard (Dmag) (a)	0.75 μm	0.50 μm	None	None

Easy (Demag)	Easy axis demagnetisation.
Hard (Demag)	Hard axis demagnetisation.
None	None of the particles had non-solenoidal domain structures.
----	This group of particles was not suitable for examination.

(a) and (b) These are two sets of particles, in the one array, which were fabricated orthogonally to each other.

structure which resulted from a hard axis a.c. demagnetisation was either a Landau-Lifshitz structure or one of the type shown in fig. 5.21.

It should be noted that the results depend critically on the exact direction of the applied field with respect to the axes of the particle. Hence the results obtained when the applied field was directed "along the hard axis", e.g. section 4.4.2, should be interpreted with extreme care. In some cases applying the field at approximately 1° away from the hard axis direction results in a remanent non-solenoidal a.c. demagnetised structure.

5.4.3 QUANTITATIVE MAGNETISATION MAPS

It has been suggested in various parts of this thesis that in non-solenoidal states, the end closure structures are present to reduce the magnetostatic energy contribution to the total energy of the particle. It would be highly beneficial if the form of the magnetisation distribution around the end closure structure can be found. In practice neither the Fresnel nor Foucault modes are capable of providing such information. However, the large particles which show non-solenoidal structures can be examined using quantitative Kerr microscopy in order to obtain surface magnetisation maps. Quantitative magnetisation maps were obtained from suitable particles following the method given by Rave and Hubert (1990), a brief outline of which is given below.

The dependence between the total light intensity, ($I(m_l,m_t)$), and the magnetisation distribution in a sample is given by (Rave and Hubert (1990));

$$I(m_l,m_t) = A_o + m_l A_1 + m_t B_1 + (m_l^2 - m_t^2)A_2 + m_l m_t B_2 \qquad (5.2)$$

where m_l and m_t are the longitudinal and transverse in-plane components of magnetisation. The coefficients A_o to B_2 are determined by a calibration process in which the sample is saturated along eight different directions of applied field. The procedure is repeated for both the longitudinal and

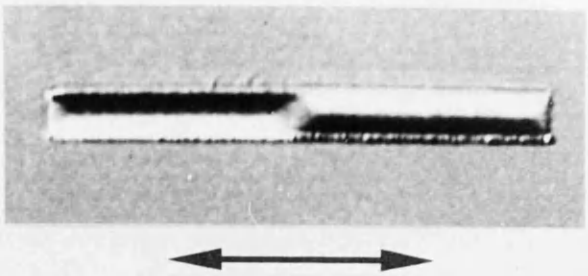

Fig. 5.21 Kerr M-O image showing the remanent domain structure of a 32 by 3μm particle following a hard axis demagnetisation.

(a)

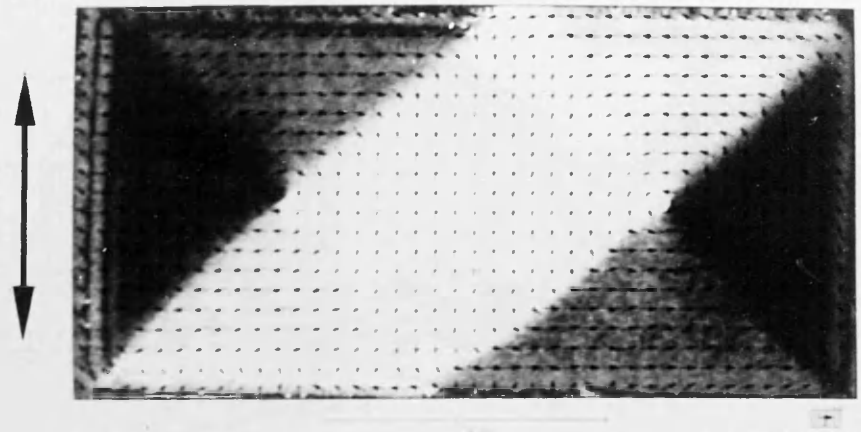

(b)

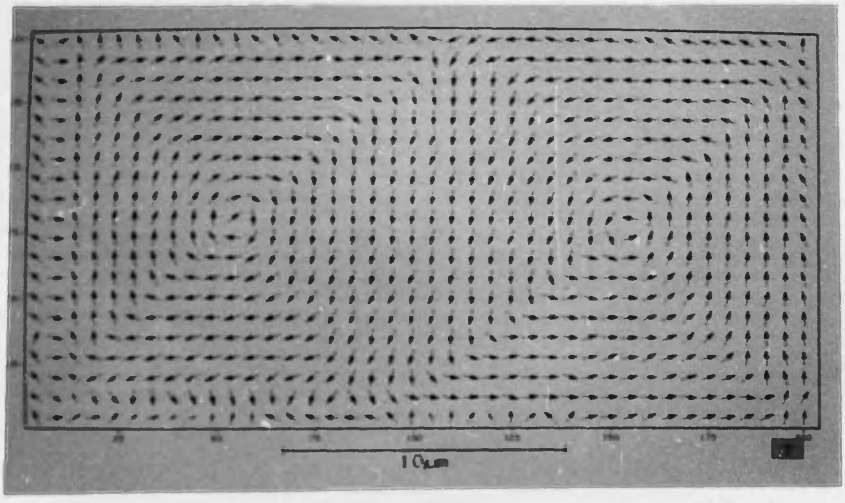

Fig. 5.22 Quantitative surface magnetisation map from a 32 by 16μm particle. In (a) the directions of the magnetisation vector has been superimposed onto a Kerr M-O image. (b) shows only the directions of the magnetisation vector.

transversely polarised incident light.

In order to map the magnetisation of a particle, the polariser and analyser settings are adjusted so that the sample is firstly illuminated by e.g. longitudinally polarised light. The particle is then saturated along one particular direction, and this "reference image" is stored in an image processor or computer. (The domain structure may be revealed by taking a difference signal between the reference image and the actual Kerr signal from an unsaturated particle.) All Kerr M-O images presented in this thesis, e.g. fig. 5.13, are difference images, and the magnetisation is mapped parallel to one edge of the particle. The particle is then saturated along seven more different directions in order to determine $I_{L/sat}(\theta)$, where $I_{L/sat}(\theta)$ is the intensity in the longitudinal component of the Kerr image when the particle is saturated along some direction θ with respect to some arbitrarily chosen axis. After eight different $I_{L/sat}(\theta)$ values have been found, the polariser and analyser settings are then changed so that the sample is illuminated with transversely polarised light, and the image is recorded as the reference signal. The sample is then saturated along the eight different directions as before, in order to determine $I_{T/sat}(\theta)$, which is the intensity in the transversely polarised component when the particle is saturated along θ.

The experimental information is then processed in a computer using a programme written by W. Rave at the University of Erlangen, and the images are displayed as two complementary grey scale images. Magnetisation maps are then readily obtained by determining, from each image, the two in-plane components of magnetisation. Arrows denoting the directions of the surface magnetisation in the sample can then be superimposed onto either of the images, as shown in fig. 5.22(a). An important point to note is that throughout this procedure it has been assumed that the magnetisation lies in the plane of the sample.

The main objective in quantitatively mapping the magnetisation is to investigate the end closure structures in non-solenoidal distributions. As the system had not previously been used to investigate such small samples,

two simpler domain structures were examined first. Firstly a 32 by 16μm particle consisting entirely of 90° walls was examined using the above procedure. The surface magnetisation distribution obtained is shown in fig. 5.22, and is in very good agreement with what would be expected using the algorithm of section 1.4.2. A second particle, 32 by 6μm which had a Landau-Lifshitz structure was then examined. The directions of magnetisation in the long length of 180° cross-tie wall are clearly shown in fig. 5.23. Both the vortex structure around the Bloch lines and the cross-ties themselves are clearly shown.

A quantitative magnetisation map from the non-solenoidal structure of fig. 5.24 is shown in fig. 5.25. The specific region of interest, the end closure structure was examined in more detail using higher density sampling and is shown in fig. 5.26(b). It can clearly be seen from this structure that close to the Bloch line at A, there are four distinct 90° walls. In the domain with the curved domain walls, the magnetisation can be seen to rotate towards the direction of the central domain. The gradual rotation of the magnetisation throughout this domain results in $\nabla . \underline{M} \neq 0$, and hence volume charge is distributed throughout this domain. Little surface charge is present in this type of domain structure.

5.4.4 SUMMARY

The M-O facilities at the University of Regensburg, Germany, enabled valuable information to be gathered concerning the domain structure of both solenoidal and non-solenoidal domain structures. Although the resolution of the imaging technique meant that particles larger than were examined in the TEM were studied, their behaviour in the presence of an applied field was in general characteristic for all values of R, although there were slight variations introduced as the dimensions of a particle with a specific R value are varied. Probably the most valuable information which was given by the Kerr M-O technique was in providing surface magnetisation maps. Quantitative

(a)

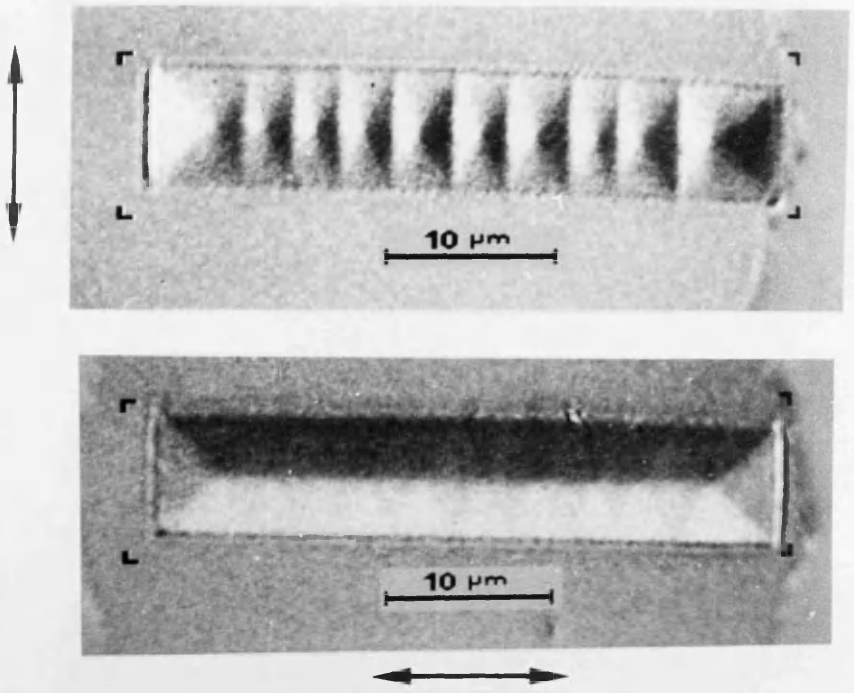

(b)

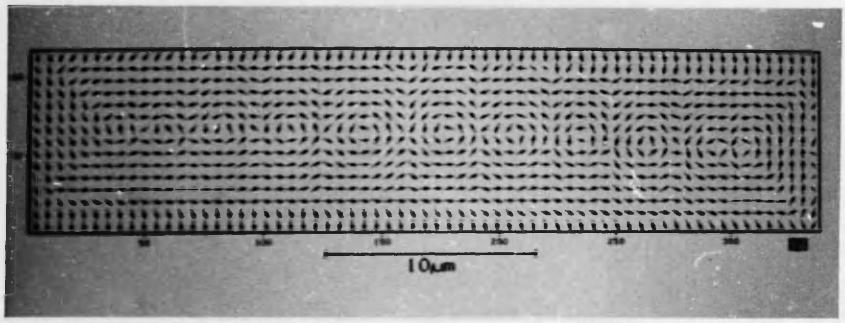

Fig. 5.23 (a) Kerr M-O images from a 32 by 6μm particle which has a long section of 180° cross-tie wall.

(b) The directions of magnetisation deduced from Kerr M-O images from the 32 by 6μm particle.

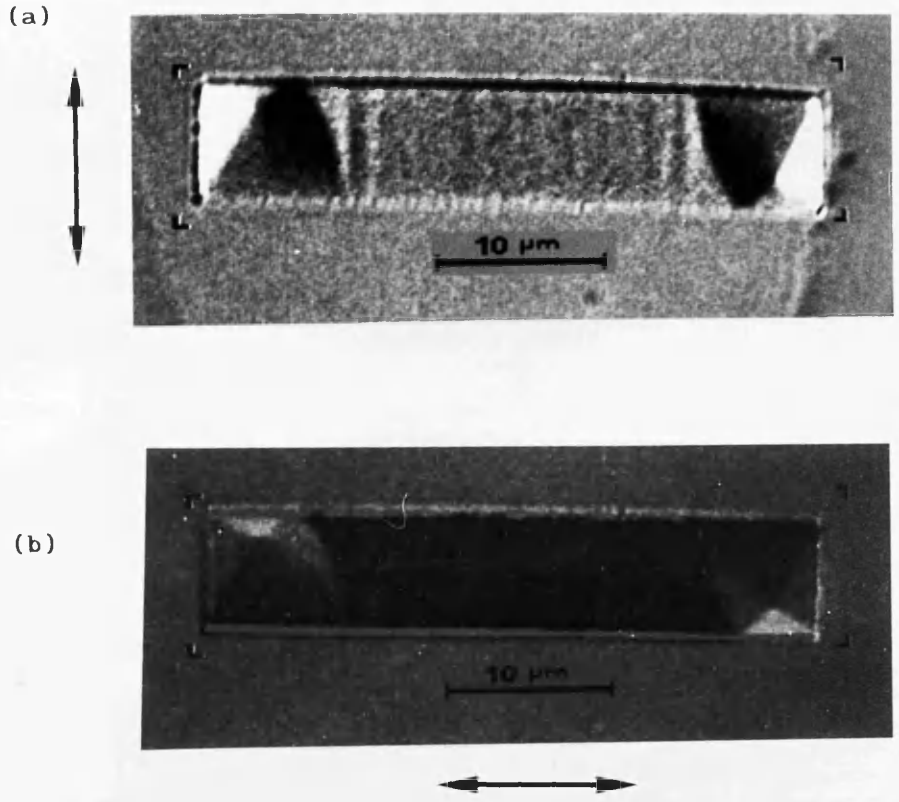

Fig. 5.24 Two Kerr M-O images of a 32 by 6 μm particle which has a non-solenoidal domain structure. (b) maps magnetisation parallel to the long axis of the particle. (a) maps components parallel to the short axis.

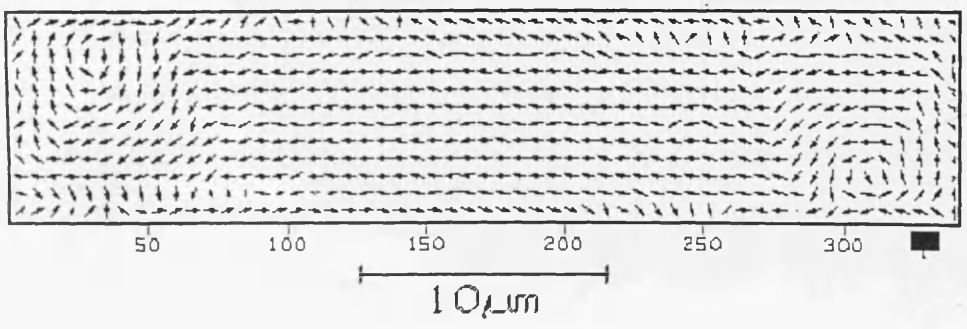

Fig. 5.25 Surface magnetisation map deduced from the images of fig. 5.24.

(a)

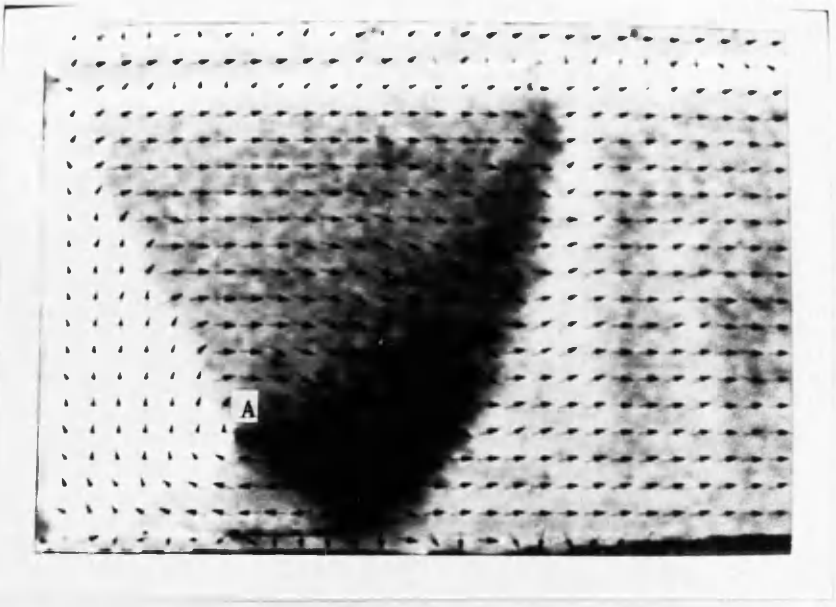

(b)

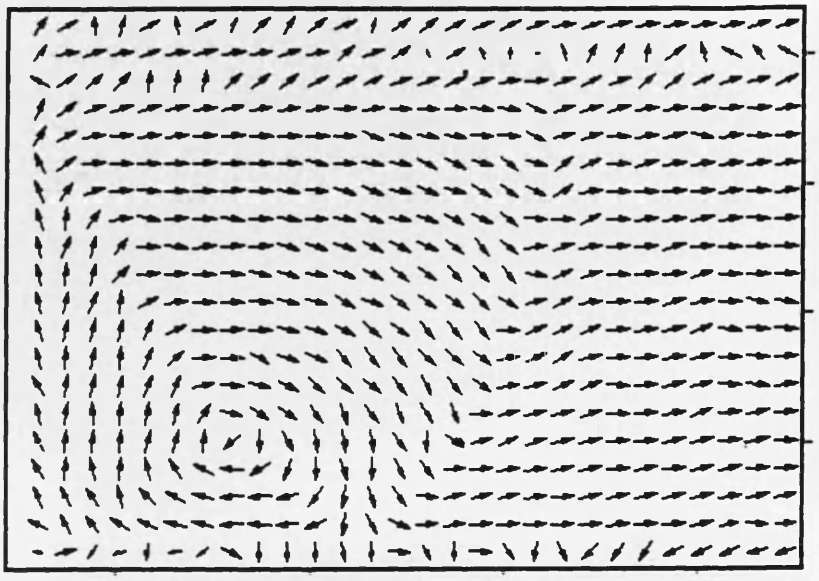

Fig. 5.26 Enlargement of the end closure structure of the particle above. (a) has the directions of the vector superimposed on top of the image, while (b) shows only the directions of the magnetisation vector.

magnetisation maps from various structures were produced and the form of the end closure structure, fig. 5.26, enabled the magnetisation distribution in the vicinity of the end of the particle to be determined.

CHAPTER 6

EXPERIMENTAL STUDIES ON Co PARTICLES

6.1 INTRODUCTION

Chapters 4 and 5 described the domain structures of numerous $Ni_{82.5}Fe_{17.5}$ particles. The particles were studied in their as-grown and remanent states as well as during in-situ magnetising experiments. As the $Ni_{82.5}Fe_{17.5}$ particles have negligible magnetocrystalline anisotropy and magnetostriction, the magnetic properties of these particles are primarily influenced by the shape of the particle. In order to examine the domain structure and magnetic behaviour of the particles when they were made of a different material, particles were fabricated using cobalt. In the form of a hexagonal close packed (h.c.p.) structure, cobalt has a strong uniaxial anisotropy ($K = 4.1 \times 10^2$ $kJ.m^{-3}$ (Jiles (1991))) directed along the c-axis. From the analysis of cobalt films and particles given in section 3.4, the thermally evaporated cobalt consists of polycrystalline grains which have an h.c.p. structure. The influence of a randomly distributed uniaxial magnetocrystalline anisotropy on the domain structure and magnetic behaviour of various thicknesses of Co particles will be described in this chapter.

In section 6.2, the as-grown domain structures of three different thicknesses of Co particles are described. The remanent domain structures of these particles were then examined following both an a.c. demagnetisation and application of a $960kA.m^{-1}$ field; the results are described in section 6.3. Section 6.4 then describes the in-situ magnetising experiments conducted on the cobalt particles and in a similar manner to section 5.3, hysteresis loops were constructed for some of the particles.

In the case of the $Ni_{82.5}Fe_{17.5}$ particles described in chapters 4 and 5, the domain structures of the particles were, in general, very reproducible, and

the as-grown domain structure and magnetic behaviour of a $Ni_{82.5}Fe_{17.5}$ particle with a particular value of thickness and in-plane aspect ratio could be predicted with considerable confidence. Although, as discussed in sections 6.2 to 6.4, this was again found to be the case for some of the cobalt particles, there were exceptions, and these are described in section 6.6. This section also summarises some of the more important conclusions which can be drawn from the investigations on cobalt particles.

6.2 AS-GROWN DOMAIN STRUCTURES OF COBALT PARTICLES.

6.2.1 17nm THICK COBALT PARTICLES

The as-grown domain structures of various 17nm thick particles are shown in fig. 6.1, with a schematic shown in fig. 6.2. It was noted that as the value of R increases and the particles become smaller, the domain structures become more regular and start to resemble the types of solenoidal structures which were found in the $Ni_{82.5}Fe_{17.5}$ particles. This fact is discussed in greater detail in section 6.2.4. As was found in the $Ni_{82.5}Fe_{17.5}$ particles, some of the particles existed in solenoidal structures while others were in non-solenoidal structures. At this thickness the value of in-plane aspect ratio at which the transition from solenoidal to non-solenoidal as-grown domain structures took place was found to be approximately 12. In contrast to the $Ni_{82.5}Fe_{17.5}$ particles it is found that the total domain wall energy which is present in some of the particles is not minimised and there are many short lengths of wall present, e.g. fig. 6.1(b).

A feature which is apparent in Foucault images of Co particles, e.g. the non-solenoidal domain structure of fig. 6.3, and which is different from the $Ni_{82.5}Fe_{17.5}$ particles is that the contrast generated by both the domains within the particle, and the stray field, was considerably stronger in the case of cobalt. This would imply that the deflection angles of electrons passing through cobalt are greater than those for $Ni_{82.5}Fe_{17.5}$. The larger

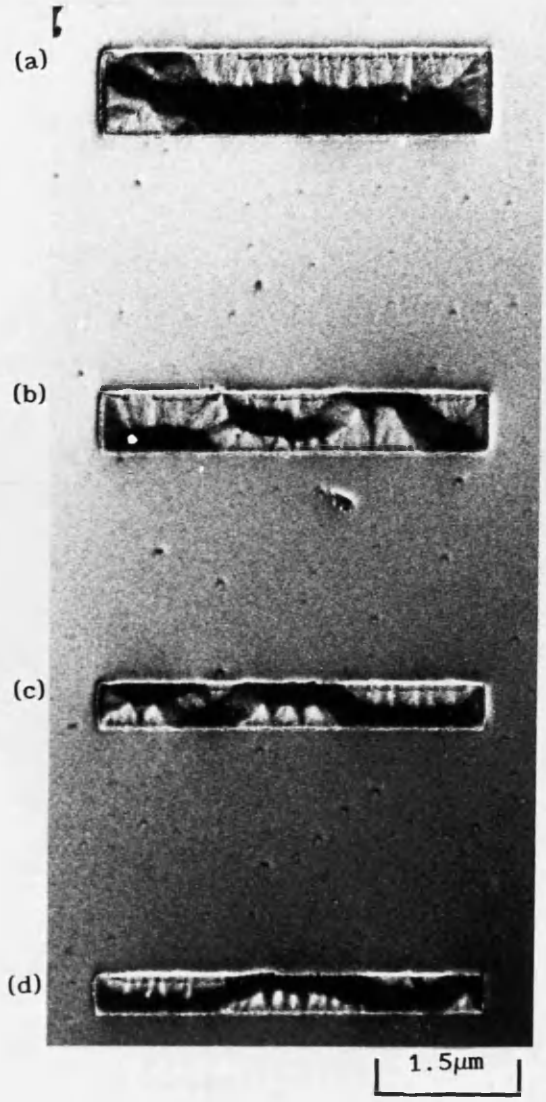

Fig. 6.1 Foucault image of the as-grown domain structure of 17nm thick cobalt particles.

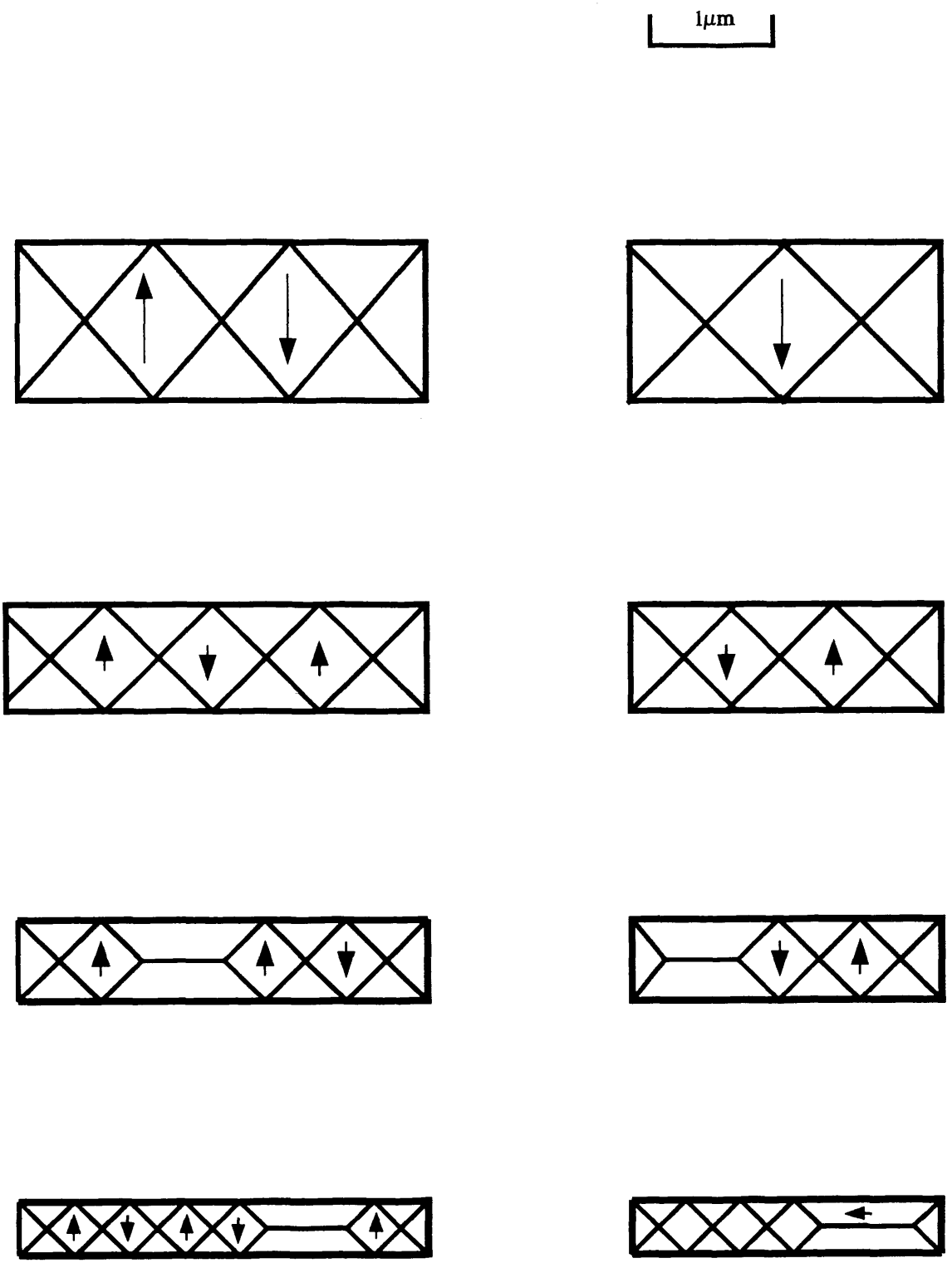

Fig. 6.2 Schematic diagram of the as-grown structures of various 17nm thick cobalt particles.

Fig. 6.3 Foucault image of a 17nm thick particle with a non-solenoidal structure.

deflection angles arise from the fact that saturation magnetisation of cobalt is approximately twice that of $Ni_{82.5}Fe_{17.5}$ and therefore the Lorentz deflection angles are scaled accordingly. Larger deflection angles result in an increased separation of those electrons deflected in opposite directions, and hence contrast variations are more pronounced in the Foucault mode due to the fact that the objective aperture "splits" the beam more effectively.

6.2.2 60nm THICK COBALT PARTICLES

A Foucault image of the as-grown domain structures of various 60nm thick particles is shown in fig. 6.4. It can immediately be seen that the domain structures of some of the larger particles are not as regular as those found in the 60nm thick $Ni_{82.5}Fe_{17.5}$ particles. In should be noted that as was found in the 17nm thick cobalt particles, as the dimensions of the particles decrease, the domain structures become more regular, and start to resemble those which would be predicted by the Van den Berg algorithm described in section 1.4.2. In 60nm thick cobalt particles the transition from solenoidal to non-solenoidal as-grown domain structures occurred when the value of R was approximately 12. In their as-grown states, the only 60nm thick Co particles to display non-solenoidal structures were the 4 by 0.38μm and the 4 by 0.25μm particles and it should be noted that they are oppositely magnetised. A table showing the least acicular 60nm thick cobalt particles which displays a non-solenoidal distribution is given in table 6.1.

6.2.3 95nm THICK PARTICLES

The as-grown domain structures of various 95nm thick cobalt particles are given in fig. 6.5. In a similar manner to the 60 and 17nm thick Co particles it can immediately be seen that the domain structures in some of the larger ($R<3$) particles are quite irregular. Many short lengths of domain walls were present yet all the particles appear to possess solenoidal structures as no

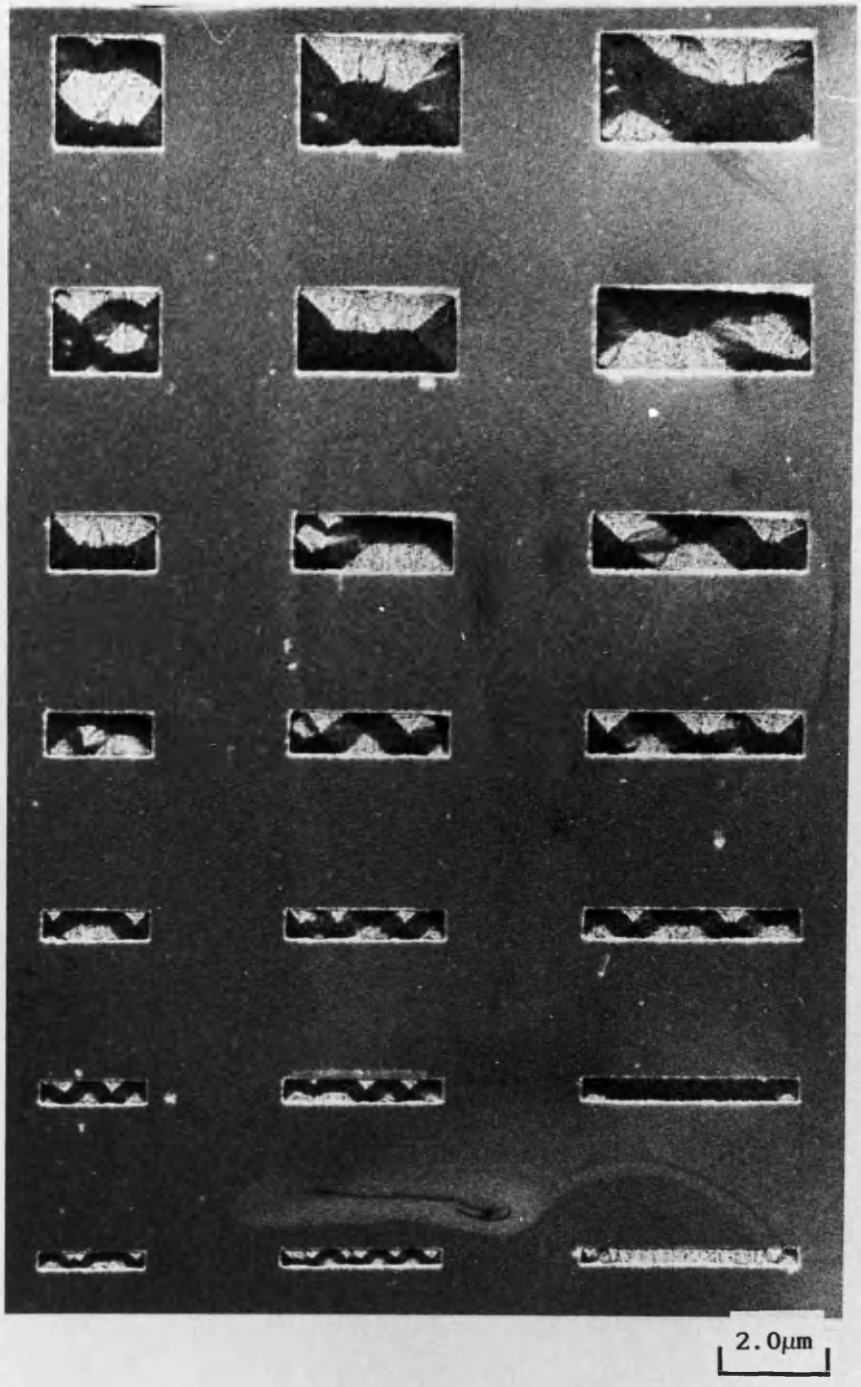

Fig. 6.4 Foucault image of the as-grown domain structure of various 60nm thick cobalt particles.

TABLE 6.1

First particles to display a Non-solenoidal structure.

17nm thick cobalt specimen

Length	4 μm	3μm	2μm
	Breadth		
As-grown	0.25μm	None	None
Easy (Demag)	0.38μm	None	None
Hard (Demag)	0.38μm	0.25μm	None

60nm thick cobalt specimen

Length	4 μm	3μm	2μm
	Breadth		
As-grown	0.38μm	None	None
Easy (Demag)	0.38μm	0.25μm	None
Hard (Demag)	0.38μm	0.25μm	None

95nm thick cobalt specimen

Length	4 μm	3μm	2μm
	Breadth		
As-grown	0.25μm	None	None
Easy (Demag)	None	None	None
Hard (Demag)	None	None	None

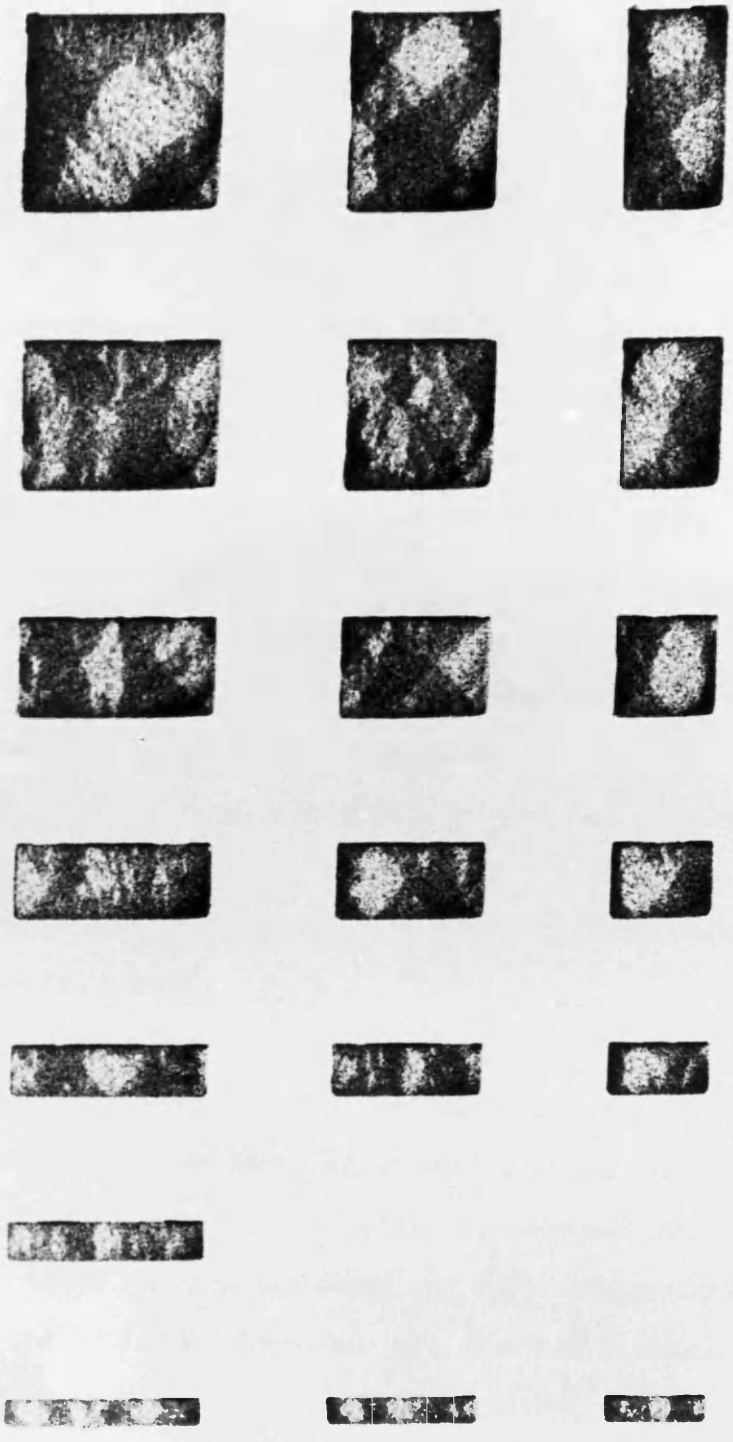

Fig. 6.5 Foucault image of the as-grown domain structure of various 95nm thick cobalt particles.

stray field was detected outside the particles. Again it is observed that as the aspect ratio increases, and the particle become smaller, the domain structures become more regular. The only 95nm thick cobalt particle to display a non-solenoidal as-grown domain structure was the 4.0 by 0.25μm particle.

6.2.4 SUMMARY

In general the cobalt particles exhibited certain characteristics which were similar to those of the $Ni_{82.5}Fe_{17.5}$ particles. However, it should be noted that some of the larger particles had quite irregular, although apparently solenoidal as-grown domain structures. As the particles become smaller (e.g. increasing R at constant length) it was observed that the shape anisotropy of the particles has a greater influence over the resultant domain structure. It should be noted that this results in the smaller particles decreasing the amount of domain wall energy towards a minimum value, and the "sub-domains", see section 6.3.1.1, are not found as commonly in these smaller particles.

6.3 THE EFFECTS OF A.C. DEMAGNETISATION AND SATURATING FIELDS ON Co PARTICLES.

The effects of an a.c. demagnetisation and also of a 960kA.m^{-1} field to the form of the remanent domain structure of the cobalt particles are described in this section. In sections 6.3.1 and 6.3.2, the remanent domain structures of 60nm thick cobalt particles following an a.c. demagnetisation directed along the easy and hard axes respectively are described in detail. The other thicknesses of cobalt particles are summarised briefly for conciseness. It should be pointed out that for the cobalt particles, the in-situ a.c demagnetisation performed along the hard direction examines only a small part of the hysteresis loop of the particle as it will not be close to saturation. The three thicknesses of particles were demagnetised again using the

experimental arrangement described in section 4.4. It should be noted that as with all the a.c. demagnetisations conducted in-situ, the field was aligned to $\pm 5^{\circ}$ with respect to either the hard or easy axes.

6.3.1 EASY AXIS A.C. DEMAGNETISATION

The a.c demagnetised states of a 60nm thick Co specimen is shown in the Foucault image of fig. 6.6(a) and schematically in fig. 6.6(b). The remanent domain structures from 17 and 95nm thick particles are shown in figs. 6.7 and 6.8. It can be seen that from fig. 6.6, the easy axis a.c. demagnetised domain structures of the larger ($R<3$) particles are now more regular than the as-grown states shown in fig 6.4. In particular, the larger particles, ($R < 3$), have considerably less domain wall energy and hence resemble the types of solenoidal domain structures found in the $Ni_{82.5}Fe_{17.5}$ particles. Also, as noted for the $Ni_{82.5}Fe_{17.5}$ particles after an easy axis a.c. demagnetisation, long sections of 180° walls are not commonly found. The length of 180° wall which is present is, in most cases, the minimum which can be accommodated by a particular aspect ratio of particle. Hence the experimental evidence would suggest;

$$2\sqrt{2}\ \sigma^{Co}_{90(i)} \leq \sigma^{Co}_{180(i)} \qquad i=17,60,\text{or } 95\text{nm} \qquad (6.1)$$

where $\sigma^{Co}_{j(i)}$ is the surface energy density of a domain wall in a polycrystalline h.c.p. cobalt sample of thickness i, across which the magnetisation rotates by j°.

6.3.1.1 SUB-DOMAINS

In many of the cobalt particles the domain structures appear irregular due to the presence of regions, "sub-domains", within domains which appear to be magnetised in a different direction from the rest of the "domain". A high

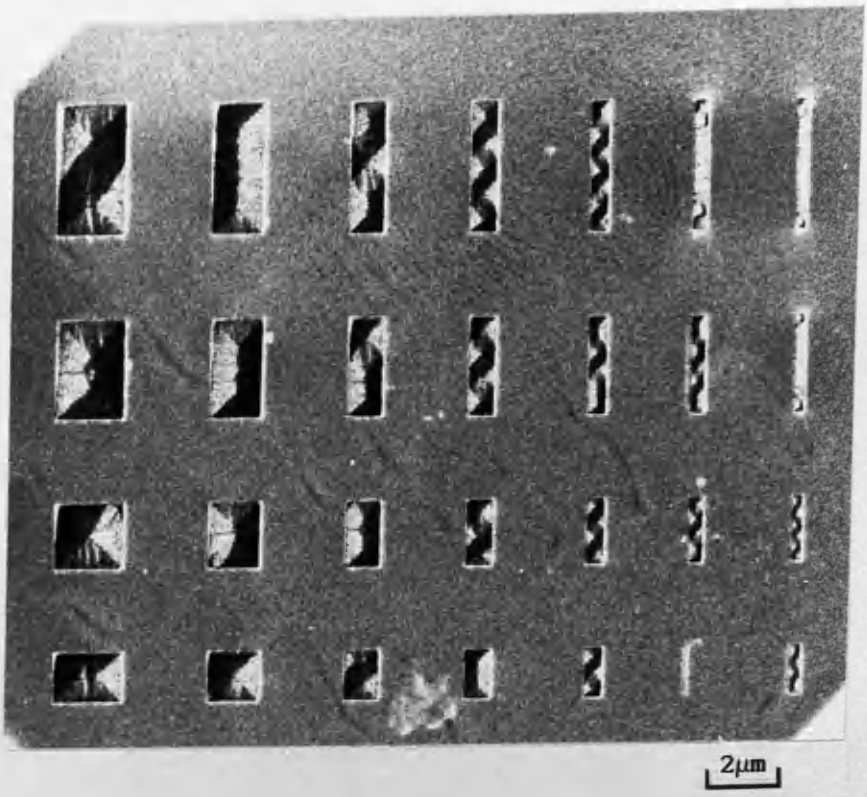

Fig. 6.6 (a) A Foucault image of the a.c. demagnetised domain structures in a 60nm cobalt sample.

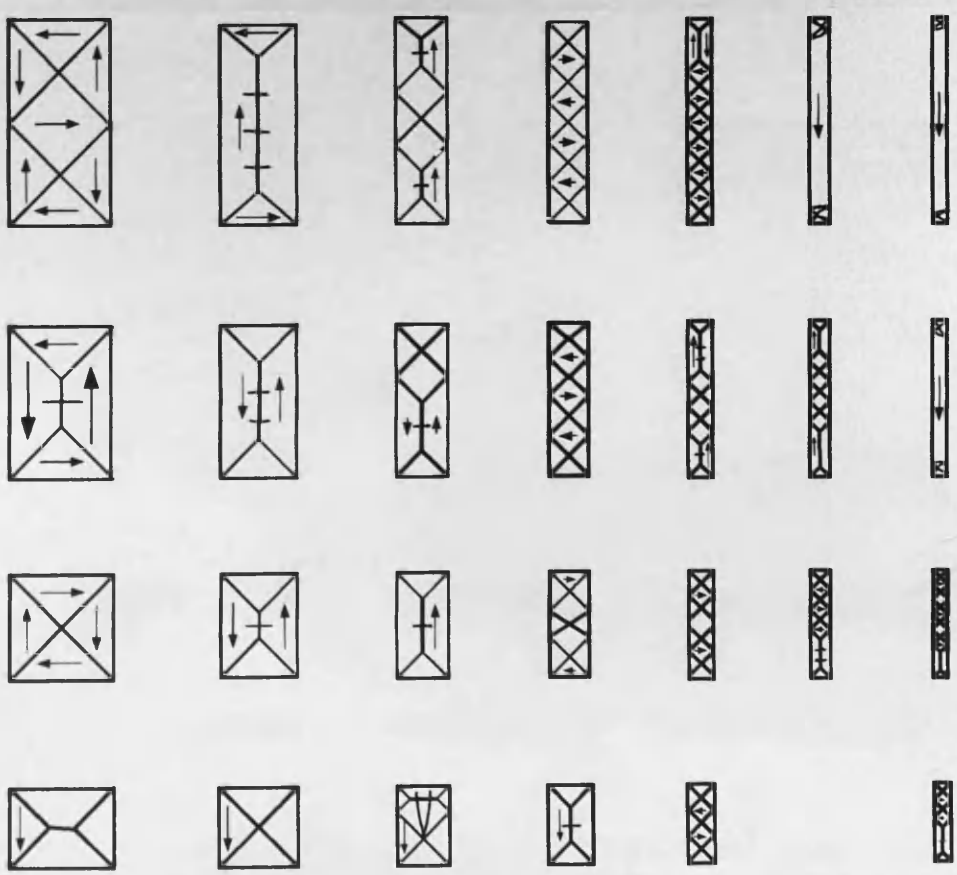

Fig. 6.6 (b) Schematic diagram of (a).

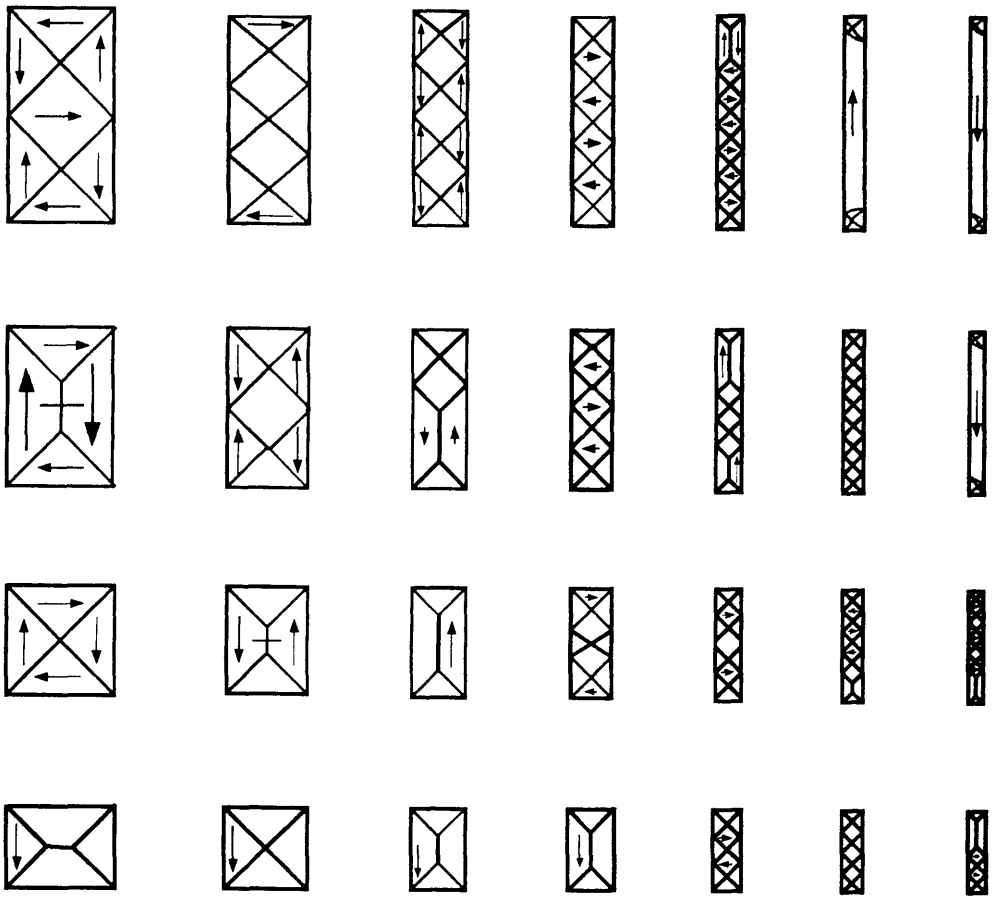

Fig. 6.7 Schematic diagram of the remanent easy axis a.c. demagnetised domain structures of a 17nm thick cobalt sample.

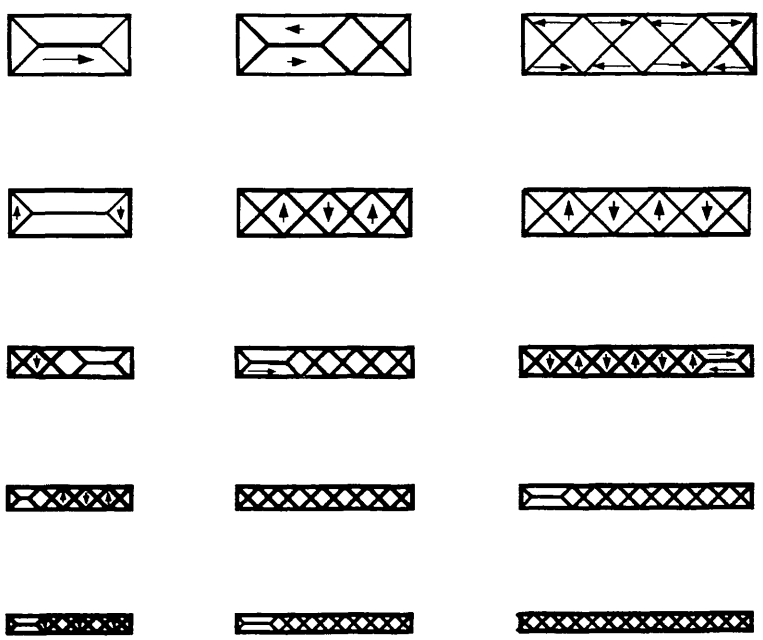

Fig. 6.8 Schematic diagram of the remanent easy axis a.c. demagnetised domain structures of a 95nm sample.

magnification Foucault image of a "sub-domain" is shown in fig. 6.9. From the intensity variations in the Foucault image, and also the Fresnel images taken of this region, the domain walls bounding these sub-domains appear quite diffuse, thus implying the presence of relatively low angle domain walls. Hence it would appear that the direction of the magnetisation within each sub-domain is quite close to the direction of the magnetisation in the "domain" itself. Detailed convergent beam diffraction studies and high magnification images taken in the vicinity of the sub-domains revealed no significant difference between the physical form of these regions and the rest of the particle. There are various possible reasons for the presence of the sub-domains and these are discussed in greater depth in section 6.6.

6.3.2 HARD AXIS A.C DEMAGNETISATION

The remanent domain structures of 95, 60 and 17nm thick cobalt particles following a hard axis a.c. demagnetisation are shown in fig. 6.10 to 6.12. The dimensions of the least acicular particles which display non-solenoidal domain structures are given in table 6.1 for various thicknesses of cobalt particles. In close agreement with the hard axis a.c. demagnetised domain structures of the $Ni_{82.5}Fe_{17.5}$ particles, long lengths of 180° walls were again found. The remanent domain structures of the cobalt particles are, however, significantly more irregular than those which were found when the field was directed along the easy axis. It was observed that the smaller ($R > 3$) particles had quite regular structures and Landau-Lifshitz structures are found regularly, e.g. figs. 6.10 to 6.12. That some of the structures are more irregular may be a consequence of the fact that during the in-situ a.c. demagnetisation, the maximum field which can be delivered to the specimen is only $64kA.m^{-1}$. This value of field is likely to be insufficient to fully eradicate the end closure structures of the cobalt particles. These end closure structures have a profound influence on the form of the resultant domain structures, and so the fact that they may be not fully eradicated will

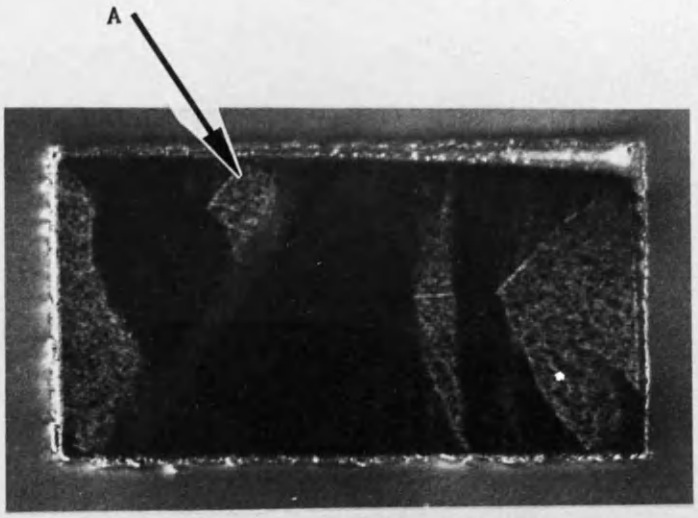

Fig. 6.9 A high magnification Foucault image of a "sub-domain", marked A.

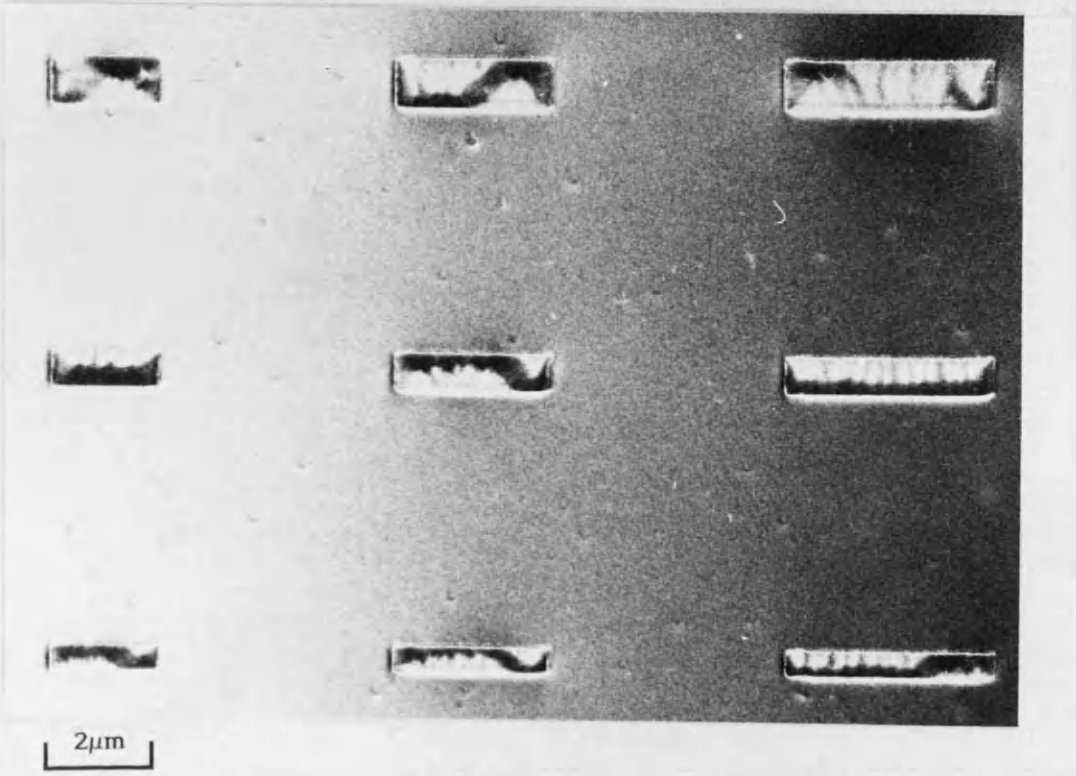

Fig. 6.10 The remanent domain structures of various 17nm thick cobalt particles after a hard axis a.c. demagnetisation.

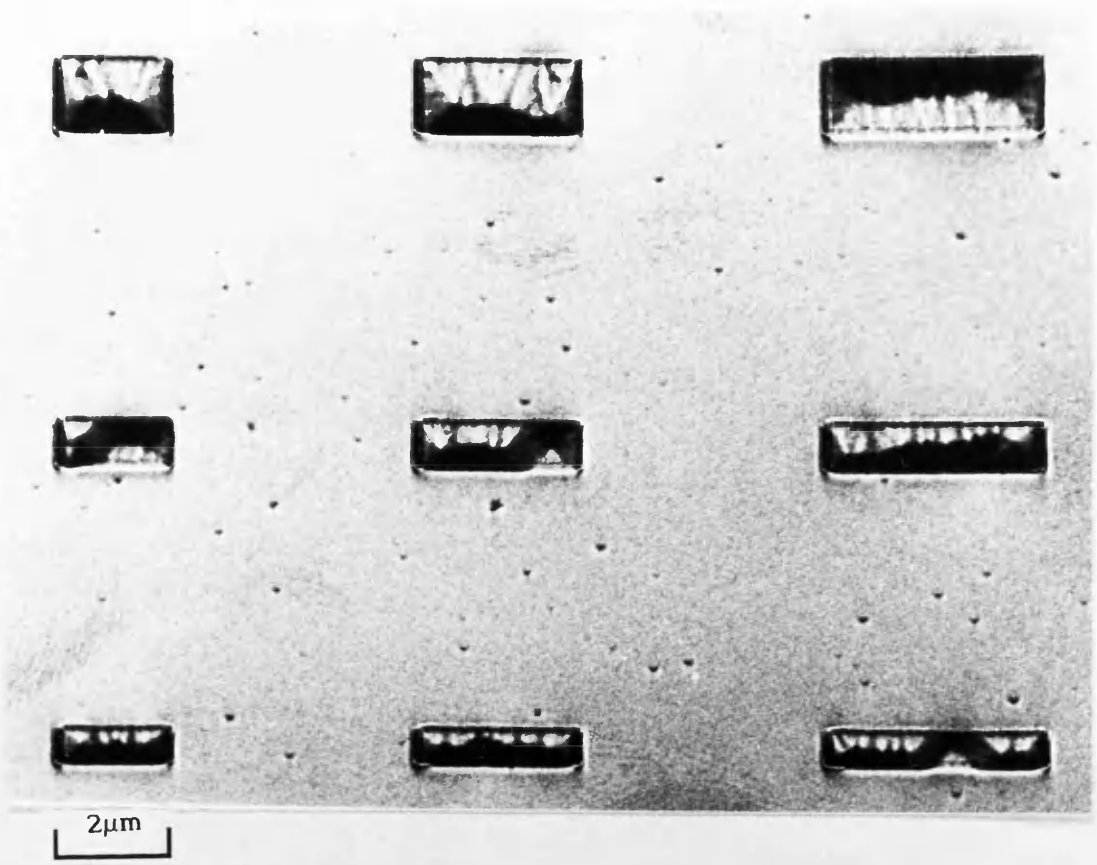

Fig. 6.11 The remanent domain structures of various 60nm thick cobalt particles after a hard axis a.c. demagnetisation.

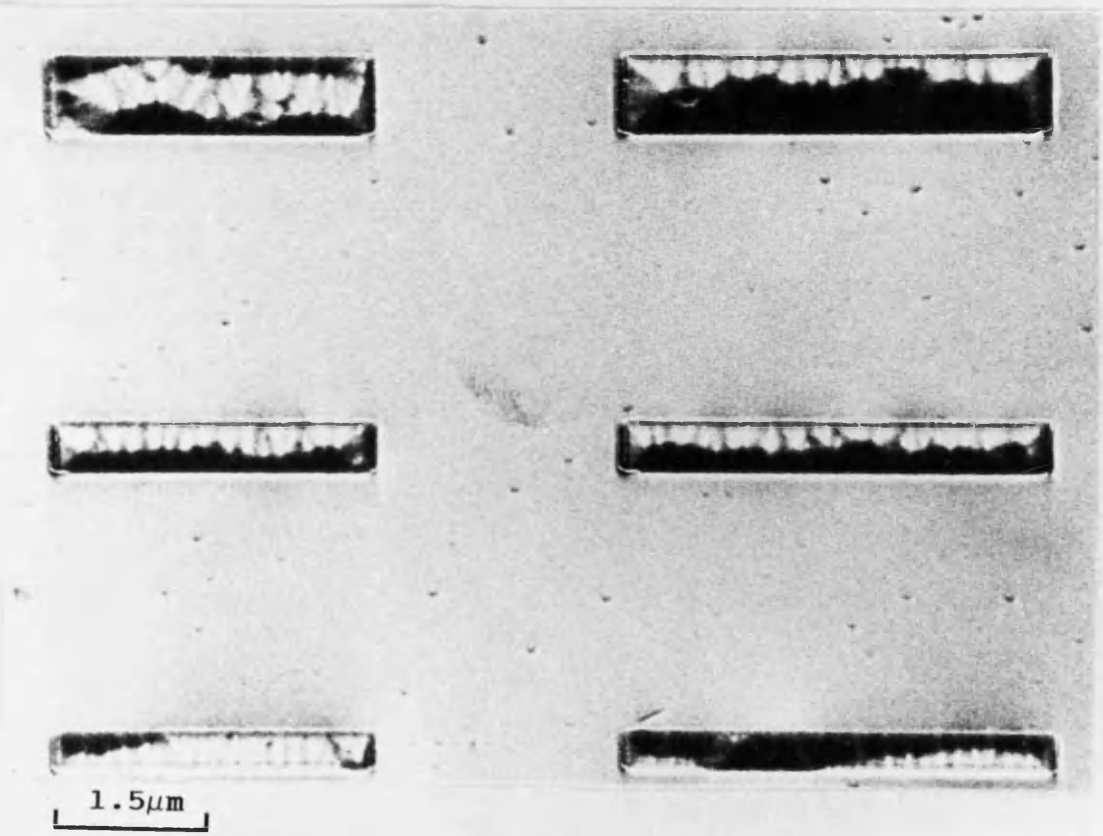

Fig. 6.12 The remanent domain structures of various 95nm thick cobalt particles after a hard axis a.c. demagnetisation.

then affect the form of the a.c. demagnetised domain structure.

6.3.3 SATURATING FIELDS

In a similar fashion to the $Ni_{82.5}Fe_{17.5}$ particles, the Co particles were also subjected to an external 960kA.m^{-1} field. The resultant remanent domain structures following the application of a 960kA.m^{-1} field along the easy axis were very similar to those following an easy axis a.c. demagnetisation. Non-solenoidal structures occurred more frequently when the field was directed along the easy rather than the hard axis, and the least acicular particle which had a remanent non-solenoidal structure is given in table 6.1. Again it was noted that more irregular domain structures occurred in larger (4μm and 3μm long, $R \leq 3$) cobalt particles.

Upon saturating the particles along the hard axis, the domain structures were almost identical to those found following a hard axis a.c. demagnetisation. The long lengths of 180° walls which were found in the case of the $Ni_{82.5}Fe_{17.5}$ particles were again found in the cobalt particles, although some of the larger ($R<3$) particles did display quite irregular domain structures.

As was found to be the case for the $Ni_{82.5}Fe_{17.5}$ particles, (section 5.4.2), the remanent domain structures of the more acicular particles depended critically on the exact direction of the "hard axis" demagnetising field. In the case of the 3 thicknesses of cobalt particles, the value of the least acicular particle to display a non-solenoidal domain structure is given in table 6.1, and the value which is quoted is that which was found most frequently.

6.4 DYNAMIC EXPERIMENTS ON Co PARTICLES

6.4.1 17nm THICK PARTICLES

The in-situ magnetising experiments on 17nm thick particles were conducted using fields which were directed along the easy axis of the particles and the results are described in this section. Using the procedure described in section 5.2, hysteresis loops from various 4μm long, 17nm thick cobalt particles were constructed, and these are shown in fig. 6.13. It can immediately be seen that the particles display types A and B hysteresis loops. The two more acicular particles with R=10.7 and 16.0, have type A loops and as such, neither particle can support a remanent solenoidal domain structure. The other hysteresis loops in fig. 6.13 are type B. In both of the particles having type B hysteresis loops the transitions from solenoidal to non-solenoidal domain structures took place in excess of $10kA.m^{-1}$. These transitions were produced using the pulsed mode of the magnetising stage, and it is for this reason that the hysteresis loops appear incomplete. The dashed lines on each of the loops in figs. 6.14 to 6.16 have been extrapolated from the solid lines which were determined experimentally. The dashed lines are present for clarity only. Also in figs. 6.14 to 6.16, the maximum field which can be applied to the specimen using the constant field mode of the magnetising stage is denoted by the double dashed line at $10kA.m^{-1}$.

Using the definitions of H_{S1}, H_{S2} and H_S given in section 5.4.3, it can be seen from fig. 6.13 that the variations of all three parameters with R follow the same trends that were exhibited by the $Ni_{82.5}Fe_{17.5}$ particles. It should be noted that when comparing two particles of the same size but fabricated from cobalt and $Ni_{82.5}Fe_{17.5}$, the value of $(^{d(RM)}/_{dH})$, (while the particle supports a solenoidal distribution), is less for the cobalt particle. Points such as this are discussed in greater depth in section 6.5. Values of H_{S1}, H_{S2}, H_S, squareness and hysteresis loop type for various sizes of 17nm thick

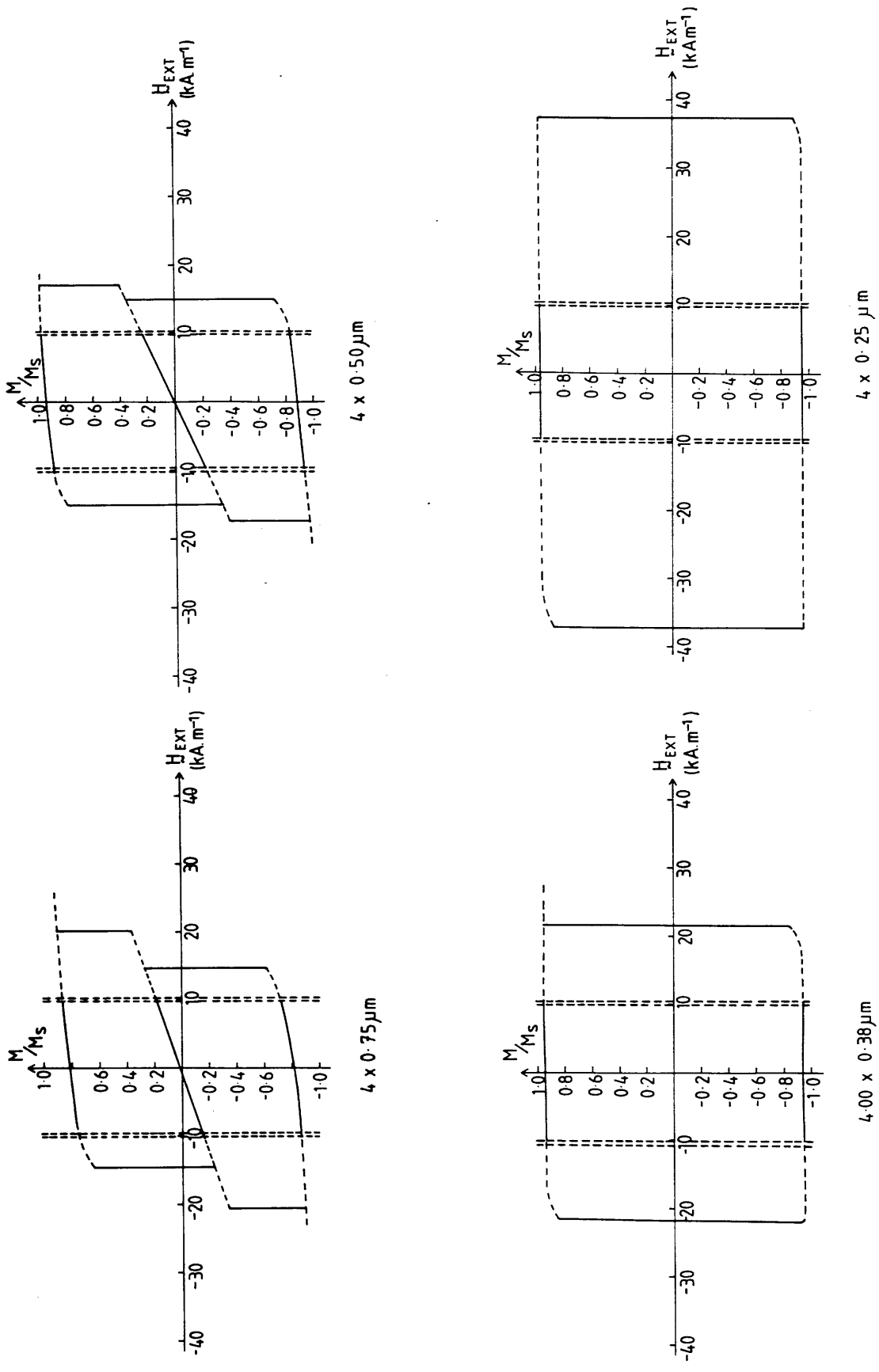

Fig. 6.13 Hysteresis loops from four 4µm long, 17nm thick cobalt particles.

cobalt particles are given in table 6.2.

6.4.2 60nm THICK PARTICLES

The dynamic behaviour of various 60nm thick Co particles was also examined using the in-situ magnetising stage. Hysteresis loops from five 4μm long particles of varying in-plane aspect ratio are given in fig. 6.14. It can immediately be seen that these five loops are quite different to those of the 60nm thick $Ni_{82.5}Fe_{17.5}$ particles shown in fig. 5.9. For the two particles with R=4 and R=5.3, the maximum constant field available using the magnetising stage, ($10kA.m^{-1}$), is insufficient to drive the domain walls into the side of the particle in order to form a non-solenoidal distribution. Hence as the domain walls move without any significantly large discontinuous jumps, the parts of the hysteresis loops examined have a shape as shown in fig. 6.14(a) and (b). It is likely that if the specimen could be observed under the influence of larger fields, that non-solenoidal states could be formed. As this was not possible, fields up to $64kA.m^{-1}$ were applied using the pulsed mode of the magnetising stage. No remanent non-solenoidal domain structures could be found for these two particles. It is probable that they have type C hysteresis loops, but that the values of both H_{s1} and H_{s2} are greater than $10kA.m^{-1}$. In fig 6.14 it can be seen that the three more acicular particles show type A and B hysteresis loops which are quite similar in shape to those shown by the $Ni_{82.5}Fe_{17.5}$ particles. A table showing values of squareness, switching field and hysteresis loop type for various 4, 3 and 2μm long 60nm thick cobalt particles are given in table 6.3.

6.4.3 95nm THICK PARTICLES

Hysteresis loops from various 4μm long 95nm thick cobalt particles are shown in fig. 6.15. These hysteresis loops have shapes which are similar to those of the 60nm and 17nm thick Co particles shown in figs. 6.13 and 6.14. It

Table 6.2: The magnetisation process in 17nm thick cobalt particles.

In-plane dimensions (μm)	R	Hysteresis loop type	Squareness	H_s ($kA.m^{-1}$)	H_{s1} ($kA.m^{-1}$)	H_{s2} ($kA.m^{-1}$)
4.00x0.75	5.3	B	0.80		20.0	-15.0
4.00x0.50	8.0	B	0.90		17.0	-16.0
4.00x0.38	10.7	A	0.92	22.0		
4.00x0.25	16.0	A	0.97	37.0		
3.00x0.75	4.0	B	0.65		20.0	-15.0
3.00x0.50	6.0	B	0.84		20.0	-17.0
3.00x0.38	8.0	A	0.90	21.0		
3.00x0.25	12.0	A	0.94	27.0		

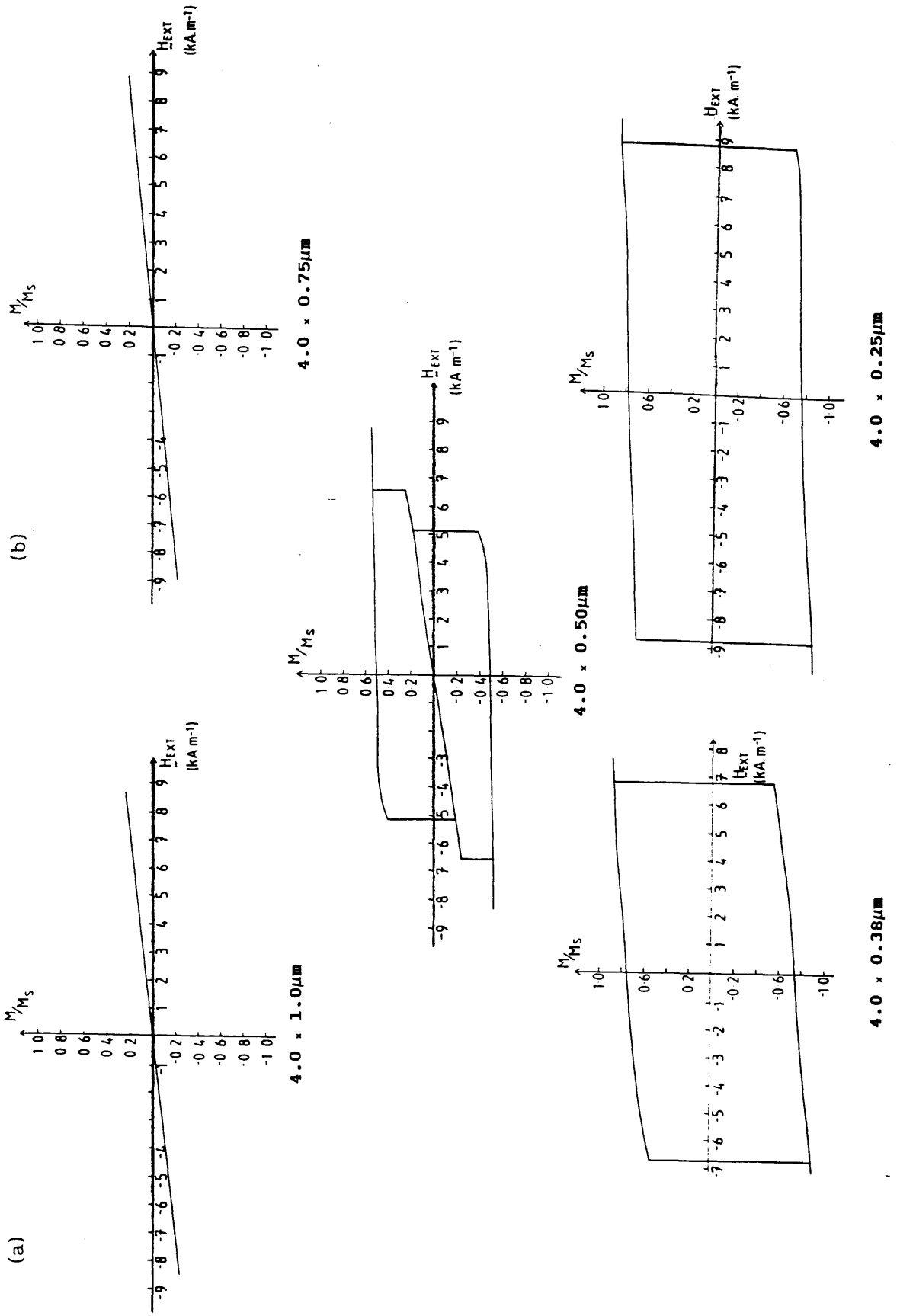

Fig. 6.14 Hysteresis loops from five 4µm long, 60nm thick cobalt particles.

Table 6.3: The magnetisation process in 60nm thick cobalt particles.

In-plane dimensions (μm)	R	Hysteresis loop type	Squareness	H_s ($kA.m^{-1}$)	H_{s1} ($kA.m^{-1}$)	H_{s2} ($kA.m^{-1}$)
4.00x1.00	4.0	(C)	----		>10.0	>10.0
4.00x0.75	5.3	(C)	----		>10.0	>10.0
4.00x0.50	8.0	B	0.52		6.5	-5.2
4.00x0.40	10.0	A	0.76	6.8		
4.00x0.25	16.0	A	0.78	8.8		
3.00x0.50	6.0	(C)	----		>10.0	>10.0
3.00x0.38	8.0	B	0.60		7.0	-4.0
3.00x0.25	12.0	A	0.76	7.8		
2.00x0.25	8.0	A	0.70	5.4		

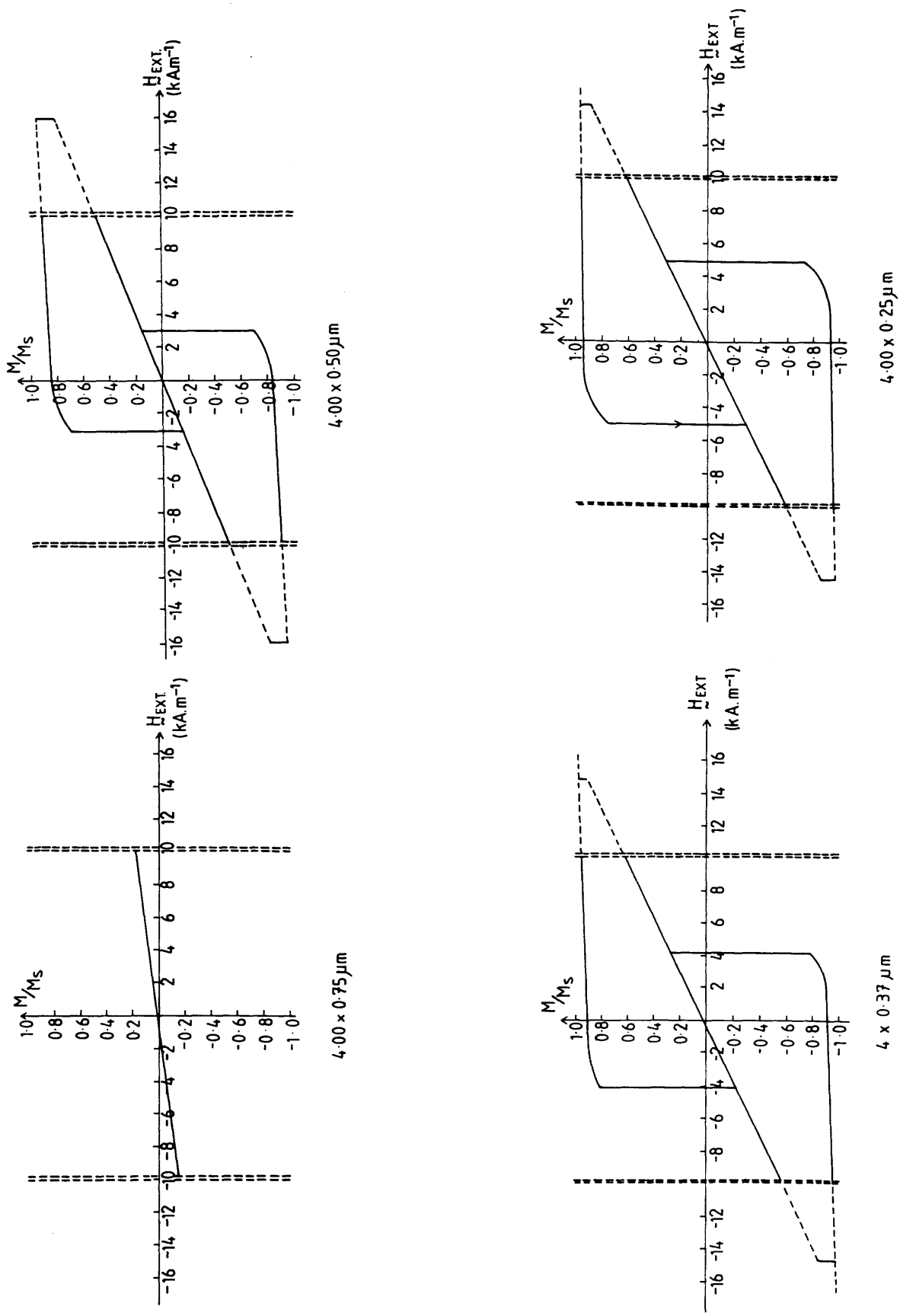

Fig. 6.15 Hysteresis loops from various 4µm long, 95nm thick cobalt particles.

should again be noted that the values of fields necessary to produce transitions from solenoidal to non-solenoidal states are greater than the maximum value available using the constant field mode of the magnetising stage. The large values of fields necessary to induce transitions from solenoidal to non-solenoidal states were again produced using the pulsed mode of the stage. (As mentioned in section 6.4.2, using the magnetising stage in this way precludes observing type C hysteresis loops, however as some of the particles have type B hysteresis loops, the remanent non-solenoidal structures could again be detected.)

In general the variation of hysteresis loop type, switching field and squareness with particle size follow the same trends exhibited by the $Ni_{82.5}Fe_{17.5}$ and other thicknesses of cobalt particles. A table showing the values of squareness, switching field and type of hysteresis loop for particles of this thickness is given in table 6.4.

6.5 SUMMARY

The types of solenoidal and non-solenoidal domain structures and hysteresis loops displayed by the cobalt particles were in some respects quite similar to those found in the $Ni_{82.5}Fe_{17.5}$ particles. Some of the similarities as well as differences between the domain structures of particles fabricated using the two materials are discussed below.

Upon analysing the variation of H_{S1}, H_{S2}, H_S, squareness and hysteresis loop type with R for cobalt particles presented in section 6.4, the same trends that were found in the $Ni_{82.5}Fe_{17.5}$ can be observed in the cobalt particles, and these effects may be explained in the same manner, (see section 5.3.4).

That the values of R^* for cobalt particles are larger than for the corresponding thickness of $Ni_{82.5}Fe_{17.5}$ particles may result firstly from the total energy of non-solenoidal distributions increasing due to the larger value of saturation magnetisation in cobalt, thus solenoidal distributions become more favoured even for the more acicular particles. Secondly as the

Table 6.4: The magnetisation process in 95nm thick cobalt particles.

In-plane dimensions (μm)	R	Hysteresis loop type	Squareness	H_s ($kA.m^{-1}$)	H_{s1} ($kA.m^{-1}$)	H_{s2} ($kA.m^{-1}$)
4.00x0.75	5.3	(C)	----		>10.0	>10.0
4.00x0.50	8.0	B	0.60		16.0	-2.8
4.00x0.40	10.0	A	0.76		15.0	-4.2
4.00x0.25	16.0	A	0.78		14.5	-5.0
3.00x0.50	6.0	B	0.70		20.0	-2.3
3.00x0.38	8.0	A	0.76		18.0	-2.5
3.00x0.25	12.0	A	0.82		16.0	-4.3

domain wall energy in polycrystalline h.c.p. cobalt is different from that of $Ni_{82.5}Fe_{17.5}$, (Kittel (1986)) the variation of domain wall energy with material must also be taken into account when considering the energetic stability of solenoidal or non-solenoidal domain structures.

It was noted in figs. 6.13 to 6.15 that the value of $(^{d(RM)}/_{dH})$ for the cobalt particles was less than for the same thickness of $Ni_{82.5}Fe_{17.5}$ particle. It is most likely that the local magnetocrystalline anisotropy axis within each of the grains makes the domain wall motion more difficult due to the presence of local magnetocrystalline anisotropy derived energy barriers. These barriers have to be overcome before the wall can move across a grain and hence $(^{d(RM)}/_{dH})$ is less in the case of the cobalt particles. It should also be noted that as the orientations of the c-axes (of the grains comprising the particles) are random, their effect on the shape anisotropy of the particle is nullified.

6.6 INVESTIGATIONS ON "ABNORMAL" Co PARTICLES

The cobalt particles described in sections 6.2 to 6.4 all displayed domain structures and dynamic behaviour which was quite similar to the $Ni_{82.5}Fe_{17.5}$ particles. However, certain cobalt samples displayed characteristics which were radically different from those described previously. The as-grown domain structures of an "abnormal" 60nm thick cobalt specimen is shown in fig. 6.16. As can clearly be seen from these images, the domain structures are not at all regular, nor do any of the structures resemble those found in the previous samples. Diffraction patterns and high magnification images obtained from these particles are shown in figs. 6.17 and 6.18 respectively. From these figures alone it would appear that there is no significant difference in the physical microstructure of particles which display "abnormal" domain structures from that of the "normal" cobalt particles. In particular no texturing was evident.

The particles described above were also subjected to a series of in-situ

Fig. 6.16 The as-grown domain structures of cobalt particles with "abnormal" domain structures.

Fig. 6.17 Selected area diffraction pattern pattern from a cobalt particle which had an "abnormal" domain structure.

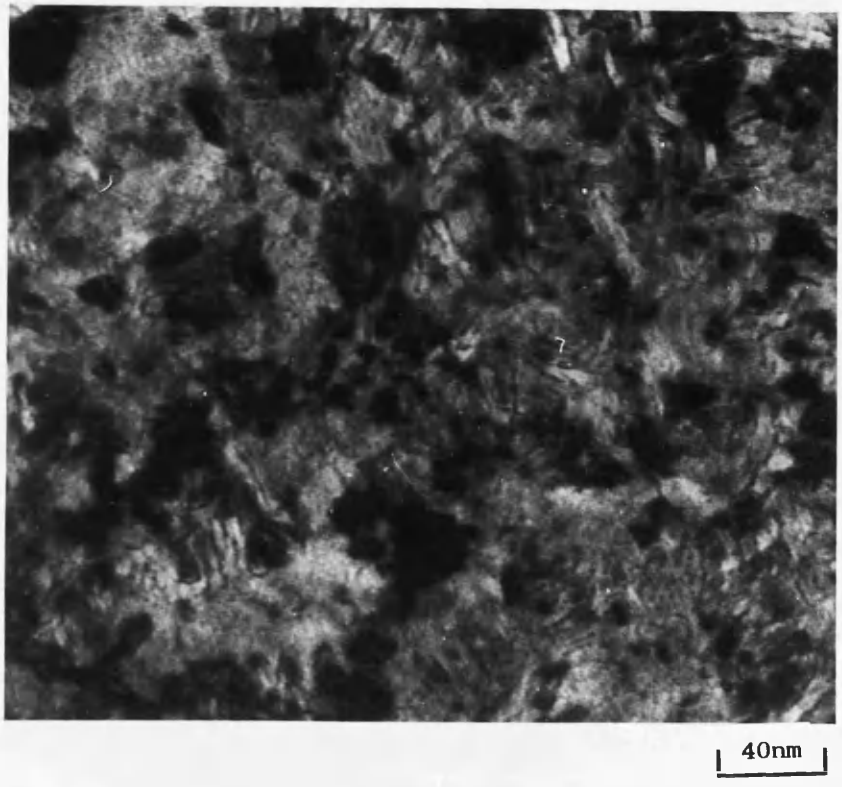

Fig. 6.18 High magnification image from a cobalt particle which had an "abnormal" domain structure.

magnetising experiments. During the course of the experiments, conducted using the magnetising stage, no observable differences could be detected in the domain structures of any of the particles. At the maximum steady field which could be applied to the specimen, the domain structures of all the particles were almost identical to the as-grown states. Using the in-situ magnetising stage it was not possible to switch any of the particles, nor could any of the domain walls be moved over large parts of the particle.

Upon subjecting the particles to a 960kA.m^{-1} field applied external to the microscope, again it was found that the remanent domain structures were almost identical to those found in the as-grown state.

In addition to the cobalt particles described above as "abnormal", it was also found that some cobalt samples displayed domain structures and dynamic behaviour which was almost "hybrid" between the "abnormal" and the "normal" cobalt specimens described above and in sections 6.3 respectively. One example of is shown in fig. 6.19, which shows a 60nm thick Co sample. It can be seen from this figure that the domain structures, although more regular than those of fig. 6.16, are not as regular as would be predicted by the Van den Berg algorithm. Dynamic experiments performed on these particles showed that the domain walls could be moved, and that the particles could be switched, however comparing two such "hybrid" samples showed that the range of switching fields for a particular size of particle could vary greatly.

It would appear that from the series of experiments conducted on different cobalt samples, the dynamic behaviour and domain structures are not as regular, nor easily predicted, as those found in the $Ni_{82.5}Fe_{17.5}$ particles.

All of the cobalt samples of widely varying properties were made on Si/Si_3N_4 substrates which were fabricated and spun with resist at the same time. Hence it would appear unlikely that any abnormality in the Si, Si_3N_4 or resist would affect the magnetic properties of the particles in such a dramatic manner. A more likely explanation is that during the evaporation process, residual gases in the evaporator are affecting the chemical composition of the particles, or the crystallites making up the particles.

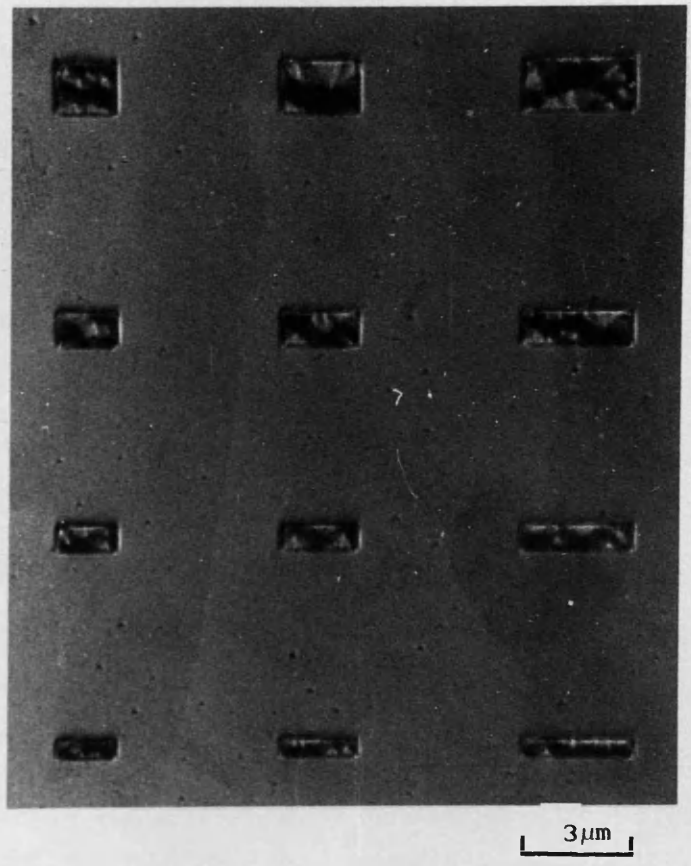

Fig. 6.19 A Foucault image of a 60nm thick cobalt sample whose as-grown domain structure could be described as a hybrid between "normal" and "abnormal".

There are two ways in which this could occur. Firstly and inadvertently, the rate of evaporation may become slower at the same pressure, or alternatively, the vacuum may, again inadvertently, deteriorate with the evaporation rate remaining at its normal value. In both cases, the ratio of the number of residual gas atoms to evaporated metal atoms will increase. One effect this could cause is to form a thin oxide layer on the surface of the crystallites, or alternatively the residual gases could become incorporated into the crystallites, resulting in some abnormal metal-oxide alloy. Alternatively the various other gases present in the system (e.g. N_2 or hydrocarbon chains from the diffusion pump oil) could either form a compound with the cobalt or simply stick to the surface of the evaporated film. In all cases the presence of a layer, which is not cobalt, on or near the surface of the crystallites would affect the exchange coupling between adjacent crystallites. This has the effect of decreasing the coupling length within each of the particles. In such cases the shape anisotropy does not affect the domain structure of the particles, as each crystallite may now have magnetic charge at its boundaries. In the case of a polycrystalline film, where the grains are normally exchange coupled, the coupling length is generally quite large and so the entire film acts more like a continuous film, and hence any shape anisotropy present would have a large influence over the resultant domain structure. That the coupling length in "abnormal" cobalt particles is decreased with respect to the normal cobalt particles could also account for the fact that the properties of the cobalt particles vary dramatically. The ratio of residual gas atoms in the evaporator to evaporated metal atoms hitting the substrate surface is a function of both the pressure and the evaporation rate. Hence if different quantities of gases were trapped between, or causing surface oxidation of, the crystallites, the magnetic properties would vary according to the final resultant coupling length. During the course of this project, evaporations were always performed at supposedly "standard" conditions. Of the two possible sources of error which may have been introduced, the more likely is

that the vacuum pressure increased (i.e. deteriorated) and this resulted in the coupling length of the particles decreasing, thus altering the magnetic properties of the particles. More detailed experiments would require to be conducted to confirm or deny this hypothesis, and these will be discussed in greater depth in chapter 8. If the crystallites are indeed not exchange coupled, and magnetic charge is present at some of the grain boundaries, then the volume magnetic charge within the particle is not equal to zero. In this case, the Van den Berg algorithm cannot be used to predict the solenoidal domain structures of the particles.

It should also be noted from fig. 6.16 that the contrast in the Foucault image is significantly less than for the more "normal" cobalt samples. The lack of contrast arises from smaller Lorentz deflection angles. If some of the grains within such "abnormal" specimens are not exchange coupled then magnetic charge could be present at the grain boundaries. In this case, were this to produce an magnetic field above and below the particle, in a direction which opposes the direction of induction in the grain itself, the Lorentz deflection angle would be decreased, so leading to a reduction in the contrast in the final image.

It was noted that the domain structures of some of the particles appear abnormal due to the presence of "sub-domains". These regions arise due to local exchange coupling and magnetocrystalline anisotropy effects which result in the direction of magnetisation within these isolated regions being in a different direction from the rest of the domain.

CHAPTER 7

MICROSCOPIC PROPERTIES OF Si-DOPED GaAs QUANTUM WIRES FABRICATED BY ELECTRON BEAM LITHOGRAPHY.

7.1 INTRODUCTION

In chapters 4, 5 and 6 of this thesis it has been shown that techniques available in electron microscopy can be used both to fabricate and investigate small structures whose dimensions are in the (sub)-micron range. The electron beam lithography process, described in section 3.3, and which was used to manufacture the small magnetic particles, can also be adapted to fabricate other devices and structures with small dimensions. One common use of electron beam lithography is in the manufacture "quantum wires", (Kelly (1986), Adams (1990)). These are small structures which have a precisely defined shape, and also have interesting and novel electrical and optical properties. The process by which such well defined wires are fabricated involves the use of both electron beam lithography and reactive ion etching. During this latter process the sample is bombarded with ions of energies in the range 100 to 1000eV, and this can cause deterioration of both the electrical and optical properties of the semiconductor. Damage caused in this way is often referred to as "dry etch damage".

Investigation of dry etch damage is frequently by indirect means, e.g. comparison of Schottky junctions formed on etched and unetched surfaces, (Cheung (1987) and (1988)), or Raman scattering (Watt (1988)). Although these methods do give some information regarding the extent to which dry etching causes damage, no information is obtained on the microscopic extent or form of the damage. A much improved situation would involve direct imaging of the damaged regions in such devices.

This chapter outlines a method using transmission electron microscopy, which enables the damaged regions in quantum wires to be characterised more completely. Section 7.2 describes the TEM imaging mode which can reveal the damaged regions of the wires. Section 7.3 discusses the fabrication process of quantum wires, with particular emphasis being placed on the slight modifications which must be introduced in order that the wires can be analysed in the transmission electron microscope. Results from the analysis of the wires are then given in section 7.4.

7.2 IMAGING CONDITIONS - STRUCTURE FACTOR CONTRAST

It was stated above that various methods (e.g. Cheung (1987), (1988)) which had previously attempted to describe the extent of dry etch damage suffered from the fact that the analysis was by indirect methods. Using techniques with high spatial resolution available in the transmission electron microscope, it is possible to interpret the contrast variation within certain types of images as having arisen from damaged regions within the quantum wire itself. Direct investigation of the damage in the wires is then possible. The following section describes a contrast mechanism which can reveal the damaged regions in the wires.

A parallel beam of electrons incident on the specimen is diffracted through various different Bragg angles (θ_B), as shown schematically in fig. 7.1. Using the description first given by Bragg, (see e.g. Kittel (1986)) the "Bragg" angle (θ_B) is defined as

$$2\, d_{hkl} \sin (\theta_B) = n \lambda \qquad (7.1)$$

where d_{hkl} is the plane spacing between successive (hkl) planes; h, k and l are the Miller indices and λ is the wavelength of the incident beam of electrons.

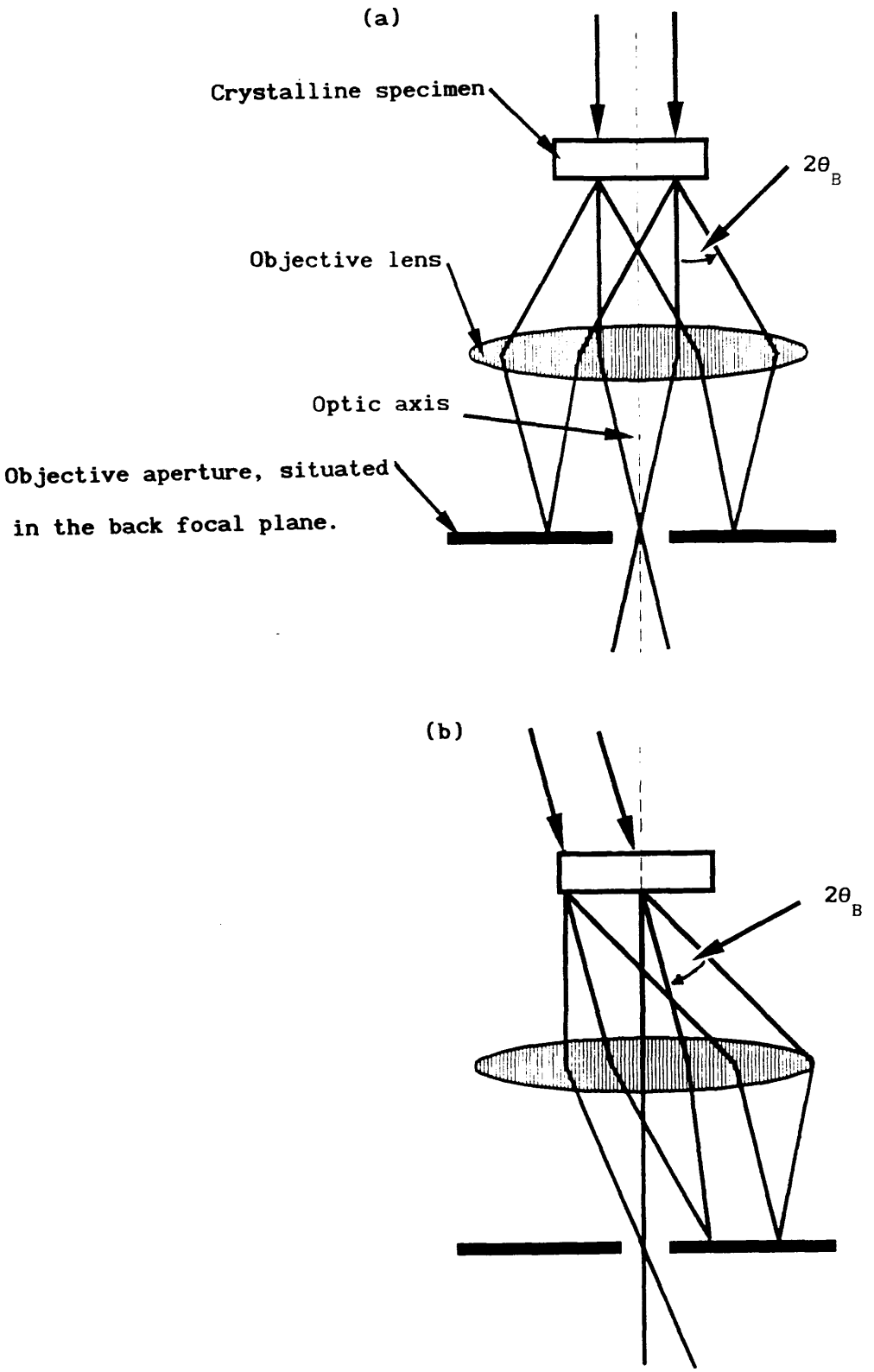

Fig. 7.1 Diagram showing the effect of the objective lens in bringing the diffracted beam to a focus (a) off-axis and (b) on the optic axis. In both cases the beam is brought to a focus in the diffraction plane.

From fig. 7.1(a), and in a similar manner to the process which occurs in the Foucault mode, (section 2.2.3) parallel incident illumination ensures that the transmitted beam is brought to a focus in the diffraction, or back focal, plane of the objective lens. Those parts of the incident beam which pass undeviated through the specimen are brought to a focus on the optic axis of the microscope, and those which are diffracted through some angle θ_B, are brought to a focus at some position off the optic axis. In order to calculate the intensity contained in each of the diffraction spots it is necessary to perform a much more detailed examination of the diffraction process. The scattering process itself arises due to the Coulombic interaction between the incident electrons, the charged nucleus and the orbiting electrons of the atom. It can be shown (Cowley (1975)) that the scattered wave is in the form of a spherical wave whose amplitude is proportional to the Fourier transform of the electrostatic lattice potential. The amplitude of the scattered wave is given by a "structure factor", $f(\theta)$, given by;

$$f(\theta) = \frac{2\pi me}{h^2} \int_{(\text{unit cell})} V(\underline{r}_i) \exp(-i \underline{K}_i \cdot \underline{r}_i) \, d\tau_i \qquad (7.2)$$

where $\underline{r}_i$ are the positions of the atoms in the unit cell; $V(\underline{r}_i)$ is the electrostatic potential at a point $\underline{r}_i$; $d\tau_i$ is an element of volume in the unit cell and $\underline{K}$ is the difference in wavevector between the incident and scattered waves. That the value of $f(\theta)$ relies on $V(\underline{r})$ means that atoms with similar distributions of potential will have similar values of $f(\theta)$, and this may occur if for example, the atomic numbers of two species are similar. Values of $f(\theta)$ for elements used in this thesis are given in table 7.1. It can be shown that eqn. 7.2 is a maximum when $\underline{K}_i$ coincides with a reciprocal lattice vector. Hence for strong scattering conditions;

$$\underline{K} = A_1 \cdot \underline{b}_1 + A_2 \cdot \underline{b}_2 + A_3 \cdot \underline{b}_3$$

where $\underline{b}_i$ are the reciprocal lattice vectors, and also

Table 7.1 List of the relativistically corrected atomic scattering factors f_a of several elements for 100keV electrons scattered through an angle 2θ of approx. 12mrad

Element	$f(2\theta)_a$ (Å)
Al	3.741
Ga	5.365
As	5.970

Table 7.1(b) Numerical values of the structure factor $F_{(002)}$ for materials relevant to this thesis.

Material	$F_{(002)}$ (Å)
GaAs	2.42
$Al_{0.7}Ga_{0.3}As$	4.37

$$\underline{r} = B_1 \cdot \underline{a}_1 + C_1 \cdot \underline{a}_2 + D_1 \cdot \underline{a}_3$$

where $\underline{a}_1$ are the lattice vectors in real space. It should be noted that by definition;

$$\underline{a}_i \cdot \underline{b}_i = \delta_{ij}$$

It can be shown that the scattering from an assembly of unit cells is given by the sum of each of the structure factors of each unit cell multiplied by the appropriate phase factor. For strong diffraction from an array of unit cells, the structure factor is given by $F(\theta)$, where

$$F(\theta) = \sum_i f_i(\theta) \exp\left(-2\pi i \left(A_1 B_i + A_2 C_i + A_3 D_i \right)\right) \qquad (7.3)$$

It is assumed throughout that the incident beam only suffers one, if any, scattering event, and also that the energy transferred to the beam during a scattering event is negligible. This is known as the Kinematic approximation, and is valid for the imaging mode used to examine the thin (≈70nm) quantum wire specimens.

From fig. 7.1(a) it can be seen that by carefully positioning an aperture, situated in the diffraction plane, only certain diffracted beams are allowed to be transmitted through the aperture in order to form the final image. Placing the aperture around e.g. the (002) spot would allow only those electrons which had been diffracted from (002) planes to form the final image. This type of image is called an (002) dark field image. In normal practice, rather than placing the aperture off-axis, as would be the case for fig. 7.1(a), the incident beam is tilted prior to the specimen in such a way that the (002) diffracted beam travels down the optic axis, as shown in fig. 7.1(b). Dark field images formed in this way tend to be significantly less astigmatic than those formed by shifting the aperture off-axis. Dark field TEM images reveal contrast which is related to the structure factor F_{hkl} of the material through which the beam has passed.

GaAs has a face centred cubic structure with a basis of 2 atoms (one Ga and one As) at each lattice point. The fractional co-ordinates of the atoms within a unit cell of GaAs are (0,0,0), $(0, \frac{1}{2}, \frac{1}{2})$, $(\frac{1}{2}, 0, \frac{1}{2})$ and $(\frac{1}{2}, \frac{1}{2}, 0)$ for Ga and $(\frac{1}{4}, \frac{1}{4}, \frac{1}{4})$, $(\frac{3}{4}, \frac{3}{4}, \frac{1}{4})$, $(\frac{1}{4}, \frac{3}{4}, \frac{1}{4})$ and $(\frac{3}{4}, \frac{1}{4}, \frac{3}{4})$ for As. From eqn. 7.3, the structure factor $F_{002}(GaAs)$ from a unit cell of GaAs is given by;

$$F_{002}(GaAs) = 4 \left(f_{002/Ga} - f_{002/As} \right) \qquad (7.4)$$

where $f_{002/Ga}$ and $f_{002/As}$ are the scattering factors of Ga and As at the Bragg angle appropriate to (002) planes. As the atomic numbers of Ga and As are similar, $f_{002/Ga}$ and $f_{002/As}$ are similar, (see table 7.1, (Doyle and Turner (1967))), and hence $F_{002}(GaAs)$ is very small. The intensity in an (002) dark field image from GaAs is given by;

$$I_{002}(GaAs) \alpha \; F_{002} F^{*}_{002} \qquad (7.5)$$

where F_{002} and F^{*}_{002} denote the (002) structure factor and complex conjugate of the (002) structure factor of GaAs respectively. From eqn. 7.4 an (002) dark field image from a perfect GaAs crystal should be very low in intensity. The situation does change, if for example there is a deviation away from stoichiometry which changes the structure factor, $F_{002}(GaAs)$, of the crystal. The effect this has on the final image intensity will be made clearer by examining the example of a GaAs/$Al_{0.3}Ga_{0.7}As$ multiple quantum well system.

Eqn. 7.4 can be expressed in more general terms as;

$$F_{002} = 4 [p_1 S_V - p_2 S_{III}] \qquad (7.6)$$

where p_1 and p_2 are the probabilities that the group five and group three

sites within a unit cell of GaAs are occupied. In pure GaAs, with no defects $p_1 = p_2 = 1$. S_V and S_{III} are the (002) structure factors of the atoms occupying the group five and group three sites in the GaAs unit cell. In the case of a perfect GaAs crystal S_V and S_{III} are given by $f_{002/As}$ and $f_{002/Ga}$ respectively, while in the case of a perfect $Al_xGa_{(1-x)}As$ cell, S_V and S_{III} are given by

$$S_V = f_{002/As}$$

$$S_{III} = x\, f_{002/Al} + (1-x)\, f_{002/Ga}$$

Hence in a perfect $Al_xGa_{(1-x)}As$ crystal ($p_1 = p_2 = 1$), the (002) structure factor is given by;

$$F_{002} = 4 \{ x\, f_{002/Al} + (1-x)\, f_{002/Ga} - f_{002/As} \} \qquad (7.7)$$

As the value of $\frac{dF_{002}}{dx} \neq 0$, variations in x will therefore lead to intensity changes in the final image. An (002) dark field image of a molecular beam epitaxially (MBE) grown GaAs/ $Al_{0.3}Ga_{0.7}As$ system fabricated at the University of Glasgow is shown in fig. 7.2. In this image the bright layers are $Al_{0.3}Ga_{0.7}As$, (x = 0.3) and the dark layers are GaAs, (x = 0).

The quality and size of GaAs/$Al_{0.3}Ga_{0.7}As$ quantum wells have been examined extensively using this structure factor contrast technique (McGibbon (1989)).

In contrast to the quantum wires to be studied, the multiple quantum well system is easier to qualitatively analyse, and hence familiarisation with the techniques of (002) dark field imaging was achieved using this material. (The cross-sectional specimen preparation technique for analysing the GaAs/$Al_{0.3}Ga_{0.7}As$ quantum well structures in the TEM is well documented (Chew and Cullis (1987).) The main point to note is that from eqns. 7.6, the image intensity in an (002) dark field image of GaAs is low, and any variations in

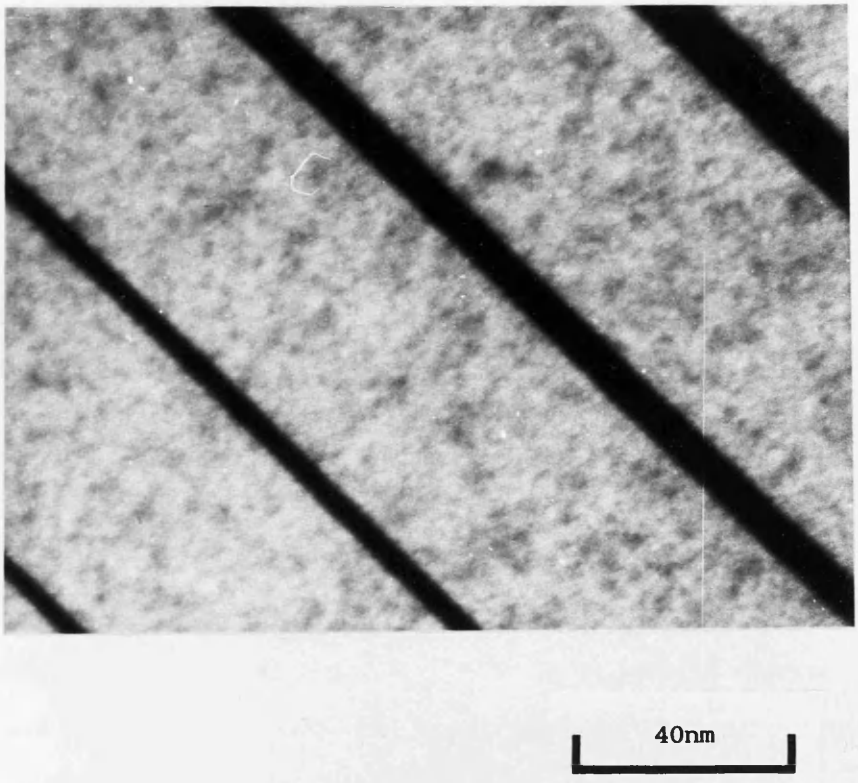

Fig. 7.2 (002) dark field image of a GaAs/ $Al_{0.3}Ga_{0.7}As$ multiple quantum well system.

the composition of the crystal, which result in a change in the value of the structure factor F_{002}(GaAs), will lead to changes in intensity in the final dark field image.

7.3 SPECIMEN PREPARATION - QUANTUM WIRES

Quantum wires are made using a series of lithographic and dry and wet etching steps; various parts of the fabrication process bear a strong similarity to those described in section 3.3. Wires suitable for analysis using TEM were fabricated using the technique shown in figs. 7.3 and 7.4.

In a similar manner to the process of section 3.3.2, two layers of electron beam sensitive resist with high and low molecular weights, (4% BDH in xylene and 4% Elvacite in chlorobenzene) were spun onto a thick, (0.5mm) Si-doped (2.0×10^{17} cm^{-3}) GaAs substrate, fig. 7.3(a). A suitable pattern was then exposed, again using the Philips PSEM 500, and the resist was developed as described in section 3.3.4. The two layer system comprising high and low molecular weights again results in an undercut profile, as shown in fig. 7.3(b). A 50nm thick Ti layer is then thermally evaporated, under vacuum, over the entire sample, fig. 7.3(c). (The reason for using Ti will be discussed below.) The metal which is in contact with the resist is removed along with the resist by placing the sample in a suitable solvent. Only the metal which is in contact with the GaAs substrate remains. The sample is then dry etched in either $SiCl_4$ or a 1:5 mixture of CH_4/ H_2 in order to etch away the GaAs substrate, so leaving the wires standing as shown in fig. 7.3(d). A plan view of the wire and the supporting structures is shown in fig. 7.3(e).

It was during this last stage that the use of Ti as a metal mask was very important. When used as a mask for dry etching of GaAs, Ti has a selectivity of 1:10, i.e. for each micron of Ti etched away, 10μm are etched of GaAs. The dry etching process is a highly anisotropic process, being dependent on

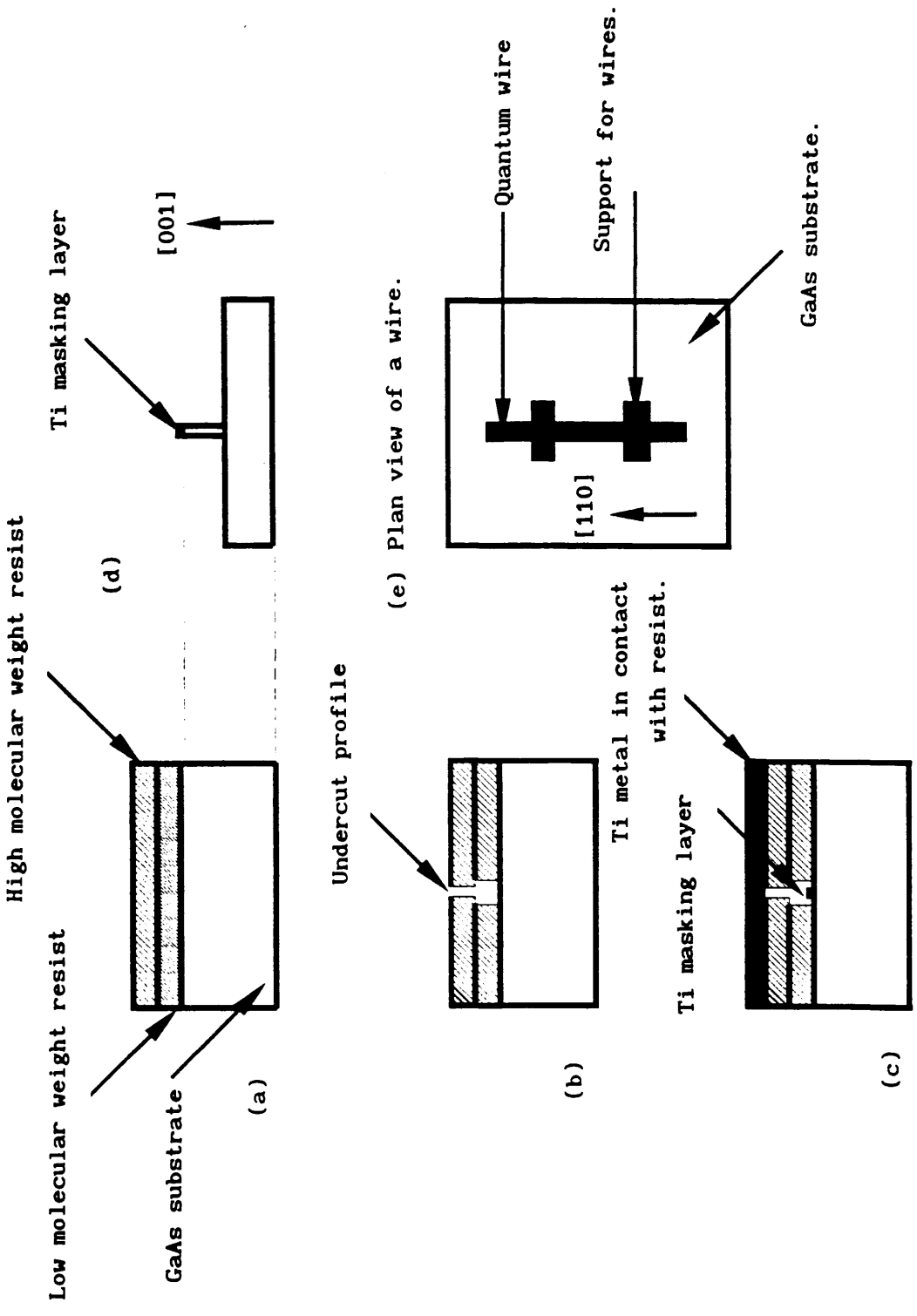

Fig. 7.3 Schematic diagram showing the first stages of the specimen preparation technique used to fabricate the quantum wires.

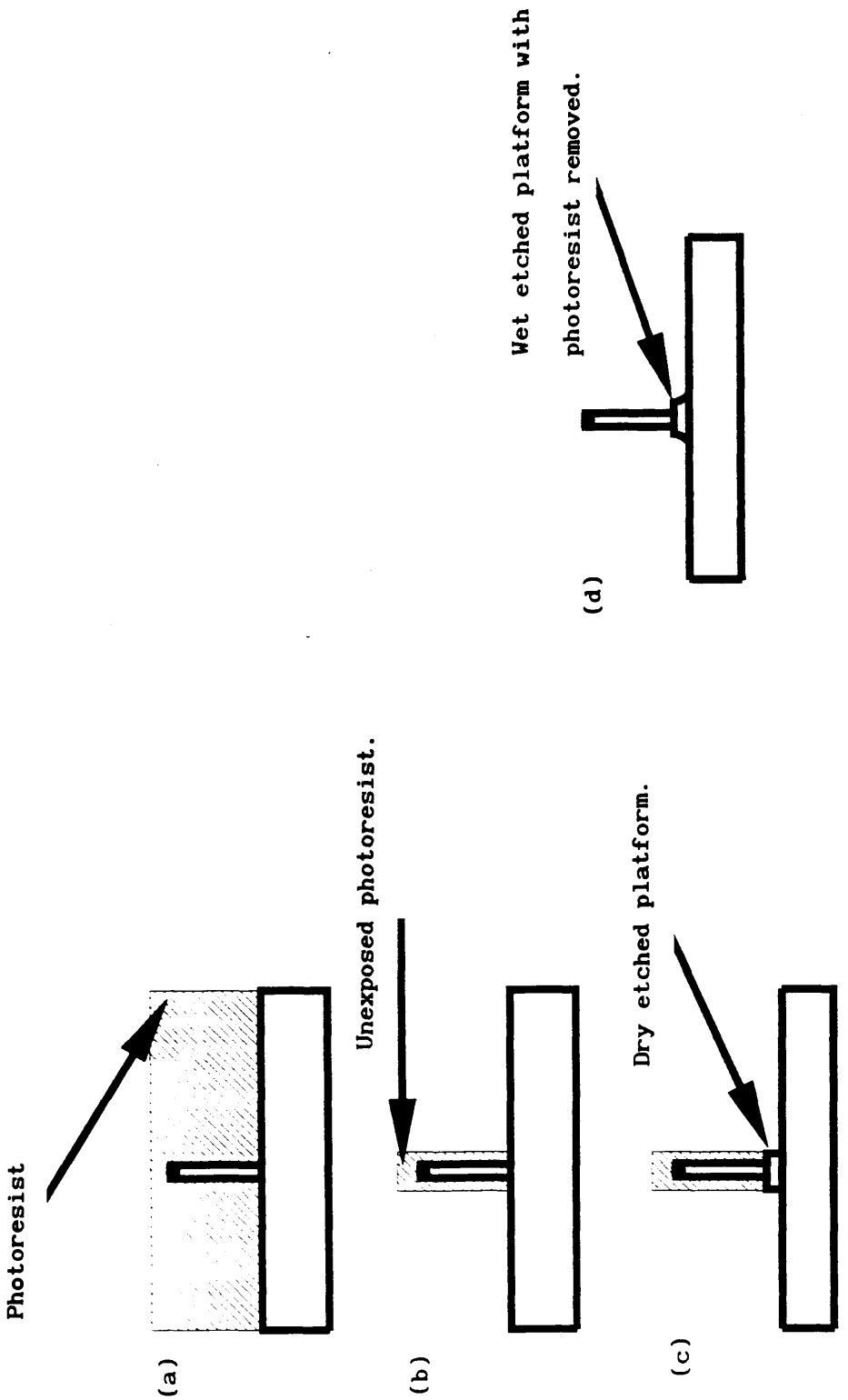

Fig. 7.4 Schematic diagram of the later stages of the specimen preparation technique used to make the quantum wires.

the incident directions of the etchant (e.g. $SiCl_4$). Therefore, when combined with the use of Ti, the wires tend to have very well defined shapes, with quite vertical walls, as shown by the SEM image of a wire in fig. 7.5. The wires are approximately 50nm thick and 500nm high, although both parameters may vary depending on the exact etching conditions used. However, although under normal circumstances the fabrication of the quantum wires is now complete, they are not yet particularly suitable for examination in a TEM.

As discussed in section 7.2, the damaged regions in the wires are revealed by forming dark field images. In order to have the wires in the correct orientation with respect to the incident beam, the wires should be able to be tilted about the [110] axis. Hence wires of the type shown in fig. 7.5 were fabricated in such a way that the long axis of the wires lay parallel to a [110] axis of the substrate on a (001) plane, as shown in fig. 7.3(d) and (e). Suitable mounting of the wires thus ensured that electrons, incident on the wire as shown in fig. 7.6, were close to being perpendicular to the (110) plane. A sample holder was specially constructed which would enable the incident electrons to be directed approximately along the [110] direction, and this is shown in fig. 7.7. As the wires are in general only 500nm high, tilting about the [110] axis would be made considerably easier if the wires were on a high, yet narrow platform. This type of platform would mean that as the wires are tilted, neither the incident nor diffracted beams would collide with either the platform or the GaAs substrate.

To make a suitable platform, the entire specimen is coated with an ultra violet sensitive photoresist, fig. 7.4(a). The photoresist is then covered with a suitable mask, exposed, and then developed, after which the sample is as shown in fig. 7.4(b). After exposure and development of the u.v. sensitive photoresist, the entire sample is dry etched in a $SiCl_4$ plasma. This results in a platform which, as a direct result of the highly anisotropic nature of the dry etching technique, has straight walls. In

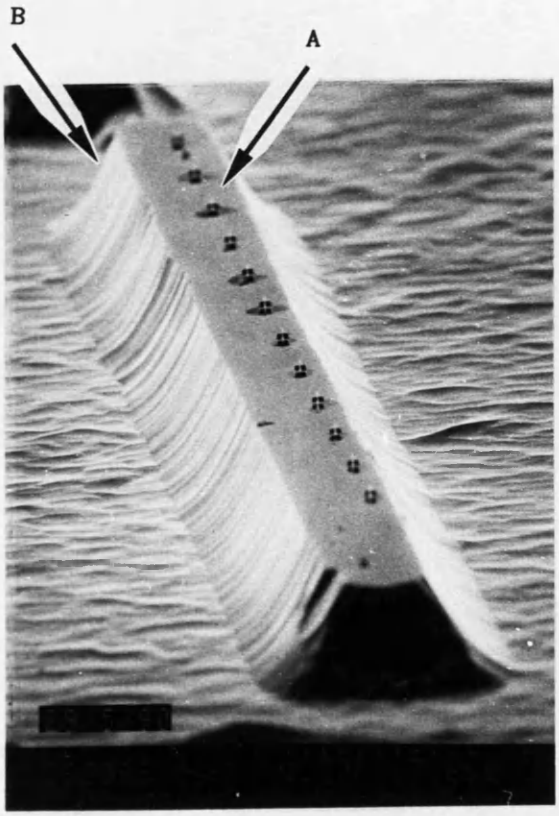

Fig. 7.5 A secondary electron microscope (SEM) image of a quantum wire. Note the wet etched platform (B) on which the wire (A) sits.

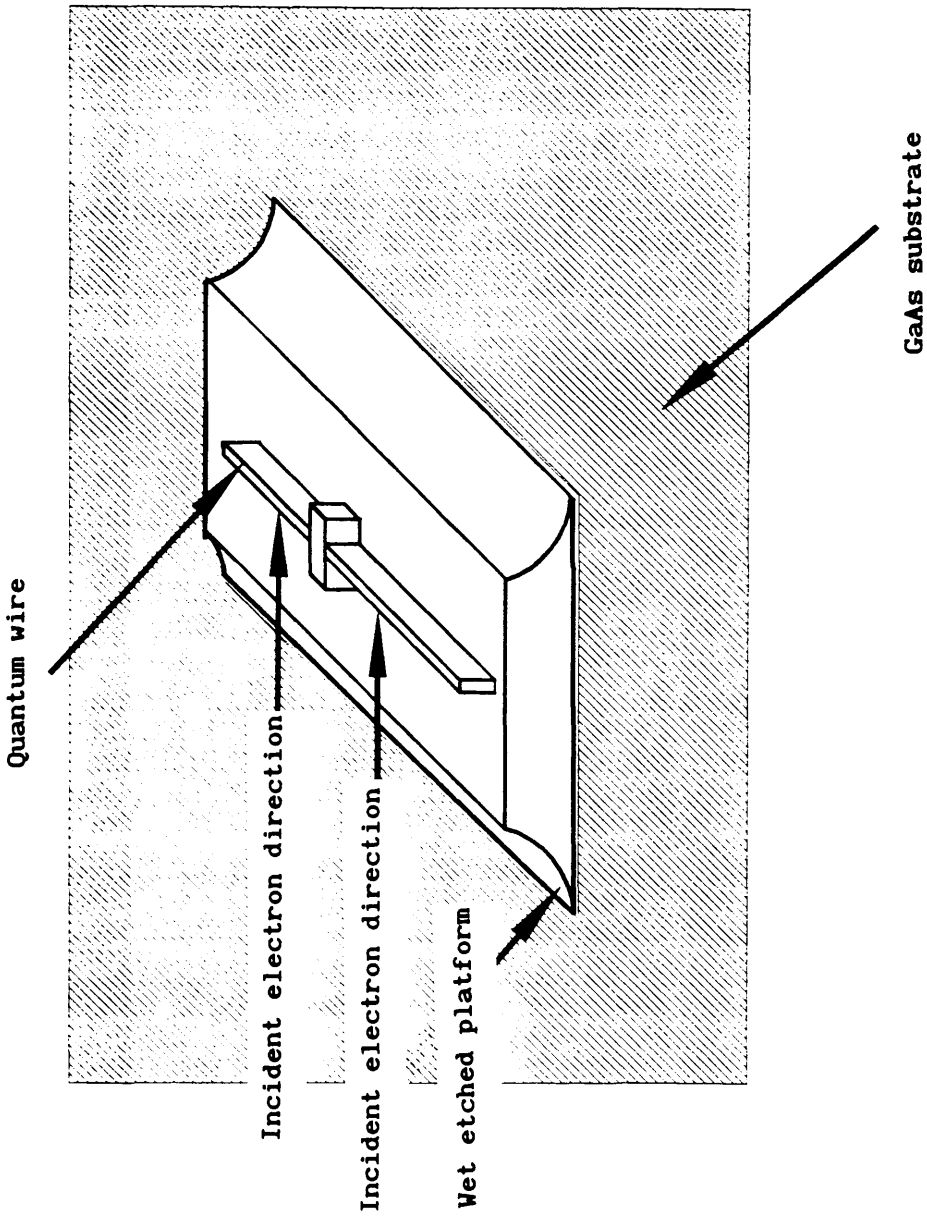

Fig. 7.6 Schematic diagram showing the initial direction of the electrons relative to the wires.

(a)

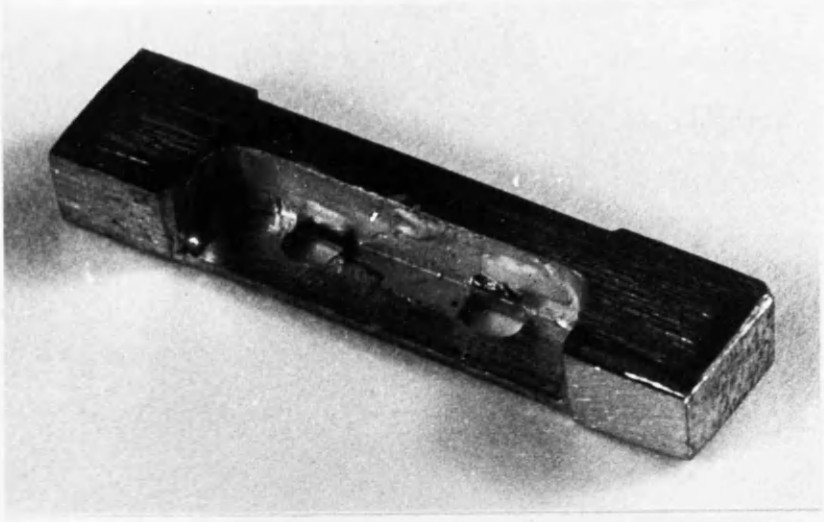

(b)

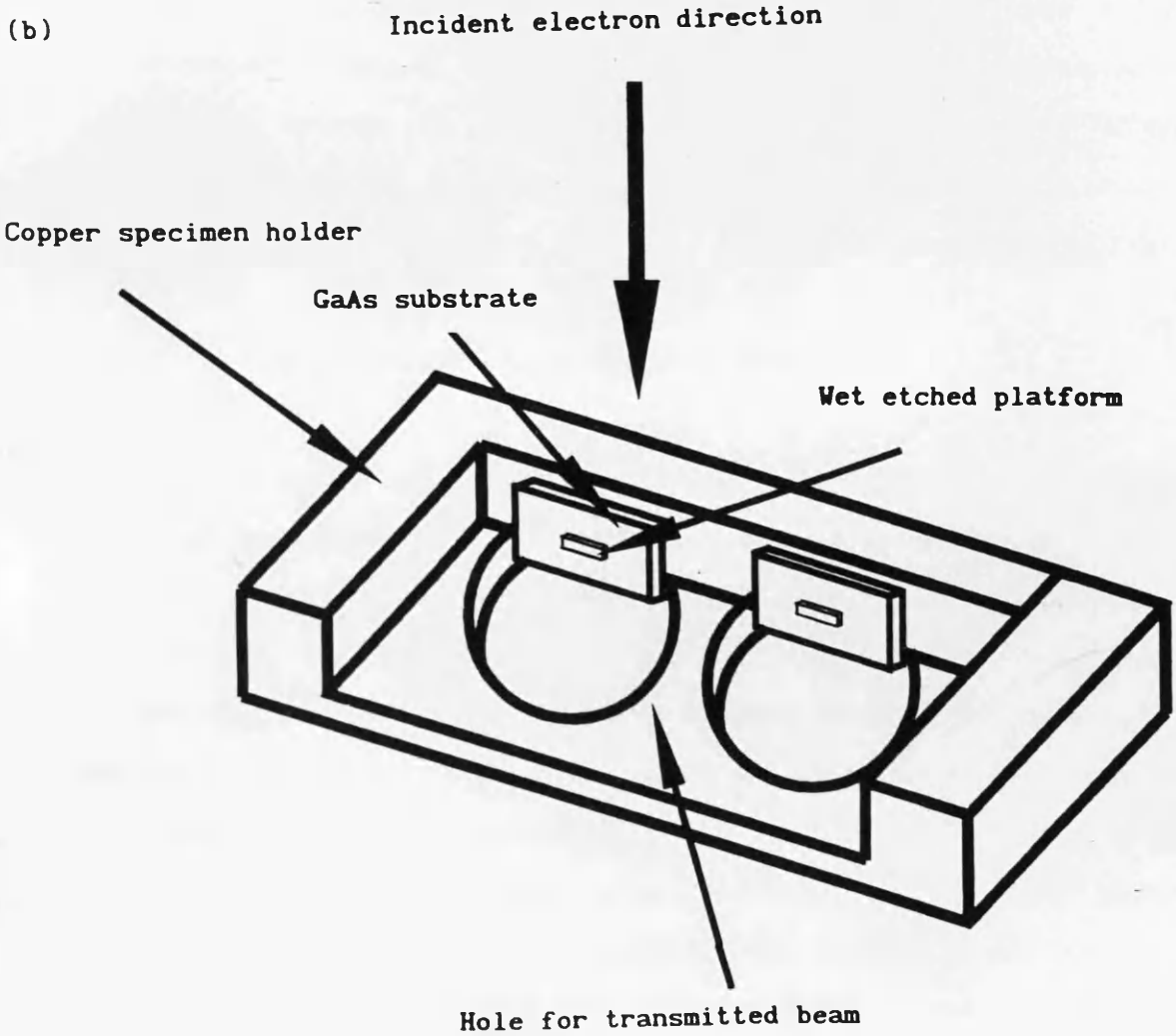

Fig. 7.7 Photograph of the specimen holder constructed in order that the wires are near the correct orientation for analysis. A schematic diagram is also shown (but not to scale) in (b).

order to etch the top of the platform back towards the base of the wires, thus reducing the area of the top surface of the platform, the sample was wet etched in a 1:8:1 solution of $H_2O:H_2O_2:H_2SO_4$. Wet etching, in contrast to dry etching is an isotropic process, and hence the platform is etched not only at its base, but also along the vertical sidewalls of the platform. After removal of the unexposed photoresist, the platform has a profile as shown in fig. 7.4(d). Platforms of this type allow the specimen to be tilted through relatively large angles, thus enabling the sample to be oriented correctly. The analysis of the wires is also made considerably easier. An SEM image of dry etched wires mounted on a wet etched platform is shown in fig. 7.5.

Quantum wires fabricated using this procedure were examined using the dark field imaging techniques discussed in section 7.2. The dry etching process carried out between fig. 7.3(c) and 7.3(d) was done using two different etching compounds viz. $SiCl_4$ and CH_4/H_2 and the damage which each causes to the wires is discussed separately in sections 7.4.1 and 7.4.2 respectively.

7.4 RESULTS FROM GaAs QUANTUM WIRES

Wires suitable for examination by TEM were prepared using the method described in section 7.3. The experimental arrangement for the study of the wires is outlined below. Diffraction patterns formed from suitably oriented wires allowed identification of the (002) diffraction spot. A diffraction pattern obtained from one of the wires is shown in fig. 7.8(a), and each of the spots is indexed in fig. 7.8(b). Only just over half of the pattern can be observed as the other half collides with the platform or the substrate, and hence is obscured. Further, using the Kikuchi (Cowley (1975)) pattern, formed with convergent incident illumination, the intensity in the (002) spot could be maximised by placing the appropriate Kikuchi band on top of the relevant spot, i.e. the intensity in an (002) spot is maximised by having the

(a)

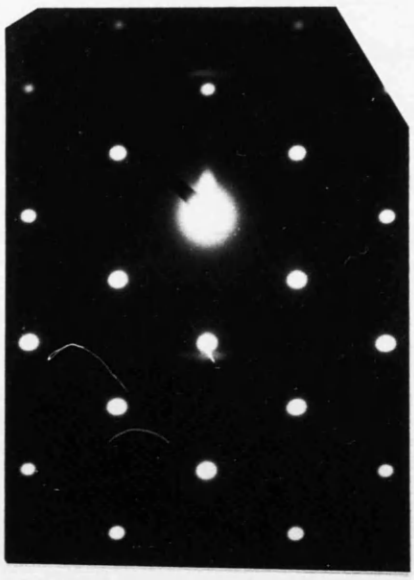

(b)

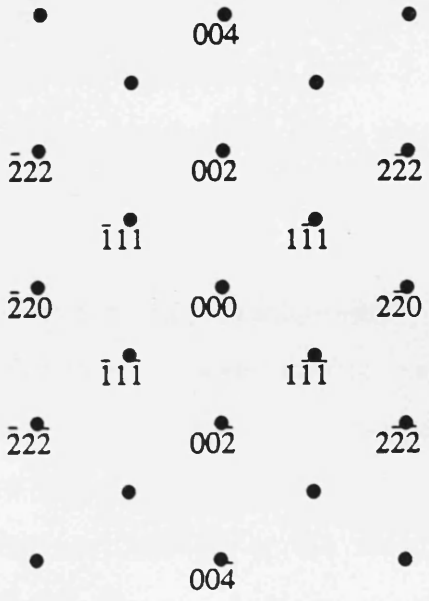

Fig. 7.8 (a) Diffraction pattern obtained from a GaAs quantum wire, with the spots indexed in (b).

(002) Kikuchi band on top of that spot. In practice the (002) Kikuchi band is so weak that it cannot be observed and so the intensity in the (002) is maximised by placing the (004) Kikuchi band (which is visible) approximately midway between the (002) and (004) diffraction spots. The specimen is then tilted slightly, while observing the (002) diffraction spot, in order to determine the orientation which maximises the intensity in the (002) spot. This ensures that the incident beam is at the Bragg angle appropriate to the (002) plane.

7.4.1 ANALYSIS OF WIRES ETCHED IN $SiCl_4$

In the case of wires etched in $SiCl_4$ the etching took place at a pressure of 12mT for 2 mins., with r.f. power of 100W and a corresponding d.c. bias of 260V. (These are standard etching conditions which have been optimised for etching GaAs using $SiCl_4$.)

The crystallinity of the wires was first examined in order to study if there was any loss of the crystal structure along the length of the wire. To enable this type of study to be undertaken, the smallest "spot" size (section 2.2) was selected on the microscope, and then focused on the wire. Diffraction patterns from chosen areas of the specimen were then formed with a convergent incident beam, (section 3.4). Under these circumstances a diffraction pattern is obtained from a region which is approximately 50nm in diameter. As the specimen is moved relative to the spot, any loss of crystallinity in the wire would be accompanied by a change in the form of the diffraction pattern. As the focused spot was moved over the wire, and in particular over the region near the end of the wire, (which had been exposed to the $SiCl_4$) no significant changes could be detected in the form of the diffraction pattern. It is therefore assumed that there is no apparent loss of the crystal structure at any point along the length of the wire.

A series of images were obtained in the TEM for various $SiCl_4$ etched wires.

In each case an (000) or bright field and (002) dark field images were recorded. An image formed by electrons which had been inelastically scattered was also obtained as any intensity variations in this type of image would be indicative of thickness variations along the length of the wire itself. An (000) image of the end of a wire etched in $SiCl_4$ is shown in fig. 7.9, with the corresponding (002), and inelastic images in figs. 7.10 to 7.11. It can clearly be seen that in the (002) image there is a bright band at the edge of the wire extending approximately 50nm along the length of the wire. From eqn. 7.6 intensity variations in the (002) image would indicate that any or all of p_1, p_2, S_V or S_{III} could be varying. By definition p_1 and p_2 represent the probability that the group five and three sites are occupied respectively. If the etching process were to introduce defects into the crystal structure, either or both of p_1 and p_2 would vary, so resulting in an intensity variation in the (002) image. However if the 50nm broad bright band in the image were caused by defects on this scale, the form of the diffraction pattern would vary around this region, and this was not found to be the case. Alternatively if vacancies did exist at e.g. group three sites and were subsequently filled by group five atoms, this would again result in intensity variations in the final (002) image as S_{III} would vary. Intensity variations in the (002) image only serve to indicate that there is some deviation away from stoichiometry in those regions which appear darker or brighter than the apparently undamaged crystal. It should also be noted that thickness variations must also be accounted for, because were the wire to become thinner towards the end of the wire, this would result in a similar change in intensity. Examination of the inelastic dark field image, fig. 7.11, and also the SEM image, fig. 7.12, indicates that there is a negligible thickness variation along the length of the wire and therefore the changes in intensity in the (002) image are not attributable to thickness variations. The intensity variations in the images can therefore be attributed to changes in the value of the structure factor, caused by compositional changes in the

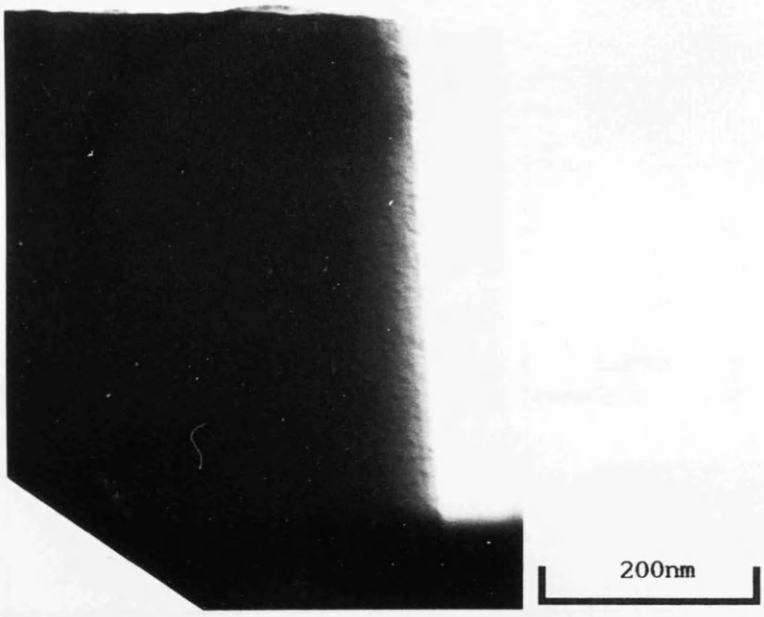

Fig. 7.9 (000) bright field image of a wire which had been dry etched in $SiCl_4$.

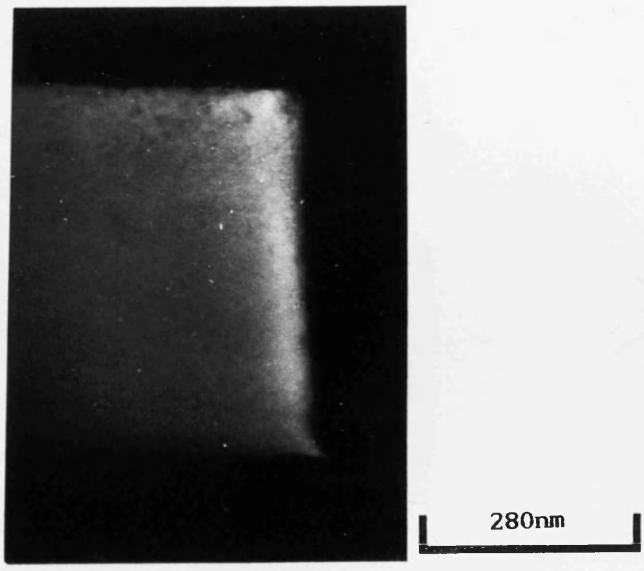

Fig. 7.10 (002) dark field image of a wire which had been dry etched in $SiCl_4$.

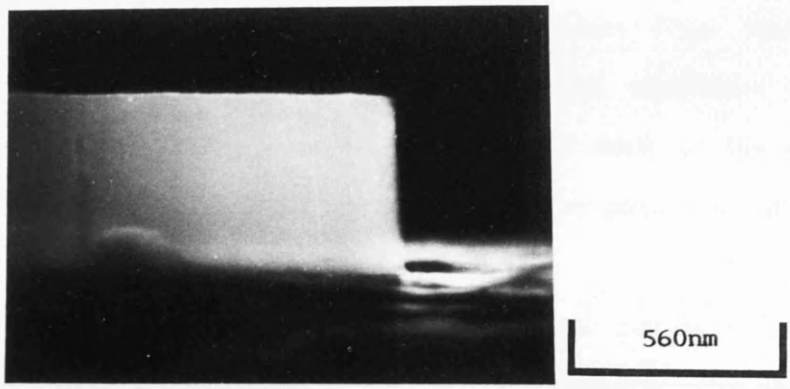

Fig. 7.11 Dark field image formed using electrons which had been inelastically scattered. The wire which had been dry etched in $SiCl_4$.

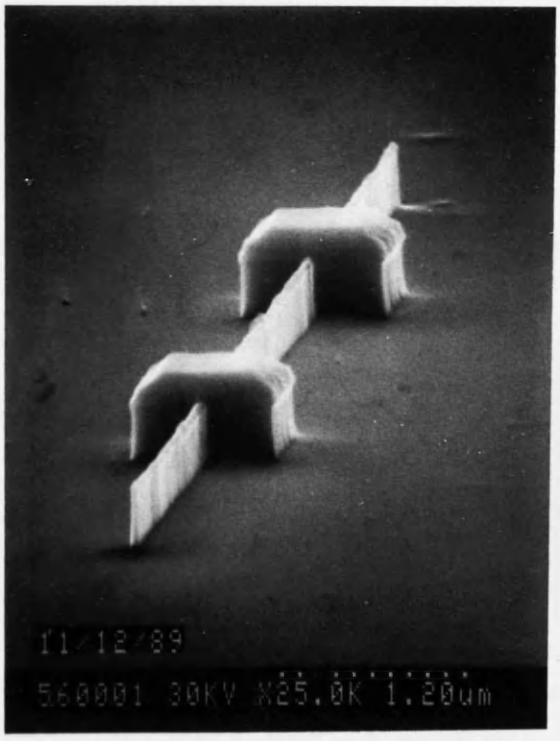

Fig. 7.12 SEM image of a wire which had been etched in $SiCl_4$.

material.

Such features have very recently been reported by Cheung (1990), during an investigation of thicker $SiCl_4$ etched wires. It appears from the (002) image, fig. 7.10, that the extent of the damage is quite significant over a distance of ≈ 50nm. From the intensity variations, the scale of the damage appears to decrease monotonically with increasing distance away from the edge of the wire.

From eqn. 7.6 it can be seen that using the relatively simple (002) dark field imaging technique it is impossible to suggest whether the intensity variations arise from changes in S_V or S_{III}. This is due to the fact that the intensity in an (002) dark field image is proportional to the SQUARE of the difference in structure factors. However that such intensity variations do exist would indicate that there are deviations away from stoichiometry in the GaAs crystal. Points such as this will be discussed further in chapter 8.

7.4.2 QUANTUM WIRES ETCHED IN CH_4/ H_2

Wires which had been dry etched in CH_4/ H_2 at a pressure of 16mT, with a gas ratio of 1:5 of CH_4/ H_2 and flow rates of 6:30sccm respectively for 14 minutes were also examined using the above procedure. The r.f. power was 150W and a d.c bias of 940V was used. These conditions are again standard and optimised for etching GaAs using CH_4/H_2.

A series of (000), (002), and inelastic images were obtained from the CH_4/ H_2 etched wires, and are shown in figs. 7.13 to 7.15. It should be noted that the Ti metal mask is marked A in fig. 7.13. From the (000) image, fig. 7.13, it is apparent that there is some coating, marked B, which extends over the entire specimen. Analysis of fig. 7.13 and the high magnification SEM image shown in fig. 7.16, indicates that this is most probably a thin residual layer of u.v. sensitive photoresist which has not been removed in the

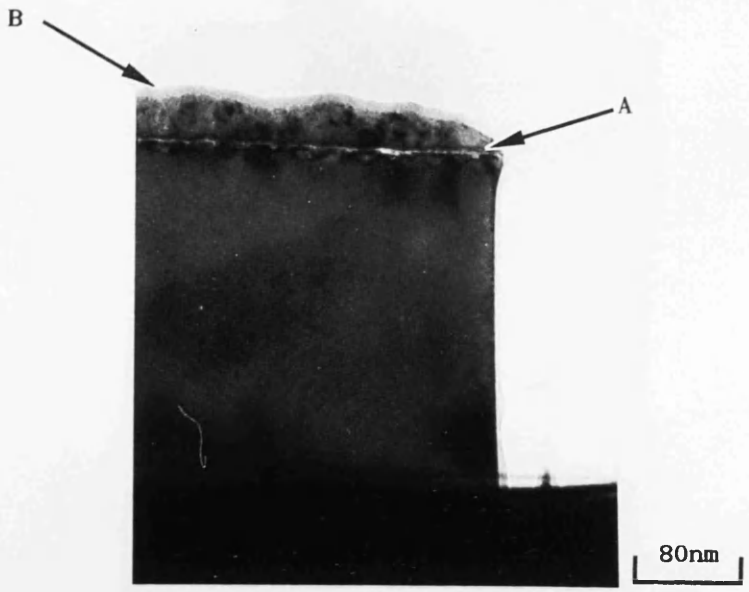

Fig. 7.13 (000) bright field image of a wire which had been dry etched in CH_4/H_2.

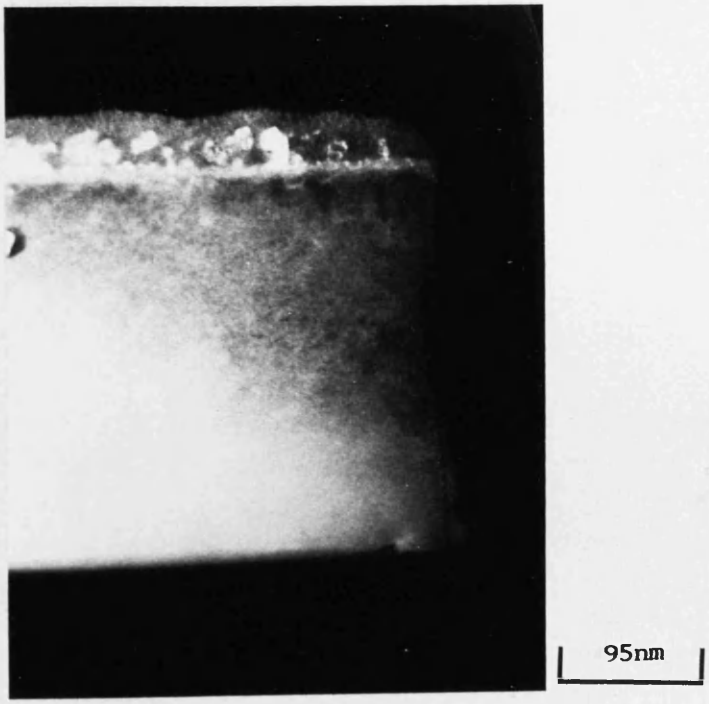

Fig. 7.14 (002) dark field image of a wire which had been dry etched in CH_4/H_2.

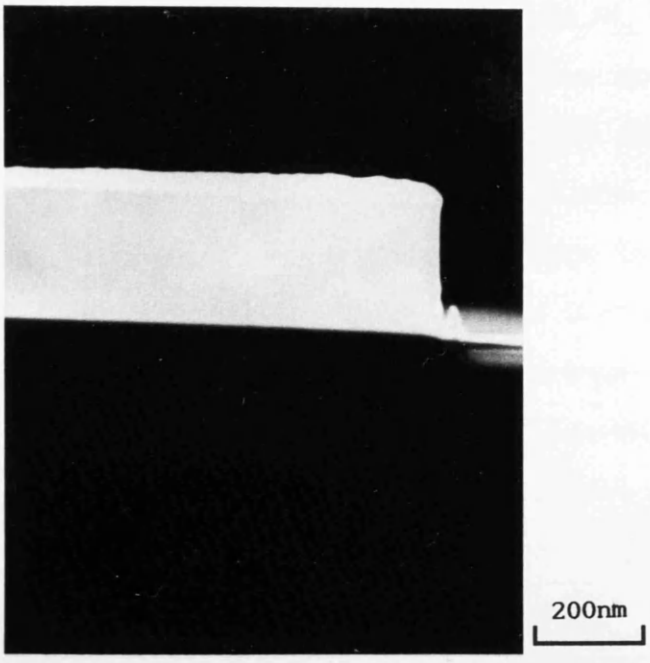

Fig. 7.15 Dark field image formed using electrons which had been inelastically scattered. The wire which had been dry etched in CH_4/H_2.

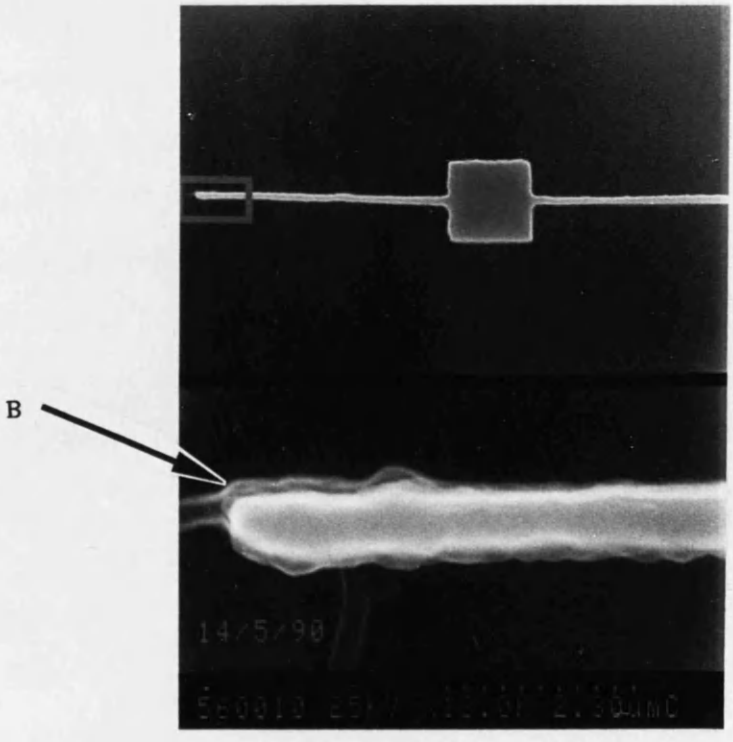

Fig. 7.16 High magnification image of a CH_4/H_2 etched wire showing the residual coating of photoresist, marked B.

development stage. From the series of TEM images, figs. 7.13 to 7.15, it is immediately apparent that the nature of the damage in the CH_4/H_2 etched wires is very different from that of the $SiCl_4$ etched wires. From the (002) dark field image the wires appear to be "spotty". Features which resemble those observed in the wires have been reported by Freiser (1985) after dry etching of Si. These features were attributed to dislocation loops in the crystal caused by the dry etching process. From images such as those of fig. 7.14, it was estimated that these dislocation loops had an average diameter of approximately 7nm. Defects of this kind have also been reported by Sandana (1985) following proton implantation of GaAs. From (002) dark field images recorded along the length of the wires no compositional changes could be detected. Convergent beam diffraction patterns were also recorded from various points along the wire, and no observable changes in the form of the pattern could be detected. It should be noted that the spot size used to form the diffraction patterns had a diameter of approximately 50nm, and that the average dislocation loop is 7nm in diameter.

GaAs wires etched in CH_4/H_2 differ significantly in their electrical and optical performance from those etched in $SiCl_4$. This was due to the presence of hydrogen trapped in the GaAs lattice after the etching process and which passivates the Si dopant. As the diffusion coefficient of hydrogen in GaAs is relatively high, this effect is normally overcome by annealing the specimen at 380C for 1s in order that the hydrogen diffuses out of the lattice. The images of the CH_4/H_2 etched wires shown in figs. 7.13 to 7.15 were obtained prior to annealing. Images recorded from the same wire after annealing showed that the dislocation loops were still present, and in fact there were no observable differences in the form of the wires after annealing. The features attributed to dislocation loops are still present, there was no apparent loss of the crystal structure, nor was there any observable change in the composition of the crystal.

7.4.3 SUMMARY

From the results described in sections 7.4.1 and 7.4.2, it has been shown that the damaged regions which are caused by the reactive ion etching can be investigated in the transmission electron microscope using dark field imaging techniques. The nature of the damage caused by the two different etching process was quite different in form; in the case of etching in $SiCl_4$, compositional changes were detected near the ends of the wires. For those wires which had been etched using CH_4/H_2, small features which are most probably attributable to dislocation loops were present in the finished wire.

Eqn. 7.6 shows that intensity variations in (002) dark field images can result from variations in any or all of p_1, p_2, S_V, or S_{III}. Compositional changes away from stoichiometry would result in brighter or darker regions in the (002) images, while dislocation loops (p_1 and/or $p_2 \neq 0$) would also result in brighter or darker regions. It should be noted that the (002) imaging mode is very useful for identifying those regions of the crystal which are damaged, however various parameters can vary and still produce the same effect, i.e. intensity changes in the final image. Interpreting (002) dark field images should therefore be done with care and also in conjunction with diffraction studies which serve to indicate the degree of crystallinity of the specimen.

CHAPTER 8

CONCLUSIONS AND FUTURE WORK

8.1 INTRODUCTION

The basic aim of this project was to use the techniques available in electron microscopy to gain further insight into the properties of structures whose shapes could be precisely defined and which have dimensions in the (sub)-micron range. The project was initially two pronged, viz. examining the magnetic properties of small magnetic particles and secondly the microstructural properties of GaAs quantum wires. During the course of the project, as a direct result of the vast amount of data produced by the in-situ magnetising experiments described in chapters 4 to 6, the bulk of the experimental work was directed towards analysing the magnetic properties of the small magnetic particles. Chapter 3 of this thesis detailed the specimen preparation process which played an integral role in defining the form of the structures to be investigated. Possibly the most important attribute of the electron beam lithography is the high spatial resolution available, as this resulted in structures, magnetic or semiconductor, whose shape is precisely controlled with a spatial resolution of ≈10nm. The conclusions drawn from the magnetising experiments on the regularly shaped particles are described in section 8.2. The results obtained from the analysis of the microstructural properties of Si doped GaAs quantum wires are discussed in section 8.3. Finally some suggestions for the possible continuation of the work are given in section 8.4.

8.2 CONCLUSIONS (MAGNETIC PARTICLES)

The domain structures and magnetic behaviour of various particles were extensively described in chapters 4 to 6. In general it was found that the

as-grown domain structures of the particles were very reproducible. The precise control over the shape and size of the particles ensured that the domain structures and magnetic behaviour was, in general, influenced primarily by the shape of the particle. It was noted that for both the $Ni_{82.5}Fe_{17.5}$ and cobalt particles, some of the particles had solenoidal as-grown domain structures while others had non-solenoidal as-grown structures. The value of R at which this transition occurs takes place at a different value for each thickness and composition of the particles. The conclusions drawn from the experiments conducted on $Ni_{82.5}Fe_{17.5}$ and cobalt particles are given separately in sections 8.2.1 and 8.2.2 respectively.

8.2.1 $Ni_{82.5}Fe_{17.5}$ PARTICLES

The as-grown domain structures and dynamic behaviour of all of the $Ni_{82.5}Fe_{17.5}$ particles was found to be very reproducible. This reflects the fact that at such small dimensions the shape of the particle exerts a dominant influence over the form of the domain structure.

In chapter 4, results obtained using the in-situ magnetising stage were presented in which the images were recorded using the Fresnel mode of Lorentz electron microscopy. Although this imaging mode does have serious limitations, it is quite well suited to the analysis of particles whose smaller in-plane dimension is in excess of approximately 0.5μm. In particular, valuable information regarding the dynamic behaviour of particles with R<4 was obtained. A most interesting feature which became apparent in the analysis of these particles is the role of the edge cluster in affecting the type of domain structures which a particle will adopt in the presence of an applied field. Edge clusters are free to move along the edge of a particle, and they move in such a way as to help to preserve the continuity relationships which must be satisfied across each domain wall. The movement of the edge clusters avoids the introduction of lengths of curved (or

charged) domain walls, such as was observed in particles with only corner and free clusters. Although most of the particles had well defined shapes, it was noted that one of the more common features of "badly" defined particles was that the corners of the particles would be rounded. In-situ magnetising experiments were also conducted on this type of particle, and again it was found that although their remanent domain structures were slightly different from that of a well defined particle, the influence of the particle shape was still sufficient that the dynamic behaviour was very reproducible. The Fresnel imaging mode, although permitting analysis of the larger particles was not suitable for the study of those particles whose smaller in-plane dimension was less than approximately 0.5μm. This was particularly unfortunate as it was the smaller and more acicular particles which displayed non-solenoidal structures.

The non-solenoidal domain structures were, however, well suited for analysis using the Foucault mode of Lorentz microscopy. A further advantage with this imaging mode was that hysteresis loops could be constructed from each isolated particle. By performing a series of in-situ experiments on the more acicular particles described in chapter 5, a series of hysteresis loops were constructed for a range of different particles. Three different shapes of hysteresis loop were found. These different forms of hysteresis loop served to illustrate how the stability of solenoidal or non-solenoidal types of domain structures varied according to the size, thickness and aspect ratio of the particle. As described in chapter 5, the range of fields over which solenoidal and non-solenoidal domain structures are stable for each particle could be qualitatively explained by examining the relative contributions to the total free energy of each particle. Acquiring hysteresis loops from various different particles made it possible to explain why certain particles were found to exist in various different solenoidal, and/or non-solenoidal types of domain structures. Once again it was found that the precisely defined shapes of the particles ensured that the dynamic behaviour of a

particular size of $Ni_{82.5}Fe_{17.5}$ particle could be quite confidently predicted.

During the analysis of the non-solenoidal domain structures, complex end closure structures were observed in all thicknesses of particles. Using the techniques available in the electron microscope, a quantitative analysis of the distribution of the magnetisation in the vicinity of the closure structure is not a simple task due to the fact that the electrons interact with induction rather than the magnetisation. For this reason, the regions around the end closure sections were examined using Kerr M-O techniques at the University of Erlangen in Germany. The magnetisation vector maps from this region were given in chapter 5 and proved most informative. The distribution of the magnetisation vector around the closure structure results in an area in which volume charge is distributed mainly in the domain with the curved walls. From the magnetisation maps presented in chapter 5, it was also observed that the positions of the domain walls in the end closure structures ensured that little or no surface charge is present at the ends of the particle.

8.2.2 COBALT PARTICLES

All of the results presented in chapters 4 and 5 were obtained from particles which had been fabricated using thermally evaporated $Ni_{82.5}Fe_{17.5}$. Due to the composition of this alloy, the magnetostriction and magnetocrystalline anisotropy have negligibly small values, and as such the resultant domain structures are determined primarily from a minimisation of the sum of the magnetostatic and domain wall energies. In order to investigate the effect of a different material on the resultant domain structure and magnetic behaviour, particles with the same range of dimensions were fabricated from cobalt. The thermally evaporated cobalt particles, as the diffraction studies of chapter 3 demonstrated, consisted of polycrystalline grains of

h.c.p. cobalt in which there was no significant texturing and the c-axis anisotropy was randomly oriented. The effect of randomly oriented magnetocrystalline anisotropy axes on the domain structures and magnetic behaviour of the particles is extensively described in chapter 6. In most cases, although there were slight differences between "normal" cobalt and $Ni_{82.5}Fe_{17.5}$ particles, both types of particles displayed the same types of solenoidal and non-solenoidal domain structures. Also they exhibited the same forms of hysteresis loops. It was noted that the local anisotropy within the grains comprising the cobalt particles produced hysteresis loops in which, during that part of the loop in which (displaced) solenoidal domain structures exist, the value of $(^{d(RM)}/_{dH})$ was less than the same thickness of $Ni_{82.5}Fe_{17.5}$ particle.

One major factor which did emerge from the studies on the cobalt particles was that the rate of evaporation and vacuum pressure are crucially important parameters in determining the magnetic properties of the particles. This is most probably due to some residual gas or water vapour in the evaporator which changes the chemical composition of the particles and hence alters the coupling length, and thus the magnetic properties of the particles. Although a great deal of care was taken to ensure that the conditions were reproduced during each evaporation, it is possible that the vacuum pressure inadvertently increased. Chemical analysis of the cobalt particles would verify or deny this hypothesis, and a method which would enable such a study to be undertaken is described in section 8.4. A consequence of the possible change in coupling length between different cobalt samples is that examination of the variation in the shape of hysteresis loop and values of switching fields are only consistent when comparing particles from the same sample. Comparing the values of H_{S1}, H_{S2}, and H_S for a particular size of 17 and 95nm thick cobalt particles, and subsequently drawing conclusions may be misleading as the coupling length in the two cases could be different.

Although this effect was most obvious in the cobalt particles, the same would

be likely to occur in $Ni_{82.5}Fe_{17.5}$ had the ratio of residual gas atoms to evaporated metal atoms increased to a value which would affect the coupling between the $Ni_{82.5}Fe_{17.5}$ crystallites. It would appear that at the rates of evaporation chosen during this project, cobalt is more susceptible to this type of behaviour.

8.2.3 SUMMARY

The results presented in chapters 4 to 6 have shown the direct influence of the various energy terms on the domain structure and magnetic behaviour of precisely defined regularly shaped particles. At this point, a brief comparison between the experimental results presented in this thesis and the theoretical predictions of Van den Berg (1984) should be made. In his treatise, (as stated in chapter 1), it is proved that the exchange energy is of second order importance and can therefore be neglected. After neglecting this energy term, and assuming no anisotropy, an algorithm was derived which could predict the possible (solenoidal) domain structures of a two dimensional body. Although the algorithm does produce good agreement with some of the experimental results presented in this thesis, there are some discrepancies, and in particular it can in no way account for any of the non-solenoidal domain structures found in the particles.

As the calculations of Kittel (1946) and Neel (1947) demonstrated, solenoidal domain structures become energetically unfavourably when the dimensions of the particle become sufficiently small. In the range of dimensions of particles used in this study, it was demonstrated that this effect would appear to occur at a value of R, (=R*), specific to the size, thickness and composition of the particle. At values of R in excess of R*, the particles will adopt non-solenoidal structures. The precise value of R* at which this transition occurs is a complex problem relating the magnetostatic and domain wall energy terms. Both of these quantities vary with size, thickness and

composition of the particle.

It was demonstrated in chapter 5 that particles which can support non-solenoidal domain structures have only (two sets of) four different non-solenoidal structures. When this fact is considered in conjunction with the experimental evidence, which would suggest that the total domain wall energy within a solenoidal domain structure is minimised, it becomes apparent that there are only a finite number of solenoidal structures which can be adopted by the particle. A simple example is shown in fig. 8.1, in which a particle with R=2 has two different solenoidal structures. These two different structures are the only distributions found in this type of particle after an a.c. demagnetisation. As the Van den Berg algorithm does not consider the domain wall energy, no predictions are offered as to why the structures of fig. 8.1 would be present rather than some other. Obviously, however, as an infinite number of structures can be predicted by the algorithm, the two structures shown in fig. 8.1 could be predicted.

Detailed theoretical micromagnetic calculations have very recently been performed by Fredkin and Koehler (1990) on particles of sizes comparable to those studied in this thesis. The details of the calculation, which involves discretisation of the particle into small elements are given elsewhere, (Fredkin and Koehler (1990)). The final results are however most interesting. The micromagnetic models of Fredkin and Koehler are able to predict the two different domain structures of fig. 8.1. They do not find any of the other possible structures which can be predicted by the Van den Berg algorithm.

Throughout this thesis it has been assumed that there is no anisotropy present in the particles. Although the use of $Ni_{82.5}Fe_{17.5}$ ensures that the magnetocrystalline anisotropy and magnetostriction terms are very low, one of the more interesting points raised by the experimental results pertains to the differences in the remanent domain structures which are present in the particles following an a.c. demagnetisation along the hard and easy

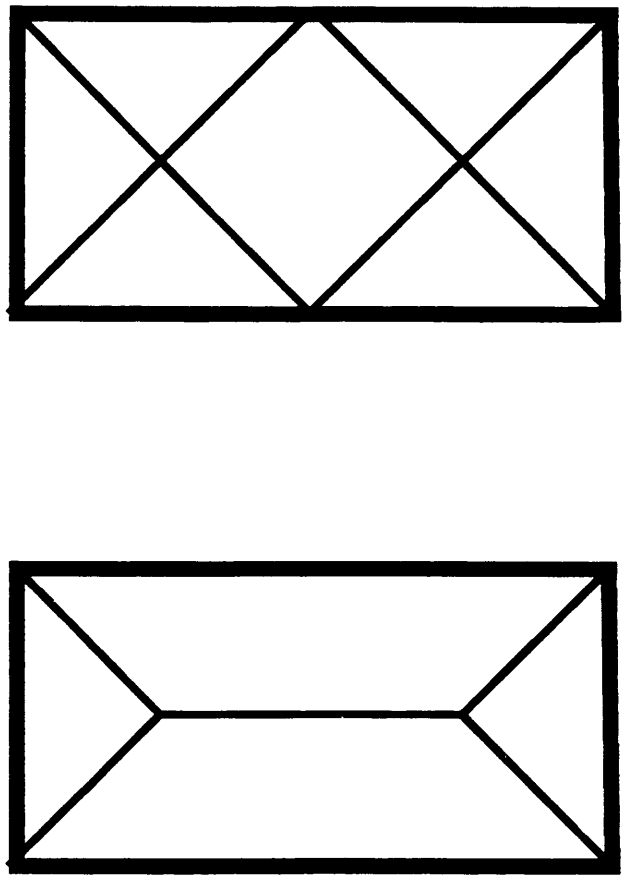

Fig. 8.1 Two posible domain structures from a particle with R=2.

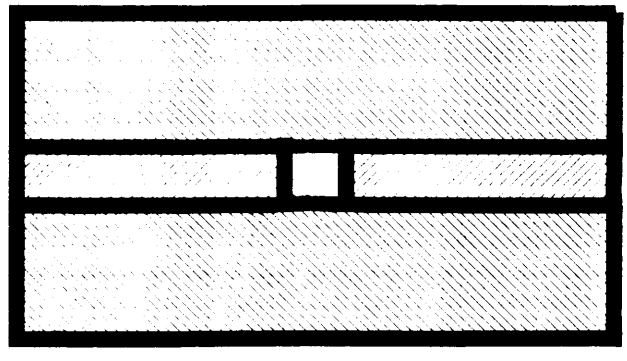

Fig 8.2 The relative orientation of four rectangles composing a particle such that they result in a void in the centre.

directions. In general it was found that careful alignment of the hard axis field resulted in solenoidal remanent domain structures which consist of long lengths of 180° walls. It is also observed that after a hard axis a.c. demagnetisation, solenoidal remanent domain structures occur in particles which do not exhibit such structures when the field is directed along the easy axis. As stated above it is assumed thst no anisotropy is present, however if this effect is caused by some local induced anisotropy, the source of the anisotropy, if it even exists, is very unclear. In particular, as the as-grown domain structures and dynamic behaviour of particles deposited orthogonally with respect to each other is very similar, it would seem unlikely that the residual laboratory field is responsible.

A most interesting observation which is evident from the analysis of the particles is the fact that the length of 180° wall present in the as-grown domain structures is frequently the minimum possible for each value of R. This would imply that the directions of the magnetisation in the end domains are predetermined in order that their relative orientations will minimise the total domain wall energy of the as-grown solenoidal structure.

8.3 CONCLUSIONS FROM ANALYSIS OF GaAs QUANTUM WIRES

The results described in chapter 7 showed that the specimen preparation techniques available using electron lithography are not only confined to the manufacture of small regularly shaped particles, but can also be adapted for various other uses. The quantum wires analysed in chapter 7 again demonstrated the ability of electron beam lithography to fabricate devices with precisely defined shapes with spatial resolutions of the order of 10nm.

As detailed in chapter 7 the structure factor contrast imaging mode in GaAs can identify the regions of the wire which have been damaged during the reactive ion etching process. The (002) dark field images allow the nature and form of the damaged regions within each of the wires to be characterised

more completely than was previously possible using other indirect techniques. The images revealed the fact that the damage within the $SiCl_4$ etched wires consisted of compositional variations near the end of the wire. This type of damage was significantly different from the damage caused by the CH_4/H_2 etching, in which features resembling the dislocation loops observed by Freiser (1983) were detected. In both cases the damaged regions were accompanied by no apparent loss of the crystal structure, and in the case of the CH_4/H_2 etched wire, no differences were observed in the form of the wire either before or after annealing.

Although the dark field imaging analysis of the quantum wires provided valuable information on the form of the damage, much work is necessary before a more complete picture is formed. Potential solutions to overcome the problems inherent to the (002) dark field imaging mode are described in section 8.4.

8.4 FUTURE WORK

The experiments carried out on the small regularly shaped particles allowed many of the questions regarding their domain structure and magnetic behaviour to be answered. Although the results from the $Ni_{82.5}Fe_{17.5}$ particles were very reproducible, this was not always the case for the cobalt particles. From the results on the cobalt particles it would appear that the ratio of residual gas atoms to evaporated metal atoms is a very important parameter. The coupling length within each of the particles would appear to depend on this parameter and also on the metal itself. It was noted that the magnetic properties of cobalt were much more susceptible to the changes in vacuum pressure or evaporation rate than those of $Ni_{82.5}Fe_{17.5}$. The changes in the coupling length would be likely to occur in $Ni_{82.5}Fe_{17.5}$ if the ratio of residual gas atoms to evaporated metal atoms increased sufficiently. In order to clarify this matter more fully, recent experiments have been

conducted by H. Wong at the University of Glasgow. In this set of experiments the vacuum pressure was held constant while the rate of evaporation was varied in a systematic manner. From this set of experiments it would appear that as the rate of evaporation decreases, from 5Å/sec to 0.2Å/sec, the as-grown domain structures and the magnetic behaviour of the particles begin to resemble those classified in chapter 6 as "abnormal".

In order to verify the chemical composition of the cobalt samples, they could also be examined by e.g. energy dispersive x-ray analysis (Bullock (1986)) in order to determine chemical composition of each sample. With a high spatial resolution technique such as EDX, it would be possible to examine the possible existence of e.g. an oxide layer on the surface of some of the crystallites. It should be noted that the impurities which may be present may made analysis of this kind quite difficult.

Therefore, although the samples gave reasonably consistent results, there is still much work to be done before the magnetic behaviour of these particles can be fully understood.

Another point which requires restating is that the shape of the particles greatly influenced the resulting domain structure and magnetic behaviour. This is primarily due to the fact that the particles have very little anisotropy other than that due to the shape of the particle. The lack of anisotropy, while being responsible for the extremely regular domain structures present in the particles was also responsible for the complex end closure structures present in each of the non-solenoidal structures. If some anisotropy could be introduced along the length of the particle, it may then be possible to eradicate this end structure, so leaving a single domain particle. If such particles could be prepared it would then allow the interesting proposition of comparing the experimental behaviour of single domain particles with the many theoretical predictions which have been formulated regarding their magnetic behaviour. In particular the variation of switching field with particle size could easily be examined using the

magnetising stage. Further, obtaining D.P.C. images from such particles would allow comparison of "real" images with the theoretical images given in chapter 2.

In order to introduce some anisotropy into the particles, various methods could be attempted, viz. depositing the metal in the presence of a magnetic field, increasing the temperature of the substrate during deposition, or deposition of the metal at non-normal incidence. This last method may have complications during the lift-off stage which may limit its success.

All of the results described throughout this thesis relate to non-interacting particles. Due to the ease with which the patterns can be scanned in the Philips PSEM, the arrangement of the particles could easily be changed to include interacting particles.

Initiating a study into interactions between particles of this type is a most complex problem in which a vast number of experimental parameters can be changed, e.g. the particles could be arranged "head to tail" or alongside each other as well as being grouped in twos, threes, etc..

A further possibility which could be explored is the introduction of defects into some of the particles. This can easily be achieved by defining each rectangular particle as being composed of 4 rectangles arranged in such a way that they do not made up the entire large rectangle, but leave a void, or defect, as shown in fig. 8.2. The effect of the defect on the domain structure and resulting dynamic behaviour can then be investigated.

Analysis of the types of domain walls present in small particles of similar dimensions was performed by McVitie (1988) on 20 and 60nm thick particles. As the thicknesses of particles used in this study are almost identical to those of McVitie, it would be safe to assume that the same types of walls exist in the particles used in this study. However, the types of domain walls present in 95nm thick particles have not been examined. From the types of domain structures found in the 95nm sample, it would appear that the walls are in some cases vortex type. Analysis using e.g. D.P.C. would allow the

wall structure to be examined more completely.

In chapter 7 the investigation of damaged regions in quantum wires proved relatively successful as a first step towards a more complete analysis of the damage induced during reactive ion etching. Unfortunately the imaging mode used did have its shortcomings. One of the major problems with this mode was the inability of the (002) images to identify which of Ga or As was deficient in the $SiCl_4$ etched wires. The structure factor imaging mode can only detect changes to the value of the structure factor, although the underlying reasons for this change remains a mystery. Analysis of the quantum wire samples using (002) dark field imaging in conjunction with high spatial resolution EDX analysis would allow firstly the damaged regions to be identified in the normal fashion, after which, using EDX, a more complete high spatial resolution compositional analysis could then take place.

Further investigation of what would appear to be dislocation loops in the CH_4/H_2 etched wires is a much more complex problem. The (002) and (000) images recorded in the JEOL 1200EX do not conclusively prove that the features tentatively identified as dislocation loops are in fact this at all. Lattice imaging using e.g. high resolution electron microscopy (HREM) may be able to provide more conclusive evidence, however in order to form lattice images the specimen requires to be very thin (<10nm). This could be achieved by over etching the specimen during the wet etching process. Although this would provide thin areas suitable for analysis by HREM, the presence of dislocation loops could affect the wet etching process, or, worse, the etching process itself may introduce dislocation loops as it thins the specimen. Therefore although these dislocation loops could be detected using HREM, their origin may remain unclear.

APPENDIX 1

CALCULATION OF THE TIME CONSTANT OF THE COILS IN THE MAGNETISING STAGE.

The magnetising stage described in chapter 2, was initially constructed with air coils. Measuring the field from this set of coils it was found that for a current of 2A, the field at the specimen was $4kA.m^{-1}$. Comparing this value with that from the coils with the soft iron core thus allows the value of the relative permeability of soft iron to be determined. It was found that the value of μ_r was 4.3.

The time constant, τ, of the coils is given by;

$$\tau = {}^{L}/_{R}$$

where L is the inductance of the coils and R is the resistance of the coils. The resistance was measured to be 0.65Ω. The inductance of the coils is given by;

$$L = {}^{N\Phi}/_{I}$$

where N is the total number of turns in the coils, Φ is the total flux and I is the current.

The magnetic field (H), and flux density (B) at the centre of the coils (assumed to be infintly long at this point) is given by;

$$H = N' I$$

$$B = \mu_o \mu_r N' I$$

where N' is the number of turns per unit length. Hence the flux is given by the area at the ends of the coils (S), multiplied by the flux density (B). Therefore, the inductance L is given by

$$L = \frac{\mu_0 \mu_r N^2 S}{l}$$

The inductance L must now be modified due to the fact that they are not infinitely long. The value of the radius of the coils divided by the length is approximately 2, and hence the value of L must be decreased by a factor of K=0.7, (Lorrain and Corrson (1970)).

$$L = \frac{\mu_0 \mu_r N^2 S}{l} \times K$$

From the above eqn. for L, the inductance of the coils was found to be 2.8×10^{-5} Henrys. Hence the time constant of the coils was found to be 4×10^{-5}s.

APPENDIX 2

FORMULAE FOR THE MAGNETIC FIELD H FROM A UNIFORMLY MAGNETISED BLOCK.

The full formulae for the components of the magnetic field (H) from a block of (x,y,z) dimensions $2L_1$ by $2L_2$ by $2L_3$ are given below. The block is centred at the origin, and is uniformly magnetised along the y direction. The three components of H are denoted by H_x, H_y, and H_z and the following notation is used for clarity;

$$x-x' = \alpha \qquad z-z' = \gamma$$

$$x-L_1 = a_- \qquad y-L_2 = b_- \qquad z-L_3 = c_-$$

$$x+L_1 = a_+ \qquad y+L_2 = b_+ \qquad z+L_3 = c_+$$

The x component of H is given by the expression;

$$H_x = \frac{M_s}{4\pi} \{ \ln(c_+ + [a_-^2 + b_-^2 + c_+^2]^{1/2} - \ln(c_+ + [a_+^2 + b_-^2 + c_+^2]^{1/2})$$

$$- \ln(c_- + [a_-^2 + b_-^2 + c_-^2]^{1/2} - \ln(c_- + [a_+^2 + b_-^2 + c_-^2]^{1/2})$$

$$- \ln(c_+ + [a_-^2 + b_+^2 + c_+^2]^{1/2} - \ln(c_+ + [a_+^2 + b_+^2 + c_+^2]^{1/2})$$

$$+ \ln(c_- + [a_-^2 + b_-^2 + c_-^2]^{1/2} - \ln(c_- + [a_+^2 + b_-^2 + c_-^2]^{1/2})$$

The y component of H is given by the expression;

$$H_y = \frac{M_s}{4\pi} \{ \tan \left(\frac{a_+}{b_-} \sin \left(\tan^{-1} \left[\frac{c_+}{(a_+^2 + b_-^2)^{0.5}} \right] \right) \right)$$

$$- \tan\left(\frac{a_+}{b_-} \sin\left(\tan^{-1}\left[\frac{c_-}{(a_+^2 + b_-^2)^{0.5}} \right]\right)\right) - \tan\left(\frac{a_-}{b_-} \sin\left(\tan^{-1}\left[\frac{c_+}{(a_-^2 + b_-^2)^{0.5}} \right]\right)\right)$$

$$+ \tan\left(\frac{a_-}{b_-} \sin\left(\tan^{-1}\left[\frac{c_-}{(a_-^2 + b_-^2)^{0.5}} \right]\right)\right) - \tan\left(\frac{a_+}{b_+} \sin\left(\tan^{-1}\left[\frac{c_+}{(a_+^2 + b_+^2)^{0.5}} \right]\right)\right)$$

$$+ \tan\left(\frac{a_+}{b_+} \sin\left(\tan^{-1}\left[\frac{c_-}{(a_+^2 + b_+^2)^{0.5}} \right]\right)\right) - \tan\left(\frac{a_-}{b_+} \sin\left(\tan^{-1}\left[\frac{c_+}{(a_-^2 + b_+^2)^{0.5}} \right]\right)\right)$$

$$- \tan\left(\frac{a_-}{b_+} \sin\left(\tan^{-1}\left[\frac{c_-}{(a_-^2 + b_+^2)^{0.5}} \right]\right)\right)\}$$

The z component of H is given by the expression;

$$H_z = \frac{M_s}{4\pi} \{ \ln(a_+ + [a_+^2 + b_-^2 + c_-^2]^{1/2} - \ln(a_+ + [a_+^2 + b_-^2 + c_+^2]^{1/2})$$

$$- \ln(a_- + [a_-^2 + b_-^2 + c_-^2]^{1/2} - \ln(a_- + [a_+^2 + b_-^2 + c_-^2]^{1/2})$$

$$- \ln(a_+ + [a_+^2 + b_+^2 + c_-^2]^{1/2} - \ln(a_+ + [a_+^2 + b_+^2 + c_+^2]^{1/2})$$

$$+ \ln(a_- + [a_-^2 + b_+^2 + c_-^2]^{1/2} - \ln(a_- + [a_-^2 + b_+^2 + c_+^2]^{1/2})$$

REFERENCES

CHAPTER 1

H.A.M. Van den Berg Ph. D. Thesis, Univ. of Delft, (1984)

F. Bloch, Z. Phys., **74**, 295 (1931)

R. Collette, J. Appl. Phys., **35**, 3294 (1964)

Feldkeller E., Z. Agnew. Phys. **15**, 206 (1963)

W. Heisenberg, Z. Physik, **49**, 619 (1928)

E.E. Huber Jr., D.O. Smith and J.G. Goodenough, J. Appl. Phys., **29**, 294, (1958)

A. Hubert, Phys. Stat. Sol., **32**, 519 (1969)

Kirchener R. and Döring W., J. Appl. Phys., **39**, 855 (1968)

R. Kosinski, Acta Physica Polonica, **A51**, 647 (1977)

A.E. LaBonte, J. Appl. Phys., **39**, 855 (1969)

S. Middelhoek, J. Appl. Phys., **34**, 1054 (1963)

Nesbitt E.A. and Wernick J.H., "Rare earth permanent magnets", pubs. Academic Press, 1973.

H. Riedel and A. Seeger, Phys. stat. sol. (b), **46**, 377 (1971)

P Weiss, J. Phys., **6**, 661 (1907)

W.F. Brown, "Micromagnetics", pubs., Interscience, (1963)

CHAPTER 2

Y. Aharonov and D. Bohm, Phys. Rev., **115**, 485 (1959)

B.E. Argyle, B. Petek and D.A. Herman Jr., J. Appl. Phys., **61**, 4303 (1987)

F. Bitter, Phys. Rev., **38**, 1903 (1931)

W.F. Brown, "Micromagnetics", pubs. Interscience, (1963)

J.N. Chapman, S. McVitie and S.J. Hefferman., accepted for publication in J. Appl. Phys., (1990)

J.N. Chapman and G.R. Morrison, J. Mag. Mag. Mat., **35**, 254 (1983)

Corb B.W., IEEE Trans Mag. MAG-**24** 2386 (1988)

J.F. Dillon Jr., J. Appl. Phys., **29**, 1286 (1958)

Goto K. and Sakurai T., Appl. Phys. Lett., **30** 356 (1977)

J.P. Jakubovics, Phil. Mag., **30**, 983 (1974)

L. Landau and E. Lifshitz, Phys. Z. Sowjetunion, **8**, 153 (1935)

Martin Y., Abraham D.W., Hobbs P.C.D. and Wickramasinghe H.K., J. Electrochemical Soc., submitted Nov 1989

I. R. McFadyen, Ph.D. Thesis, Univ. of Glasgow (1986)

S. Mcvitie, Ph.D. Thesis, University of Glasgow (1988)

Rave W. and Hubert A. IEEE Trans. Mag. MAG-**26** 2813 (1990)

Ruhrig M., Bartsch W., Vieth M. and Hubert A., IEEE Trans. Mag. MAG-**26** 2807 (1990)

Tsuno K. and Taoka T., Japan J. Appl. Phys. **22** (1983)

H.A.M. Van den Berg, Ph.D. Thesis, Univ. of Delft, (1984)

H.A.M. Van den Berg, J. Appl. Phys., **60**, 1104 (1986)

CHAPTER 3

B.E. Argyle, B. Petek and D.A. Herman Jr., J. Appl. Phys., **61**, 4303 (1987)

K.L. Chopra "Thin Film Ferromagnetic media" pubs. McGraw-Hill (1969)

Corb B.W., IEEE Trans Mag. MAG-24 2386 (1988)

Cosimini G.J., Lo D.S., Zierhut L.G., Paul M.C., Dean R.H. and Matysic K.J., IEEE Trans Mag. MAG-24 2060 (1988)

Flanders P.J. and Doyle W.D., Rev. Sci. Instrum., **30**, 7, 548 (1962)

Frenkel J. and Dorfman J., Nature **126**, 274 (1930)

Fredkin D.R. and Koehler T.R. IEEE Trans. MAg. MAG-**26** 1518 (1990)

Huijer E. and Watson J.K., J. Appl. Phys 50 2149 (1979)

Kittel C., Phys. Rev. 70 965 (1946)

Lo D.S., Cosimini G.J., Zierhut L.G., Dean R.H. and Paul M.C., IEEE Trans Mag. MAG-21 1776

W.S. Mackie, Ph.D. Thesis, Univ. of Glasgow (1984)

W.S. Mackie and S.P. Beaumont, Solid State Tech., **28**, 117 (1985)

S. Mcvitie, Univ. of Glasgow (1988)

S. Mcvitie and J.N. Chapman, IEEE Trans. Mag. MAG-**24** 1778 (1988)

Neel L., Compt. rend. 2224, 1488, 1550 (1947)

Rührig M., Bartsch W., Vieth M. and Hubert A., IEEE Trans. Mag. MAG-**26** 2807

(1990)

Schabes M.E. and Bertram H.N., J. Appl. Phys. 64 1347 (1988)

Schabes M.E. and Bertram H.N., J. Appl. Phys. 64 5832 (1988)

Tanaka T., Yazawa K. and Masuya H., IEEE TRANS MAG. MAG-21 2090 (1985)

Van der Voort F.A.N. and Van den Berg H.A.M., IEEE Trans mag. MAG-23 250 (1987)

Vershinin V.V. Pol'skiy A.I. and Yakovchuk V.Yu., Phys. Met. Metall. 54 58 (1982)

Williams W. and Dunlop D.J., Nature 337 634 (1989)

Zhu J-G. and Bertram H.N., J. Appl. Phys., 63 3248 (1988)

CHAPTER 4

S. Mcvitie, Univ. of Glasgow (1988)

S. Mcvitie and J.N. Chapman, IEEE Trans. Mag. MAG-**24** 1778 (1988)

M. Ruhrig, private communication (1989)

CHAPTER 5

A. Hubert, private communication (1990)

A. Hubert, Phys. Stat. Sol., **32**, 519 (1969)

Jiles D. "Introduction to Magnetism and Magnetic Materials" pubs. Chapman and Hall (1991)

Rave W. and Hubert A. IEEE Trans. Mag. MAG-**26** 2813 (1990)

Rhodes P. and Rowlands G. Proc. Leeds Phil and Lit. Soc. **6** 191 (1954)

H.A.M. Van den Berg, Ph.D. Thesis, Univ. of Delft, (1984)

H.A.M. Van den Berg, J. Appl. Phys. **61** 4194 (1987)

CHAPTER 6

Jiles D. "Introduction to Magnetism and Magnetic Materials" pubs. Chapman and Hall (1991)

CHAPTER 7

Adams J.A., Thayne I.G., Cameron N.I., Taylor M.R.S., Beaumont S.P., Wilkinson C.D.W., Johnson N.P., Kean A.H. and Stanley C.R., "Microcircuit Engineering 89" ed. Ahmed et al, pubs. Elsevier (1990)

Cheung R., Thoms S., Beaumont S.P., Doughty G., Law V. and Wilkinson C.D.W. Electronic Lett., **23** 857 (1987)

Cheung R., Thoms S., McIntyre I., Wilkinson C.D.W. and Beaumont S.P., J. Vac. Sci. Technol., 6 1911 (1988) Cheung R., Birnie A., Chapman J.N. and Wilkinon C.D.W. "Microcircuit Engineering 89" ed. Ahmed et al, pubs. Elsevier (1990)

Cowley J. M., "Diffraction Physics" pubs. North-Holland (1975)

Freiser R.G., Montillo F.J., Zingerman N.B., Chu W.K. and Mader S.R., J. Electrochem. Soc., **130** 2237 (1983)

Kelly M. and Weisbuch C., "Physics and fabrication of microstructures and microdevices." pubs. Berlin: springer (1986)

Kittel C., "Introduction to Solid State Physics", pubs. Wiley, (1986)

McGibbon A., Ph.D. Thesis, University of Glasgow, (1989)

Sadana D.K., Zavada J.M., Jenkinson H.A. and Sands T., Appl. Phys. Lett., **47** 691 (1985)

Watt M., Sottomayor-Torres C.M., Cheung R., Wilkinson C.D.W., Arnot H.E.G. and Beaumont S.P., J. Modern Optics **35** 365 (1988)

CHAPTER 8

J.F. Bullock, J.M. Tichmarsh and C.J. Humphreys, Semicond. Sci. Technol. **1** 343 (1986).

Fredkin D.R. and Koehler T.R. IEEE Trans. MAg. MAG-**26** 1518 (1990)

Freiser R.G., Montillo F.J., Zingerman N.B., Chu W.K. and Mader S.R., J. Electrochem. Soc., **130** 2237 (1983)

Kittel C., Phys. Rev. 70 965 (1946)

Neel L., Compt. rend. 2224, 1488, 1550 (1947)

S. Mcvitie, Ph.D. Thesis, University of Glasgow (1988)

H.A.M. Van den Berg, Ph.D. Thesis, Univ. of Delft, (1984)

Appendix 1

P. Lorrain and D. Corson, "Electromagnetic fields and waves", pubs. W.H. Freeman and Co., (1970)